

**AN EFFICIENT AB-INITIO NON-EQUILIBRIUM GREEN'S
FUNCTION APPROACH TO CARRIERS DYNAMICS IN
MANY-BODY INTERACTING SYSTEMS**

Dissertation
zur Erlangung des Doktorgrades
an der Fakultät für Mathematik, Informatik und Naturwissenschaften
Fachbereich Physik
der Universität Hamburg

vorgelegt von

Fabio Covito

Hamburg

2019

Gutachter/innen der Dissertation:

Prof. Dr. Daniela Pfannkuche
Prof. Dr. Angel Rubio

Zusammensetzung der Prüfungskommission:

Prof. Dr. Peter Schmelcher
Prof. Dr. Daniela Pfannkuche
Prof. Dr. Angel Rubio
Prof. Dr. Alexander Lichtenstein
Dr. Andrea Trabattoni

Vorsitzender der Prüfungskommission:

Prof. Dr. Peter Schmelcher

Datum der Disputation:

19.03.2020

Vorsitzender Fach-Promotionsausschusses PHYSIK:

Prof. Dr. Günter H. W. Sigl

Leiter des Fachbereichs PHYSIK:

Prof. Dr. Wolfgang Hansen

Dekan der Fakultät MIN:

Prof. Dr. Heinrich Graener

Eidesstattliche Versicherung / Declaration on oath

Hiermit versichere ich an Eides statt, die vorliegende Dissertationsschrift selbst verfasst und keine anderen als die angegebenen Hilfsmittel und Quellen benutzt zu haben.

Die eingereichte schriftliche Fassung entspricht der auf dem elektronischen Speichermedium.

Die Dissertation wurde in der vorgelegten oder einer ähnlichen Form nicht schon einmal in einem früheren Promotionsverfahren angenommen oder als ungenügend beurteilt.

Hamburg, den 16.12.2019

Unterschrift des Doktoranden

Preface

This thesis work has been carried out at the Max Planck Institute for the Structure and Dynamics of Matter (MPSD) of Hamburg and at the University of Hamburg from November 2015 to December 2019 under the supervision of Prof. Angel Rubio, Prof. Gianluca Stefanucci and Prof. Daniela Pfannkuche. The project has been funded by the European Research Council (ERC-2015-AdG-694097).

I would like to express my deep gratitude to my advisor, Prof. Angel Rubio, for his guidance and support throughout my whole Ph.D. and for giving me the opportunity to work in such a great environment. All the interesting (and intense) discussions kept me motivated and focused all along. Grazie, Angel, per tutto!

My special thanks also go to Prof. Gianluca Stefanucci and Dr. Enrico Perfetto, for introducing and guiding me into the world of non-equilibrium Green's function and for teaching me so much, ranging from technical matters, to more fundamental ones, starting already during my undergraduate program. My Ph.D. would have been impossible without you – grazie!

I would also like to thank Prof. Pfannkuche for the great discussions we had during the course of my doctoral studies and for all the interesting comments.

My gratitude, of course, also goes to Florian for all the help and guidance in the projects on transport. Even though it was never “just a quick

little project”, I learned a lot while working with you and I had a lot of fun doing it. You are welcome for all the lifts, but thank you a lot for everything!

Thanks go to Michael Sentef and Riku Tuovinen for the collaboration on thermo-electric transport. Thanks to Nicolas Tancogne-Dejean, Micael Oliveira and Iris Theophilou for the discussions and support with technical matters and to Ute Ramseger for the administrative support (especially in the last phase). Thanks Ruggi for the laughs and discussions! Thanks to my office mates Gabriel, Davis and Vasilis for being awesome “neighbors” and making the whole Ph.D. experience more fun. Thanks for signing, listening to loud metal music or old school gangster rap. It was always fun!

Of course the acknowledgements would not be complete without thanking the “acquired” Italians. Thanks Riku for your finnish coffee, it was great looking at the sea. Thanks José for being my fasting buddy and for being my “simonista” companion.

Now to the real Italians. I cannot thank you enough, Simone and Enrico. Thanks for all the laughs and stupid things done together. Thanks Enrico for all the crazy dialect, for the sausages and for all the things I really cannot write here. Thanks Simone for being my coach other than annoying friend, “kind of ok” collaborator, time waster and modelling colleague. Please, never forget that “te devi muove!”.

Thanks to everybody that made my stay in Hamburg fun, interesting and full of good memories and to all that made also my time away from Hamburg great – you are too many to mention here. Thanks also to my mostri Andrea and Gabriele for being great friends, even at long distance.

Thanks Benedetta for always being there no matter what. Thanks for always repeating me I can solve all difficulties when things don’t go as

planned. Thanks for your unconditional and unending support and thank you for so much more.

Infine, ma decisamente non per ordine di importanza, grazie mamma e papà! Grazie per avermi sempre supportato senza fare troppe domande e per esserci sempre. Tutto questo davvero non sarebbe stato possibile senza di voi. Grazie per tutti i “pacchi da giù”, per tutte le telefonate su skype e grazie per tutto. Non posso ringraziarvi abbastanza.

Grazie anche alla mia famiglia e alle nonne che, nonostante vedano “il tedesco” due volte l’anno, non smettono mai di dimostrare il loro orgoglio nei miei confronti e farmi sentire il calore di una bella, grossa famiglia italiana in ogni momento.

Abstract

The study of ultrafast electron dynamics has drawn much attention in the past few years with the advent of advanced experimental techniques to access physical observables at the femtoseconds timescale. Many applications in physics, chemistry and biology are based on electron dynamics and understanding and controlling the flow of electrons would not only answer fundamental questions about physical processes, but further technological advances. While, in principle, solving the nonrelativistic Schrödinger equation would completely determine any physical phenomenon, an arbitrarily accurate resolution is essentially impossible for any case other than Hydrogen-like systems. For this reason, great effort has been put in the resolution of the many-electron problem, but many questions still go unanswered due to the highly complex nature of electronic correlations and the lack of computationally efficient methods.

In this thesis, a study of the role of electron correlations is carried out, with focus on the description of ultrafast electron dynamics in finite systems. To this extent, a first-principle non-equilibrium Green's function (NEGF) approach based on the Generalized Kadanoff-Baym Ansatz (GKBA) for the study of ultrafast electron dynamics is put forward. The method is built upon approximations aimed at increasing the efficiency of the otherwise computationally cumbersome NEGF equations, while correctly describing physical phenomena. By trimming down on the complexity of the calculation of the correlation self-energy one can analyze the ultrafast dy-

namics of systems with up to tens of electrons, otherwise inaccessible with standard methods, which lack the required efficiency or accuracy. To complement this study, an analysis of correlation has been carried out in the context of Time-Dependent Density-Functional Theory. A construction for the exchange correlation potential, encoding electronic correlations and memory effects, is developed, to study transport in nanoscale devices.

In conclusion, this thesis aims to deepen our understanding of non-equilibrium electron dynamics by providing the methodology to study never-before simulated phenomena and gain insight into the role of correlations in electron-electron interaction.

Zusammenfassung

Die Untersuchung ultraschneller Elektronendynamik hat in den letzten Jahren viel Aufmerksamkeit erregt, insbesondere durch die Entwicklung fortschrittlicher experimenteller Techniken, welche physikalische Beobachtungen im Zeitraum von Femtosekunden ermöglichen. Viele Anwendungen in Physik, Chemie und Biologie basieren auf der Dynamik der Elektronen, und das Verständnis und die Kontrolle des Elektronenflusses würde nicht nur grundlegende Fragen zu physikalischen Prozessen beantworten, sondern auch technologischen Fortschritt ermöglichen. Während die Lösung der nicht-relativistischen Schrödingergleichung prinzipiell jedes physikalische Phänomen vollständig bestimmt, ist eine beliebig genaue Lösung in der Praxis, für alles außer wasserstoffähnliche Systeme, unmöglich. Deshalb sind große Anstrengungen unternommen worden, um das Vielteilchenproblem wechselwirkender Elektronen zu lösen, aber viele Fragen bleiben aufgrund der hohen Komplexität elektronischer Korrelationen und des Fehlens effizienter numerischer Methoden unbeantwortet.

Im Rahmen dieser Arbeit wird eine Studie über die Rolle der Korrelationen von Elektronen durchgeführt, mit Schwerpunkt auf der Beschreibung ultraschneller Elektronendynamik in endlichen Systemen. Im Speziellen wird eine first-principle, non-equilibrium Green's Function (NEGF) Methode, basierend auf der Grundlage des Generalized Kadanoff-Baym Ansatzes (GKBA), zur Untersuchung ultraschneller Elektronendynamik vorgeschlagen. Das Verfahren basiert auf Näherungen, welche darauf abzielen die nu-

merische Effizienz der Lösung der rechenintensiven NEGF-Gleichungen zu erhöhen, und gleichzeitig physikalische Phänomene korrekt zu beschreiben. Durch Reduzierung der Komplexität der Berechnung der Korrelations-Selbstenergie kann ultraschnelle Dynamik von Systemen mit zehn oder mehr Elektronen analysiert werden, was mit Standardmethoden, welche nicht über die erforderliche Effizienz oder Genauigkeit verfügen, bisher nicht möglich ist. Zur Ergänzung dieser Studie wird eine Analyse der Beschreibung von Korrelation im Rahmen der zeitabhängigen Dichtefunktionaltheorie durchgeführt. Dazu wird eine Näherungen für das sogenannte Austauschkorrelationspotenzial konstruiert, welche elektronische Korrelationen und Retardationseffekte beschreibt, um Elektronentransport durch Schaltkreisen im Nanobereich zu untersuchen.

Das Hauptziel dieser Arbeit ist es unser Verständnis von Nichtgleichgewichtsprozessen und Dynamik von Elektronen zu vertiefen, indem Methoden entwickelt und zur Verfügung gestellt werden, um nie zuvor simulierte Phänomene zu untersuchen und Einblicke in die Rolle von Korrelationen in der Elektronenwechselwirkung zu gewinnen.

List of Publications

Publication I

Real-time dynamics of Auger wave packets and decays in ultrafast charge migration processes

Fabio Covito, Enrico Perfetto, Angel Rubio and Gianluca Stefanucci, *Physical Review A*, **97** (6), 061401 (2018).

Publication II

Benchmarking nonequilibrium Green's functions against configuration interaction for time-dependent Auger decay processes

Fabio Covito, Enrico Perfetto, Angel Rubio and Gianluca Stefanucci, *The European Physical Journal B*, **91** (10), 216 (2018).

Publication III

Efficient computation of the second-Born self-energy using tensor-contraction operations

Riku Tuovinen, Fabio Covito, Michael A. Sentef, *Journal of Chemical Physics*, **97**, 174110 (2019).

Publication IV

Laser-assisted ionisation of adenine as a protection mechanism against radiation damage

Erik P. Månsson, Simone Latini, Fabio Covito, Vincent Wanie, Mara Galli, Enrico Perfetto, Gianluca Stefanucci, Hannes Hübener, Umberto De Giovanni, Mattea C. Castrovilli, Andrea Trabattoni, Fabio Frassetto, Luca Polletto, Jason B. Greenwood, François Légaré, Mauro Nisoli, Angel Rubio and Francesca Calegari, *Submitted to Nature Physics*.

Publication V

Transient charge and energy flow in the wide-band limit

Fabio Covito, Florian G. Eich, Riku Tuovinen, Michael A. Sentef and Angel Rubio, *Journal of Chemical Theory and Computation*, **14**, pp 2495–2504 (2018).

Publication VI

Non-adiabatic electron dynamics in tunneling junctions: lattice Exchange-Correlation potential

Fabio Covito, Angel Rubio and Florian G. Eich, *Journal of Chemical Theory and Computation*, accepted, (2019), DOI: 10.1021/acs.jctc.9b00893.

Contents

Preface	i
Abstract	v
Zusammenfassung	vii
List of Publications	ix
Contents	xi
1 Introduction	1
2 Introduction to NEGF	7
2.1 Quantum mechanical theory and connection to experiment .	7
2.2 Keldysh-Green's function	8
2.3 The Kadanoff-Baym equations	9
2.4 The embedding self-energy	15
2.5 The Generalized Kadanoff-Baym Ansatz	22
Publication I	25
Publication II	41
Publication III	51

Publication IV	61
3 Introduction to TDDFT	101
3.1 Basics of (TD)DFT	101
3.2 Adiabatic functionals	106
3.3 Transport within TDDFT	107
Publication V	111
Publication VI	125
4 Conclusion	137
Bibliography	145

Chapter 1

Introduction

Almost a century has gone by since the introduction of the Schrödinger equation [1] and the numerous attempts to its resolution have given access to the understanding of the quantum mechanical world beyond any imagination. Nonetheless, even after years of extensive study of its implications, its appeal has nowadays all but dimmed. The Schrödinger equation can be cast in a time-independent framework, and its resolution allows the study of static properties of quantum systems, such as: states of matter in equilibrium, formation energies, crystal geometries, electronic density, and so on. The time-dependent counterpart extends this understanding to the time domain, giving insight also into the out-of-equilibrium situations and its resolution still represents a challenge for scientific progress. Particular interest in non-equilibrium quantum mechanics has arisen with the advent of more sophisticated tools for observing and influencing physical processes at the microscopic level, e.g. laser light, magnetic fields, etc. This is of crucial importance to science and technology in the fields of physics, chemistry and biology. Light and its interaction with matter, electron dynamics, transport in nanoscale circuitry, analysis and control of chemical reactions, transport of bio-signals and change in the structure of biological systems, are just a few examples of out-of-equilibrium quantum phenomena. In this

realm, a central role is played by electrons, whose dynamical properties can change even on the femto- to attosecond timescale due to their mutual interaction as well as the interaction with other degrees of freedom. How on a microscopical level electron dynamics influences these processes, though, is an ongoing matter of investigation in the scientific world.

One of the most successful means of influencing and probing physical processes is undoubtedly the laser. Since its invention in 1960 [2, 3], the characteristics of available lasers have drastically improved thanks to advances in the technologies used for their production as well as their theoretical modeling, paving the way for new research areas, such as: cold atoms in optical traps, nanoscale transport, molecular transport, nonequilibrium phase transitions, etc. We have nowadays pushed the intensity, focus size, peak energy and duration of lasers to a point where we can manipulate and track electron dynamics down to the attosecond timescale, giving birth to a branch of science referred to as “attosecond physics” [4]. The challenges in this field are diverse, ranging from the manufacture of lasers of high enough quality to the theoretical understanding of the processes induced and observed. Theory has the role of closing the gap between the measured physical observables and microscopic variables. As stated before, electrons are of central importance at these length- and timescales, and their properties are affected by their mutual interaction, their interaction with light and their coupling to nuclear motion. A schematic depiction of the timescales in question can be found in Fig. 1.1. In general, shorter timescales are associated with electronic motion, but less energetic electronic processes can easily overlap with nuclear dynamics. Moreover, collective phenomena happen at longer timescales compared to processes involving single electrons or nuclei, e.g. collective fermionic or bosonic excitations in solids, formation of new states of matter due to hybridization with light, and so

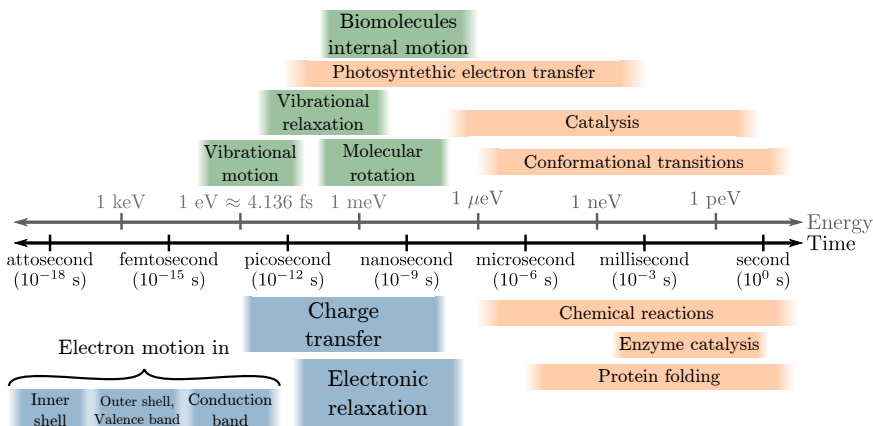


Figure 1.1: Characteristic energy and timescales of the microscopic world in the domain of interest of this work. Processes associated with nuclear motion are in green, the ones associated with electron dynamics are in light blue and in orange more complex processes involving both nuclear and electronic motion.

on. All the mechanisms mentioned in Fig. 1.1 are important in the description of the technological processes mentioned earlier.

Although all the above-mentioned effects are described within the Schrödinger equation, its exact solution cannot be practically calculated even for small molecules, as the computational power required to solve such a problem can easily exceed the processing capability of any computing unit by many orders of magnitude. For this reason, simplifications to the Schrödinger equation have to be employed to study the quantum mechanical behavior of matter. A common simplification regarding nuclear motion is the so-called Born-Oppenheimer approximation [5], which considers the electronic motion to be decoupled from the motion of nuclei, given the large difference in the masses (and in turn, velocities) of the two. In other words the electron dynamics relax before the nuclear motion takes

place. In the case of light-matter interaction, the simplest and most widely used simplification is the so-called dipole approximation [6, 7], which considers the electric field associated with light to have no spatial dependence. This is justified if its wavelength is much larger than the system; it is in fact also referred to as long wavelength approximation. In this work, the focus is on the description of electronic interaction. The complication here is represented by the many-body nature of the problem, as the mutual interaction among electrons induces their correlation and makes the description of the many-body electronic wavefunction highly non-trivial. The simplest approach to a many-body problem is to consider each particle to feel the effective collective potential due to the rest of the particles, hence the name mean-field approximation. Various approaches have been developed over the years to go beyond this theory, such as: Many-Body Perturbation Theory, Configuration Interaction [8], Density-Functional Theory [9, 10], Green's Function based methods, Coupled Cluster [11], Quantum Monte Carlo [12], Dynamical Mean-Field Theory [13] and many more. Different approaches approximate one or more particular aspects of the many-body problem, trying to best describe a certain process or class of processes. What these methods have in common is a recurring difficulty in the practical resolution of the equations involved when, e.g. the system size grows larger and/or a more accurate description of the electron-electron interaction is sought – there is always, in fact, a balance between these two aspects. The focus of this work is to present advances in the Non-Equilibrium Green's Function (NEGF) [14, 15] approach for the description of ultra-fast electron dynamics and discuss thermo-electric transport in nanoscale devices within TDDFT.

The equilibrium Green's function formalism had been proposed in the late 50's and early 60's as a reformulation of the many-body problem [15–

17], found by applying ideas of quantum field theory to statistical mechanics. The construction of its non-equilibrium extension has been pioneered by Keldysh [18], who introduced a particular time-contour named after him, which spans over real and imaginary time, and extended the definition of Green's function on it. The concept of imaginary time, although not concrete, allows for a general description of in and out-of-equilibrium phenomena. The system of equations resulting from this theory are the so called (Keldish-)Kadanoff-Baym equations (KBE). The KBE are an exact reformulation of the many-body problem, and although the first attempt to their numerical solution was proposed almost 50 years ago [19], more accurate approximations allowing for a better description of quantum phenomena are, to this day, still a matter of investigation. In the next chapter a more exhaustive discussion on the matter is presented, together with the contribution to the state of the art brought by this work.

As the system's size grows larger, solving of the KBE becomes unpractical. In fact, the computational time associated with their resolution scales rather unfavourably with the simulation time and the size of the system. A more cost-effective and widely used method for the study of quantum phenomena at the microscopical level, up to systems of the picometer size, is Time-Dependent Density-Functional Theory [20]. Like its static counterpart, this method exploits the one-to-one correspondence between the external potential and the electron density. The many-body problem is then recast in terms of this quantity, which is found through the use of a fictitious system of non-interacting particles in an effective potential, giving the same density as the interacting one. Although this is an exact reformulation of the time-dependent Schrödinger equation, the form of this effective potential remains unknown. In fact, approximations to this quantity have to be found for the practical solution to this problem and since there is no

systematic way of determining better approximations, this task is rather complex and represents a line of research on its own. The second part of this work is devoted to the use of TDDFT for the study of electric transport through nanoscale devices and the development of an approximation to the effective potential used to describe the system.

This thesis is divided in two sections. The first part gives a more thorough introduction to the non-equilibrium Green's function approach and highlights the contributions to the state of the art achieved within this work. The second part is devoted to the study of transport within TDDFT and, in the same way, emphasis is put on the advances accomplished in the field. At the end of each part, the corresponding publications stemming from the work will be discussed. To further clarify some aspects and complete the presentation, each publication will be preceded by a brief introduction highlighting the implications of the work and the questions that remain open, followed by general comments and details of relevance, not explicitly discussed in the publications, in an effort to share with future readers the knowledge acquired through experience.

Chapter 2

Introduction to NEGF

This chapter is devoted to an introduction to the non-equilibrium Green's function formalism together with a more complete motivation to this work. Starting from the basic concepts of NEGF we will introduce the main equations necessary for the understanding of the progress in the field achieved by this work, presented in the papers at the end of this chapter. For a more complete discussion on NEGF, refer to [14, 21].

2.1 Quantum mechanical theory and connection to experiment

In quantum mechanics, physical systems are completely described by their state $|\Psi\rangle$. How they behave and evolve in time is dictated by the Hamiltonian operator \hat{H} through the Schrödinger equation:

$$i \frac{d}{dt} |\Psi(\vec{r}, \sigma, t)\rangle = \hat{H}(t) |\Psi(\vec{r}, \sigma, t)\rangle , \quad (2.1)$$

where \vec{r} and σ are the spatial and spin coordinates. In the previous equation we have set $\hbar = 1$ and we use atomic notation throughout the thesis, unless otherwise specified. Although this equation is exhaustive and de-

describes all the physical properties of any system once the Hamiltonian is defined, its exact resolution is unpractical for essentially any system with more than a few interacting particles. The information carried by the state $|\Psi\rangle$ is enormous as the number of particles can be large and their degrees of freedom can span over large spaces. Fortunately, most quantities measured in experiments can be expressed in terms of certain physical observables which only depend on a restricted number of degrees of freedom. Examples of this class of observables are: electronic density, electronic currents, photoionization yield, and so on. We can therefore trim down the amount of information needed and solve the equations of motion of the operators associated with these observables instead of solving the Schrödinger equation. This approach though, only shifts the problem, as the equation of motion of the reduced quantities still represent a computational challenge. The advantage of these equation lies in the possibility of better using physical intuition to find suitable and sensible approximations to practically resolve them. We will expand on this in the next sections.

2.2 Keldysh-Green's function

The class of operators our formalism focuses on is field operator correlators and, in particular, their statistical averages, the Keldysh-Green's function (GF). We will focus on the one-body Keldysh-Greens' function, defined as:

$$G(1; 2) \equiv -i \text{Tr} \left[\hat{\rho} \mathcal{T} \left\{ \hat{\psi}_H(1) \hat{\psi}_H^\dagger(2) \right\} \right]. \quad (2.2)$$

Here 1 and 2 represent two collective indices for the position-spin coordinates and time, i.e. $1 = (x_1, t) = (\mathbf{r}_1, \sigma_1, t)$, $\hat{\rho}$ is the density operator, \mathcal{T} is the time-ordering operator and $\hat{\psi}_H^\dagger(1)$ and $\hat{\psi}_H(2)$ are the electron cre-

ation and annihilation operators in the Heisenberg picture. Although the one-body Green's function is the lowest order correlator of this kind, many physical observables relevant to experiment can be calculated from it, since

$$i \lim_{t_2 \rightarrow t_1^+} G(1; 2) = \Gamma_1(x_1; x_2, t_1), \quad (2.3)$$

with $\Gamma_1(x_1; x_2)$ the one-body density matrix, and the expectation value of any one-body operator $\hat{O}(t)$ can be computed from it, according to

$$O(t) = \int dx_1 dx_2 O(x_1, x_2, t) \Gamma_1(x_1, x_2, t). \quad (2.4)$$

The two-times one-body GF can be further used to calculate the total energy of the system, which is not an obvious task, as the total energy contains two body operators, which in principle would require the two-body GF.

2.3 The Kadanoff-Baym equations

We consider a general Hamiltonian in second quantization:

$$\begin{aligned} \hat{H} = & \int dx dx' h(x, x', t) \hat{\psi}^\dagger(x) \hat{\psi}(x') \\ & + \frac{1}{2} \int dx dx' v(x, x') \hat{\psi}^\dagger(x) \hat{\psi}^\dagger(x') \hat{\psi}(x') \hat{\psi}(x), \end{aligned} \quad (2.5)$$

where $h(x, x', t)$ and $v(x, x')$ represent the one particle Hamiltonian and the electron-electron interaction, respectively. The single-body part of the Hamiltonian can include the effect of external (classical) fields, relativistic effects like the spin-orbit coupling, etc. With this Hamiltonian, the equa-

tions of motion for the one-body Green's function are:

$$\left[i \frac{d}{dt_1} - h(1) \right] G(1; 2) = \delta(1; 2) - i \int d3 v(1; 3) G_2(1, 3; 2, 3^+) , \quad (2.6a)$$

$$G(1; 2) \left[-i \frac{\overleftarrow{d}}{dt_2} - h(2) \right] = \delta(1; 2) - i \int d3 v(2; 3) G_2(1, 3^-; 2, 3) . \quad (2.6b)$$

Here we drop the double space-spin dependence of the single-particle Hamiltonian for simplicity, without loss of generality. As we can see from the previous equations, the time evolution of the one-body Green's function depends on the two-body GF $G_2(1, 2; 1', 2')$. Accordingly, the equation of motion for the two-body Green's function will depend on the three-body one and so on. This system of co-dependent equation is referred to as the Martin-Schwinger hierarchy [16]. A truncation of the hierarchy is needed in order to be able to practically find a solution. Before presenting any approximation, we introduce the so-called self-energy defined by the equivalence:

$$\int d3 \Sigma(1; 3) G(3; 2) \equiv -i \int d3 v(1; 3) G_2(1, 3; 2, 3^+) . \quad (2.7)$$

This quantity describes the effect of interaction on the time evolution of the system. It is non-local in space and time, meaning it cannot be interpreted as a conventional potential, but it is able to take into account memory effects, which are of vital importance for the description of non-equilibrium. By substituting the definition of the self-energy into equations (2.6) they can be rewritten as:

$$\left[i \frac{d}{dt_1} - h(1) \right] G(1; 2) = \delta(1; 2) + \int d3 \Sigma(1, 3) G(3, 2) , \quad (2.8a)$$

$$G(1;2) \left[-i \frac{\overleftarrow{d}}{dt_2} - h(2) \right] = \delta(1;2) + \int d3 G(1;3) \Sigma(3;2) , \quad (2.8b)$$

where the arrow pointing left on the time derivative indicates that it acts on the object on its left side. The relative order of the two times t_1 and t_2 defines different “components” of the Green’s function. Without going into too much detail, we focus on the lesser/greater components $G^{\lessgtr}(t_1, t_2)$ of the GF, for which $t_1 \lessgtr t_2$. The equations of motion (2.8) for $G^{\lessgtr}(t_1, t_2)$ are the so-called Kadanoff-Baym equations (KBE). The physical interpretation of the lesser/greater GF is easily comprehensible from their definition. For the lesser component we have

$$\begin{aligned} G^<(1,2) &= \text{Tr} \left[\hat{\rho} \hat{\psi}_H^\dagger(2) \hat{\psi}_H(1) \right] \\ &= i \sum_k \rho_k \langle \Psi_k | \hat{\psi}_H^\dagger(2) \hat{\psi}_H(1) | \Psi_k \rangle . \end{aligned} \quad (2.9)$$

A generic term of this sum can be rewritten, using the definition of the field operators in the Heisenberg picture, as

$$\langle \Psi_k | \hat{\psi}_H^\dagger(2) \hat{\psi}_H(1) | \Psi_k \rangle = \langle \Psi_k | \hat{U}(t_0, t_2) \hat{\psi}^\dagger(x_2) \hat{U}(t_2, t_1) \hat{\psi}(x_1) \hat{U}(t_1, t_0) | \Psi_k \rangle , \quad (2.10)$$

with $\hat{U}(t, t')$ the evolution operator from time from t' to t and t_0 the initial time. This term is then the probability amplitude of evolving the state $|\Psi_k\rangle$ from t_0 to t_1 , removing a particle at position-spin x_1 , letting this state evolve to time t_2 and finding the same state as evolving $\langle \Psi_k |$ from t_0 to t_2 and removing a particle at position-spin x_2 .

With the KBE we have an exact reformulation of the many-body problem in terms of the Green’s Function. Although this quantity holds less information than the full many-body wavefunction, the practical resolution

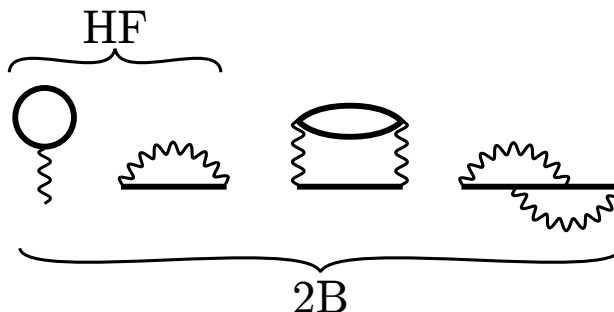


Figure 2.1: Self-energy diagrams up to second order in the bare Coulomb interaction. Solid thick lines represent the Green's function while wiggly lines depict the Coulomb interaction.

of the KBE still represents a formidable task. However, from the definition of the self-energy, by direct comparison with the expansion of the two-body Green's function in terms of one-body GF and using the Wick's theorem [22], one can find an expression of the self-energy in terms of Feynman diagrams. This formulation is a powerful approach to the description of electronic interaction, as it gives a systematic way of producing approximations. Moreover, each self-energy diagram has a direct physical interpretation in terms of the process it describes. In the following, we focus on the first two orders of the expansion of the electronic self-energy in terms of the bare Coulomb interaction, giving rise to the the Hartree-Fock (HF) and the second-Born (2B) approximations. Although, in principle, including higher orders is formally simple, the computational load associated with higher order self-energies is much more considerable. The diagrams associated to these terms of the expansion can be found in Fig 2.1. In the first diagram of Fig 2.1, called “tadpole” diagram, the electron “feels” (through the bare interaction) an effective potential that depends on the position of

all other electrons (closed loop). Even though there is only a single loop in this diagram, one has to take into account that the self-energy results from the sum of all possible such diagrams. The second term, the “first-order exchange”, describes the same process, but taking into account the statistics of electrons, which require the wavefunction to be antisymmetric. What these two diagrams embody is the mean-field effect of the Coulomb interaction, as each electron feels the effective potential of all other electrons. The sum of these first two diagrams represents the Hartree-Fock approximation. The other two diagrams are second order in the bare interaction and start taking into account particle scattering. The first of the two, the so-called “bubble” diagram, describes processes where an electron scatters with a second electron which leaves a hole behind and this electron-hole pair evolves before scattering with the initial electron, recombining – these are polarization effects. The last diagram, the “second-order exchange” term, again, takes into account symmetry properties of electrons in the bubble diagram. The sum of all four diagrams is the second-Born approximation, which has been successfully employed to describe a wealth of correlated phenomena [23–29]. Choosing a self-energy approximation closes the Kadanoff-Baym equations onto the GF itself and a solution can be found. Finally, we observe that the HF self-energy, being the mean-field contribution to interaction, is as an effective potential acting on electrons. This means that the HF potential $V_{HF}(t)$ can be added to the one-body Hamiltonian. The effects beyond the HF approximation are referred to as “electronic correlations” and need to be accounted for through the so-called correlation self-energy $\Sigma_c(1; 2)$.

The calculation of the correlation self-energy is itself a formidable task, even at the lowest levels of approximation, due to the summing over all internal degrees of freedom. With the exception of a few special cases, a

calculation of the self-energy in real space and time is prohibitive and so is the solution to the KBE. We must therefore expand the field operators, and in turn all other quantities, over some finite discrete (therefore incomplete) basis. In the basis, the GF and self-energy are represented by matrices, and the Coulomb interaction $v(x, x')$ by a four-dimensional tensor; but the equations of motion stay unchanged for the new objects. A general 2B self-energy matrix element, in a single-particle basis, reads

$$\begin{aligned} \Sigma_{ij}(t, t') = & 2 \sum_{\substack{mn \\ pq \\ rs}} v_{irpn} v_{mqsj} G_{nm}(t, t') G_{sr}(t', t) G_{pq}(t, t') \\ & - \sum_{\substack{mn \\ pq \\ rs}} v_{irpn} v_{mqsj} G_{nq}(t, t') G_{sr}(t', t) G_{pm}(t, t'). \end{aligned} \quad (2.11)$$

Even though the summation runs over six indices, the computation of this expression scales like N^5 , where N is the size of the basis. This is because the contraction of the Coulomb integrals tensor with a Green's function appears twice, but only needs to be computed once, effectively getting rid of one sum. Although still computationally demanding, eq. (2.11) can be evaluated for realistic systems. More technical details for the efficient computation of the 2B self-energy can be found in Publication III.

In a single particle basis, the Coulomb interaction tensor might have negligible elements, e.g. the coulomb integral tends to zero for states with vanishing overlap. This means that not all of the elements contribute to the sum in eq. (2.11). In particular cases, it might be even possible to identify a certain class of Coulomb integrals which contribute to specific physical processes more than others, which in turn could be discarded. These two approximations are discussed in the publications I and II, where their validity is assessed for the description of Auger decay in the ultrafast

electron dynamics of atoms and molecule.

2.4 The embedding self-energy

Up until now the class of systems considered has not been thoroughly specified, if not for the decomposition of their Hamiltonian in a single particle part and a two-body interaction. Before we further specify the Hamiltonian, we make the observation that completely isolated systems are a fictitious theoretical tool. In fact, all systems are in principle connected to the environment surrounding them – they are “open” in contrast to isolated or “closed” systems. The environment may not be of particular interest to us, but its interaction with the system of interest, when strong enough, can influence it or even alter its properties. An example is the coupling of a quantum device to macroscopic electric contacts: we might not be interested in the electron dynamics in the contacts, but electrons in the device can escape through the leads under the action of an electric field. A similar example is the continuum: the uncountable infinity of unbound states describing free particles. Its description and its coupling to the bound electrons of a molecule are of vital importance to characterize any ionization process. The photo-electrons themselves might not be important to the process we want to describe, but the hole dynamics they trigger in the parent molecule are crucial to the description of electron dynamics. Exactly these two examples are important for this work and are discussed in more detail later. For the reasons aforementioned, the inclusion of the environment and its coupling to the system is in order for a more complete description of quantum systems. Taking into account these considerations, we write the Hamiltonian as

$$\hat{H} = \hat{H}_0 + \hat{H}_{\text{int}} . \quad (2.12)$$

The non-interacting part \hat{H}_0 reads

$$\begin{aligned} \hat{H}_0 = & \sum_{mn\sigma\sigma'} T_{m\sigma n\sigma'} \hat{d}_{m\sigma}^\dagger \hat{d}_{n\sigma'} \\ & + \sum_{k\sigma} \epsilon_k \hat{c}_{k\sigma}^\dagger \hat{c}_{k\sigma} + \sum_{m\sigma k} \left(V_{mk} \hat{d}_{m\sigma}^\dagger \hat{c}_{k\sigma} + V_{km} \hat{c}_{k\sigma}^\dagger \hat{d}_{m\sigma} \right), \end{aligned} \quad (2.13)$$

where the first line is the single-particle Hamiltonian of our system of interest, from now on simply referred to as “the system” or “impurity”, and the second line models the environment and its hybridization with the system. Regarding the system part, $\hat{d}_{m\sigma}^\dagger$ ($\hat{d}_{m\sigma}$) is creation (annihilation) operator for a particle in the system with generic quantum number m and spin σ and $T_{m\sigma n\sigma'}$ is a generic matrix element of the single particle Hamiltonian. For the environment, $\hat{c}_{k\sigma}^\dagger$ ($\hat{c}_{k\sigma}$) is the creation (annihilation) operator for a particle of quantum number k and spin σ in the environment with associated energy ϵ_k . Finally, V_{mk} and V_{km} are the generic matrix elements for the coupling between the system and the environment. We model the environment as a single reservoir coupled to the system, but the formalism is general and can account for any number of reservoirs for the description of the environment. The interacting part of the Hamiltonian \hat{H}_{int} is

$$\hat{H}_{\text{int}} = \frac{1}{2} \sum_{ijmn\sigma\sigma'} v_{ijmn} \hat{d}_{i\sigma}^\dagger \hat{d}_{j\sigma'}^\dagger \hat{d}_{m\sigma'} \hat{d}_{n\sigma}, \quad (2.14)$$

where v_{ijkl} is the generic matrix element of the Coulomb interaction. Here the sum is restricted to indices in the system, which means that the reservoirs are non-interacting. This approximation is taken on the basis of what discussed before: we want to include the environment and its interaction with the system, but we are not interested in its dynamics. Clearly, this approximation affects the overall dynamics, therefore it must be treated

with care, not to introduce artificial effects into our description. An explicit time-dependence of the Hamiltonian has not been specified, but it can be accounted for by using time-dependent matrix elements, e.g. $T_{m\sigma n\sigma'} \rightarrow T_{m\sigma n\sigma'}(t)$ for including varying electromagnetic fields, $V_{mk} \rightarrow V_{mk}(t)$ for a time-dependent contacting of the system to the reservoirs, etc. The formalism we are presenting, though, is general and is not affected by this: the time-independent notation will be kept throughout.

Since we are now treating both system and environment, it is advantageous to write the non-interacting Hamiltonian and the Green's function matrices in a block form:

$$\mathbf{H}_0 = \begin{pmatrix} \mathbf{H}_S & \mathbf{H}_{SR} \\ \mathbf{H}_{RS} & \mathbf{H}_R \end{pmatrix} \quad \mathbf{G}(t, t') = \begin{pmatrix} \mathbf{G}_S(t, t') & \mathbf{G}_{SR}(t, t') \\ \mathbf{G}_{RS}(t, t') & \mathbf{G}_R(t, t') \end{pmatrix}, \quad (2.15)$$

where the subscript 'S' stands for "system" and 'R' for "reservoir" and the bold font is used to represent matrices. Here each element is a matrix itself, spanning over the indices of the corresponding space, e.g. \mathbf{H}_S is the block of the matrix \mathbf{H}_0 spanning over the system's degrees of freedom only, i.e. the matrix \mathbf{T} of eq. (2.13). Correspondingly, $\mathbf{H}_{SR} = \mathbf{H}_{RS}^\dagger$ is the system-reservoir coupling matrix \mathbf{V} . The interaction is taken care of through the use of the self-energy. This also takes on a matrix form

$$\mathbf{\Sigma}(t, t') = \begin{pmatrix} \mathbf{\Sigma}_c(t, t') & \mathbf{0} \\ \mathbf{0} & \mathbf{0} \end{pmatrix}. \quad (2.16)$$

This trivial form stems from the fact that the interacting Hamiltonian is non-zero only in the system's sector. The subscript 'c' stands for "correlation". Note the double dependence of the self-energy on time, reflecting its dependence on the Green's function. The equations of motion for the

different blocks of the Green's function, according to eq. (2.8), read¹

$$\left[i \mathbb{1}_S \frac{d}{dt} - \mathbf{H}_S \right] \mathbf{G}_S(t, t') = \mathbb{1}_S \delta(t, t') + \mathbf{H}_{SR} \mathbf{G}_{RS}(t, t') + \int d\bar{t} \Sigma_c(t, \bar{t}) \mathbf{G}_S(\bar{t}, t') , \quad (2.17a)$$

$$\left[i \mathbb{1}_R \frac{d}{dt} - \mathbf{H}_R \right] \mathbf{G}_{RS}(t, t') = \mathbf{H}_{RS} \mathbf{G}_S(t, t') , \quad (2.17b)$$

$$\left[i \mathbb{1}_R \frac{d}{dt} - \mathbf{H}_R \right] \mathbf{g}_R(t, t') = \mathbb{1}_R \delta(t, t') , \quad (2.17c)$$

where $\mathbf{g}_R(t, t')$ is the non-interacting GF of the uncontacted reservoir, $\mathbb{1}$ is the identity in the subspace indicated by the corresponding subscript and matrix multiplication operations are implied. Eq. (2.17c) is the homogeneous equation associated with eq. (2.17b). Hence, the solution of the latter reads

$$\mathbf{G}_{RS}(t, t') = \int d\bar{t} \mathbf{g}_R(t, \bar{t}) \mathbf{H}_{RS} \mathbf{G}_S(\bar{t}, t') . \quad (2.18)$$

Substituting this solution into the equation of motion for the system's GF, we have

$$\left[i \mathbb{1}_S \frac{d}{dt} - \mathbf{H}_S \right] \mathbf{G}_S(t, t') = \mathbb{1}_S \delta(t, t') + \int d\bar{t} (\Sigma_c(t, \bar{t}) + \Sigma_{\text{em}}(t, \bar{t})) \mathbf{G}_S(\bar{t}, t') , \quad (2.19)$$

where we define the embedding self-energy

$$\Sigma_{\text{em}}(t, t') = \mathbf{H}_{SR} \mathbf{g}_R(t, t') \mathbf{H}_{RS} . \quad (2.20)$$

The role of the embedding self-energy is clear from its definition and from how it appears in the equation of motion for the system's GF: it accounts for

¹The same exact derivation can be carried out for the adjoint equations.

the possibility of particles to hop into the reservoirs, propagate there and re-enter the system. For non-interacting reservoirs, the embedding self-energy at all times is known once the equilibrium Hamiltonian is specified. An interesting feature of open systems is the presence of time non-local effects, buried into the memory kernel $\Sigma_{\text{em}}(t, t')$ of eq. (2.19), even for non-interacting systems, i.e. $\Sigma_c(t, t') = \mathbf{0}$. The derivation presented here is quite general and applies to all non-interacting reservoirs linearly coupled to the system's electronic degrees of freedom.

In this work, we use this approach in two different cases: to include the coupling of quantum devices to electric contacts in the study of transport through nanojunctions and to describe ionization by a laser pulse in the case of the study of ultrafast electron dynamics in atoms and molecules.

In the first case, the electric contacts are modeled as non-interacting metallic wires, where electrons coming from the impurity can freely propagate. The associated self-energy can be computed from eq. (2.20) and is, in general, a complicated object with two time arguments. Although the introduction of the embedding self-energy makes the inclusion of macroscopic elements into the description of quantum systems computationally feasible, it is appealing to further speed-up calculations, to study larger and larger devices. Let us assume that the leads are time-independent, apart from a possible potential quench at the initial time. In this case the Green's function of the leads only depends on time differences. This means we can Fourier transform to a single energy argument, obtaining

$$\Sigma_{\text{emb}}(z) = \frac{\mathbf{V}_\alpha \mathbf{V}_\alpha^T}{t_\alpha} S\left(\frac{z - \epsilon_\alpha}{2t_\alpha}\right), \quad (2.21)$$

where z is a complex energy, α labels the leads, \mathbf{V}_α is the coupling amplitude, $4t_\alpha$ is the bandwidth of the lead, ϵ_α is the center of the lead's band and

$S(z) = (z - \sqrt{z-1}\sqrt{z+1})$. Even with this simplification, memory effects are still included in the description of transport. While this is a desirable feature, it does not always have great impact onto the dynamics. An additional simplification is brought by considering the form of the self-energy in energy space. If we expand the function $S(z)$ around $z = 0$, the zeroth order expansion is purely imaginary and the self-energy from eq. (2.21) reads

$$\Sigma_{\text{emb}}^{A/R}(z) \simeq \pm i \frac{\mathbf{V}_\alpha \mathbf{V}_\alpha^T}{t_\alpha}, \quad (2.22)$$

where we only write out the advanced/retarded components of the self-energy. Transforming back to the time domain we have

$$\Sigma_{\text{emb}}^{A/R}(t, t') = \pm i \frac{\mathbf{V}_\alpha \mathbf{V}_\alpha^T}{t_\alpha} \delta(t - t'), \quad (2.23)$$

meaning that the memory effects are lost. This is known as Wide-Band Limit Approximation (WBLA) and is broadly used in the study of electronic transport. This approximation is justified when the expansion (2.22) is accurate, i.e. the argument of the function S in (2.21) tends to zero. This is achieved if the leads' bandwidths ($\propto t_\alpha$) are much larger than any energy scale in the system and than the applied bias or, equivalently, if the coupling constants are much smaller than the bandwidths $|t_\alpha| \gg [|\mathbf{V}_\alpha|]_{ij}$. In Publication V an analysis of the implications of the WBLA in the study of thermo-electric transport is presented.

The second instance of an embedding scheme in this work is in the description of ionization of isolated systems. The absorption of photons in atoms and molecules promotes an electron to a different state. This can be an excited state bound to the molecule or not, depending on its energy. The choice of the basis used for calculations is therefore crucial to the de-

scription of the dynamics, i.e. if unbound states are not included in the basis, ionization cannot be described. On the other hand, unbound states are infinite as all energies are allowed. Hence, the representation of the continuum of unbound states is not feasible as it would require an equally infinite amount of resources for the simulations. In a practical calculation we select a subset of quantized unbound states that describes the continuum in the class of experiments we are simulating. This subset is chosen on physical grounds: the relevant energy window of interest is known a priori from the system's bound states and the laser energies and, for a defined simulation box, the number of unbound states that fall in that window is given. We consider the case of dipole coupling of the electric field, we can therefore write the corresponding ionization (embedding) self-energy, according to eq. (2.20) as

$$\Sigma_{\text{ion}}(t, t') = (E(t)\mathbf{d}_{SC})\mathbf{G}_C^0(t, t')(E(t')\mathbf{d}_{CS}), \quad (2.24)$$

where the subscript 'C' indicates the continuum subspace, $E(t)$ is the electric field, \mathbf{d} is the dipole matrix in the sector of the corresponding subscripts, and $\mathbf{G}_C^0(t, t')$ is the continuum Green's function [30]. Note that the latter will be diagonal in the approximation of non-interacting continuum states. This is the case in publications I, II and IV. While ionization itself is faithfully described within the dipole approximation under the conditions considered here², imposing the continuum states to be non-interacting, of course, prevents us to describe certain physical processes, such as streaking, multiphoton processes, photoemission satellites and so on. In the aforementioned publications, though, we only focus on simulations of experi-

²Although the dipole approximation is valid in the case studied here, going beyond this approximation would be necessary in other circumstances, e.g. core level time-dependent spectroscopy, strong light-matter phenomena, and so on.

ments where these effects are not important or negligible.

2.5 The Generalized Kadanoff-Baym Ansatz

In the previous sections we presented the Kadanoff-Baym equations for the description of isolated or open quantum systems. Once the system is specified and the approximation for the self-energy chosen, dynamical properties, in form of one-body observables, can be calculated from the time-dependent single-particle Green's function $G(t, t')$. This framework is more advantageous than solving the Schrödinger equation, allowing for the study of atomic systems and small molecules (possibly connected to reservoirs) for propagation times of few femtoseconds. This approach is, however, still limited by computational complexity. In fact, the scaling of the equation of motion with respect to systems size and simulation time is not particularly favorable. The Green's function itself is a $N \times N$ matrix, where N is the basis size, with two time arguments. The time-propagation of this object involves an additional integral over time, giving an overall computational cost that scales with T_{sim}^3 , where T_{sim} is the total simulation time. Finally, we recall that the calculation of the second-Born self-energy matrix scales like the fifth power of the size of the basis set used for computation, if no other approximations are used.

Previously we stated that the expectation value of any single particle observable can be calculated from the one-body density matrix $\Gamma_1(x_1, x_2, t)$ according to eq. (2.4). This means the full two-time structure of the Green's function is redundant to compute this class of observables. It is therefore tempting to write the equation of motion for $\mathbf{G}^<(t, t^+) = i \rho(t)$, where $\rho(t)$ is the time-dependent one-body reduced density matrix in a general single particle basis, since this has a single time argument. To arrive at

this equation, we subtract the second equation (2.8) from the first, in the case of $t_1 < t_2$, ensuring we consider the lesser component of the Green's function:

$$i \left(\frac{d}{dt} + \frac{d}{dt'} \right) \mathbf{G}^<(t, t') - \mathbf{h}_{HF}(t) \mathbf{G}^<(t, t') + \mathbf{G}^<(t, t') \mathbf{h}_{HF}(t') = \quad (2.25)$$

$$[\boldsymbol{\Sigma}^< \cdot \mathbf{G}^A + \boldsymbol{\Sigma}^R \cdot \mathbf{G}^< - \mathbf{G}^< \cdot \boldsymbol{\Sigma}^A - \mathbf{G}^R \cdot \boldsymbol{\Sigma}^<] (t, t'),$$

where matrix multiplication is implicit, $h_{HF}(t) = h(t) + V_{HF}(t)$, A and R indicate the advanced and retarded components of self-energy and Green's function and the symbol \cdot is used to indicate the integration operation, i.e. $[\boldsymbol{\Sigma}^< \cdot \mathbf{G}^A] (t, t') \equiv \int d\bar{t} \boldsymbol{\Sigma}^<(t, \bar{t}) \mathbf{G}^A(\bar{t}, t')$. Note that the self-energy includes both correlation and embedding effects, i.e. $\boldsymbol{\Sigma} = \boldsymbol{\Sigma}_{\text{corr}} + \boldsymbol{\Sigma}_{\text{em}}$. Taking the limit $t \rightarrow t'$, eq. (2.25) becomes

$$\frac{d}{dt} \boldsymbol{\rho}(t) + i [\mathbf{h}_{HF}(t), \boldsymbol{\rho}(t)] = [\boldsymbol{\Sigma}^< \cdot \mathbf{G}^> - \boldsymbol{\Sigma}^< \cdot \mathbf{G}^>] (t, t) + H.C., \quad (2.26)$$

where *H.C.* stand for Hermitian Conjugate of the object in the square brackets, referred to as collision integral. The retarded/advanced components turned into lesser/greater because of the limit $t \rightarrow t'$. As we can see, the equation of motion for $\boldsymbol{\rho}(t)$ is not a closed equation as it still requires the knowledge of the off-diagonal (in time) of different Green's function components, also appearing in the self-energy. In 1986 Lipavský *et al.* [31] proposed the so-called Generalized Kadanoff-Baym Ansatz (GKBA) to solve this problem. This ansatz for the lesser/greater component of the GF in

terms of the density matrix reads

$$\begin{aligned} \mathbf{G}^<(t, t') &= i\mathbf{G}^R(t, t')\mathbf{G}^<(t', t') - i\mathbf{G}^<(t, t)\mathbf{G}^A(t, t') \\ &= -\mathbf{G}^R(t, t')\boldsymbol{\rho}(t') + \boldsymbol{\rho}(t)\mathbf{G}^A(t, t') , \end{aligned} \quad (2.27a)$$

$$\mathbf{G}^>(t, t') = \mathbf{G}^R(t, t')\bar{\boldsymbol{\rho}}(t') - \bar{\boldsymbol{\rho}}(t)\mathbf{G}^A(t, t') , \quad (2.27b)$$

with $\bar{\boldsymbol{\rho}}(t) = \mathbb{1} - \boldsymbol{\rho}(t)$. Although this approximation gets rid of the two-times lesser/greater GF, it does not simplify the problem, since the retarded and advanced GF still appear, and the computational effort associated with the resolution of their equations of motion still scales with T_{sim}^3 . This problem is bypassed if we provide a retarded/advanced GF, whose calculation scales faster than T_{sim}^3 . The simplest approximation of this kind is to use the Hartree-Fock retarded/advanced Green's function, i.e.

$$\mathbf{G}^R(t, t') = -i\theta(t - t')\mathcal{T} \left\{ e^{-i\int_{t'}^t d\bar{t} \mathbf{h}_{HF}(\bar{t})} \right\} , \quad (2.28a)$$

$$\mathbf{G}^A(t, t') = +i\theta(t' - t)\mathcal{T} \left\{ e^{i\int_t^{t'} d\bar{t} \mathbf{h}_{HF}(\bar{t})} \right\} . \quad (2.28b)$$

This choice allows us to close equation (2.26) onto the density matrix only, reducing its computational scaling to T_{sim}^2 . This scheme is referred to as HF-GKBA. The validity of this approximation has been extensively tested in the past years [21, 25, 27, 32–38]. This level of approximation for the GKBA has the interesting characteristic of being exact in the Hartree-Fock approximation in isolated systems, i.e. $\Sigma = 0$; this can be seen directly by plugging the HF-GKBA in eq. (2.26).

Publication I

Real-time dynamics of Auger wave packets and decays in ultrafast charge migration processes

Fabio Covito, Enrico Perfetto, Angel Rubio and Gianluca Stefanucci, *Physical Review A*, **97** (6), 061401 (2018).

The Auger decay is a non-radiative relaxation mechanism for excited or ionized atoms and molecules with an inner-shell vacancy. In this process the hole is filled by a bound electron and the energy gained is transferred to a second electron, named Auger electron, which is expelled from the atom, see Fig. 2.2 for a pictorial representation of the mechanism. Auger spectra and linewidths have been extensively studied in the long time limit [39–41], but less is known about the dynamics of this process. The Auger decay is an energy-dissipation mechanism happening at the femtosecond timescale, making its understanding vital for the description of ultrafast dynamics of targets hit by radiation capable of exciting core vacancies. The inclusion of this decay channel in ab-initio methods is a complex task and often disregarded altogether because of this. Its complexity stems from the need of an accurate description of electronic correlation in order to catch this effect. While wavefunction-based methods have, in principle, this capability, practical computations are presently prohibitive, as discussed previously. On the other hand, computationally more efficient approaches like TDDFT lack suitable approximations for the exchange and correlation functionals that can reproduce the Auger decay. This would, in fact, require non-adiabatic functionals—which include memory effects such as the Auger decay—whose development still represents a challenge. In this publication a first-principles approach based on NEGF for the study of real-time Auger scattering in atoms and molecules with up to tens of active electrons is put forward. The method is based on an approximation to the 2B self-energy

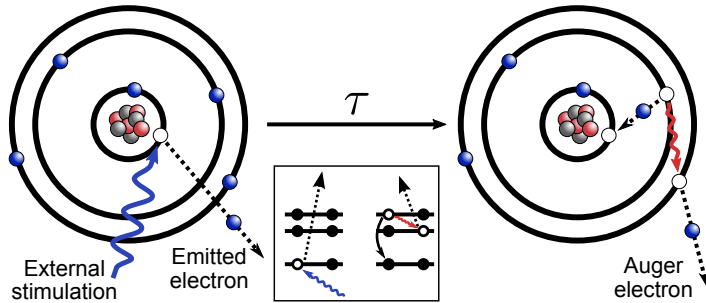


Figure 2.2: Schematic two-step depiction of the Auger recombination in an atom. Once a core hole is created by an external perturbation (left panel), the recombination can take place in an associated characteristic time τ (right panel). The core hole is filled by a valence electron and the excess energy (red wiggly line) is transferred to a second valence electron, which is then expelled from the atom. The inset shows the energetics of the two-step process.

which considers only a subset of all possible scatterings included in the dynamics. In particular, all internal dynamics are preserved and only the Auger-like scatterings towards the continuum are considered. To validate the applicability of this approach, we compare the results with accurate grid calculations in 1-dimensional model systems. We find the Auger scattering to be faithfully described by the proposed method, while gaining a considerable computational speed-up. Moreover, we predict a highly asymmetric profile of the Auger wavepacket, with a wavefront depending on the perturbation creating the initial hole and a long tail showing ripples whose temporal spacing depends on the inverse of the energy of the Auger electron.

The proposed method is applicable to finite systems, but can, in principle, be extended to deal with periodic systems: this would represent an interesting possibility to explore in the future. Another possible path to investigate would be an extension of the method to include the effect of valence-valence repulsion, which is known to play an important role in the Auger decay, without giving up on computational efficiency.

In the following, I add a few remarks, which are not explicitly addressed in the published manuscript, but complement the discussion of the work.

Thermalization. For time-dependent simulations, a crucial role is played by the initial state of the system, and this can greatly affect results. In our results, an adiabatic preparation of the correlated initial state has been performed, i.e. the system is prepared in the HF initial state and correlations are adiabatically switched on. The switch-on time has to be converged to ensure the system ends up in the (stable) correlated initial state. This is not visible in the results presented in the paper, as all quantities are shown starting from the thermalized initial state.

Ionization. The inclusion of ionization processes is quite different between the NEGF@grid and coupled NEGF calculations. While in the former the dipole coupling between all states is used and all states are fully interacting, in the latter an embedding scheme is used, which also means that states in the continuum are non interacting. To overcome these differences, the laser intensity has to be tuned to yield the same ionization in the two cases. The differences visible in the results presented in the paper, then, do not only arise from the approximations imposed on the self-energy and Green's function of the continuum, but also on the different transitions induced by the coupling with the electric field.

Auger wave-packet. Although the Auger wave-packet has intrinsic characteristic features, like its asymmetric profile and spatial ripples, other properties, like the amplitude of the ripples or the wavefront shape depend on the perturbation. This difference stems from the temporal profile of the hole creation and on how the pump ionizes the system. In particular, for the same core hole induced, a shorter pump will give rise to a steeper wavefront compared to a more gradual, longer pump, and different valence populations will give different ripples amplitude.

Real-time dynamics of Auger wave packets and decays in ultrafast charge migration processes

F. Covito,¹ E. Perfetto,^{2,3} A. Rubio,^{1,4,5} and G. Stefanucci^{3,6}¹Max Planck Institute for the Structure and Dynamics of Matter and Center for Free-Electron Laser Science, Luruper Chaussee 149, 22761 Hamburg, Germany²CNR-ISM, Division of Ultrafast Processes in Materials (FLASHit), Area della ricerca di Roma 1, Monterotondo Scalo, Italy³Dipartimento di Fisica, Università di Roma Tor Vergata, Via della Ricerca Scientifica, 00133 Rome, Italy⁴Center for Computational Quantum Physics (CCQ), The Flatiron Institute, 162 Fifth Avenue, New York, New York 10010, USA⁵Nano-Bio Spectroscopy Group, Universidad del País Vasco, 20018 San Sebastian, Spain⁶INFN, Sezione di Roma Tor Vergata, Via della Ricerca Scientifica 1, 00133 Roma, Italy

(Received 15 December 2017; revised manuscript received 27 March 2018; published 6 June 2018)

The Auger decay is a relevant recombination channel during the first few femtoseconds of molecular targets impinged by attosecond XUV or soft x-ray pulses. Including this mechanism in time-dependent simulations of charge-migration processes is a difficult task, and Auger scatterings are often ignored altogether. In this work we present an advance of the current state-of-the-art by putting forward a real-time approach based on nonequilibrium Green's functions suitable for first-principles calculations of molecules with tens of active electrons. To demonstrate the accuracy of the method we report comparisons against accurate grid simulations of one-dimensional systems. We also predict a highly asymmetric profile of the Auger wave packet, with a long tail exhibiting ripples temporally spaced by the inverse of the Auger energy.

DOI: 10.1103/PhysRevA.97.061401

The subfemtosecond dynamics of the hole density created by an ionizing attosecond XUV or soft x-ray pulse precedes any nuclear rearrangement and dictates the relaxation pathways of the underlying molecular structure [1,2]. This ultrafast charge oscillation, also referred to as ultrafast charge migration (UCM), is driven exclusively by electronic correlations up to a few femtoseconds [3–7]. At these time scales the Auger scattering is the only possible energy-dissipation mechanism and, in addition to shake-up and polarization effects [8], a relevant recombination channel.

Recent advances in pump-probe spectroscopy have made it possible to follow the Auger decay in atomic targets [2,9–12]. Accurate measurements have been performed and successfully interpreted in terms of transitions between excited cationic states. The theory behind these experiments shows that the Auger electron is a “courier” of the complex dynamics occurring in the parent cation [13–15]. Unfortunately, *ab initio* analysis relying on many-electron eigenfunctions and eigenvalues are possible for single atoms but soon become prohibitive for larger systems. In fact, first-principles approaches that include Auger scatterings in the UCM dynamics of molecules have not yet been developed.

Time-dependent density functional theory [16–18] (TDDFT) is the method of choice for large-scale simulations. However, the vast majority of TDDFT calculations are performed using an adiabatic exchange-correlation (xc) potential, i.e., a functional of the instantaneous density. As shown in Ref. [19], adiabatic approximations are unable to capture the Auger effect [20]. Learning how to include memory effects in the xc functional is a major line of research to which the present work could provide new insights.

In this Rapid Communication we present a first-principles real-time nonequilibrium Green's function [21,22] (NEGF)

approach which incorporates Auger scatterings in the UCM dynamics of molecules hit by attosecond pulses. In analogy with the NEGF formulation of quantum transport where the dynamics of electrons in the junction is simulated without dealing explicitly with the electrons in the leads [23–25], we close the NEGF equations on the molecule and deal only partially with the degrees of freedom of the Auger electrons. The computational effort changes slightly with respect to previous NEGF implementations [26–28], thereby making it possible to simulate the UCM of molecules with tens of active electrons.

We demonstrate that the approach well captures qualitative and quantitative aspects of the Auger physics through comparisons against real-time simulations of one-dimensional (1D) atoms on a grid. The Auger wave packet can, in principle, be reconstructed from NEGF through a postprocessing procedure. For three-dimensional (3D) molecules such procedure is numerically (too) demanding but for the considered 1D atom the calculation is doable and the agreement with the full-grid results is again satisfactory. Interestingly, we highlight a universal feature of the asymmetric Auger wave packet, namely, a long tail with superimposed ripples temporally spaced by the inverse of the Auger energy.

Method. We consider a finite system (an atom or molecule) with single-particle Hartree-Fock (HF) basis $\varphi_i(\mathbf{r})$ for bound electrons and $\varphi_\mu(\mathbf{r})$ for electrons in the continuum (for simplicity we work with spin-degenerate systems). Let $\hat{c}_{i\sigma}$ ($\hat{c}_{\mu\sigma}$) be the annihilation operator for an electron on φ_i (φ_μ) with spin σ . In the absence of external fields the total Hamiltonian

$$\hat{H}^{\text{eq}} = \hat{H}_{\text{bound}} + \hat{H}_{\text{Auger}} + \hat{H}_{\text{cont}} \quad (1)$$

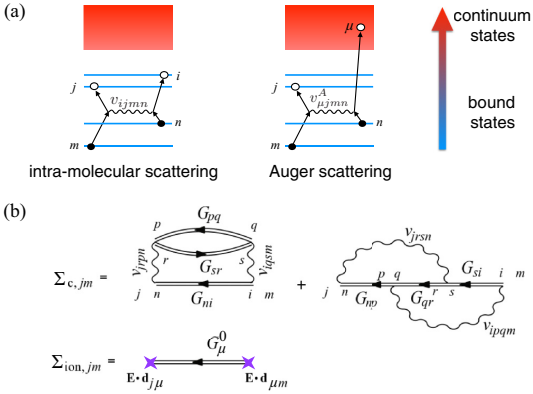


FIG. 1. (a) Schematic illustration of intramolecular (left) and Auger (right) scattering. (b) Correlation self-energy in the 2B approximation (top) and ionization self-energy (bottom).

is the sum of the bound-electrons Hamiltonian $\hat{H}_{\text{bound}} = \sum_{ij} h_{ij} \hat{c}_{i\sigma}^\dagger \hat{c}_{j\sigma} + \frac{1}{2} \sum_{ijmn} v_{ijmn} \hat{c}_{i\sigma}^\dagger \hat{c}_{j\sigma}^\dagger \hat{c}_{m\sigma'} \hat{c}_{n\sigma}$, the Auger interaction $\hat{H}_{\text{Auger}} = \sum_{ijm\mu} v_{ijm\mu}^A (\hat{c}_{i\sigma}^\dagger \hat{c}_{j\sigma'}^\dagger \hat{c}_{m\sigma} \hat{c}_{\mu\sigma} + \text{H.c.})$, and a free-continuum part $\hat{H}_{\text{cont}} = \sum_{\mu\sigma} \epsilon_\mu \hat{c}_{\mu\sigma}^\dagger \hat{c}_{\mu\sigma}$. Here h_{ij} are the one-electron integrals, ϵ_μ are the continuum single-particle energies, and v_{ijmn} ($v_{ijm\mu}^A$) are the four-index Coulomb integrals responsible for intramolecular (Auger) scatterings [see Fig. 1(a)].

The system is perturbed either by the sudden removal of a bound electron or by an external laser field. In the dipole approximation the laser-system interaction reads

$$\hat{H}^E(t) = \hat{H}_{\text{bound}}^E(t) + \hat{H}_{\text{ion}}^E(t), \quad (2)$$

where $\hat{H}_{\text{bound}}^E(t) = \mathbf{E}(t) \cdot \sum_{ij} \mathbf{d}_{ij} \hat{c}_{i\sigma}^\dagger \hat{c}_{j\sigma}$ describes intramolecular transitions, whereas $\hat{H}_{\text{ion}}^E(t) = \mathbf{E}(t) \cdot \sum_{i\mu} (\mathbf{d}_{i\mu} \hat{c}_{i\sigma}^\dagger \hat{c}_{\mu\sigma} + \text{H.c.})$ is responsible for ionization. The vector \mathbf{d}_{ij} ($\mathbf{d}_{i\mu}$) is the matrix element of the dipole operator between states φ_i and φ_j (φ_μ). In Eqs. (1) and (2) we are discarding the off-diagonal elements $h_{i\mu}$, $h_{\mu\mu'}$, and $\mathbf{d}_{\mu\mu'}$ as well as all Coulomb integrals with two or more indices in the continuum. We anticipate that this simplification only marginally affects the results presented below.

The electron dynamics is simulated using NEGF. Without Auger scatterings the equation of motion for the one-particle density matrix $\rho_{ij}(t) = \langle \hat{c}_{i\sigma}^\dagger(t) \hat{c}_{j\sigma}(t) \rangle$ (with indices in the bound sector) has been derived elsewhere [26] and reads $\dot{\rho} = -i[h_{\text{HF}}[\rho], \rho] - \mathcal{I}[\rho] - \mathcal{I}^\dagger[\rho]$. Here the HF Hamiltonian $h_{\text{HF}}(t) \equiv h + V_{\text{HF}}(t) + \mathbf{E}(t) \cdot \mathbf{d}$ is a functional of ρ through the HF potential $V_{\text{HF},ij}(t) = \sum_{mn} \rho_{nm}(t) w_{imnj}$, with $w_{imnj} \equiv 2v_{imnj} - v_{imjn}$. Dynamical correlation and ionization processes are described by the generalized collision integral

$$\mathcal{I}(t) = \int_0^t d\bar{t} [\Sigma^>(t, \bar{t}) G^<(\bar{t}, t) - \Sigma^<(t, \bar{t}) G^>(\bar{t}, t)], \quad (3)$$

where $\Sigma^{\lessgtr} \equiv \Sigma_c^{\lessgtr} + \Sigma_{\text{ion}}^{\lessgtr}$ is the sum of the lesser or greater correlation (Σ_c) and ionization (Σ_{ion}) self-energies. Both are time-nonlocal functionals of ρ through the generalized Kadanoff-Baym ansatz [29] (GKBA) [see Supplemental Material (SM) for details [30]]. Figure 1(b) illustrates the diagrammatic representation of Σ_c in the second-Born (2B) approximation and Σ_{ion} . The computational cost of these NEGF calculations scales like $N_t^2 N_{\text{bound}}^p$ where N_t is the number of time steps, N_{bound} is the number of HF bound states, and the power $3 \leq p \leq 5$ depends on how sparse v_{ijmn} is. Real-time simulations of, e.g., organic or biologically relevant molecules can easily be carried out up to 30–40 fs [28].

The inclusion of Auger scattering processes leads to a coupling between the density matrix $\rho(t)$ and the occupations $f_\mu(t) = \langle \hat{c}_{\mu\sigma}^\dagger(t) \hat{c}_{\mu\sigma}(t) \rangle$ of the continuum states. For these quantities we have derived (see SM) the following coupled system of NEGF equations of motion:

$$\begin{aligned} \dot{\rho} &= -i[h_{\text{HF}}[\rho], \rho] - \mathcal{I}[\rho, f] - \mathcal{I}^\dagger[\rho, f], \\ \dot{f}_\mu &= -\mathcal{J}_\mu[\rho, f] - \mathcal{J}_\mu^*[\rho, f]. \end{aligned} \quad (4)$$

The generalized collision integral $\mathcal{I}[\rho, f]$ is defined as in Eq. (3) but $\Sigma[\rho] \rightarrow \Sigma[\rho] + \Sigma_{\text{Auger}}[\rho, f]$. The Auger self-energy is calculated from the second-order (in v^A) diagrams, in accordance with Refs. [31,32], and reads

$$\begin{aligned} \Sigma_{\text{Auger},ij}^{\lessgtr}(t, \bar{t}) &= \sum_{mn} \sum_{pq} \sum_{\mu} G_{mn}^{\lessgtr}(t, \bar{t}) \\ &\times [G_{\mu}^{\lessgtr}(t, \bar{t}) G_{pq}^{\lessgtr}(\bar{t}, t) (v_{iqm\mu}^A w_{\mu npj}^A + v_{iq\mu m}^A w_{n\mu pj}^A) \\ &+ G_{pq}^{\lessgtr}(t, \bar{t}) G_{\mu}^{\lessgtr}(\bar{t}, t) v_{ijpm}^A w_{nq\mu j}^A], \end{aligned} \quad (5)$$

where we neglected the off-diagonal elements of the continuum Green's function, i.e., $G_{\mu\nu}^{\lessgtr} = \delta_{\mu\nu} G_{\mu}^{\lessgtr}$. As we shall demonstrate, this approximation is remarkably accurate. Through the GKBA, Σ_{Auger} is a time-nonlocal functional of ρ and f_μ . Finally, the collision integral \mathcal{J}_μ reads

$$\mathcal{J}_\mu(t) = \int_0^t d\bar{t} [K_{\mu\mu}^>(t, \bar{t}) f_\mu^<(\bar{t}) + K_{\mu\mu}^<(t, \bar{t}) f_\mu^>(\bar{t})], \quad (6)$$

where the kernel

$$\begin{aligned} K_{\mu\nu}^{\lessgtr}(t, \bar{t}) &= i \sum_{mn} \sum_{pq} \sum_{sr} v_{\mu r p m}^A w_{n q s v}^A \\ &\times G_{mn}^{\lessgtr}(t, \bar{t}) G_{pq}^{\lessgtr}(t, \bar{t}) G_{sr}^{\lessgtr}(\bar{t}, t) e^{-i\epsilon_\nu(\bar{t}-t)} \end{aligned} \quad (7)$$

is a time-nonlocal functional of ρ only. Equations (4), together with the definitions that follow it, constitute the first (methodological) result of this Rapid Communication. The implementation of Eqs. (4) does not alter the quadratic scaling with N_t . The scaling with the number of basis functions changes from N_{bound}^p to $\max[N_{\text{bound}}^p, N_{\text{bound}}^q N_{\text{cont}}]$ where N_{cont} is the number of continuum states and $2 \leq q \leq 4$. Therefore, the proposed equations can be used to simulate a large class of molecules of current interest.

Assessment of NEGF approach. To demonstrate the reliability of the coupled NEGF Eqs. (4) we consider a 1D atom with soft Coulomb interactions. On the grid points $x_n = na$ with $|n| < N_{\text{grid}}/2$, the single-particle Hamiltonian reads $h(x_n, x_m) = \delta_{n,m} [2\kappa + V_n(x_n)] - \delta_{|n-m|,1} \kappa$, where the nuclear

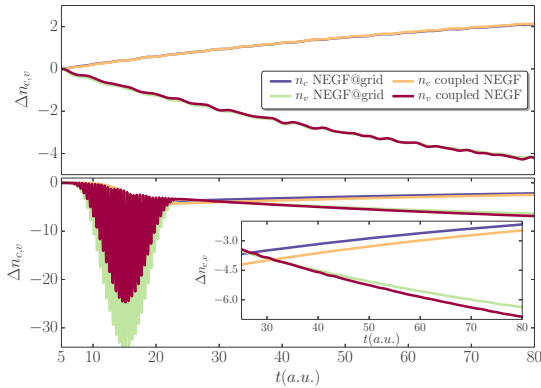


FIG. 2. Variation of the TD occupations (per spin) $n_c(t)$ [core, increasing blue (dark-gray) and orange (light-gray) curves] and $n_v(t)$ [valence, decreasing green (light-gray) and red (dark-gray) curves] calculated using NEGF@grid and coupled NEGF Eqs. (4) for the sudden creation of a core hole (top) and the action of a laser pulse (bottom). The inset shows a magnification of $n_c(t)$ and $n_v(t)$ after the end of the pulse. Vertical axes have been scaled up by a factor 10^2 .

potential $V_n(x) = U_{en}/\sqrt{x^2 + a^2}$ for $|x| \leq R$ and $V_n(x) = 0$ otherwise. Electrons interact only in a box of length $2R$ centered around zero through $v(x, x') = ZU_{ee}/\sqrt{(x - x')^2 + a^2}$. The coupling to an external laser pulse is accounted for by adding $\delta_{nm}x_n E(t)$ to $h(x_n, x_m)$.

We take $N_{\text{grid}} = 400$ and (henceforth all quantities are expressed in atomic units) $a = 0.5$, $\kappa = 2$, $Z = 4$, $U_{en} = 2$, $U_{ee} = U_{en}/2$, and $R = 10a$. With four electrons the HF spectrum has $N_{\text{sys}} = 5$ bound states (per spin) and $N_{\text{cont}} = N_{\text{grid}} - N_{\text{sys}}$ continuum states. The occupied levels have energy $\epsilon_c = -4.33$ (core) and $\epsilon_v = -1.65$ (valence). The HF states are used to construct the Hamiltonian in Eqs. (1) and (2). The results obtained by solving the coupled NEGF Eqs. (4) (where ρ is a $N_{\text{sys}} \times N_{\text{sys}}$ matrix and f is a N_{cont} -dimensional vector) are benchmarked against NEGF calculations on the full grid (NEGF@grid). NEGF@grid simulations are performed by solving the original equation [26] $\dot{\rho} = -i[h_{\text{HF}}[\rho], \rho] - \mathcal{I}[\rho] - \mathcal{I}^\dagger[\rho]$ where all quantities are $N_{\text{grid}} \times N_{\text{grid}}$ matrices in the x_n basis and \mathcal{I} is given by Eq. (3) with $\Sigma = \Sigma_c$ (see SM for details). By construction, NEGF@grid simulations include the off-diagonal elements $h_{i\mu}, h_{\mu\mu'}, \mathbf{d}_{\mu\mu'}$ and all Coulomb integrals with two or more indices in the continuum. Notice that NEGF@grid scales cubically with N_{cont} and it is therefore not exportable to large systems.

In Fig. 2 we show the time-dependent (TD) occupation (per spin) of the core, n_c , and valence, n_v , levels. In the top panel we suddenly remove 4% of charge from the core, hence $\rho_{cc} \rightarrow \rho_{cc} - n_h$ with $n_h = 0.04$, and let the system evolve *without* external fields. In the bottom panel the equilibrium system is driven by the external pulse

$$E(t) = E_0 \sin^2\left(\frac{\pi t}{T}\right) \sin(\Omega t) \quad (8)$$

with central frequency $\Omega = 6.2$, active from $t = 0$ until $t = T = 20$. The frequency is large enough for the energy of the

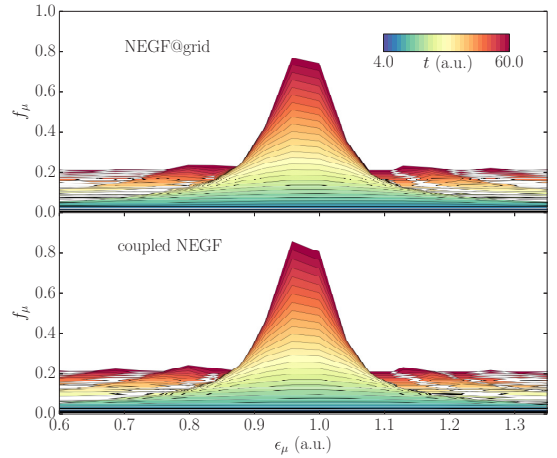


FIG. 3. Time-dependent occupations $f_\mu(t)$ of the continuum states versus their energy ϵ_μ after the sudden creation of a core hole. The results are obtained from the solution of the NEGF@grid equation (top) and coupled NEGF Eqs. (4) (bottom). In both cases the maximum occurs at $\epsilon_\mu = \epsilon_{\text{Auger}}$. Vertical axes have been scaled up by a factor 10^2 .

photoelectron not to overlap with the energy of the Auger electron. The intensity has been chosen to have the same amount of expelled charge as in the case of the sudden removal: $E_0 = 2.0$ for NEGF@grid and $E_0 = 1.5$ for the coupled NEGF Eqs. (4)—the difference in the value of E_0 is due to the neglect of the dipole elements $d_{\mu\mu'}$ in Eq. (2). The results perfectly agree in the top panel, whereas only a minor discrepancy is observed in the bottom panel. In both type of simulations the Auger decay slightly depends on how the core hole is created. In fact, the laser pulse is also responsible for expelling charge from the valence level, thereby hindering the refilling of the core. The core-hole lifetime agrees well with the inverse linewidth function $\Gamma(\epsilon_{\text{Auger}}) = 2\pi \sum_\mu |v_{c\mu\nu\nu}|^2 \delta(\epsilon_{\text{Auger}} - \epsilon_\mu) \simeq 10^{-2}$ in all cases. It is worth emphasizing that no time-local approximation of Σ_{Auger} would yield the behavior $n_c(t) = 1 - n_h e^{-\Gamma t}$. We performed TD HF simulations both in the grid basis and by solving Eqs. (4) with $\mathcal{J}_\mu = \Sigma_c = \Sigma_{\text{Auger}} = 0$, and found that $n_c(t)$ remains essentially constant (not shown). This is consistent with similar findings obtained in TDDFT using adiabatic xc potentials [19].

After the sudden creation of a core hole the electronic density populates the continuum states ϕ_μ . In Fig. 3 we show the corresponding time-dependent occupations $f_\mu(t)$ versus their energy ϵ_μ . Again simulations have been performed using NEGF@grid (top panel) and the coupled NEGF Eqs. (4) (bottom panel). As time passes the total expelled charge increases and $f_\mu(t)$ gets peaked at the Auger energy $\epsilon_{\text{Auger}} = 2\epsilon_v - \epsilon_c \simeq 1$. The final profile of the peak has a width $\Gamma \equiv \Gamma(\epsilon_{\text{Auger}})$, independently of how the core hole is created (suddenly or due to a laser pulse). On the contrary, the photoelectron peak attains a width $\sim 2\pi/T$ immediately after the end of the pulse (see animation continuum_occupations.mp4 in the SM). We also observe that the exact energy of the Auger

electron $\epsilon_{\text{Auger}}^{\text{exact}} = 2\epsilon_v - \epsilon_c - v_{vvvv}$ is not within reach of the second-order approximation in Eq. (5): the shift v_{vvvv} (due to the valence-valence repulsion) would require a T -matrix treatment [33,34]. However, such shift has only a minor impact on the internal dynamics of 3D systems like, e.g., organic molecules, since the repulsion between two valence holes is typically less than 1 eV.

Auger wave-packet reconstruction. We now use the coupled NEGF Eqs. (4) to study the 1D atom on larger boxes (hence one- and two-electron integrals are calculated from HF states that spread over a large number of grid points). The output has been postprocessed to reconstruct the density of the Auger wave packet according to $n_{\text{Auger}}(x,t) = \sum_{\mu\nu} \varphi_{\mu}^*(x) f_{\mu\nu}(t) \varphi_{\nu}(x)$, where $f_{\mu\nu}(t) = \langle \hat{c}_{\nu\sigma}^{\dagger}(t) \hat{c}_{\mu\sigma}(t) \rangle$ is the off-diagonal density matrix in the continuum sector. The latter is obtained by integrating the NEGF equation of motion (see SM for the derivation)

$$\dot{f}_{\mu\nu} = -i(\epsilon_{\mu} - \epsilon_{\nu})f_{\mu\nu} - \mathcal{J}_{\mu\nu}[\rho, f] - \mathcal{J}_{\nu\mu}^*[\rho, f], \quad (9)$$

where $\mathcal{J}_{\mu\nu}$ is given by the right-hand side of Eq. (6) after the replacement $K_{\mu\mu}^{\lessgtr}(t, \bar{t}) f_{\mu}^{\lessgtr}(\bar{t}) \rightarrow K_{\mu\nu}^{\lessgtr}(t, \bar{t}) f_{\nu}^{\lessgtr}(\bar{t})$.

In Fig. 4 we display the Auger wave packet for $N_{\text{grid}} = 1600$ grid points. In the top panel the core hole is suddenly created (see also animation Auger_wavpacket.mp4 in the SM), whereas in the middle panel the atom is driven by the ionizing laser of Eq. (8). The first observation is that the wave front depends on the perturbation (sudden creation or laser), being steeper the shorter it takes to create the hole. The wave packet moves rightward at the expected speed $v = \partial\epsilon/\partial p \simeq 2\sqrt{\kappa\epsilon_{\text{Auger}}} = 2.2$ and its length is approximately v/Γ far away from the nucleus. Interestingly, the tail of the wave packet exhibits spatial ripples that tend to accumulate nearby the origin. The amplitude of the ripples depends on the perturbation (sudden creation or laser), whereas their spacing is an *intrinsic* feature. In the bottom panel of Fig. 4 we show the period T_r of the ripples, i.e., the elapsing time between two consecutive maxima of $n_{\text{Auger}}(x_0, t)$, at the interface $x_0 = 30a$, versus the number of periods. We present results for three different values of range and strengths of the Coulomb force ($R, U_{\text{en}}, U_{\text{ce}} = (10a, 2, 1)$, $(100a, 2.6, 2.08)$, and $(10a, 2.7, 2.025)$ yielding Auger energies $\epsilon_{\text{Auger}} = 1.02$, 1.76, and 2.66, respectively. In all cases we find that T_r attains a finite limit given by

$$T_r = 2\pi/\epsilon_{\text{Auger}}. \quad (10)$$

The occurrence of ripples and the intrinsic period T_r is not an artifact of the self-energy approximation. These features as well as the overall shape of the Auger wave packet are indeed confirmed by Configuration Interaction (CI) calculations. Starting at time $t = 0$ with the photoexcited state $|\Phi_x\rangle = \hat{c}_{\uparrow}^{\dagger} \hat{c}_{\downarrow}^{\dagger} \hat{c}_{\uparrow}^{\dagger} |0\rangle$ and evolving with the Hamiltonian in Eq. (1) one finds $n_{\text{Auger}}(x,t) = |\varphi_{\text{Auger}}(x,t)|^2$ with $\varphi_{\text{Auger}}(x,t) = \sum_{\mu} a_{\mu}(t) \varphi_{\mu}(x)$ and

$$a_{\mu}(t) \simeq -v_{c\mu vv} e^{-iE_{\mu}t} \frac{e^{i(\epsilon_{\mu} - \epsilon_{\text{Auger}} + i\Gamma/2)t} - 1}{\epsilon_{\mu} - \epsilon_{\text{Auger}} + i\Gamma/2}. \quad (11)$$

The CI Auger wave packet is in excellent agreement with NEGF (see the SM). In the SM we further show that the ripples

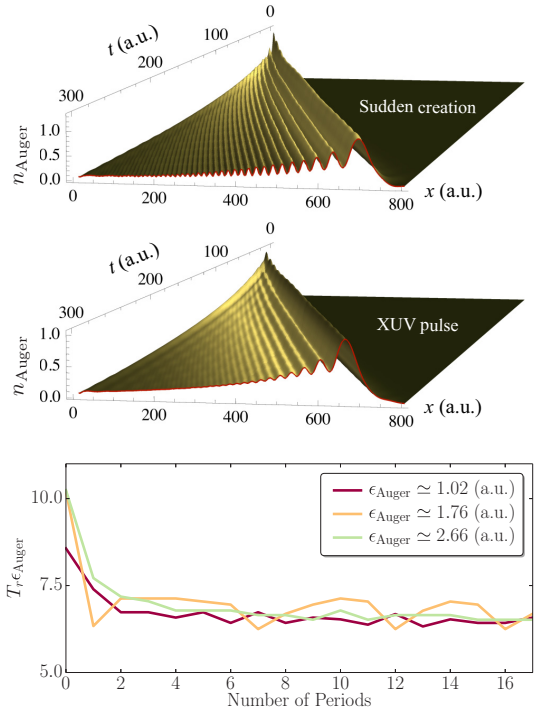


FIG. 4. Snapshots of the density of the Auger wave packet after the sudden creation of a core hole (top) and the action of a laser pulse (middle). The bottom panel shows the period of the ripples at an interface versus the number of periods for three different values of range and strengths of the Coulomb force (see main text) yielding Auger energies $\epsilon_{\text{Auger}} = 1.02$ [red (dark-gray)], 1.76 [yellow (gray)], and 2.66 [green (light-gray)].

occur even in two or three dimensions and, therefore, they are a fingerprint of the Auger electron.

To summarize, we have included Auger decays in a first-principles NEGF approach to simulate the UCM dynamics of molecules driven by attosecond pulses. The computational effort is comparable to that of previous NEGF implementations [26–28], thereby allowing for studying systems with tens of active electrons up to tens of femtoseconds. Benchmarks in 1D atoms demonstrate that both qualitative and quantitative aspects are well captured. We also predict a highly asymmetric profile of the Auger wave packet with a spatial extension of the order v/Γ and superimposed ripples with temporal period $T_r = 2\pi/\epsilon_{\text{Auger}}$.

Although the fundamental equations have been derived for finite systems, the proposed NEGF approach can be extended to deal with periodic systems too. In this context the equation of motion for the single-particle density matrix opens the possibility to develop current-density functional theories that include dissipation and thermalization.

Acknowledgments. G.S. and E.P. acknowledge EC funding through the RISE Co-ExAN (Grant No. GA644076). E.P. also acknowledges funding from the European Union project MaX

Materials design at the eXascale H2020-EINFRA-2015-1, Grant Agreement No. 676598 and Nanoscience Foundries and Fine Analysis-Europe H2020-INFRAIA-2014-2015, Grant Agreement No. 654360. F.C. and A.R. acknowledge financial

support from the European Research Council (ERC-2015-AdG-694097), Grupos Consolidados (IT578-13), and European Union Horizon 2020 program under Grant Agreement No. 676580 (NOMAD).

- [1] F. Calegari, D. Ayuso, A. Trabattori, L. Belshaw, S. De Camillis, S. Anumula, F. Frassetto, L. Poletto, A. Palacios, P. Decleva *et al.*, *Science* **346**, 336 (2014).
- [2] M. Uiberacker, T. Uphues, M. Schultze, A. J. Verhoef, V. Yakovlev, M. F. Kling, J. Rauschenberger, N. M. Kabachnik, H. Schröder, M. Lezius *et al.*, *Nature (London)* **446**, 627 (2007).
- [3] A. I. Kuleff and L. S. Cederbaum, *J. Phys. B* **47**, 124002 (2014).
- [4] A. I. Kuleff, N. V. Kryzhevoi, M. Pernpointner, and L. S. Cederbaum, *Phys. Rev. Lett.* **117**, 093002 (2016).
- [5] J. Breidbach and L. S. Cederbaum, *J. Chem. Phys.* **118**, 3983 (2003).
- [6] N. V. Golubev and A. I. Kuleff, *Phys. Rev. A* **91**, 051401 (2015).
- [7] K. Nagaya, H. Iwayama, A. Sugishima, Y. Ohmasa, and M. Yao, *Appl. Phys. Lett.* **96**, 233101 (2010).
- [8] M. Kutzner, V. Maycock, J. Thorarinson, E. Pannwitz, and J. A. Robertson, *Phys. Rev. A* **66**, 042715 (2002).
- [9] T. Uphues, M. Schultze, M. F. Kling, M. Uiberacker, S. Hendel, U. Heinzmann, N. M. Kabachnik, and M. Drescher, *New J. Phys.* **10**, 025009 (2008).
- [10] M. Drescher, M. Hentschel, R. Kienberger, M. Uiberacker, V. Yakovlev, A. Scrinzi, Th. Westerwalbesloh, U. Kleineberg, U. Heinzmann, and F. Krausz, *Nature (London)* **419**, 803 (2002).
- [11] S. Zherebtsov, A. Wirth, T. Uphues, I. Znakovskaya, O. Herrwerth, J. Gagnon, M. Korbman, V. S. Yakovlev, M. Vrakking, M. Drescher *et al.*, *J. Phys. B* **44**, 105601 (2011).
- [12] J. M. Schins, P. Breger, P. Agostini, R. C. Constantinescu, H. G. Muller, G. Grillon, A. Antonetti, and A. Mysyrowicz, *Phys. Rev. Lett.* **73**, 2180 (1994).
- [13] O. Smirnova, V. S. Yakovlev, and A. Scrinzi, *Phys. Rev. Lett.* **91**, 253001 (2003).
- [14] A. K. Kazansky, I. P. Sazhina, and N. M. Kabachnik, *J. Phys. B* **42**, 245601 (2009).
- [15] A. K. Kazansky, I. P. Sazhina, and N. M. Kabachnik, *J. Phys. B* **44**, 215601 (2011).
- [16] E. Runge and E. K. U. Gross, *Phys. Rev. Lett.* **52**, 997 (1984).
- [17] C. Ullrich, *Time-Dependent Density-Functional Theory* (Oxford University Press, Oxford, 2012).
- [18] N. T. Maitra, *J. Chem. Phys.* **144**, 220901 (2016).
- [19] C. S. Cucinotta, D. Hughes, and P. Ballone, *Phys. Rev. B* **86**, 045114 (2012).
- [20] The inadequacy of the adiabatic approximation is easily understandable. The Auger electron adds to the main quasiparticle peak a secondary peak in the spectral function of the parent cation. An adiabatic approximation can, at most, renormalize the main quasiparticle peak.
- [21] L. P. Kadanoff and G. A. Baym, *Quantum Statistical Mechanics: Green's Function Methods in Equilibrium and Nonequilibrium Problems* (Benjamin, New York, 1962).
- [22] G. Stefanucci and R. van Leeuwen, *Nonequilibrium Many-Body Theory of Quantum Systems: A Modern Introduction* (Cambridge University Press, Cambridge, 2013).
- [23] P. Myöhänen, A. Stan, G. Stefanucci, and R. van Leeuwen, *Phys. Rev. B* **80**, 115107 (2009).
- [24] P. Myöhänen, A. Stan, G. Stefanucci, and R. van Leeuwen, *Europhys. Lett.* **84**, 67001 (2008).
- [25] S. Latini, E. Perfetto, A.-M. Uimonen, R. van Leeuwen, and G. Stefanucci, *Phys. Rev. B* **89**, 075306 (2014).
- [26] E. Perfetto, A.-M. Uimonen, R. van Leeuwen, and G. Stefanucci, *Phys. Rev. A* **92**, 033419 (2015).
- [27] E. V. Boström, A. Mikkelsen, C. Verdozzi, E. Perfetto, and G. Stefanucci, *Nano Lett.* **18**, 785 (2018).
- [28] E. Perfetto, D. Sangalli, A. Marini, and G. Stefanucci, *J. Phys. Chem. Lett.* **9**, 1353 (2018).
- [29] P. Lipavský, V. Špička, and B. Velický, *Phys. Rev. B* **34**, 6933 (1986).
- [30] See Supplemental Material at <http://link.aps.org/supplemental/10.1103/PhysRevA.97.061401> for the derivation of the theoretical framework as well as for the animations of the continuum occupations and Auger wave packet in real space.
- [31] C.-O. Almbladh, A. L. Morales, and G. Grossmann, *Phys. Rev. B* **39**, 3489 (1989).
- [32] C.-O. Almbladh and A. L. Morales, *Phys. Rev. B* **39**, 3503 (1989).
- [33] M. Cini, *Solid State Commun.* **88**, 1101 (1993).
- [34] G. A. Sawatzky, *Phys. Rev. Lett.* **39**, 504 (1977).

Real-time dynamics of Auger wavepackets and decays in ultrafast charge migration processes

– Supplemental Material –

F. Covito,¹ E. Perfetto,^{2,3} A. Rubio,^{1,4,5} and G. Stefanucci^{3,6}

¹*Max Planck Institute for the Structure and Dynamics of Matter and Center for Free-Electron Laser Science, Luruper Chaussee 149, 22761 Hamburg, Germany*

²*CNR-ISM, Division of Ultrafast Processes in Materials (FLASHit), Area della ricerca di Roma 1, Monterotondo Scalo, Italy*

³*Dipartimento di Fisica, Università di Roma Tor Vergata, Via della Ricerca Scientifica, 00133 Rome, Italy*

⁴*Center for Computational Quantum Physics (CCQ), The Flatiron Institute, 162 Fifth Avenue, New York NY 10010*

⁵*Nano-Bio Spectroscopy Group, Universidad del País Vasco, 20018 San Sebastian, Spain*

⁶*INFN, Sezione di Roma Tor Vergata, Via della Ricerca Scientifica 1, 00133 Roma, Italy*

(Dated: May 15, 2018)

To distinguish the labels of equations and figures in the Supplemental Material from those of the main text we add “-I” to the latter.

I. DERIVATION OF NEGF EQUATIONS IN HF BASIS

The starting point is the equation of motion for the Green’s function $\mathcal{G}(z, z')$ with times z, z' on the Keldysh contour. For the Hamiltonian in Eqs. (1-I) and (2-I) it is convenient to write \mathcal{G} and the correlation self-energy Σ in a block form

$$\mathcal{G}(z, z') = \begin{pmatrix} G(z, z') & \Delta(z, z') \\ \bar{\Delta}(z, z') & C(z, z') \end{pmatrix}, \quad (1)$$

$$\Sigma(z, z') = \begin{pmatrix} \Sigma_G(z, z') & \Sigma_\Delta(z, z') \\ \bar{\Sigma}_\Delta(z, z') & \Sigma_C(z, z') \end{pmatrix}, \quad (2)$$

where G is a matrix with indices in the bound sector, C is a matrix with indices in the continuum sector and $\Delta, \bar{\Delta}$ are the off-diagonal blocks. The blocks of the self-energy have the same structure. For the self-energy we make the following approximation

(i) All self-energy diagrams containing Δ or $\bar{\Delta}$ propagators are set to zero (see below for the justification).

From the approximation (i) it follows that $\Sigma_\Delta = \bar{\Sigma}_\Delta = 0$ and that the Hartree-Fock (HF) potential has indices only in the bound sector since the Coulomb integrals in \bar{H}^{eq} have at most one index in the continuum. The explicit form of the HF potential is

$$V_{\text{HF},ij}(z) = -i \sum_{mn} G_{nm}(z, z^+) w_{imnj}, \quad (3)$$

where $w_{imnj} \equiv 2v_{imnj} - v_{imjn}$.

The equations of motion for the different blocks of \mathcal{G} then read (in matrix form)

$$\left[i \frac{d}{dz} - h_{\text{HF}}(z) \right] G(z, z') - (\mathbf{E}(z) \cdot \mathbf{d}) \bar{\Delta}(z, z') = \delta(z, z') + \int d\bar{z} \Sigma_G(z, \bar{z}) G(\bar{z}, z') \quad (4)$$

$$\left[i \frac{d}{dz} - \mathcal{E} \right] \bar{\Delta}(z, z') - (\mathbf{E}(z) \cdot \mathbf{d}) G(z, z') = \delta(z, z') + \int d\bar{z} \Sigma_C(z, \bar{z}) \bar{\Delta}(\bar{z}, z') \quad (5)$$

$$\left[i \frac{d}{dz} - \mathcal{E} \right] C(z, z') = \delta(z, z') + \int d\bar{z} \Sigma_C(z, \bar{z}) C(\bar{z}, z') \quad (6)$$

where in Eq. (4) we have defined the nonequilibrium single-particle HF Hamiltonian

$$h_{\text{HF}} = h + V_{\text{HF}} + \mathbf{E} \cdot \mathbf{d}, \quad (7)$$

and in the last two equations we have defined the matrix $\mathcal{E}_{\mu\nu} = \delta_{\mu\nu} \epsilon_\mu$. The blocks of the dipole matrix are unambiguously determined by the contractions and we do therefore use the same symbol for all four blocks. Notice that no coupling with the electric field appears in Eq. (6) since we set $\mathbf{d}_{\mu\mu'} = 0$ in Eq. (2-I).

Next we observe that if the energy-window of the photoelectron does not overlap with that of the Auger electron then we can make the approximation:

$$(ii) \Sigma_C(z, \bar{z}) \bar{\Delta}(\bar{z}, z') \simeq 0.$$

With the approximation (ii) we easily integrate Eq. (5) and obtain

$$\bar{\Delta}_{\mu j}(z, z') = \sum_n \int d\bar{z} C_\mu^0(z, \bar{z}) (\mathbf{E}(\bar{z}) \cdot \mathbf{d}_{\mu n}) G_{nj}(\bar{z}, z'), \quad (8)$$

where C^0 is the solution of Eq. (6) with $\Sigma_C = 0$. Since \mathcal{E} is diagonal so is C^0 .

Inserting Eq. (8) into Eq. (4) we get

$$\left[i \frac{d}{dz} - h_{\text{HF}}(z) \right] G(z, z') = \delta(z, z') + \int d\bar{z} [\Sigma_G(z, \bar{z}) + \Sigma_{\text{ion}}(z, \bar{z})] G(\bar{z}, z'), \quad (9)$$

where we have defined the ionization self-energy

$$\Sigma_{\text{ion},ij}(z, \bar{z}) \equiv \sum_{\mu} (\mathbf{E}(z) \cdot \mathbf{d}_{i\mu}) C_{\mu}^0(z, \bar{z}) (\mathbf{E}(\bar{z}) \cdot \mathbf{d}_{\mu j}). \quad (10)$$

The diagrammatic representation of the ionization self-energy is displayed in the bottom diagram of Fig. 1(b)-I where, to avoid a proliferation of different symbols, we used G_{μ}^0 instead of C_{μ}^0 (in the main text we also used $G_{\mu\nu}$ instead of $C_{\mu\nu}$). Notice that Σ_{ion} vanishes for times at which the external pulse is zero.

We now have to specify the approximation for the correlation self-energy. For weakly interacting closed systems (no continuum states) the self-consistent second-Born approximation (2B) has been shown to be accurate in several nonequilibrium situations [1–10]. The very same approximation describes Auger scatterings provided that we also consider interaction lines with one index in the continuum [11, 12]. We therefore approximate Σ_G and Σ_C as the sum of the 2B diagrams. It is easy to show that for a \mathcal{G} initially block diagonal (no electrons in the continuum in the ground state) the off-diagonal blocks remain zero for all times in the 2B approximation. This justifies the approximation (i).

The 2B diagrams for Σ_G can be split into diagrams with interaction lines having all indices in the bound sector (v) and diagrams with interaction lines having one index in the continuum sector (v^A):

$$\Sigma_G = \Sigma_c + \Sigma_{\text{Auger}}. \quad (11)$$

Using the Feynman rules, see top and middle panel of Fig. 1, one finds

$$\Sigma_{c,ij}(z, z') = \sum_{mn,pq,sr} v_{irpm} w_{nqsj} \times G_{mn}(z, z') G_{pq}(z, z') G_{sr}(z', z), \quad (12)$$

and

$$\Sigma_{\text{Auger},ij}(z, z') = \sum_{mn,pq} \sum_{\mu} G_{mn}(z, z') \times [C_{\mu\nu}(z, z') G_{pq}(z', z) (v_{iq\mu}^A w_{\nu npj}^A + v_{iq\mu}^A w_{\nu npj}^A) + G_{pq}(z, z') C_{\mu\nu}(z', z) v_{ipm}^A w_{nq\mu j}^A]. \quad (13)$$

The correlation self-energy Σ_c is also given in the top diagram of Fig. 1(b)-I.

The 2B diagrams for Σ_C do instead contain only v^A interaction lines since both indices of Σ_C are in the continuum sector. From the bottom diagram of Fig. 1 one

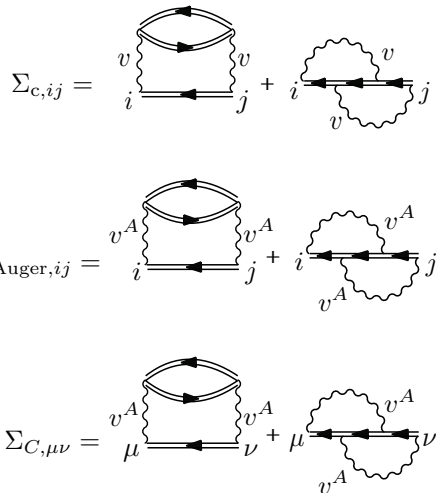


FIG. 1: Self-energy diagrams with indices in the bound sector for intramolecular scattering (top) and Auger scattering (middle). Self-energy diagrams for Auger electrons (bottom).

finds

$$\Sigma_{C,\mu\nu}(z, z') = \sum_{mn,pq,sr} v_{\mu r p m}^A w_{n q s \nu}^A \times G_{mn}(z, z') G_{pq}(z, z') G_{sr}(z', z). \quad (14)$$

For a short and weak laser pulse the off-diagonal matrix elements of C are small. We therefore make the approximation

$$(iii) C_{\mu\nu} \simeq \delta_{\mu\nu} C_{\mu} \text{ in } \Sigma_{\text{Auger}}$$

Implementing (iii) in Eq. (13) and extracting the lesser/greater component we get precisely the self-energy in Eq. (5-I).

To summarize, with the approximations (i-iii) the equations of motion become

$$\left[i \frac{d}{dz} - h_{\text{HF}}(z) \right] G(z, z') = \delta(z, z') + \int d\bar{z} \Sigma(z, \bar{z}) G(\bar{z}, z') \quad (15)$$

$$\left[i \frac{d}{dz} - \mathcal{E} \right] C(z, z') = \delta(z, z') + \int d\bar{z} \Sigma_C(z, \bar{z}) C(\bar{z}, z') \quad (16)$$

where in Eq. (15) we have defined

$$\Sigma \equiv \Sigma_c + \Sigma_{\text{ion}} + \Sigma_{\text{Auger}}. \quad (17)$$

Taking the adjoint of Eqs. (15,16), summing the resulting equations to Eqs. (15,16) and evaluating the result in $z = z^+ = t$ we get the equation of motion for

the density matrices $\rho_{ij}(t) = -iG_{ij}(z, z^+)$ and $f_{\mu\nu}(t) = -iC_{\mu\nu}(z, z^+)$:

$$\dot{\rho} = -i[h_{\text{HF}}, \rho] - \mathcal{I} - \mathcal{I}^\dagger, \quad (18)$$

$$\dot{f}_{\mu\nu} = -i(\epsilon_\mu - \epsilon_\nu)f_{\mu\nu} - \mathcal{J}_{\mu\nu} - \mathcal{J}_{\nu\mu}^*, \quad (19)$$

where

$$\mathcal{I}(t) = \int_0^t d\bar{t} [\Sigma^>(t, \bar{t})G^<(\bar{t}, t) - \Sigma^<(t, \bar{t})G^>(\bar{t}, t)], \quad (20)$$

$$\mathcal{J}(t) = \int_0^t d\bar{t} [\Sigma_C^>(t, \bar{t})C^<(\bar{t}, t) - \Sigma_C^<(t, \bar{t})C^>(\bar{t}, t)]. \quad (21)$$

Equations (18,19) do not close on ρ and f since the right hand side depends on G and C calculated at different times. To close the equations we make the Generalized Kadanoff-Baym Ansatz [13] (GKBA). According to the GKBA we can replace all G^{\lessgtr} and C^{\lessgtr} appearing in \mathcal{I} and \mathcal{J} with

$$G^{\lessgtr}(t, \bar{t}) = \mp [G^{\text{R}}(t, t')\rho^{\lessgtr}(t') - \rho^{\lessgtr}(t)G^{\text{A}}(t, t')], \quad (22)$$

$$C^{\lessgtr}(t, \bar{t}) = \mp [C^{\text{R}}(t, t')f^{\lessgtr}(t') - f^{\lessgtr}(t)C^{\text{A}}(t, t')], \quad (23)$$

where $\rho^< = \rho$, $\rho^> = 1 - \rho$ and similarly $f^< = f$, $f^> = 1 - f$. For the retarded/advanced Green's function we consider the HF approximation according to which

$$G^{\text{R}}(t, t') = [G^{\text{A}}(t', t)]^\dagger = -i\theta(t - t')\mathcal{T} \left[e^{-i \int_{t'}^t d\bar{t} h_{\text{HF}}(\bar{t})} \right], \quad (24)$$

$$C_{\mu\nu}^{\text{R}}(t, t') = [C_{\nu\mu}^{\text{A}}(t', t)]^* = -i\delta_{\mu\nu}\theta(t - t')e^{-i\epsilon_\mu(t - t')}. \quad (25)$$

Since h_{HF} is a functional of ρ we see that Eqs. (18,19) become nonlinear integro-differential equations for $\rho_{ij}(t)$ and $f_{\mu\nu}(t)$. Notice also that in the equation for ρ the dependence on f is only through the diagonal elements $f_\mu \equiv f_{\mu\mu}$ appearing in Σ_{Auger} , due to the approximation (iii). If we set $\mu = \nu$ in Eq. (19) then for the right hand side to depend only on f_μ we have to make the approximation

$$(iv) f_{\mu\nu} = \delta_{\mu\nu}f_\mu \text{ in } \mathcal{J}$$

which is consistent with the approximation (iii).

It is easy to show that in this way the equation for ρ becomes the first of Eqs. (4-I) and that the equation for $f_{\mu\nu}$ becomes Eq. (9-I), which for $\mu = \nu$ reduces to the second of Eqs. (4-I).

II. NEGF@GRID VERSUS COUPLED NEGF CALCULATIONS

To assess the accuracy of the approximations made at the level of the Hamiltonian with Eqs. (1-I,2-I) and at the level of NEGF with (i-iv), we considered a 1D atom on a grid. In the grid basis the total Hamiltonian in second quantization reads

$$\begin{aligned} \hat{H}(t) = & \sum_{mn} \psi_\sigma^\dagger(x_m)h(x_m, x_n)\psi_\sigma(x_n) \\ & + \frac{1}{2} \sum_{mn} \psi_\sigma^\dagger(x_m)\psi_{\sigma'}^\dagger(x_n)v(x_m, x_n)\psi_{\sigma'}(x_n)\psi_\sigma(x_m) \\ & + E(t) \sum_{\sigma} x_m \psi_\sigma^\dagger(x_m)\psi_\sigma(x_m). \end{aligned} \quad (26)$$

where the one-particle Hamiltonian $h(x, x')$ and the interaction $v(x, x')$ are defined in the main text. The equation of motion for the density matrix in grid basis $\rho(x_m, x_n, t) = G(x_m, z; x_n, z^+)$ in the 2B approximation is

$$\begin{aligned} \dot{\rho}(x_m, x_n, t) = & -i \sum_p [h_{\text{HF}}(x_m, x_p, t)\rho(x_p, x_n, t) \\ & - \rho(x_m, x_p, t)h_{\text{HF}}(x_p, x_n, t)] \\ & - \mathcal{I}_g(x_m, x_n, t) - \mathcal{I}_g^*(x_n, x_m, t). \end{aligned} \quad (27)$$

In Eq. (27) we have the HF Hamiltonian in grid basis

$$h_{\text{HF}}(x_m, x_p, t) = h(x_m, x_p) + V_{\text{HF}}(x_m, x_p, t) + \delta_{mp}E(t)x_m, \quad (28)$$

with HF potential

$$\begin{aligned} V_{\text{HF}}(x_m, x_p, t) = & 2\delta_{nm} \sum_q v(x_m, x_q)\rho(x_q, x_q, t) \\ & - v(x_m, x_p)\rho(x_m, x_p, t), \end{aligned} \quad (29)$$

and the collision integral in grid basis

$$\begin{aligned} \mathcal{I}_g(x_m, x_n, t) = & \sum_p \int_0^t d\bar{t} [\Sigma_g^>(x_m, t; x_p, \bar{t})G^<(x_p, \bar{t}; x_n, t) \\ & - \Sigma_g^<(x_m, t; x_p, \bar{t})G^>(x_p, \bar{t}; x_n, t)], \end{aligned} \quad (30)$$

with the 2B self-energy

$$\begin{aligned} \Sigma_g^{\lessgtr}(x_m, t; x_p, \bar{t}) = & \sum_{rs} v(x_m, x_r)v(x_p, x_s) \\ & \times \left[2G^{\lessgtr}(x_m, t; x_p, \bar{t})G^{\lessgtr}(x_r, t; x_s, \bar{t})G^{\gtrless}(x_s, \bar{t}; x_r, t) \right. \\ & \left. - G^{\lessgtr}(x_m, t; x_s, \bar{t})G^{\gtrless}(x_s, \bar{t}; x_r, t)G^{\lessgtr}(x_r, t; x_p, \bar{t}) \right]. \end{aligned} \quad (31)$$

The NEGF@grid results have been obtained by solving Eq. (27) with lesser/greater Green's function evaluated at the GKBA level. Except that for the 2B approximation

to Σ_g , no other approximation has been made. For a system with N_{grid} points this requires to propagate and store matrices $N_{\text{grid}} \times N_{\text{grid}}$.

In order to apply the coupled NEGF scheme based on Eqs. (4-I) we first solve the self-consistent HF problem and extract the equilibrium bound eigenfunctions $\varphi_i(x_n)$ and continuum eigenfunctions $\varphi_\mu(x_n)$ of energy ϵ_i and ϵ_μ respectively. The HF eigenfunctions are then used to calculate the matrix elements in the bound sector of the one-particle Hamiltonian

$$h_{ij} = \sum_{mn} \varphi_i^*(x_m) h(x_m, x_n) \varphi_j(x_n), \quad (32)$$

the dipole operator

$$d_{ij} = \sum_m \varphi_i^*(x_m) x_m \varphi_j(x_m), \quad (33)$$

and the Coulomb repulsion

$$v_{ijpq} = \sum_{mn} \varphi_i^*(x_m) \varphi_j^*(x_n) v(x_m, x_n) \varphi_p(x_n) \varphi_q(x_m). \quad (34)$$

The continuum HF eigenfunctions are used to calculate the bound-continuum matrix elements of the dipole operator

$$d_{i\mu} = \sum_m \varphi_i^*(x_m) x_m \varphi_\mu(x_m), \quad (35)$$

and the Coulomb repulsion responsible for Auger scatterings

$$v_{ijp\mu}^A = \sum_{mn} \varphi_i^*(x_m) \varphi_j^*(x_n) v(x_m, x_n) \varphi_p(x_n) \varphi_\mu(x_m). \quad (36)$$

With this information we approximate the original Hamiltonian in Eq. (26) in accordance with Eqs. (I-1,2-I), i.e.,

$$\begin{aligned} \hat{H}(t) = & \sum_{ij} h_{ij} \hat{c}_{i\sigma}^\dagger \hat{c}_{j\sigma} + \frac{1}{2} \sum_{ijpq} v_{ijpq} \hat{c}_{i\sigma}^\dagger \hat{c}_{j\sigma'}^\dagger \hat{c}_{p\sigma'} \hat{c}_{q\sigma} \\ & + \sum_{\mu\sigma} \epsilon_\mu \hat{c}_{\mu\sigma}^\dagger \hat{c}_{\mu\sigma} + \sum_{ijp\mu} v_{ijp\mu}^A \left(\hat{c}_{i\sigma}^\dagger \hat{c}_{j\sigma'}^\dagger \hat{c}_{p\sigma'} \hat{c}_{\mu\sigma} + \text{h.c.} \right) \\ & + E(t) \sum_{ij} d_{ij} \hat{c}_{i\sigma}^\dagger \hat{c}_{j\sigma} + E(t) \sum_{i\mu} \left(d_{i\mu} \hat{c}_{i\sigma}^\dagger \hat{c}_{\mu\sigma} + \text{h.c.} \right), \quad (37) \end{aligned}$$

where $\hat{c}_{i\sigma}$ ($\hat{c}_{\mu\sigma}$) are annihilation operators for an electron in the HF orbital φ_i (φ_μ) with spin σ . Of course, had we included in Eq. (37) the off-diagonal one-electron terms containing $h_{i\mu}$, $h_{\mu\mu'}$ and $d_{\mu\mu'}$ and the interaction terms containing $v_{ij\mu\mu'}$, $v_{i\nu\mu\mu'}$ and $v_{\nu'\nu\mu\mu'}$ we would have got the same Hamiltonian as in Eq. (26) but in the HF basis.

With the approximate Hamiltonian in Eq. (37) we solve the coupled NEGF equations (4-I) which, we emphasize again, have been derived by making the additional approximations (i-iv) of the previous section. The

agreement between the full-grid simulations and the simulations based on Eqs. (4-I) indicate that the latter are enough to capture qualitatively and quantitatively the physics of the Auger decay.

We observe that in the grid simulations the self-energy Σ_g contains all possible scatterings, including those contained in the self-energies Σ_c and Σ_{Auger} of the coupled NEGF scheme. Furthermore, in the grid simulations no ionization self-energy appears since the photoionization is accounted for by explicitly including all grid points (even those far away from the nucleus). In other words, *all* elements $\rho(x_m, x_n, t)$ are coupled and propagated in time.

III. CI VERSUS COUPLED NEGF CALCULATIONS

To further check the quality of the NEGF Eqs. (4-I) we have also solved the time-dependent problem using a Configuration Interaction (CI) expansion.

The neutral 1D atom described in the main text of the paper has four electrons, two in the core and two in the valence levels. We are interested in suddenly removing a core electron of, say, spin down, and in studying how the system evolves with the Hamiltonian in Eq. (37). For the CI expansion we use the following three-body states

$$|\Phi_x\rangle = \hat{c}_{c\uparrow}^\dagger \hat{c}_{v\downarrow}^\dagger \hat{c}_{v\uparrow}^\dagger |0\rangle, \quad (38)$$

$$|\Phi_g\rangle = \hat{c}_{c\uparrow}^\dagger \hat{c}_{c\downarrow}^\dagger \hat{c}_{v\uparrow}^\dagger |0\rangle, \quad (39)$$

$$|\Phi_\mu\rangle = \hat{c}_{c\uparrow}^\dagger \hat{c}_{c\downarrow}^\dagger \hat{c}_{\mu\uparrow}^\dagger |0\rangle, \quad (40)$$

describing the initially photoionized state (Φ_x), the cationic ground state (Φ_g) and the Auger states (Φ_μ). We expand the state of the system at time t according to

$$|\Psi(t)\rangle = a_x(t)|\Phi_x\rangle + a_g(t)|\Phi_g\rangle + \sum_{\mu} a_{\mu}(t)|\Phi_{\mu}\rangle, \quad (41)$$

and impose the initial condition $a_x(0) = 1$ and $a_g(0) = a_{\mu}(0) = 0$. Using the fact that in the HF basis h_{HF} is diagonal, it is easy to show that the cationic ground state decouples and the dynamics is governed by the equations below

$$i\dot{a}_x = E_x a_x + \sum_{\mu} v_{c\mu v v} a_{\mu}, \quad (42)$$

$$i\dot{a}_{\mu} = v_{c\mu v v} a_x + E_{\mu} a_{\mu}. \quad (43)$$

The three-body energies are

$$E_x = 2\epsilon_v + \epsilon_c - v_{cccc} - 4v_{cvvc} + 2v_{cvcv} - v_{vvvv}, \quad (44)$$

$$E_{\mu} = \epsilon_{\mu} + 2\epsilon_c - v_{cccc} - 4v_{cvvc} + 2v_{cvcv}, \quad (45)$$

where the HF energies of the core and valence levels are given by

$$\epsilon_c = h_{cc} + v_{cccc} + 2v_{cvvc} - v_{cvcv}, \quad (46)$$

$$\epsilon_v = h_{vv} + v_{vvvv} + 2v_{vccv} - v_{vvcv}. \quad (47)$$

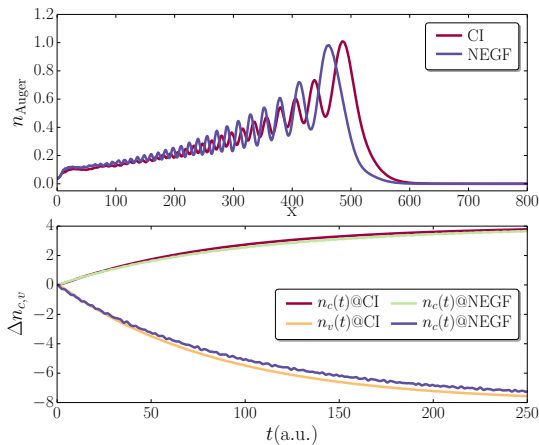


FIG. 2: Auger wavepacket (top) and variation of the occupations of the core and valence levels (bottom) in CI and in coupled NEGF. Same parameters as in top panel of Fig. 4-I.

The energy $\epsilon_{\text{Auger}} = \epsilon_{\mu_A}$ of the Auger electron is determined by the condition $E_{\mu_A} = E_x$ which yields

$$\epsilon_{\text{Auger}} = 2\epsilon_v - \epsilon_c - v_{vvvv} \quad (48)$$

as it should. The red-shift v_{vvvv} is due to the repulsion of the two holes in the final state. In order to capture this red-shift using Many-Body Perturbation Theory (MBPT) one should go beyond the 2B approximation for the self-energy and consider the T -matrix approximation in the particle-particle sector [14, 15]. We observe, however, that for weakly correlated molecules, like organic molecules and biomolecules, the magnitude of the valence-valence repulsion is typically less than 1 eV; hence, neglecting this repulsion does not substantially affect the dynamics during the first ten of femtoseconds or so.

For the 1D atom the valence-valence repulsion is mainly responsible for reducing the speed of the Auger electron. The form of the Auger wavepacket as well as the time-dependent behavior of the refilling of the core-hole are not altered if we set $v_{vvvv} = 0$ in Eq. (44). For a fair comparison with the coupled NEGF Eqs. (4-I) we therefore solve Eqs. (42,43) using $E_x^{2B} = E_x + v_{vvvv}$ in place of E_x . In Fig. 2 we compare the Auger wavepacket (top panel) and the occupation of the core and valence levels (bottom panels) calculated using CI and the coupled NEGF equations (4-I). Also in this case the agreement is rather satisfactory.

The analytic calculation can be carried on further if we assume that the broadening

$$\Gamma(\omega) = 2\pi \sum_{\mu} |v_{c\mu vv}|^2 \delta(\omega - \epsilon_{\mu}) \quad (49)$$

is a weakly dependent function of ω for $\omega \simeq \epsilon_{\text{Auger}}$. In this case it is straightforward to show that the amplitudes

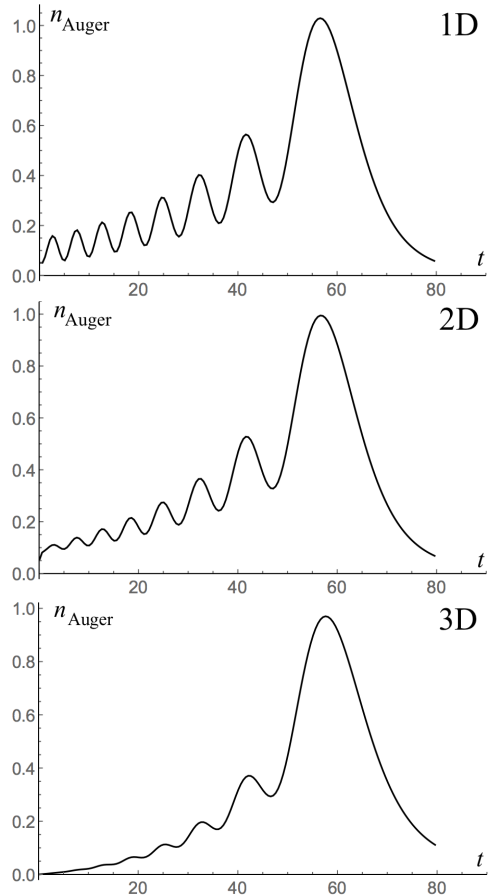


FIG. 3: Auger wavepacket (in arbitrary units) for $\Gamma = 0.05$ and $\epsilon_{\text{Auger}} = 1$ after a time $t = 50$ from the sudden removal of a core electron. Top: $n_{\text{Auger}}(r, t)$ in 1D. Middle: $rn_{\text{Auger}}(r, t)$ in 2D. Bottom: $r^2n_{\text{Auger}}(r, t)$ in 3D.

a_{μ} are given by

$$a_{\mu}(t) = -v_{c\mu vv} e^{-iE_{\mu}t} \frac{e^{i(\epsilon_{\mu} - \epsilon_{\text{Auger}} + i\Gamma/2)t} - 1}{\epsilon_{\mu} - \epsilon_{\text{Auger}} + i\Gamma/2} \quad (50)$$

which coincides with Eq. (11-I). The occurrence of ripples on the tail of the Auger wavepacket stems from the structure of the a_{μ} 's. In fact, the ripples are independent of the dimension of the system and of the details of the continuum states in the vicinity of the nucleus. As an example, let $\mu = \mathbf{p}$ be the momentum in D dimension and let us use planewaves $\varphi_{\mu}(\mathbf{r}) = \varphi_{\mathbf{p}}(\mathbf{r}) = e^{i\mathbf{p}\cdot\mathbf{r}}$ for the continuum states. We further consider a free dispersion $\epsilon_{\mu} = \epsilon_{\mathbf{p}} = p^2/2$ and, for simplicity, an Auger interaction $v_{c\mu vv} = v_{c\mathbf{p}vv}$ independent of \mathbf{p} so that $a_{\mu} = a_p$ depends only on the modulus $p = |\mathbf{p}|$ of the momentum,

see Eq. (50). Then, the Auger wavepacket is spherically symmetric and its density is given by

$$n_{\text{Auger}}(r, t) = \left| \int \frac{d^D p}{(2\pi)^D} a_p(t) e^{i\mathbf{p}\cdot\mathbf{r}} \right|^2. \quad (51)$$

In Fig. 3 we show $n_{\text{Auger}}(r, t)$ for $\Gamma = 0.05$ and an Auger energy $\epsilon_{\text{Auger}} = 1$ after a time $t = 50$ from the sudden removal of the core electron. The figure shows $n_{\text{Auger}}(r, t)$ in 1D (top), $rn_{\text{Auger}}(r, t)$ in 2D (middle) and $r^2 n_{\text{Auger}}(r, t)$ in 3D (bottom). In all cases we appreciate the occurrence of ripples although they tend to get smeared out as the dimension increases.

IV. DESCRIPTION OF ANIMATIONS

The animation `continuum_occupations.mp4` shows the evolution of the occupations f_μ of the continuum HF states for the 1D atom driven by the external laser pulse of Eq. (8-I). Same parameters as in the bottom panel of Fig. (2-I).

The animation `Auger_wavepacket.mp4` shows the evolution of the Auger wavepacket as obtained by solving first Eqs.(4-I) and then Eq. (9-I). Same parameters as in the top panel of Fig. 4-I.

-
- [1] K. Balzer, S. Bauch, and M. Bonitz, *Phys. Rev. A* **82**, 033427 (2010), URL <https://link.aps.org/doi/10.1103/PhysRevA.82.033427>.
- [2] K. Balzer, S. Hermanns, and M. Bonitz, *EPL (Europhysics Letters)* **98**, 67002 (2012), URL <http://stacks.iop.org/0295-5075/98/i=6/a=67002>.
- [3] N. Säkkinen, M. Manninen, and R. van Leeuwen, *New Journal of Physics* **14**, 013032 (2012), URL <http://stacks.iop.org/1367-2630/14/i=1/a=013032>.
- [4] S. Hermanns, N. Schlünzen, and M. Bonitz, *Phys. Rev. B* **90**, 125111 (2014), URL <https://link.aps.org/doi/10.1103/PhysRevB.90.125111>.
- [5] N. Schlünzen and M. Bonitz, *Contrib. Plasma Phys.* **56**, 5 (2016), ISSN 1521-3986, URL <http://dx.doi.org/10.1002/ctpp.201610003>.
- [6] M. Hopjan, D. Karlsson, S. Ydman, C. Verdozzi, and C.-O. Almbladh, *Phys. Rev. Lett.* **116**, 236402 (2016), URL <https://link.aps.org/doi/10.1103/PhysRevLett.116.236402>.
- [7] Y. B. Lev and D. R. Reichman, *EPL (Europhysics Letters)* **113**, 46001 (2016), URL <http://stacks.iop.org/0295-5075/113/i=4/a=46001>.
- [8] N. Schlünzen, J.-P. Joost, F. Heidrich-Meisner, and M. Bonitz, *Phys. Rev. B* **95**, 165139 (2017), URL <https://link.aps.org/doi/10.1103/PhysRevB.95.165139>.
- [9] A.-M. Uimonen, E. Khosravi, A. Stan, G. Stefanucci, S. Kurth, R. van Leeuwen, and E.K.U. Gross, *Phys. Rev. B* **84**, 115103 (2011).
- [10] E. V. Boström, A. Mikkelsen, C. Verdozzi, E. Perfetto, and G. Stefanucci, *Nano Lett.* **18**, 785 (2018), <https://doi.org/10.1021/acs.nanolett.7b03995>, URL <https://doi.org/10.1021/acs.nanolett.7b03995>.
- [11] C.-O. Almbladh, A. L. Morales, and G. Grossmann, *Phys. Rev. B* **39**, 3489 (1989), URL <https://link.aps.org/doi/10.1103/PhysRevB.39.3489>.
- [12] C.-O. Almbladh and A. L. Morales, *Phys. Rev. B* **39**, 3503 (1989), URL <https://link.aps.org/doi/10.1103/PhysRevB.39.3503>.
- [13] P. Lipavský, V. Špička, and B. Velický, *Phys. Rev. B* **34**, 6933 (1986), URL <https://link.aps.org/doi/10.1103/PhysRevB.34.6933>.
- [14] M. Cini, *Solid state communications* **88**, 1101 (1993).
- [15] G. A. Sawatzky, *Phys. Rev. Lett.* **39**, 504 (1977), URL <https://link.aps.org/doi/10.1103/PhysRevLett.39.504>.

Publication II

Benchmarking nonequilibrium Green's functions against configuration interaction for time-dependent Auger decay processes

Fabio Covito, Enrico Perfetto, Angel Rubio and Gianluca Stefanucci, *The European Physical Journal B*, **91** (10), 216 (2018).

This work is dedicated to a comparison of the coupled NEGF approach with a truncated Configuration Interaction (CI) calculation. A first assessment of the coupled NEGF method has been done in Publication I, where the comparison has been carried out with full grid NEGF calculations. A more thorough benchmark with an external method, though, gives us insight into the advantages and limitations of the method, independent of the underlying possible restrictions of the NEGF approach. In fact, the implications of using the approximations at the base of the proposed method within the GKBA have to be assessed. Our comparison, carried out in a 1-dimensional model system, shows consistency between the two approaches and the differences are explained as known limitations of the 2B approximation of the self-energy, which means that they are independent of the additional approximations made to derive the coupled NEGF equations. These differences, originating from the neglect of valence-valence repulsion within the 2B approximation for the self-energy, are expected to be negligible in realistic atoms and molecules. Importantly, the asymmetric profile of the Auger wavepacket is confirmed by the CI calculations and its intrinsic properties remain consistent.

This work represents a further assessment of the coupled NEGF approach for the description of the Auger decay, confirming the predicted behavior and properties. Future applications of the method could shine some light on the study of ultrafast electron dynamics following ionization in molecular systems, where correlation, and in turn the Auger decay, play a central role and where state-of-the-art

methods either fail to describe the physics or are computationally too involved.

In the following, I add a remark, which is not explicitly addressed in the published manuscript, but complements the discussion of the work.

Numerical solution of CI equations. Although it is a standard technique, it is worth mentioning how the numerical solution of the system of equations derived in the CI approach was performed. In fact, a stable solution could only be found by using a predictor corrector scheme. In particular, I used an approach based on Euler's method with the trapezoidal rule, yielding, for a general equation of the kind $y' = f(t, y)$, the time-stepping

$$y_{i+1} = y_i + \frac{1}{2} \Delta t (f(t_i, y_i) + f(t_{i+1}, \tilde{y}_{i+1})) , \quad (2.29)$$

with Δt the time-step and $\tilde{y}_{i+1} = y_i + \Delta t f(t_i, y_i)$ the initial guess (found through Euler's method).

Benchmarking nonequilibrium Green's functions against configuration interaction for time-dependent Auger decay processes*

Fabio Covito¹, Enrico Perfetto^{2,3}, Angel Rubio^{1,4,5}, and Gianluca Stefanucci^{3,6,a}

¹ Max Planck Institute for the Structure and Dynamics of Matter and Center for Free-Electron Laser Science, Luruper Chaussee 149, 22761 Hamburg, Germany

² CNR-ISM, Division of Ultrafast Processes in Materials (FLASHit), Area della ricerca di Roma 1, Monterotondo Scalo, Italy

³ Dipartimento di Fisica, Università di Roma Tor Vergata, Via della Ricerca Scientifica, 00133 Roma, Italy

⁴ Center for Computational Quantum Physics (CCQ), The Flatiron Institute, 162 Fifth Avenue, New York, NY 10010, USA

⁵ Nano-Bio Spectroscopy Group, Universidad del País Vasco, 20018 San Sebastián, Spain

⁶ INFN, Sezione di Roma Tor Vergata, Via della Ricerca Scientifica 1, 00133 Roma, Italy

Received 13 March 2018 / Received in final form 25 June 2018

Published online 1 October 2018

© EDP Sciences / Società Italiana di Fisica / Springer-Verlag GmbH Germany, part of Springer Nature, 2018

Abstract. We have recently proposed a nonequilibrium Green's function (NEGF) approach to include Auger decay processes in the ultrafast charge dynamics of photoionized molecules. Within the so-called generalized Kadanoff–Baym ansatz the fundamental unknowns of the NEGF equations are the reduced one-particle density matrix of bound electrons and the occupations of the continuum states. Both unknowns are one-time functions like the density in time-dependent functional theory (TDDFT). In this work, we assess the accuracy of the approach against configuration interaction (CI) calculations in one-dimensional model systems. Our results show that NEGF correctly captures qualitative and quantitative features of the relaxation dynamics provided that the energy of the Auger electron is much larger than the Coulomb repulsion between two holes in the valence shells. For the accuracy of the results dynamical electron–electron correlations or, equivalently, memory effects play a pivotal role. The combination of our NEGF approach with the Sham–Schlüter equation may provide useful insights for the development of TDDFT exchange–correlation potentials with a history dependence.

1 Introduction

Photo-ionized many-body systems relax to lower energy states through nuclear rearrangement and charge redistribution. Nuclear dynamics does typically play a role on longer time scales, although there are situations where electron–nuclear and electron–electron interactions compete on the same timescale, e.g., in the vicinity of a conical intersection. At the (sub)femtosecond timescale, however, the most relevant relaxation channel of core-ionized molecules is the Auger decay which is exclusively driven by the Coulomb interaction [1].

Recent advances in pump-probe experiments made it possible to follow the attosecond dynamics of atoms after the sudden expulsion of a core electron [2–6]. Theoretical

frameworks describing the Auger decay have been proposed, the more accurate being the ones based on many-body wavefunctions, see also reference [7]. Although these methods are in principle applicable to atoms as well as molecules, they quickly become prohibitive for systems with more than a few active electrons. For instance, Auger decays in ionized small molecules or molecules of biological interest are extremely difficult to cope with wavefunction approaches due to the large number of states involved in the process. Still, Auger decays contribute to the relaxation dynamics of these more complex systems, which are currently attracting an increasing interest and attention [8–12]. It is therefore crucial to develop first-principles approaches capable of capturing the (sub)femtosecond relaxation mechanisms induced by electronic correlations and applicable to atoms as well as molecules.

The most widely used method for large scale real-time simulations is time-dependent density functional theory [13–15] (TDDFT), which gives an adequate and computationally affordable tool for the description of systems

* Contribution to the Topical Issue “Special issue in honor of Hardy Gross”, edited by C.A. Ullrich, F.M.S. Nogueira, A. Rubio, and M.A.L. Marques.

^a e-mail: gianluca.stefanucci@roma2.infn.it

consisting of up to thousands of atoms. The most efficient and extensively used functionals for TDDFT calculations are the space-time local exchange-correlation (xc) functionals. It has been shown numerically in reference [16] that these approximate functionals fail in capturing Auger decays, the fundamental reason being that they lack memory effects – the xc potential depends on the instantaneous density only.

We have recently proposed a first-principles nonequilibrium Green's function (NEGF) approach [17], which overcomes the limitation of adiabatic functionals and that may inspire new ideas for the inclusion of memory effects in the TDDFT functionals. The method is applicable to molecules with up to tens of atoms and at its core there is an equation to simulate the electron dynamics in the parent cation without dealing explicitly with the Auger electrons. The idea is similar in spirit to the embedding scheme in time-dependent quantum transport where the electron dynamics in the molecular junction is simulated without dealing explicitly with the electrons in the leads [18–22]. However, whereas in quantum transport the integration out of electrons in the leads gives an embedding self-energy which is independent of the density in the junction, the integration out of the Auger electrons gives an Auger self-energy which is a functional of the density in the molecule.

In order to assess the quality of the NEGF approach in this work, we use the time-dependent charge distribution of the bound electrons to reconstruct the Auger wavepacket in free space, and then benchmark the results against exact configuration interaction (CI) calculations. We perform NEGF and CI simulations in a model one-dimensional (1D) system and study the real space-time shape of the Auger wavepacket as well as the Auger spectrum. The main outcome of this investigation is that the results of the NEGF approach are in excellent agreement with those from CI provided that the repulsion between the valence holes is much smaller than the energy of the Auger electron.

2 Description of the system and theory

Let us consider a 1D finite system described by the one-particle Hartree–Fock (HF) basis $\{\varphi_i, \varphi_\mu\}$, where roman indices run over bound states and greek indices run over continuum states. The equilibrium Hamiltonian can be conveniently written as the sum of three terms

$$\hat{H}^{\text{eq}} = \hat{H}_{\text{bound}} + \hat{H}_{\text{Auger}} + \hat{H}_{\text{cont}}, \quad (1)$$

where \hat{H}_{bound} is the bound electrons Hamiltonian, \hat{H}_{Auger} is the Auger interaction and \hat{H}_{cont} is the free-continuum part. In our basis, these are written as

$$\hat{H}_{\text{bound}} = \sum_{ij} h_{ij} \hat{c}_i^\dagger \hat{c}_j + \frac{1}{2} \sum_{ijmn} v_{ijmn} \hat{c}_i^\dagger \hat{c}_j^\dagger \hat{c}_m \hat{c}_n, \quad (2a)$$

$$\hat{H}_{\text{Auger}} = \sum_{ijm} \sum_{\mu} \left(v_{ijm\mu}^A \hat{c}_i^\dagger \hat{c}_j^\dagger \hat{c}_m \hat{c}_\mu + \text{H.c.} \right), \quad (2b)$$

$$\hat{H}_{\text{cont}} = \sum_{\mu} \epsilon_{\mu} \hat{c}_{\mu}^{\dagger} \hat{c}_{\mu}, \quad (2c)$$

where c_i^{\dagger} (c_i) is the creation (annihilation) operator for the state φ_i (the same convention applies to the continuum index μ), h_{ij} the one-electron integrals, ϵ_{μ} the continuum single-particle HF energies and v_{ijmn} ($v_{ijm\mu}^A$) are the two-electron Coulomb integrals responsible for intra-molecular (Auger) scatterings. The one- and two-electron integrals are defined as

$$h_{ij} \equiv \int dx \varphi_i^*(x) \left[-\frac{1}{2} \nabla_x^2 + V_n(x) \right] \varphi_j(x), \quad (3a)$$

$$v_{ijmn} \equiv \int dx dx' \varphi_i^*(x) \varphi_j^*(x') V_e(x, x') \varphi_m(x') \varphi_n(x), \quad (3b)$$

with $V_n(x)$ and $V_e(x, x')$ the nuclear and electron–electron potential. Note that the Auger Coulomb integrals $v_{ijm\mu}^A$ are defined according to equations (3b) with $n = \mu$. In equation (1) we discard all the off-diagonal contribution $h_{i\mu}$, $h_{\mu\mu'}$ as well as all Coulomb integrals with more than one index in the continuum. This approximation does not affect the physical description of the dynamics as demonstrated by comparisons against full grid calculations in reference [17]. In fact, in the HF basis both $h_{i\mu}$ and $h_{\mu\mu'}$ are much smaller than h_{ij} and ϵ_{μ} whereas Coulomb integrals with two or more indices in the continuum are responsible for scattering process that are highly suppressed by phase-space arguments if the photoelectron energy is much larger than the kinetic energy of the Auger electron. Henceforth, this condition is assumed to be fulfilled.

The explicit simulation of the ionization process with a laser field does not represent a complication for the NEGF method. In fact, the general framework presented in reference [17] accounts for the coupling of external fields with the bound-bound and bound-continuum dipole matrix elements. Instead, the framework discards the coupling of external fields with the continuum–continuum dipole matrix elements and, therefore, light-field streaking experiments relevant to, e.g., attosecond metrology [23], or multiphoton ionization processes are left out.

In this work, we focus on the dynamics induced by the sudden removal of a core electron, thus the ionization process is not simulated. An additional simplification used for the simulations below (which is however not essential for the approach) consists in keeping only integrals of the form $v_{c\mu v_1 v_2}^A$, where c labels the state of the suddenly created core hole, v_1 and v_2 label two valence states and μ an arbitrary continuum state. We also observe that the HF wavefunctions are real since the Hamiltonian is invariant under time-reversal. This implies that the Coulomb integrals have the following symmetries

$$v_{ijmn} = v_{jimn} = v_{ijnm} = v_{njmi}, \quad (4)$$

and the like with $n \rightarrow \mu$.

2.1 NEGF equations

The derivation of the NEGF equations within the so called generalized Kadanoff-Baym ansatz (GKBA) [24] has been presented elsewhere [17]; here we only describe the structure of these equations without entering into the complex mathematical and numerical details.

Let ρ be the one-particle reduced density matrix in the bound sector and f_μ be the occupations of the continuum states. Then the NEGF equations read

$$\begin{cases} \dot{\rho} = -i[h_{\text{HF}}[\rho], \rho] - \mathcal{I}[\rho, f] - \mathcal{I}^\dagger[\rho, f] \\ \dot{f}_\mu = -\mathcal{J}_\mu[\rho, f] - \mathcal{J}_\mu^*[\rho, f], \end{cases} \quad (5)$$

where the single-particle HF Hamiltonian is defined according to

$$h_{\text{HF},ij} = h_{ij} + \sum_{mn} (v_{imnj} - v_{imjn}) \rho_{nm}. \quad (6)$$

The matrix \mathcal{I} and the scalar \mathcal{J}_μ at time t are explicit functionals of ρ and f at all previous times. They are evaluated using the so-called second-Born (2B) approximation which has been shown to contain the fundamental scattering of the Auger process [25,26]. The dependence on ρ and f occurs through the lesser and greater GKBA Green's functions [24]

$$G^{\lessgtr}(t, \bar{t}) = \mp \left[G^{\text{R}}(t, t') \rho^{\lessgtr}(t') - \rho^{\lessgtr}(t) G^{\text{A}}(t, t') \right], \quad (7)$$

and the like for G^{\lessgtr} with indices in the continuum. Here, the retarded (G^{R}) and advanced (G^{A}) Green's functions are evaluated in the HF approximation (and hence they are functionals of ρ and f too). The functional \mathcal{I} (\mathcal{J}_μ) is linear in G^{\lessgtr} with indices in the continuum and quartic (cubic) in G^{\lessgtr} with indices in the bound sector. Their calculation requires to perform an integral from some initial time, say $t = 0$, up to time t . The implementation of equation (5) does therefore scale quadratically with the number of time steps. Notice that by setting $\mathcal{I} = \mathcal{J}_\mu = 0$ is equivalent to perform time-dependent HF simulations. Like the adiabatic approximations in TDDFT, HF is local in time and therefore it is unable to describe Auger decays.

The scaling of the calculation of \mathcal{I} and \mathcal{J}_μ with the number of basis functions is $\max[(N_{\text{bound}})^{\text{p}}, (N_{\text{bound}})^{\text{q}} N_{\text{cont}}]$, where N_{bound} is the number of bound states, N_{cont} the number of continuum states and the exponents $3 \leq \text{p} \leq 5$, $2 \leq \text{q} \leq 4$ depend on the number of nonvanishing Coulomb integrals [17]. Currently, both \mathcal{I} and \mathcal{J}_μ are implemented in the CHEERS code [27] which, for $\mathcal{J}_\mu = 0$, has been recently used to study the charge transfer dynamics in a donor- C_{60} model dyad [28] and the ultrafast charge migration in the phenylalanine aminoacid upto 40 fs [29]. Since the calculation of \mathcal{J}_μ is not heavier than the calculation of \mathcal{I} , the NEGF approach can be used to study time-dependent Auger processes driven by XUV or X-ray pulses in molecules with up to tens of atoms.

2.2 CI calculation

Let us consider the simplest possible case of a system with one occupied core state, one occupied valence state and a continuum of empty states. We are interested in describing the evolution of the system starting from the initial state

$$|\phi_x\rangle = c_{c\uparrow}^\dagger c_{v\downarrow}^\dagger c_{v\uparrow}^\dagger |0\rangle, \quad (8)$$

representing a core-hole of down spin. The evolution operator defined by the Hamiltonian in equation (1) mixes $|\phi_x\rangle$ with (we recall that only Coulomb integrals of the form $v_{c\mu v v}$ and the like related by symmetries are nonvanishing, see Sect. 2)

$$|\phi_g\rangle = c_{c\uparrow}^\dagger c_{c\downarrow}^\dagger c_{v\uparrow}^\dagger |0\rangle, \quad (9a)$$

$$|\phi_\mu\rangle = c_{c\uparrow}^\dagger c_{c\downarrow}^\dagger c_{\mu\uparrow}^\dagger |0\rangle, \quad (9b)$$

where $|\phi_g\rangle$ is the ‘‘intermediate’’ state with the filled core, i.e., the ground state of the parent cation, and $|\phi_\mu\rangle$ is the state describing the dication with an Auger electron in the continuum state μ . Carrying out the calculations it is easy to show that these states are coupled by the Hamiltonian as follows

$$\hat{H}^{\text{eq}} |\phi_x\rangle = E_x |\phi_x\rangle + T |\phi_g\rangle + \sum_\mu V_\mu |\phi_\mu\rangle, \quad (10a)$$

$$\hat{H}^{\text{eq}} |\phi_g\rangle = E_g |\phi_g\rangle + T |\phi_x\rangle, \quad (10b)$$

$$\hat{H}^{\text{eq}} |\phi_\mu\rangle = E_\mu |\phi_\mu\rangle + V_\mu |\phi_x\rangle, \quad (10c)$$

where the energies E_x , E_g , E_μ , T and V_μ are given by

$$E_x = h_{cc} + 2h_{vv} + 2v_{vvvc} + v_{vvvv} - v_{vcvc}, \quad (11a)$$

$$E_g = 2h_{cc} + h_{vv} + 2v_{vvvc} + v_{cccc} - v_{vcvc}, \quad (11b)$$

$$E_\mu = 2h_{cc} + \epsilon_\mu + v_{cccc}, \quad (11c)$$

$$T = h_{cv} + v_{ccvc} + v_{cvvv}, \quad (11d)$$

$$V_\mu = v_{vv\mu c}. \quad (11e)$$

The simplification brought about by the HF basis is now evident. The HF Hamiltonian $h_{\text{HF},ij} = h_{ij} + \sum_k^{\text{occ}} (2v_{ikjk} - v_{ijkj})$ is diagonal in the HF basis, therefore

$$\begin{aligned} 0 = h_{\text{HF},cv} &= h_{cv} + (2v_{cccv} - v_{ccvc}) + (2v_{cvvv} - v_{cvvv}) \\ &= h_{cv} + v_{cccv} + v_{cvvv} \equiv T. \end{aligned} \quad (12)$$

Thus the ‘‘intermediate’’ state $|\phi_g\rangle$ decouples from the dynamics.

We write the three-body wave function at time t as

$$|\psi(t)\rangle = a_x(t) |\phi_x\rangle + \sum_\mu a_\mu(t) |\phi_\mu\rangle, \quad (13)$$

with initial condition $|\psi(0)\rangle = |\phi_x\rangle$. Taking into account equations (10), the time-dependent Schrödinger equation yields a set of coupled equations for the coefficients of the

expansion

$$\begin{cases} i\dot{a}_x(t) = E_x a_x(t) + \sum_{\mu} V_{\mu} a_{\mu}(t) \\ i\dot{a}_{\mu}(t) = V_{\mu} a_x(t) + E_{\mu} a_{\mu}(t), \end{cases} \quad (14)$$

to be solved with boundary conditions $a_x(0) = 1$ and $a_k(0) = 0$.

From the definitions in equations (11) it follows that for the continuum three-body state to have the same energy of the initial state, i.e., $E_{\mu} = E_x$, the energy ϵ_{μ} of the Auger electron has to be

$$\epsilon_{\mu} \equiv \epsilon_{\text{Auger}}^{\text{CI}} = 2\epsilon_v^{\text{HF}} - \epsilon_c^{\text{HF}} - v_{vvvv}, \quad (15)$$

where

$$\epsilon_c^{\text{HF}} = h_{cc} + v_{ccc} + 2v_{cvc} - v_{cvc}, \quad (16a)$$

$$\epsilon_v^{\text{HF}} = h_{vv} + v_{vvv} + 2v_{vcv} + v_{vcv}, \quad (16b)$$

are the core and valence HF energies, respectively. It is therefore reasonable to expect a peak in the continuum occupations f_{μ} for the μ corresponding to an energy close to the value in equation (15).

In the next section we solve numerically equations (14). However, in order to get some physical insight into the solution we here make a ‘‘wide-band-limit approximation’’ (WBLA) and carry on the analytic treatment a bit further. Integrating the second equation (14) we have

$$a_{\mu}(t) = -i \int_0^t dt' e^{-iE_{\mu}(t-t')} V_{\mu} a_x(t'), \quad (17)$$

which correctly satisfies the boundary conditions $a_{\mu}(0) = 0$. Substituting this result into the first equation (14) we get

$$i\dot{a}_x(t) = E_x a_x(t) + \int_0^{\infty} dt' K(t-t') a_x(t'), \quad (18)$$

where

$$\begin{aligned} K(t-t') &= -i\theta(t-t') \sum_{\mu} V_{\mu}^2 e^{-iE_{\mu}(t-t')} \\ &\equiv \int \frac{d\omega}{2\pi} e^{-i\omega(t-t')} \left[\Lambda(\omega) - \frac{i}{2} \Gamma(\omega) \right], \end{aligned} \quad (19)$$

and

$$\Lambda(\omega) - \frac{i}{2} \Gamma(\omega) = \sum_{\mu} \frac{V_{\mu}^2}{\omega - E_{\mu} + i0^+}. \quad (20)$$

The real function Λ is connected to Γ through a Hilbert transform, i.e.,

$$\Lambda(\omega) = \int \frac{d\omega'}{2\pi} \frac{\Gamma(\omega')}{\omega - \omega'}, \quad (21)$$

and from equations (20) it is easy to show that

$$\Gamma(\omega) = 2\pi \sum_{\mu} V_{\mu}^2 \delta(\omega - E_{\mu}). \quad (22)$$

For systems in a box of length L the continuum wave-functions are proportional to $1/\sqrt{L}$ and hence V_{μ}^2 scales like $1/L$, see definition in equation (3b). In the limit $L \rightarrow \infty$ the discrete sum in equation (22) becomes an integral and $\Gamma(\omega)$ becomes a smooth function of ω . Assuming that E_x is a few times larger than $\Gamma(E_x)$ and that $\Gamma(\omega)$ is a slowly varying function for $\omega \simeq E_x$, we can then neglect the frequency dependence in Γ :

$$\Gamma(\omega) \simeq \Gamma(E_x) \equiv \gamma, \quad (23)$$

which implies, see equation (21), that we can approximate $\Lambda \simeq 0$, see equation (21). This is the so called WBLA, according to which the kernel K in equations (19) can be approximated as

$$K(t-t') = -\frac{i}{2} \gamma \delta(t-t'). \quad (24)$$

Substituting this result into equation (18) and then using equation (17) it is straightforward to find the following analytic solution

$$a_x(t) = e^{-iE_x t - \frac{\gamma}{2} t}, \quad (25a)$$

$$a_{\mu}(t) = -V_{\mu} \frac{e^{-i(E_x - \frac{i}{2}\gamma)t} - e^{-iE_{\mu}t}}{E_{\mu} - E_x + \frac{i}{2}\gamma}. \quad (25b)$$

From equations (25) we infer that the occupation of the continuum states is peaked at $E_{\mu} = E_x$ or, equivalently, at $\epsilon_{\mu} = \epsilon_{\text{Auger}}^{\text{CI}}$, in agreement with the discussion above equation (15). We emphasize that this conclusion is based on the WBLA. The exact solution contains a small correction which is proportional to the Hilbert transform of $\Gamma(\omega)$ at frequency $\omega \simeq E_x$.

2.3 Comparing NEGF with CI

In the NEGF approach at the 2B level of approximation two holes, in addition to feel an average (HF) potential generated by all other electrons, scatter directly once. However, for a strong enough repulsion v_{vvvv} it is necessary to include multiple valence–valence scatterings to predict the correct energy of the Auger electron. In fact, the red shift v_{vvvv} in equation (15) can be captured only by summing multiple scatterings to infinite order (T-matrix approximation) [30,31]. Since the 2B approximation includes just a single scattering, the predicted Auger energy is

$$\epsilon_{\text{Auger}}^{2\text{B}} = 2\epsilon_v^{\text{HF}} - \epsilon_c^{\text{HF}}. \quad (26)$$

In 3D molecules the neglect of v_{vvvv} has only a minor impact on the internal (bound-electrons) dynamics since v_{vvvv} is typically less than 1 eV and $\Gamma(\omega)$ varies rather slowly on this energy scales. In this work, however,

we are also interested in the description of the Auger wavepacket. Taking into account that the repulsion v_{vvvv} in 1D systems is larger than in 3D ones, a sizable difference between the CI and 2B results has to be expected. To demonstrate that such a difference does not affect the overall physical picture nor the details of the Auger wavepacket but only the speed at which the Auger electron is expelled, we isolate the effects of multiple valence–valence scatterings from the CI formulation. Let us express the energy E_x defined in equations (16a) in terms of HF energies

$$E_x = 2\epsilon_v^{\text{HF}} + \epsilon_c^{\text{HF}} - v_{cccc} - 4v_{vccv} + 2v_{vvcv} - v_{vvvv}. \quad (27)$$

The HF energy ϵ_v^{HF} is blue shifted by v_{vvvv} , see equations (16), an effect captured by the 2B approximation. The effect of multiple scatterings manifests in the red shift given by the last term of equation (27). In the next section, we show that solving equations (14) using for E_x the value in equation (27) with $v_{vvvv} = 0$ one recovers the NEGF results (notice that this is not equivalent to set $v_{vvvv} = 0$ in the Hamiltonian since this Coulomb integral renormalizes the HF energy ϵ_v^{HF}). We will refer to this CI approximation as CI2B.

3 Results

We consider a 1D atom with soft Coulomb interactions. This particular example is a severe test for the NEGF method since the continuum spectrum has a strong frequency dependence and the valence–valence repulsion energy is of the same order of magnitude of the Auger energy.

The 1D atom is defined on the points $x_n = na$ of a 1D grid, with $|n| \leq N_{\text{grid}}/2$. In our model, the Coulomb interaction is different from zero only in a box of radius R centered around the nucleus. The one-body Hamiltonian on the grid reads

$$h(x_n, x_m) = \delta_{n,m}[2\kappa + V_n(x_n)] - \delta_{|n-m|,1}\kappa, \quad (28)$$

with $V_n(x) = U_{\text{en}}/\sqrt{x^2 + a^2}$ the nuclear potential and κ the hopping integral between neighbouring points. Electrons interact through $v(x, x') = ZU_{\text{ee}}/\sqrt{(x-x')^2 + a^2}$. We analyze the system using $N_{\text{grid}} = 1601$ grid-points and choose the parameters according to (atomic units are used throughout): $a = 0.5$, $\kappa = 2$, $Z = 4$, $U_{\text{en}} = 2$, $U_{\text{ee}} = U_{\text{en}}/2$ and $R = 10a$. With four electrons the HF spectrum has five bound states (per spin), the lowest two of which are occupied. The energies of the occupied levels are $\epsilon_c^{\text{HF}} = -4.33$ and $\epsilon_v^{\text{HF}} = -1.65$ for the core and valence, respectively, yielding a 2B Auger energy $\epsilon_{\text{Auger}}^{2\text{B}} = 1.02$. We work in the sudden creation approximation, according to which the system is perturbed by suddenly removing a core electron. In the NEGF approach this is simulated by subtracting to the equilibrium density matrix ρ_{ij}^{eq} an infinitesimal amount of charge from the core, hence $\rho_{ij}(0) = \rho_{ij}^{\text{eq}} - \delta_{ic}\delta_{jc}n_h$. In the results below the hole density $n_h = 0.04$.

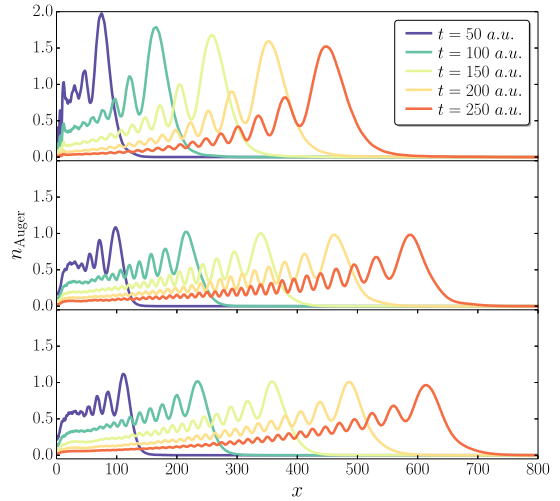


Fig. 1. Snapshots of the density of the Auger wavepacket leaving the atom (nucleus is situated in $x = 0$) calculated using CI (top), NEGF approach (middle) and CI2B (bottom). The vertical axes have been rescaled by a factor 10^4 for all a.u.s.

Subsequently to the creation of the core hole the Auger process takes place, triggering an internal electron dynamics (refilling of the core state) and the expulsion of charge toward the continuum states. The time-dependent occupation of the core state $n_c(t)$ is predicted in both CI and 2B calculations to have the following behavior $n_c(t) = 1 - n_h e^{-\Gamma t}$, where n_h is the core hole created and Γ is the inverse lifetime of the Auger decay. Due to the neglect of multiple scatterings, the Auger decay is faster in 2B and the corresponding Γ is overestimated by a factor 1.5. As already pointed out, this discrepancy is expected to be much smaller in 3D molecules since the valence–valence repulsion is not as large.

In Figure 1, we display snapshots at different times of the real-space density of the Auger wavepacket as obtained by performing CI (top), NEGF (middle) and CI2B calculations (bottom). The results in the NEGF approach closely resemble the ones in the CI2B treatment, in agreement with the discussion in Section 2.3. The CI calculation, as expected, shows a slower wavepacket. However, the overall shape, i.e., asymmetric packet with superimposed accumulating ripples on the tail, is common to all methods. We mention that the amplitude of the ripples as well as the wavefront of the Auger wavepacket change if, instead of the sudden creation of a core-hole, we would have simulated the ionization process using an external laser pulse. In fact, these features are not universal and depend on the intensity and duration of the perturbing field [17]. On the other hand, the time T_r elapsing between two consecutive maxima at any fixed position is an intrinsic feature of the Auger decay, following the law

$$T_r = \frac{2\pi}{\epsilon_{\text{Auger}}}. \quad (29)$$

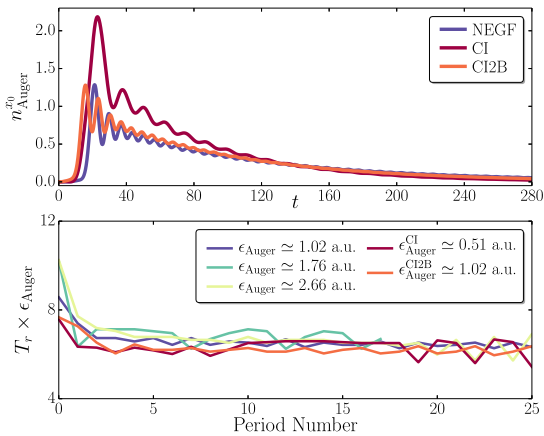


Fig. 2. The top panel shows the time-dependent density of the Auger wavepacket at a fixed distance $x_0 = 30$ from the nucleus for NEGF, CI and CI2B. The bottom panel displays the period of the ripples at x_0 versus the number of elapsing periods for the three calculations of the top panel and for two more NEGF calculations, see main text.

In the top panel of Figure 2, we show the time-dependent density $n_{\text{Auger}}(x_0, t)$ of the Auger wavepacket at a certain distance x_0 from the nucleus. The densities exhibit ripples of different frequency since the energy of the Auger electron is different in CI, NEGF and CI2B. The small discrepancy between NEGF and CI2B is due to the fact that the solution in equations (25) is valid only in the WBLA. Taking into account the frequency dependence of Γ one would find a small correction to $E_\mu - E_x$ proportional to the Hilbert transform of Γ . From the top panel of Figure 2 we see that this correction is rather small and therefore the WBLA is an excellent approximation in this case.

In the bottom panel of Figure 2, we show the value of the time T_r elapsing between two consecutive maxima of the wavepacket versus the number of maxima (counted starting from the left most maximum in the top panel). In the figure T_r is rescaled by the Auger energy. In all cases, after a short transient phase, T_r attains the value 2π . In addition to the values of T_r corresponding to the three curves of the top panel, in the bottom panel we also report the trend of T_r calculated in reference [17] for two more NEGF simulations. More specifically, we considered two different combinations of range and strengths of the Coulomb interactions $(R, U_{\text{en}}, U_{\text{ee}}) = (100a, 2.6, 2.08)$, $(10a, 2.7, 2.025)$ yielding Auger electrons at energies $\epsilon_{\text{Auger}}^{2\text{B}} = 1.76, 2.66$, respectively. As we can see, the quantity $T_r \times \epsilon_{\text{Auger}}$ remains independent of the system.

Finally, in Figure 3 we display the snapshots of the time-dependent occupations $f_\mu(t)$ of the continuum states φ_μ . After the creation of the core-hole, occurring at $t = 0$, the continuum states start to get populated and, as time passes, gradually get peaked around the Auger energy $\epsilon_{\text{Auger}}^{\text{CI}} \simeq 0.51$ for the CI calculation and $\epsilon_{\text{Auger}}^{2\text{B}} \simeq 1$ for the NEGF and CI2B calculation – the small deviation between these two calculations has been discussed previously.

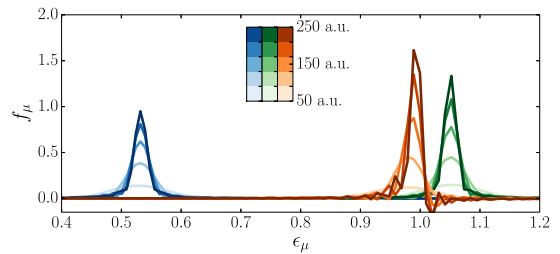


Fig. 3. Snapshots of the occupations f_μ of the continuum states versus their energy ϵ_μ for CI (blue), CI2B (green) and NEGF (orange). The times of the snapshots (from light to dark) are given by the color bars.

4 Conclusions

To summarize, we have benchmarked a recently proposed NEGF approach [17] against CI calculations in a simple 1D model atom. With the exception of the quantitative discrepancies due to the neglect of multiple valence–valence scatterings, good agreement is found for the qualitative features of the Auger process. In fact, NEGF correctly predicts an exponential law for the core-hole refilling and an asymmetric shape of the Auger wavepacket characterized by a long tail with superimposed ripples of period $T_r = 2\pi/\epsilon_{\text{Auger}}$. The quantitative difference is only related to the red shift of the energy of the Auger electron, as demonstrated by the agreement between NEGF and CI2B results. We point out that for the systems that we are interested to study in the future, i.e., organic molecules and molecules of biological interest, the valence–valence repulsion is less than 1 eV; therefore, the neglect of multiple scatterings for the description of the internal dynamics is expected to be less relevant.

The NEGF equation (5) are equations of motion for the one-particle density matrix in the bound sector and for the occupations of the continuum states, *not* for the Green's function. Both quantities are one-time functions like the charge density of TDDFT $n(\mathbf{r}, t)$. In particular, in a real space basis $\rho(\mathbf{r}, \mathbf{r}, t) = n(\mathbf{r}, t)$. Given the tight relation between ρ and n it would be interesting to use the explicit form of the functionals $\mathcal{I}[\rho, f]$ and $J_\mu[\rho, f]$ as a guide to generate approximate xc TDDFT potentials with memory. One possibility would be to combine the linearized Sham–Schlüter equation [32,33] with NEGF using the GKBA [24].

G.S. and E.P. acknowledge EC funding through the RISE Co-ExAN (Grant No. GA644076). E.P. also acknowledges funding from the European Union project MaX Materials design at the eXascale H2020-EINFRA-2015-1, Grant Agreement No. 676598 and Nanoscience Foundries and Fine Analysis-Europe H2020-INFRAIA-2014-2015, Grant Agreement No. 654360. F.C and A.R. acknowledge financial support from the European Research Council (ERC-2015-AdG-694097), Grupos Consolidados (IT578-13) and European Union Horizon 2020 program under Grant Agreement 676580 (NOMAD).

Author contribution statement

All authors contributed equally to research and writing of this paper.

References

1. R. Pazourek, S. Nagele, J. Burgdörfer, *Rev. Mod. Phys.* **87**, 765 (2015)
2. M. Uiberacker et al., *Nature* **446**, 627 (2007)
3. T. Uphues, M. Schultze, M.F. Kling, M. Uiberacker, S. Hendel, U. Heinzmann, N.M. Kabachnik, M. Drescher, *New J. Phys.* **10**, 025009 (2008)
4. M. Drescher, M. Hentschel, R. Kienberger, M. Uiberacker, V. Yakovlev, A. Scrinzi, T. Westerwalbesloh, U. Kleineberg, U. Heinzmann, F. Krausz, *Nature* **419**, 803 (2002)
5. S. Zherebtsov et al., *J. Phys. B: Atom. Mol. Opt. Phys.* **44**, 105601 (2011)
6. J.M. Schins, P. Breger, P. Agostini, R.C. Constantinescu, H.G. Muller, G. Grillon, A. Antonetti, A. Mysyrowicz, *Phys. Rev. Lett.* **73**, 2180 (1994)
7. A.K. Kazansky, I.P. Sazhina, N.M. Kabachnik, *J. Phys. B: Atom. Mol. Opt. Phys.* **44**, 215601 (2011)
8. F. Krausz, M. Ivanov, *Rev. Mod. Phys.* **81**, 163 (2009)
9. F. Gao, O. Inganas, *Phys. Chem. Chem. Phys.* **16**, 20291 (2014)
10. P. Song, Y. Li, F. Ma, T. Pullerits, M. Sun, *Chem. Record* **16**, 734 (2016)
11. C. A. Rozzi, F. Troiani, I. Tavernelli, *J. Phys.: Condens. Matter* **30**, 013002 (2018)
12. M. Nisoli, P. Decleva, F. Calegari, A. Palacios, F. Martín, *Chem. Rev.* **117**, 10760 (2017)
13. E. Runge, E.K.U. Gross, *Phys. Rev. Lett.* **52**, 997 (1984)
14. C. Ullrich, *Time-Dependent Density-Functional Theory* (Oxford University Press, Oxford, 2012)
15. N.T. Maitra, *J. Chem. Phys.* **144**, 220901 (2016)
16. C.S. Cucinotta, D. Hughes, P. Ballone, *Phys. Rev. B* **86**, 045114 (2012)
17. F. Covito, E. Perfetto, A. Rubio, G. Stefanucci, *Phys. Rev. A* **97**, 061401(R) (2018)
18. S. Kurth, G. Stefanucci, C.-O. Almbladh, A. Rubio, E.K.U. Gross, *Phys. Rev. B* **72**, 035308 (2005)
19. C. Verdozzi, G. Stefanucci, C.-O. Almbladh, *Phys. Rev. Lett.* **97**, 046603 (2006)
20. G. Stefanucci, S. Kurth, A. Rubio, E.K.U. Gross, *Phys. Rev. B* **77**, 075339 (2008)
21. P. Myöhänen, A. Stan, G. Stefanucci, R. van Leeuwen, *Phys. Rev. B* **80**, 115107 (2009)
22. G. Stefanucci, E. Perfetto, M. Cini, *Phys. Rev. B* **81**, 115446 (2010)
23. M. Hentschel, R. Kienberger, C. Spielmann, G.A. Reider, N. Milosevic, T. Brabec, P. Corkum, U. Heinzmann, M. Drescher, F. Krausz, *Nature* **414**, 509 (2001)
24. P. Lipavský, V. Špička, B. Velický, *Phys. Rev. B* **34**, 6933 (1986)
25. C.-O. Almbladh, A.L. Morales, G. Grossmann, *Phys. Rev. B* **39**, 3489 (1989)
26. C.-O. Almbladh, A.L. Morales, *Phys. Rev. B* **39**, 3503 (1989)
27. E. Perfetto, G. Stefanucci, in preparation (2018)
28. E.V. Boström, A. Mikkelsen, C. Verdozzi, E. Perfetto, G. Stefanucci, *Nano Lett.* **18**, 785 (2018)
29. E. Perfetto, D. Sangalli, A. Marini, G. Stefanucci, *J. Phys. Chem. Lett.* **9**, 1353 (2018)
30. G.A. Sawatzky, *Phys. Rev. Lett.* **39**, 504 (1977)
31. M. Cini, *Solid State Commun.* **24**, 681 (1977)
32. L.J. Sham, M. Schlüter, *Phys. Rev. Lett.* **51**, 1888 (1983)
33. R. van Leeuwen, *Phys. Rev. Lett.* **76**, 3610 (1996)

Publication III

Efficient computation of the second-Born self-energy using tensor-contraction operations

Riku Tuovinen, [Fabio Covito](#), Michael A. Sentef, *Journal of Chemical Physics*, **97**, 174110 (2019).

One attractive aspect of NEGF is the ability to account for correlation-induced effects at a much reduced computational cost in respect to, for example, wavefunction based methods. In spite of this, NEGF simulations are still limited to systems of relatively reduced size (small molecules). One of the heaviest computational tasks to perform is the calculation of the self-energy. Especially in the case of the 2B approximation used in conjunction to the GKBA, this calculation can take up to 90-95% of the CPU time, becoming the main computational bottleneck of the simulations. This is due to the unfavourable scaling of the computation of the self-energy with the size of the system, like explained in the previous chapter. For this reason, any gain in efficiency of this calculation directly translates into a computational advantage that could open the way to the study of larger systems and/or longer timescales. In this publication we propose an efficient scheme for the calculation of the 2B self-energy based on tensor contractions. The basic idea is to rewrite the expression of self-energy as a series of (multidimensional) matrix and entrywise multiplications. Using commonly available optimized linear algebra numerical libraries, we demonstrate a speed-up in the computation time associated with the calculation of the self-energy. The evaluation of the original expression is associated with a computation time that is proportional to the fifth power of the size of the basis used to perform the calculations. Instead, we demonstrate a scaling of ~ 4.3 for the proposed method. This reduced scaling is related to the optimization of matrix and tensor multiplication routines. An example is the

Strassen algorithm [42] for the calculation of matrix multiplications, which in contrast to the standard calculation, has an associated computational complexity that scales with the power $N^{\log_2 7}$ instead of N^3 , with N being the size of the matrices. The additional advantage of the proposed method is the possibility to profit, at no cost, from any advance in the implementation of external linear algebra libraries.

The idea behind this work is quite simple and general. In fact, the concept of contracting loops into tensor operations is not new and has become more interesting with the advent of GPU computing, where these operations are particularly favourable. The general idea is not restricted to the calculation of the 2B self-energy and can be used, in principle, for any computation involving looping over many indices. One could even think of ways of further contracting the collision integral, since it involves an additional matrix multiplication and a time integral. An interesting use of this method could be in combination with the dissection algorithm [43] for exploiting the possible sparsity of the Coulomb integrals tensor.

Efficient computation of the second-Born self-energy using tensor-contraction operations

Cite as: J. Chem. Phys. 151, 174110 (2019); doi: 10.1063/1.5121820

Submitted: 28 July 2019 • Accepted: 14 October 2019 •

Published Online: 6 November 2019



View Online



Export Citation



CrossMark

Riku Tuovinen,^{a)}  Fabio Covito,  and Michael A. Sentef 

AFFILIATIONS

Max Planck Institute for the Structure and Dynamics of Matter, Luruper Chaussee 149, 22761 Hamburg, Germany

^{a)} Author to whom correspondence should be addressed. Present address: QTF Centre of Excellence, Turku Centre for Quantum Physics, Department of Physics and Astronomy, University of Turku, 20014 Turku, Finland. Electronic mail: riku.tuovinen@utu.fi

ABSTRACT

In the nonequilibrium Green's function approach, the approximation of the correlation self-energy at the second-Born level is of particular interest, since it allows for a maximal speed-up in computational scaling when used together with the generalized Kadanoff-Baym ansatz for the Green's function. The present day numerical time-propagation algorithms for the Green's function are able to tackle first principles simulations of atoms and molecules, but they are limited to relatively small systems due to unfavorable scaling of self-energy diagrams with respect to the basis size. We propose an efficient computation of the self-energy diagrams by using tensor-contraction operations to transform the internal summations into functions of external low-level linear algebra libraries. We discuss the achieved computational speed-up in transient electron dynamics in selected molecular systems.

Published under license by AIP Publishing. <https://doi.org/10.1063/1.5121820>

I. INTRODUCTION

A state-of-the-art computational method for out-of-equilibrium many-body physics is the nonequilibrium Green's function (NEGF) approach.^{1–6} Mostly due to the lack of computational capabilities, the nonlinear integrodifferential Kadanoff-Baym equations (KBE) for the NEGF from the 1960s remained fairly elusive until their first numerical solutions were presented in 1984 by Danielewicz⁷ and further numerical implementations at the turn of the century.^{8–10} During the past 20 years, a considerable amount of progress has been achieved in various fields of physics employing the NEGF approach: from subatomic nuclear reactions^{11,12} to atomic and molecular scales,^{13–22} further to condensed phase^{23–33} and mesoscopic systems,^{34–39} and even to the descriptions of high-energy particle physics in cosmology.^{40–42}

However, combining the KBE with *ab initio* descriptions of realistic materials still remains a computational challenge. This challenge results from the double-time structure of the KBE, making the method very expensive for both computing time and storing the objects in RAM. The Generalized Kadanoff-Baym Ansatz (GKBA) offers a simplification by reducing the two-time-propagation of the Green's function to the time-propagation of a time-local density

matrix.⁴³ The computational complexity of the time-propagation of the GKBA equations scales as the number of time steps squared instead of the cubic scaling in the double-time KBE.⁴⁴ When a simulation to reach longer time scales is desired, this difference in computational speed becomes immense. However, this speed-up in computational scaling is only possible for the correlation self-energy approximation at the second-Born (2B) level. The 2B approximation goes beyond the mean-field description at the Hartree-Fock (HF) level, but it includes the bare interaction only up to second order, i.e., higher order correlations and screening effects are neglected, like in the higher order *T*-matrix or *GW* approximations.^{45,46} However, the viability of the 2B approximation has been assessed for a large set of systems with up to moderate interaction strength.^{47,48}

Even though the above implementations of the NEGF method have been successfully applied in many contexts, the computation of the self-energy still remains a numerical bottleneck. For larger systems to be studied, the scaling with respect to the basis size in the self-energy diagrams may be very unfavorable, making first principles simulations numerically expensive, at least in naïve implementations when looping over the full basis. Recently, a dissection algorithm has been proposed and implemented^{49,50} for identifying and utilizing the sparsity of many-body interactions. In this

paper, we propose to transform the summation expressions in the self-energy diagrams using tensor-contraction operations and to further employ external linear algebra libraries (e.g., low-level C or Fortran) taking into account, e.g., memory availability, communication costs, loop fusion, and ordering.^{51–53} [Here, we consider *tensors* simply as multidimensional objects without deeper (differential-)geometric interpretation.] With benchmark simulations in selected molecular systems, we present an efficient way to compute the 2B self-energy applicable either in full time-propagation of the KBE or in the numerically less expensive GKBA variant.

II. MODEL AND METHOD

We consider a finite and quantum-correlated electronic system described by a time-dependent Hamiltonian

$$\hat{H}(t) = \sum_{ij} h_{ij}(t) \hat{c}_i^\dagger \hat{c}_j + \frac{1}{2} \sum_{ijkl} v_{ijkl}(t) \hat{c}_i^\dagger \hat{c}_j^\dagger \hat{c}_k \hat{c}_l, \quad (1)$$

where i, j, k, l label a complete set of one-particle states $\{\varphi(\mathbf{r})\}$ and $\hat{c}^{(\dagger)}$ are the annihilation (creation) operators for electrons from (to) these states. Although we assume, for simplicity, spin-compensated electrons and invariance under spin rotations, the whole consideration could easily be generalized to include also spin degrees of freedom.^{47,54–57} The objects henceforth described will be diagonal in spin space. The one-body contribution to the Hamiltonian,

$$h_{ij}(t) = \int d\mathbf{r} \varphi_i^*(\mathbf{r}) h(\mathbf{r}, t) \varphi_j(\mathbf{r}), \quad (2)$$

may have an explicit time dependence, describing, e.g., pump-probe spectroscopies or voltage pulses. These would enter in $h(\mathbf{r}, t) = -\frac{1}{2} \nabla^2 + w(\mathbf{r}, t) - \mu$ as external fields w . We also introduced the chemical potential μ and we absorbed it into the equilibrium description of the one-body part of the Hamiltonian. Atomic units, $\hbar = m = e = 1$, are used throughout. The two-body part accounts for interactions between the electrons with the standard two-electron Coulomb integrals

$$v_{ijkl} = \int d\mathbf{r} \int d\mathbf{r}' \frac{\varphi_i^*(\mathbf{r}) \varphi_j^*(\mathbf{r}') \varphi_k(\mathbf{r}') \varphi_l(\mathbf{r})}{|\mathbf{r} - \mathbf{r}'|}. \quad (3)$$

Even though the Coulomb interaction itself is instantaneous, in Eq. (1), we allow the strength of the two-body part to be time-dependent to describe, e.g., interaction quenches or adiabatic switching. For real-valued basis functions φ , the Coulomb integrals in Eq. (3) follow 8-point permutation symmetry

$$v_{ijkl} = v_{jikl} = v_{klij} = v_{lkji} = v_{ijlk} = v_{klji} = v_{jilk} = v_{iljk}, \quad (4)$$

which can be verified by permuting dummy integration variables and by complex conjugation. The following discussion is not limited to this choice, however, and also, complex and spin-dependent basis functions could be used.

To calculate time-dependent nonequilibrium quantities, we use the equations of motion for the one-particle Green's function on the Keldysh contour γ .^{4–6} This object is defined as

$$G_{ij}(z, z') = -i \langle T_\gamma [\hat{c}_i(z) \hat{c}_j^\dagger(z')] \rangle, \quad (5)$$

where T_γ is the contour ordering operator and the variables z, z' specify the location of the Heisenberg-picture operators \hat{c} on the Keldysh contour. The contour has a forward and a backward branch on the real-time axis, $[t_0, \infty]$, and also a vertical branch on the imaginary axis, $[t_0, t_0 - i\beta]$, with inverse temperature β . The Green's function includes detailed information about particle propagation, and important physical quantities such as electric currents or photoemission spectra can be extracted from it. The Green's function G satisfies the integrodifferential equations of motion⁵

$$[i\partial_z - h(z)]G(z, z') = \delta(z, z') + \int_\gamma d\bar{z} \Sigma(z, \bar{z})G(\bar{z}, z'), \quad (6)$$

$$G(z, z') \left[-i \overleftarrow{\partial}_{z'} - h(z') \right] = \delta(z, z') + \int_\gamma d\bar{z} G(z, \bar{z}) \Sigma(\bar{z}, z'), \quad (7)$$

where all objects are matrices with respect to the basis of one-particle states $\{\varphi(\mathbf{r})\}$. The self-energy Σ accounts for the electronic interactions. While some two-particle quantities, such as interaction energies and double occupancies, can also be computed from this picture,^{58,59} the introduction of the self-energy transforms the many-body problem to an effective quasiparticle picture, and higher order correlations, such as the pair distribution function, are not directly accessible.^{60,61} Depending on the arguments z, z' , the Green's function, $G(z, z')$, and the self-energy, $\Sigma(z, z')$, defined on the time contour have components lesser ($<$), greater ($>$), retarded (R), advanced (A), left (\lceil), right (\rceil), and Matsubara (M).⁵ Typically, one concentrates on the particle and hole propagation in terms of $G^<(t, t')$ and $G^>(t, t')$, where the time arguments t and t' refer to the (real) times when a particle is added or removed from the system. Furthermore, the one-particle reduced density matrix (1RDM) is $\rho(t) \equiv -iG^<(t, t)$ from which one could compute the expectation value of any one-body operator. Taking the equal-time limit ($t' \rightarrow t^+$), one obtains from Eqs. (6) and (7),

$$i \frac{d}{dt} G^<(t, t) = [h(t) + \Sigma_{\text{HF}}(t), G^<(t, t)] + I(t), \quad (8)$$

where we defined the collision integral

$$I(t) = \int_{t_0}^t d\bar{t} \left[\Sigma_c^>(t, \bar{t}) G^<(\bar{t}, t) - \Sigma_c^<(t, \bar{t}) G^>(\bar{t}, t) + G^<(t, \bar{t}) \Sigma_c^>(\bar{t}, t) - G^>(t, \bar{t}) \Sigma_c^<(\bar{t}, t) \right]. \quad (9)$$

In addition, in Eq. (8), we separated the time-local and time-nonlocal contributions to the self-energy as $\Sigma = \Sigma_{\text{HF}} + \Sigma_c$, the former being referred to as the Hartree-Fock (HF) self-energy and the latter the correlation self-energy; see Fig. 1. This allows for the extraction of a time-local effective single-particle Hamiltonian, $h(t) + \Sigma_{\text{HF}}(t)$. The collision integrals therefore incorporate only the correlation self-energies Σ_c . Importantly, the self-energies depend on the Green's functions themselves, $\Sigma[G]$, and therefore, the equation of motion needs to be solved self-consistently. The correlation self-energies are typically obtained by a diagrammatic expansion, where terms can be systematically summed up to infinite order. In this work, we concentrate on the second-Born self-energy, $\Sigma_c = \Sigma_{2\text{B}}$ (see Fig. 1), but the consideration can be extended to other (higher order) diagrams as well.

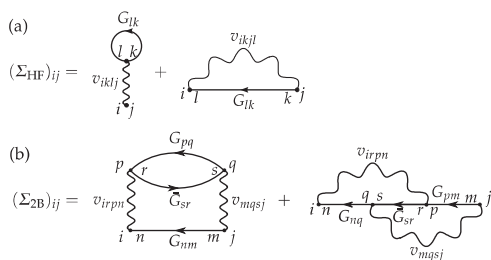


FIG. 1. Diagrammatic representations of the Hartree-Fock (a) and the second-Born (b) correlation self-energies. The straight lines denote electronic Green's functions, whereas the wiggly lines denote the electronic interactions. The internal indices are summed over. Each diagram comes with a prefactor $(-i)^{N_{\text{loop}}} i^{N_{\text{int}}}$, where N_{loop} is the number of loops and N_{int} is the number of interaction lines.⁵ The direct terms with a loop furthermore take an overall spin-degeneracy factor ξ , which in this case is $\xi = 2$.^{58,62}

Although we reduced the considered information to the description of a single-time object ρ , the double-time nature of the full equations of motion is still present in the collision integral, which requires the double-time history of $\Sigma^<$ and $G^<$ to be stored. In order to obtain a closed equation for ρ , it is customary to use the GKBA,⁴³

$$G^<(t, t') \approx i \left[G^R(t, t') G^<(t', t') - G^<(t, t) G^A(t, t') \right], \quad (10)$$

and an approximation to the double-time propagators $G^{R/A}$ at the HF level,⁶

$$G^{R/A}(t, t') \approx \mp i \theta[\pm(t - t')] T e^{-i \int_{t'}^t d\tilde{t} [h(\tilde{t}) + \Sigma_{\text{HF}}(\tilde{t})]}, \quad (11)$$

where T is the chronological time-ordering operator.⁵ The HF self-energy, being time-local, can be evaluated from the 1RDM as (see Fig. 1)

$$(\Sigma_{\text{HF}})_{ij}(t) = \sum_{kl} (2v_{iklj} - v_{ikjl}) \rho_{lk}(t). \quad (12)$$

The lesser Green's function or the 1RDM can then be solved from Eq. (8) by a numerical time-stepping algorithm and using the symmetry property $G^>(t, t) = -i + G^<(t, t)$.^{35,44,56}

In principle, the collision integral on the vertical branch of the Keldysh contour, $I^c(t) = -i \int_0^\beta d\tau \Sigma_c^1(t, \tau) G^f(\tau, t)$, should also be taken into consideration. However, using the GKBA, the initial correlations collision integral, I^c , is usually neglected due to the lack of a GKBA-like expression for the mixed components G^{lf} and Σ_c^{lf} . The correlated initial state therefore needs to be prepared by starting with an uncorrelated (or HF) system and slowly switching on the interaction (the adiabatic switching procedure).^{33,44,56,63} However, the inclusion of the initial correlations has been shown to be possible also within GKBA.⁶⁴⁻⁶⁶

III. SECOND-BORN SELF-ENERGY

For the time-propagation of Eq. (8), we are only concerned with the lesser and greater components of the Green's function and

self-energy. For the sake of notational simplicity, we then write $G \equiv G^<(t, t')$, $\tilde{G} \equiv G^<(t', t)$, and $\Sigma \equiv \Sigma_c^<(t, t')$. In the second-Born approximation (2B), the correlation self-energy takes the form^{49,56} (see Fig. 1)

$$\Sigma_{ij} = 2 \sum_{\substack{mn \\ pq \\ rs}} v_{irpn} v_{mqsj} G_{nm} \tilde{G}_{sr} G_{pq} - \sum_{\substack{mn \\ pq \\ rs}} v_{irpn} v_{mqsj} G_{nq} \tilde{G}_{sr} G_{pm}. \quad (13)$$

As can be seen from Eq. (13), computing the full self-energy matrix by direct looping takes N_b^8 operations, where N_b is the size of the basis. However, it is possible to reduce this scaling to $\propto N_b^5$ by grouping and reorganizing the objects in Eq. (13).^{49,65,67-70} We address this more thoroughly in Sec. III C. It should also be noted that the 2B self-energy is nonlocal in time, i.e., this computation needs to be performed for two times t and t' , and it is important to keep track of the correct time arguments in the objects v , G , and \tilde{G} . While the 2B approximation together with the GKBA allows for a maximal speed-up in computational scaling compared to the full two-time KBE (T^2 vs T^3 , T being the total propagation time), GKBA simulations with GW and T -matrix approximations to the self-energy have also been performed.^{71,72}

We note that the NEGF method using the 2B self-energy, sometimes referred as second-order Green's function (GF2),^{19,48,69,73} can be related to the second-order Møller-Plesset perturbative expansion (MP2).⁷⁴ The construction of the MP2 correction is similar to the 2B self-energy, although in the NEGF approach, the self-energy enters nonlinearly into an updated Green's function, and this procedure is continued until convergence is reached, whereas the MP2 can be related to the first step of this iteration.^{69,73,75}

Next, we consider three different cases for the interaction vertex: (1) diagonal basis where the Coulomb integrals take the Hubbard-like form $v_{ijkl} = U_i \delta_{ij} \delta_{ik} \delta_{il}$; (2) symmetric basis where the Coulomb integrals allow for nondiagonal or long-range interactions $v_{ijkl} = V_{ij} \delta_{il} \delta_{jk}$, but the 4-point vertex is symmetric (density-density type interaction); and (3) the general basis of the full Coulomb integral v_{ijkl} . From the resulting structures of the internal summations in the self-energy diagrams, we identify matrix or tensor operations. Instead of simply looping over the basis indices, employing well-established linear algebra libraries for the matrix and tensor operations⁵¹⁻⁵³ may speed up the construction of the self-energy.

We denote matrix multiplication by “ \times ” and entrywise multiplication (Hadamard or Schur product) by “ \circ .” For example, in Fortran and Mathematica, the entrywise products are done through simple multiplication operator “ $*$ ” whereas the matrix product is done through the “`matmul`” or “`.`” operators. In C++ with the Armadillo library,⁷⁶ the symbol “`%`” is used for entrywise products whereas “`*`” is a matrix product. In Python with the NumPy (np) numerical library,⁷⁷ the entrywise product can be done with the function “`np.multiply`” whereas the matrix or more general tensor multiplication can be done via the “`np.dot`” or the “`np.einsum`” functions.

A. Diagonal basis

For a diagonal basis, $v_{ijkl} = U_i \delta_{ij} \delta_{ik} \delta_{il}$, Eq. (13) is simplified as

$$\Sigma_{ij} = U_i U_j G_{ij} \tilde{G}_{ji} G_{ij}, \quad (14)$$

and the computational cost of constructing the full matrix therefore scales as N_b^2 . In this simple case, there are no further contractions to perform as the internal summations were already explicitly resolved due to the Kronecker δ 's in the interaction vertex. Because in many practical implementations entrywise multiplication between two objects is only possible when they have the same dimension, we rewrite the on-site interaction U_i instead as the diagonal part V_{ii} of a matrix. The resulting expression can then be recasted in matrix form as an entrywise product

$$\Sigma = \text{diag}(V) \circ \text{diag}(V) \circ G \circ \tilde{G}^T \circ G. \quad (15)$$

We anticipate that this is a faster construction for the whole self-energy matrix instead of looping over the basis indices i, j in Eq. (14) when passing the matrix operations in Eq. (15) to an external linear algebra library.

B. Symmetric basis

For a symmetric basis, $v_{ijkl} = V_{ij}\delta_{il}\delta_{jk}$, Eq. (13) is simplified as

$$\Sigma_{ij} = 2 \sum_{kl} V_{ik} V_{jl} G_{ij} \tilde{G}_{lk} G_{kl} - \sum_{kl} V_{ik} V_{jl} G_{il} \tilde{G}_{lk} G_{kj}. \quad (16)$$

We first consider the first term of Eq. (16), i.e., the second-order bubble diagram, and visualize the contraction path for efficient computation. The expression can be manipulated as

$$\begin{aligned} \Sigma_{ij}^b &= 2 \sum_{kl} V_{ik} V_{jl} G_{ij} (\tilde{G}^T)_{kl} G_{kl} \\ &= 2 \sum_{kl} V_{ik} V_{jl} G_{ij} (\tilde{G}^T \circ G)_{kl} \\ &= 2 \sum_l V_{jl} G_{ij} \sum_k V_{ik} (\tilde{G}^T \circ G)_{kl} \\ &= 2 \sum_l V_{jl} G_{ij} [V \times (\tilde{G}^T \circ G)]_{il} \\ &= 2 \sum_l V_{jl} G_{ij} \{ [V \times (\tilde{G}^T \circ G)]^T \}_{li} \\ &= 2G_{ij} \sum_l V_{jl} \{ [V \times (\tilde{G}^T \circ G)]^T \}_{li} \\ &= 2G_{ij} (V \times \{ [V \times (\tilde{G}^T \circ G)]^T \})_{ji} \\ &= 2G_{ij} \{ (V \times \{ [V \times (\tilde{G}^T \circ G)]^T \})^T \}_{ij} \\ &= 2\{G \circ [V \times \{ [V \times (\tilde{G}^T \circ G)]^T \}]^T\}_{ij}, \end{aligned} \quad (17)$$

where we identified matrix transposes, entrywise products, and matrix multiplications. The procedure outlined above, unfortunately, makes the final expressions less readable, but in the end the full self-energy matrix (for the bubble diagram part) may be constructed as a one-liner $\Sigma^b = 2G \circ [V \times \{ [V \times (\tilde{G}^T \circ G)]^T \}]^T$. However, as mentioned earlier, one must keep track of the time arguments, i.e., reading from left, the first V is evaluated at t' and the second V is evaluated at t .

Contractions on the internal summations in the self-energy diagrams do not always yield a favorable path. If we take the second term in Eq. (16), i.e., the second-order exchange diagram, obtaining an expression similar to Eq. (17) is not possible for the full self-energy matrix. However, for the diagonal part of the exchange

diagram, we obtain

$$\begin{aligned} \Sigma_{ii}^x &= - \sum_{kl} V_{ik} V_{il} G_{il} \tilde{G}_{lk} G_{ki} \\ &= - \sum_l (V \circ G)_{il} \sum_k \tilde{G}_{lk} (V^T \circ G)_{ki} \\ &= - \sum_l (V \circ G)_{il} [\tilde{G} \times (V^T \circ G)]_{li} \\ &= -\{(V \circ G) \times [\tilde{G} \times (V^T \circ G)]\}_{ii}. \end{aligned} \quad (18)$$

The off-diagonal parts would still need to be evaluated by explicit looping as in Eq. (16), but the above contraction path may also be combined with, e.g., the dissection algorithm of Ref. 49 where chosen pairs of the Coulomb integral matrix elements (according to some cut-off energy) would be used. This further reduces the requirement for looping over the basis indices.

C. General basis

For a general basis, all v_{ijkl} are nonvanishing. In this case, the multi-index summations in the self-energy diagrams and their consequent contractions are not always easy to see, but this task can be automated using, e.g., the `np.einsum_path` function in Python. The information obtained for an optimal sequence of contractions may further be combined with the symmetry properties (4) and with a predetermined subset of nonzero Coulomb integrals.⁴⁹

Manipulating Eq. (13) gives

$$\begin{aligned} \Sigma_{ij} &= 2 \sum_{np} G_{pq} \sum_{qs} \underbrace{v_{mqsj} G_{nm}}_{\equiv T_{nqsj}^{(1)}} \underbrace{\sum_r v_{irpn} \tilde{G}_{sr}}_{\equiv T_{ispn}^{(2)}} \\ &\quad - \sum_{mn} G_{pm} \sum_{qs} \underbrace{v_{mqsj} G_{nq}}_{\equiv T_{mqsj}^{(1)}} \underbrace{\sum_r v_{irpn} \tilde{G}_{sr}}_{\equiv T_{ispn}^{(2)}} \\ &= 2 \sum_{nqs} T_{nqsj}^{(1)} \sum_p G_{pq} T_{ispn}^{(2)} - \sum_{mns} T_{nmjs}^{(1)} \sum_p G_{pm} T_{ispn}^{(2)} \\ &= \sum_{nqs} (2T_{nqsj}^{(1)} T_{isqn}^{(3)} - T_{qnsj}^{(3)} T_{isnq}^{(3)}), \end{aligned} \quad (19)$$

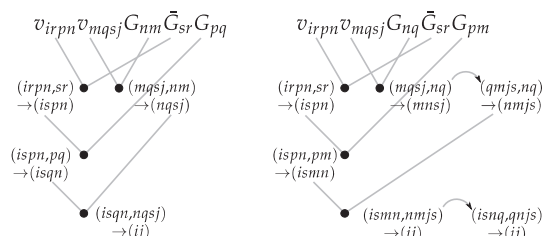


FIG. 2. Contraction paths for the computation of the self-energy in Eq. (19). The dots denote tensor-contraction operations that could be implemented, e.g., using the `np.einsum` function in Python that includes (from version 1.14 onward) optimized ordering and dispatching many operations to canonical BLAS routines.⁷⁸

where we defined tensor contractions $T^{(1,2,3)}$ and permuted indices with the help of Eq. (4), identifying similar contractions consequently. We see from the last line of Eq. (19) that for constructing the full self-energy matrix the scaling over the basis is reduced from N_b^8 to $\propto N_b^5$.^{49,68–70}

As before, the readability of the self-energy in Eq. (19) suffers a bit compared to Fig. 1 or Eq. (13). However, Eq. (19) is visualized in Fig. 2, and for the sake of efficient computation the contraction operations can be grouped together and executed essentially as

a single command, where the lower-level loop fusions and orderings of operations are handled by the underlying numerical library. We emphasize that while the reorganizations of the summations in Eq. (13) to arrive at Eq. (19) have already been considered to some degree in Refs. 49, 68, and 70, here, we concentrate on the practical computation of the self-energy by employing efficient tensor-contraction operations with a possible contraction path shown in Fig. 2. Alternative contraction paths than the one shown in Fig. 2 are also possible.

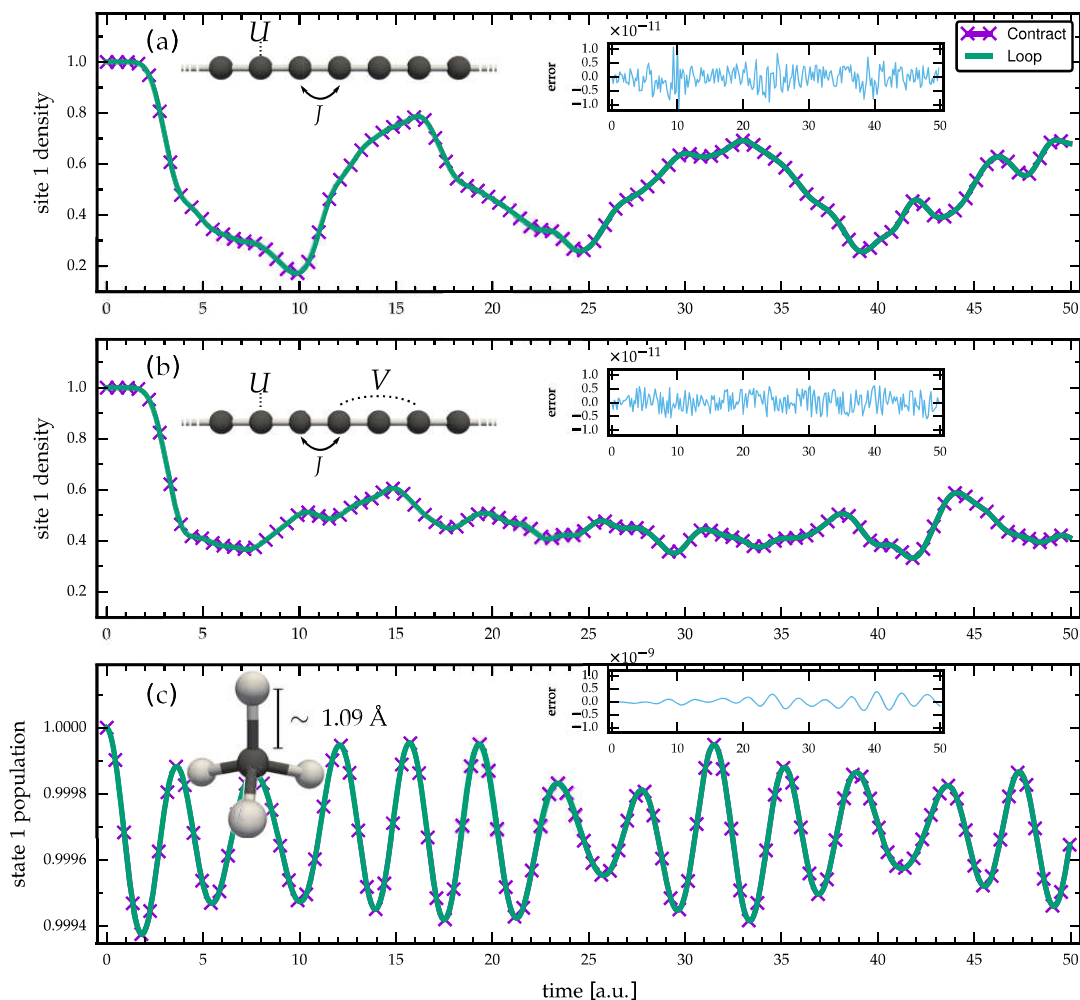


FIG. 3. Time-dependent 1RDM elements for the three different systems studied: (a) diagonal basis with local interaction, (b) symmetric basis with local and long-range interaction, and (c) general basis with the full Coulomb integrals. The insets show the relative difference between the two curves in the main plots.

IV. NUMERICAL BENCHMARKS

For the three different cases presented in Sec. III, (1) diagonal, (2) symmetric, and (3) general bases, we now present sample numerical simulations for the purpose of benchmarking and assessing the validity and accuracy of the alternative implementations of the 2B self-energy. For test cases, we choose molecular systems falling into each of the categories: 1D Hubbard chains that can be related to, e.g., conjugated polymers^{63,79–81} with local (1) and long-range interactions (2). We set the hopping energy between nearest-neighbors $J = -1$, the on-site electron-electron interaction $U = 1$, and the long-range interaction between particles at atomic sites i and j as in the Ohno model $V_{ij} = U/\sqrt{1 + |i - j|^2}$.^{82,83} For the case (3), we take a CH₄ molecule with a general one-particle Kohn-Sham (KS) basis obtained from density-functional theory (DFT) using Octopus.⁸⁴ Using this DFT calculation, the one- and two-body matrix elements [Eqs. (2) and (3)] are then constructed in the corresponding KS basis; a more detailed explanation can be found in Ref. 50.

We implement the explicit loops over the basis indices [Eqs. (14), (16), and (19)] in C++. In the cases (1) and (2), we employ the matrix operations [Eqs. (15), (17), and (18)] using the Armadillo library (version 9.200.5),⁷⁶ and in the case (3), we employ the tensor operations [Eq. (19) and Fig. 2] using the NumPy library (version 1.15.1) in Python.⁷⁷ We perform the comparisons using a regular desktop computer with an Intel Core i5-4460 @ 3.2 GHz with 6 MB cache, running on 64-bit architecture using Ubuntu 18.04 operating system incorporating the Linux kernel 4.15.0 and the GCC 7.3.0 compiler. The comparisons are done using only a single core to better benchmark the computational cost.

We perform a time-propagation à la GKBA of N_t time steps with length δ . For the sake of simpler computation, in this work, we do not employ any predictor-corrector schemes. For the polymer chain, we take $N_b = 10$ atomic sites and start the time-propagation from an initial state where $N_b/2$ particles are trapped to the $N_b/2$ leftmost sites by applying a strong confinement potential.⁶³ This configuration relaxes once the time evolution is started. For the CH₄ molecule, we represent the 4 electrons by $N_b = 10$ basis functions, and we start the time-propagation from a HF initial state, which can be obtained from a separate (time-independent) calculation, and then suddenly switch on the many-body correlations in the 2B self-energy. This sudden process can be interpreted as an interaction quench introducing transient dynamics.

For the case (1), we take $N_t = 5000$ time steps of length $\delta = 0.01$, for the case (2), $N_t = 2000$ time steps of length $\delta = 0.025$, and for the case (3), we take $N_t = 1000$ time steps of length $\delta = 0.05$. The reason for the varying number of time steps between the investigated cases is that a calculation with $N_t = 1000$ would be too fast to execute in case (1) for a meaningful comparison of runtimes, whereas $N_t > 1000$ in case (3) would lead to unpractically long execution times for the sake of the present study. Here, we are not too concerned about the physical mechanisms taking place during the transient oscillations or how accurate the 2B self-energy is compared to more sophisticated approximations, but our aim is simply to assess the validity of the proposed computation scheme, and to compare execution runtimes.

In Fig. 3, we show the transient dynamics of the three cases discussed above. The execution runtimes for each of these

TABLE I. Comparison of serial runtimes (in seconds) of sample simulations of basis size $N_b = 10$ when calculating the self-energy by looping over the basis indices or employing tensor-contraction operations. The gain factor is defined as the ratio of the runtimes (note that different number of time steps is taken for the different lines for better comparison of the runtimes).

Basis	Scaling	Time (loop)	Time (contr.)	Gain
Diagonal	N_b^2	177	164	1.08
Symmetric	N_b^4	1213	731	1.66
General	N_b^5	1527	1333	1.15

simulations are shown in Table I. We confirm that within numerical accuracy, both looping over the basis indices and employing tensor-contraction operations, give the same result. Importantly, the execution runtimes are brought down by employing the tensor-contraction operations in the computation of the 2B self-energy. Furthermore, we have checked by increasing the number of time steps that the runtimes increase accordingly, i.e., the gain factors in Table I remain roughly similar. For additional validation, we have compared our data in Fig. 3(c) against the CHEERS code⁵⁰ and we find perfect agreement. We note in passing that an ill-advised looping over the full basis in Eq. (13) ($\propto N_b^8$) instead of the reduced looping in Eq. (19) ($\propto N_b^5$) would result in considerably higher execution runtimes.

As the number of basis functions $N_b = 10$ was relatively small in the previous calculations, we expect increase in the gain factors when larger basis is used, due to profiting more from the optimized underlying numerical libraries. In Fig. 4, we show the execution runtimes corresponding to Fig. 3(c) but with varying number of basis functions. With explicit looping over the basis indices, we observe $\propto N_b^5$ behavior. For smaller basis sizes, the explicit looping is faster compared to the tensor-contraction operations done on the NumPy arrays. However, for larger basis sizes, the runtimes

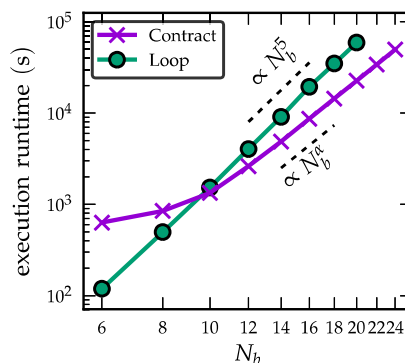


FIG. 4. Runtime scaling corresponding to Fig. 3(c) with increasing number of basis functions N_b . Using tensor-contraction operations, we find a reduced scaling law $\propto N_b^{4.3}$ compared to the explicit looping over the basis ($\propto N_b^5$).

using the tensor-contraction operations are significantly smaller, also following a power law behavior $\propto N_b^\alpha$ for which we empirically find $\alpha \approx 4.34 \pm 0.17$ (see Fig. 4). This exponent and its statistical errors were extracted by performing a nonlinear least squares fit to the flat part, $N_b \in [14, 24]$, using `gnuplot`. This reduced scaling could be related to the optimization of matrix multiplication using the Strassen algorithm⁵⁵ and to more advanced methods for tensor contraction algorithms that can scale faster than the naïve looping scheme.⁵³

V. CONCLUSION

We presented an efficient way to compute the 2B self-energy diagrams, in the NEGF approach, by using tensor-contraction operations. The apparent attraction for efficient computation of the 2B self-energy, in particular, was due to the maximal speed-up in computational scaling when used together with the GKBA. The internal summations in the self-energy calculations were transformed into matrix and tensor operations to be performed by external low-level linear algebra libraries, speeding up the computation. We anticipate that the speedup may be even more advantageous when the code is executed in parallel, taking full advantage of the optimized underlying numerical libraries. Instead of looping over the basis indices, utilizing efficiently optimized external numerical libraries for the tensor-contraction operations has the further advantage of speeding up the computation if/when future implementations of the external libraries become faster and even more efficient.⁵³

There has been recent progress in reducing the computational bottleneck of constructing various self-energy approximations by using stochastic methods.^{69,86,87} Here, we mention the work of Neuhauser, Baer, and Zgid⁶⁹ who considered the 2B self-energy in an equilibrium setting and achieved a much more favorable quadratic scaling over the fifth power. While the reduced scaling with respect to the basis size using these stochastic methods goes beyond our findings, it is not straightforward to argue how the accuracy of such a stochastic-sampling approach may affect convergence or error propagation in an out-of-equilibrium setting. In this case, one would have to sample not a single τ -axis (Matsubara) self-energy but instead a new slice of ever-expanding self-energies $\Sigma_c^<(t, t')$ in the two-time plane. However, it would be a promising venue to extend the stochastic methods also to real time in future studies.⁸⁸

The presented approach is not limited to the 2B self-energy only but could be readily used for other correlation self-energies, such as GW or T -matrix. In addition, many other similar multi-index operations, such as evaluating the initial correlations collision integral in Ref. 65, might become computationally more accessible by using the tensor-contraction representations. In the present work, we considered only the GKBA with Hartree-Fock propagators, but extensions to correlated approximations to the propagator⁵⁶ are also directly applicable in our approach. The presented simulations in selected molecular systems provided concrete evidence of the accuracy and applicability of the tensor-contraction operations. With reasonable and precise implementations or variations of the present study, we expect this procedure to allow for considerably larger basis sizes to be possible to address in forthcoming NEGF+first principles simulations.

Note added in proof: Applying the stochastic approach to real time Green's functions has recently been discussed in Ref. 89.

ACKNOWLEDGMENTS

R.T. and M.A.S. acknowledge funding by the DFG (Grant No. SE 2558/2-1) through the Emmy Noether program. We wish to thank Damian Hofmann, Gianluca Stefanucci, Michael Bonitz, and Angel Rubio for productive discussions.

REFERENCES

- 1 G. Baym and L. P. Kadanoff, *Phys. Rev.* **124**, 287 (1961).
- 2 L. P. Kadanoff and G. Baym, *Quantum Statistical Mechanics* (W. A. Benjamin, New York, 1962).
- 3 L. V. Keldysh, Zh. Eksp. Teor. Fiz. **47**, 1515 (1964) [Sov. Phys. JETP **20**, 1018 (1965), <http://www.jetp.ac.ru/cgi-bin/e/index/e/20/4/p1018?a=list>].
- 4 P. Danielewicz, *Ann. Phys.* **152**, 239 (1984).
- 5 G. Stefanucci and R. van Leeuwen, *Nonequilibrium Many-Body Theory of Quantum Systems: A Modern Introduction* (Cambridge University Press, Cambridge, 2013).
- 6 K. Balzer and M. Bonitz, *Nonequilibrium Green's Functions Approach to Inhomogeneous Systems* (Springer Berlin Heidelberg, 2013).
- 7 P. Danielewicz, *Ann. Phys.* **152**, 305 (1984).
- 8 H. S. Köhler, N. H. Kwong, and H. A. Yousif, *Comput. Phys. Commun.* **123**, 123 (1999).
- 9 D. Semkat, D. Kremp, and M. Bonitz, *Phys. Rev. E* **59**, 1557 (1999).
- 10 N.-H. Kwong and M. Bonitz, *Phys. Rev. Lett.* **84**, 1768 (2000).
- 11 W. H. Dickhoff and C. Barbieri, *Prog. Part. Nucl. Phys.* **52**, 377 (2004).
- 12 A. Rios, B. Barker, M. Buchler, and P. Danielewicz, *Ann. Phys.* **326**, 1274 (2011).
- 13 N. E. Dahlen and R. van Leeuwen, *J. Chem. Phys.* **122**, 164102 (2005).
- 14 N. E. Dahlen and R. van Leeuwen, *Phys. Rev. Lett.* **81**, 153004 (2007).
- 15 M. Galperin, M. A. Ratner, and A. Nitzan, *J. Phys.: Condens. Matter* **19**, 103201 (2007).
- 16 K. S. Thygesen, *Phys. Rev. Lett.* **100**, 166804 (2008).
- 17 K. Balzer, S. Bauch, and M. Bonitz, *J. Phys.: Conf. Ser.* **220**, 012020 (2010).
- 18 K. Balzer, S. Bauch, and M. Bonitz, *Phys. Rev. A* **81**, 022510 (2010).
- 19 J. J. Phillips and D. Zgid, *J. Chem. Phys.* **140**, 241101 (2014).
- 20 E. Peretto, A.-M. Uimonen, R. van Leeuwen, and G. Stefanucci, *Phys. Rev. A* **92**, 033419 (2015).
- 21 F. Covito, E. Peretto, A. Rubio, and G. Stefanucci, *Eur. Phys. J. B* **91**, 216 (2018).
- 22 M. Hopjan, G. Stefanucci, E. Peretto, and C. Verdozzi, *Phys. Rev. B* **98**, 041405 (2018).
- 23 J. K. Freericks, H. R. Krishnamurthy, and T. Pruschke, *Phys. Rev. Lett.* **102**, 136401 (2009).
- 24 B. Moritz, A. F. Kemper, M. Sentef, T. P. Devereaux, and J. K. Freericks, *Phys. Rev. Lett.* **111**, 077401 (2013).
- 25 A. F. Kemper, M. Sentef, B. Moritz, C. C. Kao, Z. X. Shen, J. K. Freericks, and T. P. Devereaux, *Phys. Rev. B* **87**, 235139 (2013).
- 26 M. Sentef, A. F. Kemper, B. Moritz, J. K. Freericks, Z.-X. Shen, and T. P. Devereaux, *Phys. Rev. X* **3**, 041033 (2013).
- 27 H. Aoki, N. Tsuji, M. Eckstein, M. Kollar, T. Oka, and P. Werner, *Rev. Mod. Phys.* **86**, 779 (2014).
- 28 A. F. Kemper, M. A. Sentef, B. Moritz, J. K. Freericks, and T. P. Devereaux, *Phys. Rev. B* **90**, 075126 (2014).
- 29 A. F. Kemper, M. A. Sentef, B. Moritz, J. K. Freericks, and T. P. Devereaux, *Phys. Rev. B* **92**, 224517 (2015).
- 30 M. A. Sentef, A. F. Kemper, A. Georges, and C. Kollath, *Phys. Rev. B* **93**, 144506 (2016).
- 31 D. Golež, P. Werner, and M. Eckstein, *Phys. Rev. B* **94**, 035121 (2016).

- ³²A. F. Kemper, M. A. Sentef, B. Moritz, T. P. Devereaux, and J. K. Freericks, *Ann. Phys.* **529**, 1600235 (2017).
- ³³R. Tuovinen, D. Golež, M. Schüler, P. Werner, M. Eckstein, and M. A. Sentef, *Phys. Status Solidi B* **256**, 1800469 (2018).
- ³⁴M. Brandbyge, J.-L. Mozos, P. Ordejón, J. Taylor, and K. Stokbro, *Phys. Rev. B* **65**, 165401 (2002).
- ³⁵M. F. Ludovico and L. Arrachea, *Physica B* **407**, 3256 (2012).
- ³⁶J.-S. Wang, B. K. Agarwalla, H. Li, and J. Thingna, *Front. Phys.* **9**, 673 (2014).
- ³⁷M. Ridley and R. Tuovinen, *Phys. Rev. B* **96**, 195429 (2017).
- ³⁸R. Tuovinen, E. Perfetto, R. van Leeuwen, G. Stefanucci, and M. A. Sentef, *New J. Phys.* **21**, 103038 (2019).
- ³⁹R. Tuovinen, M. A. Sentef, C. Gomes da Rocha, and M. S. Ferreira, *Nanoscale* **11**, 12296 (2019).
- ⁴⁰K. Kainulainen, T. Prokopec, M. G. Schmidt, and S. Weinstock, *Phys. Rev. D* **66**, 043502 (2002).
- ⁴¹M. Garny and M. M. Müller, *Phys. Rev. D* **80**, 085011 (2009).
- ⁴²M. Garny, A. Kartavtsev, and A. Hohenegger, *Ann. Phys.* **328**, 26 (2013).
- ⁴³P. Lipavský, V. Špička, and B. Velický, *Phys. Rev. B* **34**, 6933 (1986).
- ⁴⁴S. Hermanns, K. Balzer, and M. Bonitz, *Phys. Scr.* **2012**, 014036.
- ⁴⁵V. M. Galitskii, *Sov. Phys. JETP* **7**, 104 (1958), <http://www.jetp.ac.ru/cgi-bin/e/index/e/7/1/p104?a=list>.
- ⁴⁶L. Hedin, *Phys. Rev.* **139**, A796 (1965).
- ⁴⁷M. P. von Friesen, C. Verdozzi, and C.-O. Almbladh, *Phys. Rev. Lett.* **103**, 176404 (2009).
- ⁴⁸A. A. Rusakov and D. Zgid, *J. Chem. Phys.* **144**, 054106 (2016).
- ⁴⁹E. Perfetto and G. Stefanucci, *Phys. Status Solidi B* **256**, 1800573 (2019).
- ⁵⁰E. Perfetto and G. Stefanucci, *J. Phys.: Condens. Matter* **30**, 465901 (2018).
- ⁵¹G. Baumgartner, A. Auer, D. E. Bernholdt, A. Bibireata, V. Choppella, D. Cociorva, R. J. Harrison, S. Hirata, S. Krishnamoorthy, S. Krishnan, M. Nooijen, R. M. Pitzer, J. Ramanujam, P. Sadayappan, and A. Sibiryakov, *Proc. IEEE* **93**, 276 (2005).
- ⁵²E. Solomonik, D. Matthews, J. R. Hammond, J. F. Stanton, and J. Demmel, *J. Parallel Distrib. Comput.* **74**, 3176 (2014).
- ⁵³J. Huang, D. Matthews, and R. van de Geijn, *SIAM J. Sci. Comput.* **40**, C305 (2018).
- ⁵⁴P. Myöhänen, A. Stan, G. Stefanucci, and R. van Leeuwen, *Europhys. Lett.* **84**, 67001 (2008).
- ⁵⁵P. Myöhänen, A. Stan, G. Stefanucci, and R. van Leeuwen, *Phys. Rev. B* **80**, 115107 (2009).
- ⁵⁶S. Latini, E. Perfetto, A.-M. Uimonen, R. van Leeuwen, and G. Stefanucci, *Phys. Rev. B* **89**, 075306 (2014).
- ⁵⁷K. J. H. Giesbertz, *Phys. Chem. Chem. Phys.* **18**, 21024 (2016).
- ⁵⁸K. Balzer, "Solving the two-time Kadanoff-Baym equations. Application to model atoms and molecules." Ph.D. thesis, Christian-Albrechts-Universität zu Kiel, 2011.
- ⁵⁹K. Balzer, N. Schlünzen, and M. Bonitz, *Phys. Rev. B* **94**, 245118 (2016).
- ⁶⁰M. P. von Friesen, C. Verdozzi, and C.-O. Almbladh, *Europhys. Lett.* **95**, 27005 (2011).
- ⁶¹M. Bonitz, S. Hermanns, K. Kobusch, and K. Balzer, *J. Phys.: Conf. Ser.* **427**, 012002 (2013).
- ⁶²H. Bruus and K. Flensberg, *Many-Body Quantum Theory in Condensed Matter Physics* (Oxford University Press, New York, 2007).
- ⁶³S. Hermanns, N. Schlünzen, and M. Bonitz, *Phys. Rev. B* **90**, 125111 (2014).
- ⁶⁴D. Semkat, M. Bonitz, and D. Kremp, *Contrib. Plasma Phys.* **43**, 321 (2003).
- ⁶⁵D. Karlsson, R. van Leeuwen, E. Perfetto, and G. Stefanucci, *Phys. Rev. B* **98**, 115148 (2018).
- ⁶⁶M. Hopjan and C. Verdozzi, *Eur. Phys. J.: Spec. Top.* **227**, 1939 (2019).
- ⁶⁷J. Yang, Y. Kurashige, F. R. Manby, and G. K. L. Chan, *J. Chem. Phys.* **134**, 044123 (2011).
- ⁶⁸S. Hermanns, "Nonequilibrium green functions. Selfenergy approximation techniques." Ph.D. thesis, Christian-Albrechts-Universität zu Kiel, 2016.
- ⁶⁹D. Neuhauser, R. Baer, and D. Zgid, *J. Chem. Theory Comput.* **13**, 5396 (2017).
- ⁷⁰N. Schluenzen, S. Hermanns, M. Scharnke, and M. Bonitz, "Ultrafast dynamics of strongly correlated fermions—Nonequilibrium green functions and selfenergy approximations," *J. Phys.: Condens. Matter* (to be published).
- ⁷¹N. Schlünzen and M. Bonitz, *Contrib. Plasma Phys.* **56**, 5 (2016).
- ⁷²N. Schlünzen, J.-P. Joost, F. Heidrich-Meisner, and M. Bonitz, *Phys. Rev. B* **95**, 165139 (2017).
- ⁷³L. J. Holleboom and J. G. Snijders, *J. Chem. Phys.* **93**, 5826 (1990).
- ⁷⁴T. Helgaker, P. Jørgensen, and J. Olsen, *Molecular Electronic-Structure Theory* (John Wiley & Sons, Ltd., West Sussex, England, 2000).
- ⁷⁵J. J. Phillips, A. A. Kananenka, and D. Zgid, *J. Chem. Phys.* **142**, 194108 (2015).
- ⁷⁶C. Sanderson and R. Curtin, *J. Open Source Software* **1**, 26 (2016).
- ⁷⁷T. E. Oliphant, *A Guide to NumPy* (Trelgol Publishing, USA, 2006).
- ⁷⁸D. G. A. Smith and J. Gray, *J. Open Source Software* **3**, 753 (2018).
- ⁷⁹B. Kirtman and B. Champagne, *Int. Rev. Phys. Chem.* **16**, 389 (1997).
- ⁸⁰M. van Faassen, P. L. de Boeij, R. van Leeuwen, J. A. Berger, and J. G. Snijders, *Phys. Rev. Lett.* **88**, 186401 (2002).
- ⁸¹M. van Faassen, P. L. de Boeij, R. van Leeuwen, J. A. Berger, and J. G. Snijders, *J. Chem. Phys.* **118**, 1044 (2003).
- ⁸²K. Ohno, *Theor. Chim. Acta* **2**, 219 (1964).
- ⁸³D. Baeriswyl, D. K. Campbell, and S. Mazumdar, in *Conjugated Conducting Polymers*, edited by H. G. Giess (Springer, 1992).
- ⁸⁴M. A. Marques, A. Castro, G. F. Bertsch, and A. Rubio, *Comput. Phys. Commun.* **151**, 60 (2003).
- ⁸⁵V. Strassen, *Numer. Math.* **13**, 354 (1969).
- ⁸⁶Q. Ge, Y. Gao, R. Baer, E. Rabani, and D. Neuhauser, *J. Phys. Chem. Lett.* **5**, 185 (2014).
- ⁸⁷D. Neuhauser, Y. Gao, C. Arnsts, C. Karshenas, E. Rabani, and R. Baer, *Phys. Rev. Lett.* **113**, 076402 (2014).
- ⁸⁸Z. Ruan and R. Baer, *Mol. Phys.* **116**, 2490 (2018).
- ⁸⁹W. Dou, T. Y. Takeshita, M. Chen, R. Baer, D. Neuhauser, and E. Rabani, e-print [arXiv:1909.06525](https://arxiv.org/abs/1909.06525) (2019).

Publication IV

Laser-assisted ionisation of adenine as a protection mechanism against radiation damage

Erik P. Månsson, Simone Latini, Fabio Covito, Vincent Wanie, Mara Galli, Enrico Perfetto, Gianluca Stefanucci, Hannes Hübener, Umberto De Giovannini, Mattea C. Castrovilli, Andrea Trabattoni, Fabio Frassetto, Luca Poletto, Jason B. Greenwood, François Légaré, Mauro Nisoli, Angel Rubio and Francesca Calegari, *Submitted to Nature Physics*.

The interaction of ionizing radiation (or energetic particles) with biomolecules is of crucial importance for many biochemical and medical processes. For example, tissue damage in radiotherapy is correlated to the response of DNA sub-units to ionizing radiation. This, in fact, gives rise to a cascade of secondary electrons carrying an energy of around 20-30 eV, comparable with the one transferred through extreme ultraviolet (XUV) attosecond pulses. The impact of these carriers with DNA causes ionization, inevitably followed by fragmentation of its sub-units, leading to damage.

Although of great concern, this matter has not yet been fully understood, mainly for the lack of knowledge of the physical mechanisms initiating the processes that ultimately cause damage. The chain of events eventually leading to fragmentation and damage, is initiated by the correlation-driven ultrafast electron dynamics induced by ionization [44–47]. Gaining insight into the processes governing the dynamics at this timescale is therefore vital to the understanding of protection against ionization-induced damage.

In the following publication, a joint experimental and theoretical study addressing the issue of ionization damage in the Adenine molecule is presented. The theoretical analysis is performed using the NEGF framework developed in this

work as well as a simplified, but rather accurate, rate equations model based on perturbation theory. We uncover a novel laser-assisted stabilization mechanism that hinders fragmentation and ultimately protects from damage. Electronic correlations are found to enable this relaxation pathway stabilizing the molecule. In fact, we identify ultrafast shake-up transitions promoting electrons to excited states, which are then accessible with the use of a secondary near-infrared (NIR) pulse. The ionization of such excited electrons represents a possible energy-dissipation mechanism leading to the eventual protection from fragmentation.

The proposed analysis is directly applicable to other molecules of similar size. In fact, we are working on a comparative study³ including all nitrogenous bases where we highlight the role of electronic correlations for the stabilization mechanism and predict which bases can undergo such relaxation pathway. Preliminary results are presented in Fig. 2.3, where the time-dependent occupations of the bound excited states for the different nitrogenous bases after the action of an XUV laser are shown. This data indicates that purine bases (Adenine and Guanine) manifest the slow correlation-driven electron dynamics that enable the proposed stabilization mechanism. On the other hand, pyrimidine bases (Thymine, Cytosine and Uracil) seem to lack this ability⁴. Uracil seems to have slow dynamics, too, but a more complete analysis has to be performed to make conclusive statements.

One direction for future work is the study of larger systems, e.g. nucleobase pairs and nucleosides, for extending the study of stabilization to more complex DNA building blocks. Another path to follow would be the analysis of the role of nuclear motion in the proposed mechanism. In fact, although the shake-up dynamics are expected to take place before any nuclear motion can provide a possible stabilization mechanism, non-adiabatic effects such as conical intersection cannot be completely ruled out and could complement the study. The inclusion of nuclear degrees of freedom in the study of ultrafast correlated electron dynamics is an appealing, yet difficult challenge, given the highly complex nature of the problem already at the Born-Oppenheimer level of approximation. A description consider-

³To be submitted to Physical Review Letters.

⁴The inability of Thymine of undergoing such dynamics is confirmed by preliminary experimental data collected by the same collaborators of Publication IV.

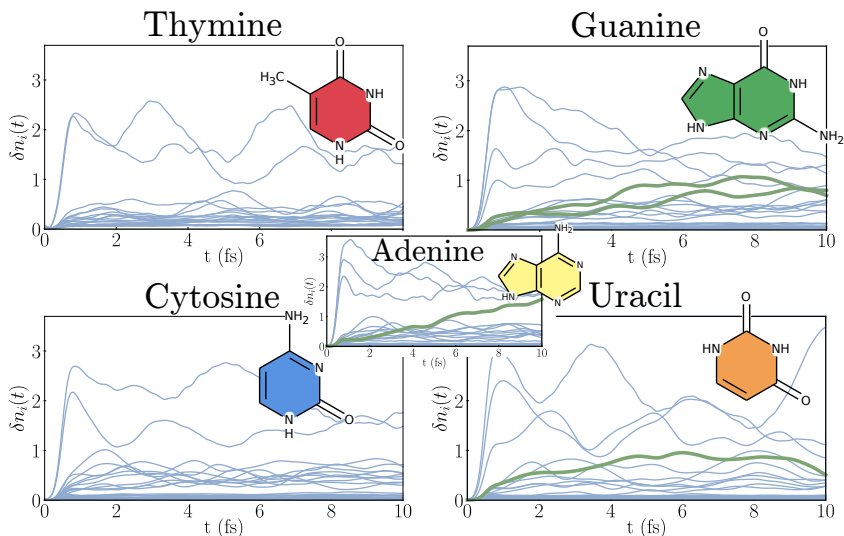


Figure 2.3: Time-dependent occupations of the bound excited states of the different nitrogenous bases after photoionization by XUV light polarized perpendicularly to the molecular plane. Consistently with Fig. 4b of Publication IV, special states populated significantly through non-instantaneous shake-up transitions are highlighted in green, while the rest are drawn in light blue. The y-axis is scaled up by a factor of 10^5 for all sub-plots.

ing non-adiabatic electron-nuclear motion would help us further understand how to harness the complicated coupled dynamics to determine stabilization pathways for other classes of molecules.

In the following, I add a few remarks, which are not explicitly addressed in the published manuscript, but complement the discussion of the work.

Convergence issues. As explained before, the self-energy encodes the effect of correlation in the NEGF formalism. This, in turn, depends on Green's functions and the bare Coulomb interaction. The latter, in a single-particle basis, is represented by the 4-dimensional tensor of the Coulomb integrals. In our framework, the transitions involving initially unoccupied states are *only* governed by “Auger-like” Coulomb integrals, i.e. with only one index above the HOMO. These Coulomb

integrals are, in general, quite small in comparison to the rest; this is exactly what is exploited to take the approximations leading to the coupled NEGF equations of Publication I and II. The reduced size of these quantities is related to the overlap between the states. Unoccupied states tend to be, in general, more delocalized compared to the occupied ones, yielding smaller overlaps with (localized) occupied states, making the important coulomb integrals quite sensible quantities to start with. This is an important matter to take care of during the computational analysis and simulations: special attention has to be paid when converging the calculations generating the basis in which the simulations are run. In fact, grid size, grid spacing and accuracy thresholds in my calculations were much finer than typical convergence parameters.

Self-interaction correction. Like mentioned in the Supplementary Information, the Average-Density Self-Interaction Correction (ADSIC) has been employed in the DFT calculations needed to construct the single-particle basis used in the NEGF calculations. The role of the ADSIC is to correct the tails of the Coulomb potential, not properly decaying to zero in conventional Generalized Gradient Approximation (GGA) functionals. The main effect of using the ADSIC is the correction of the Ionization Potential (IP) of the molecule. As a consequence, more Kohn-Sham states fall below zero energy, meaning these states help to better describe localized features in the subsequent simulation of the dynamics. We anticipate that these states become resonances in the HF basis and that these are *not* the same states one would obtain by directly solving the HF equations. It is well known, in fact, that the HF approximation yields larger gaps.

Sudden removal. For a more systematic analysis of the shake-up transitions, simulations of dynamics induced by sudden removal of a percentage of an electron from a single state have been performed for all states. The percentage removed roughly matched the generic ionization induced by the XUV pump used in the actual simulations presented in the paper. The results show no shake-up transition related to the one identified to be the gateway to the stabilization mechanism. This means a more general excited state has to be induced by the pump to give rise to the important dynamics.

Laser-assisted ionisation of adenine as a protection mechanism against radiation damage

Erik P. Månsson^{1,2}, Simone Latini³, Fabio Covito³, Vincent Wanie^{1,2,4}, Mara Galli^{1,5}, Enrico Perfetto^{6,7}, Gianluca Stefanucci^{7,8}, Hannes Hübener³, Umberto De Giovannini^{3,9}, Mattea C. Castrovilli^{2,10}, Andrea Trabattoni¹, Fabio Frassetto¹¹, Luca Poletto¹¹, Jason B. Greenwood¹², François Légaré⁴, Mauro Nisoli^{2,5}, Angel Rubio^{3,13} and Francesca Calegari^{1,2,14*}

¹ Center for Free-Electron Laser Science, DESY, Notkestr. 85, 22607 Hamburg, Germany.

² Inst. for Photonics and Nanotechnologies CNR-IFN, P.za L. da Vinci 32, 20133 Milano, Italy.

³ Max Planck Institute for the Structure and Dynamics of Matter and Center for Free Electron Laser Science, 22761 Hamburg, Germany.

⁴ INRS-EMT, 1650 Blvd. Lionel Boulet J3X 1S2, Varennes, Canada.

⁵ Department of Physics, Politecnico di Milano, Piazza L. da Vinci 32, 20133 Milano, Italy.

⁶ CNR-ISM, Division of Ultrafast Processes in Materials (FLASHit), Area della ricerca di Roma 1, Via Salaria Km 29.3, I-00016 Monterotondo Scalo, Italy.

⁷ Dipartimento di Fisica, Università di Roma Tor Vergata, Via della Ricerca Scientifica, 00133 Rome, Italy.

⁸ INFN, Sezione di Roma Tor Vergata, Via della Ricerca Scientifica 1, 00133 Roma, Italy

⁹ Dipartimento di Fisica e Chimica, Università degli Studi di Palermo, Via Archirafi 36, I-90123, Palermo, Italy.

¹⁰ Inst. for the Structure of Matter CNR-ISM, Area Ricerca di Roma1, Monterotondo, Italy.

¹¹ Inst. for Photonics and Nanotechnologies CNR-IFN, Via Trasea 7, 35131 Padova, Italy.

¹² Centre for Plasma Physics, School of Maths and Physics, Queen's University Belfast, BT7 1NN, UK.

¹³ Center for Computational Quantum Physics (CCQ), The Flatiron Institute, 162 Fifth avenue, New York NY 10010, USA.

¹⁴ Institut für Experimentalphysik, Universität Hamburg, Luruper Chaussee 149, D-22761 Hamburg.

*E-mail: francesca.calegari@desy.de.

Ionising radiation causes damage to DNA when bonds are broken in its subunits¹. Control over the molecular dissociation has so far hardly been achieved, and a better understanding of the ionisation process in nucleic-acid bases would have implications beyond the scope of physical chemistry. Here we report on a time-resolved study of adenine photo-fragmentation following ionisation by an extreme ultraviolet attosecond pulse². We find that, although adenine has a low photo-stability in this energy range³, ultrafast electronic rearrangement opens up a new efficient stabilisation pathway that can be accessed via a second ionisation event triggered by a shortly delayed laser pulse, leading to the production of intact and stable doubly charged adenine. This counter-intuitive stabilisation-by-ionisation mechanism is supported by first-principles time-dependent simulations including electronic correlation effects. Our findings pave the way for a new potential control scheme for the protection of the DNA subunits against radiation damage.

The interaction of ionising radiation with large biological molecules has a high-degree of complexity^{1,4}. In ionised molecules, the excited-states dynamics considerably interfere with a variety of processes occurring between the different subunits and between the subunits and the solvent. One of the motivations to study DNA in the gas phase is the nonpolar character of its subunits (as many other biological media do not dissolve in water), making the gas phase the ideal environment where the intrinsic reactivity can be identified⁵. Moreover, by ionising isolated nucleic-acid bases, the primary relaxation mechanisms leading to fragmentation, and therefore damage, can be identified in the complete absence of external effects. Sudden removal of one or more electrons from these molecules leads to an internal electronic rearrangement, often governed by correlated processes such as charge migration^{6,7}, shake-up or Auger⁸ and Interatomic Coulombic Decay (ICD)⁹. These processes may initiate a chain of events leading to damage, and they occur on an extremely fast time scale now accessible by attosecond laser technology^{2,10,11}. Recently, using trains of attosecond pulses, it has been possible to reveal that multi-electronic (shake-up) and non-adiabatic effects are fully entangled and their interplay can be identified in the relaxation dynamics following XUV-induced ionisation of organic molecules¹². Nevertheless, this entangled effect has been demonstrated to occur on a time scale of several tens of femtoseconds and the very early stages

of the light-molecule interaction, when pure electronic effects are expected to dominate, have not been investigated so far with sufficiently high temporal resolution. In this work, we report the first few-femtosecond time-resolved study of the dissociative dynamics of the nucleic-acid base adenine following sudden ionisation by an attosecond XUV pulse, with the motivation to track many body effects *before* non-adiabatic effects take place and potentially take advantage of them to find new molecular stabilisation protocols against radiation damage.

In our experiment, ionisation of adenine is initiated by an isolated sub-300-as XUV pulse containing photon energies from 15 to 35 eV, produced by high-harmonic generation¹³ in krypton gas through the polarisation gating technique¹⁴. A waveform-controlled 4-fs near-infrared (NIR, central photon energy 1.77 eV) probing pulse is combined with the XUV pump pulse using an interferometric approach. Adenine is sublimated and carried to the laser interaction region by using helium as a buffer gas. The produced ions are then collected as function of the XUV-pump NIR-probe delay (see Figure 1a), using a time-of-flight spectrometer. The ion mass spectrum resulting from ionisation by the XUV pulse alone is shown in Figure 1b. The observed high level of fragmentation (81% of the total yield) indicates a relatively low photo-stability of adenine in this energy range. This is also confirmed by first-principles calculations¹⁵⁻¹⁷ based on time-dependent density functional theory (TDDFT)^{18,19} and Ehrenfest dynamics²⁰ where suddenly ionised adenine undergoes bond-elongation and eventual dissociation, as shown in Figure 1c.

Further deposition of energy by the NIR pulse, simultaneously or after the XUV, leads to an overall increase of fragmentation³. Figure 2 shows the partial ion yield for several ionic fragments as a function of the pump-probe delay. The time dependent yields of the cationic fragments with mass 27, 38 and 53 u display step-like increases, followed by slower decay. The enhancement of small fragment ions occurs at the expense of the large fragments, mainly 108 u, which clearly indicates that the combination of XUV and NIR pulses leads to further excitation and therefore more efficient bond breaking. One could thus assume that the only effect of sending a control NIR laser pulse would be to decrease the photo-stability of the XUV-ionised molecule.

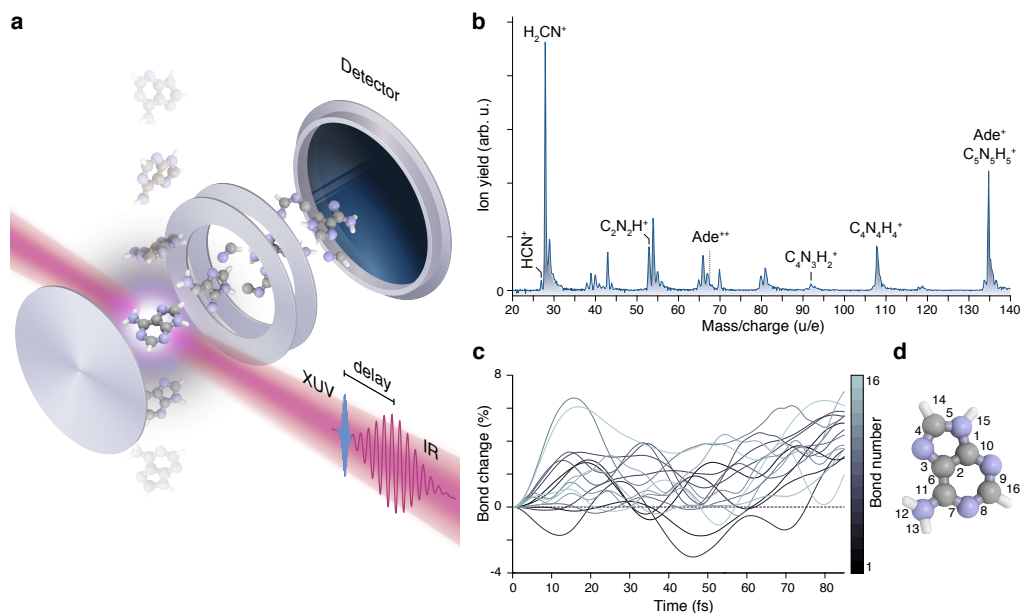


Figure 1: **Dissociation of adenine.** (a) Schematic of the experiment: a molecular beam is injected into a VMI operated in the ion time-of-flight mode. Adenine ions are accelerated towards the detector and the ion yield is measured as a function of the XUV-pump IR-probe delay. (b) Measured mass spectrum resulting from ionisation of adenine by the XUV pulse only. Fragment masses constitute 81% of the spectrum. (c) Calculated time evolution of the bond lengths following XUV ionisation, with an electron removed from the highest occupied molecular orbital. Several bond lengths are seen to evolve without reaching a new equilibrium after XUV ionisation, which is consistent with a large dissociation probability. (d) The bond numbering used in the theoretical work.

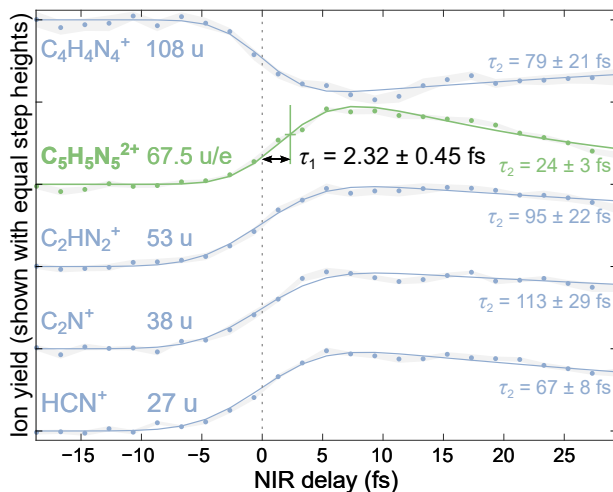


Figure 2: **Experimental results: pump-probe scan.** Normalised yield of several ions (shown with a vertical offset) as a function of the XUV-pump NIR-probe delay. The yield of the ionic fragments exhibits a distinct positive or negative step-like behaviour, while the adenine parent dication (67.5 u/e) is fitted to have an exponential risetime of $\tau_1 = 2.32 \pm 0.45$ fs (68 % confidence interval). The decay lifetime (τ_2) is significantly shorter for the dication (green curve) than for the cations. The grey shading indicates the standard error of the mean of 7 successive scans.

The most intriguing observation in the time-dependent mass spectrum is the appearance of a new ion for small positive delays at mass/charge = 67.5 u/e, corresponding to the doubly charged parent molecule (adenine²⁺)²¹⁻²³. It is worth noting that a stable dication of the parent is difficult to discern in the XUV-only signal or at negative NIR delays, and none is present if we select the portion of the XUV spectrum below 17 eV (see the Supplementary Information (SI)). Figure 2 shows that the formation of the parent dication is delayed compared to the cationic fragments. Fitting the experimental data using a curve model described in the SI, we obtain for the dication pump-probe signal a delay of 2.32 ± 0.45 fs (τ_1 , exponential risetime) and a decay time of 24 ± 3 fs (τ_2 , exponential decay). To further verify that the steps of the cationic fragments accurately represent the absolute zero time delay (XUV-NIR overlap), we also did measurements with simultaneous injection of an atomic gas (krypton). The XUV+NIR double ionisation of krypton gives a Kr^{2+} signal at a time consistent with the adenine cations (see SI), allowing us to conclude that it is the adenine dication signal which is positively delayed. The extracted delay does not appear to depend on the NIR pulse intensity, within the explored range from 7×10^{12} to 1.4×10^{13} W/cm². At the same time we observed that the dication yield scales quadratically with the NIR intensity (see SI), thus indicating that two NIR photons are required to doubly ionise the molecule. The detection of a doubly charged intact molecule indicates the presence of a stabilisation mechanism that can occur only if the control NIR laser pulse arrives with a short delay after the ionising XUV pulse.

Both singly and doubly ionised adenine have stable ground states that can be found by relaxing the molecular geometry in first-principles DFT calculations. On the other hand, as stated above, TDDFT dynamics after sudden ionisation showed bond elongation and dissociation (see SI). The observed transition to a stable doubly ionised state thus requires energy to be removed by other means, with the NIR pulse having a stabilising role. We propose the following mechanism: *I*) the XUV pulse singly ionises the molecule leaving a hole in a valence state, *II*) the hole decays in a characteristic short time and, due to electronic correlations, this can lead to excitation of a second electron to a bound excited state, hereafter called "shake-up" state, *III*) the NIR pulse extracts the excited electron, hence doubly ionising and stabilising the molecule. This stabilisation mechanism is accessible only if the NIR pulse is optimally timed with respect to the XUV pulse,

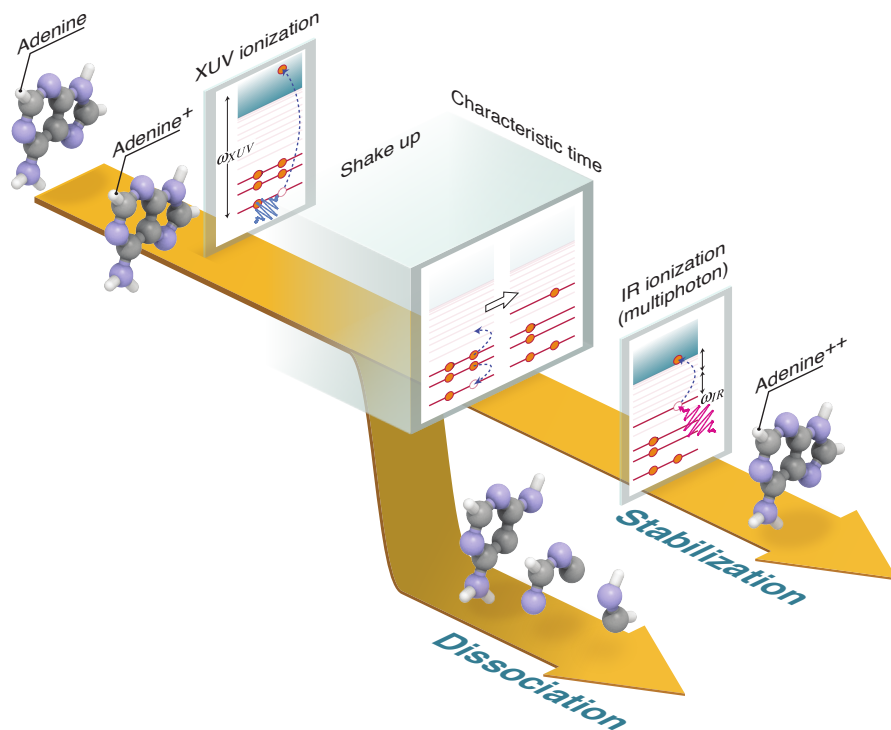


Figure 3: **Overview of the molecular dynamics.** Following XUV photoionisation, an NIR pulse can either lead to additional fragmentation or, if optimally time-delayed from the XUV, can give access to a stable dication. The start of the time-delay window within which the NIR has a stabilisation role is set by the characteristic time of a well defined shake-up process.

arriving after the shake-up process has occurred but before the excited molecular cationic state relaxes. On the other hand, if the NIR comes before the shake-up has occurred, further fragmentation is induced and the dication cannot be formed. The two possible scenarios are illustrated in Fig. 3. It is worth mentioning that, even though the NIR probe pulse acts in the very early stages of the light-matter interaction where pure electron dynamics dominates, the role of non-adiabatic effects such as conical intersections cannot be completely ruled out. Nevertheless, in such a short time window, we do not expect these effects to remove enough energy from the system to open a pathway for stabilisation.

We find that, as described below, for a particular excited electronic state the characteristic shake-up time is compatible with the experimentally observed time delay. The shake-up process (illustrated in the level diagrams in Fig. 3) is purely driven by electronic correlation (two-body Coulomb interaction), not accounted for in standard TDDFT simulations²⁴. Nevertheless, a simple estimation of the rate for the shake-up processes can be obtained using Fermi's golden rule where the Coulomb interaction is used as a scattering potential and the initial orbital resolved XUV photoionisation probability is taken into account (see SI). The inverse of the rate of the process can be interpreted as the characteristic formation time of a shake-up state. Figure 4(a) shows the characteristic shake-up transition times for different bound unoccupied orbitals (Kohn-Sham (KS) orbitals obtained with DFT ground-state calculations). Most of the calculated times are of the order of few hundreds attoseconds except for three states, one of which (the LUMO+6 indicated in green) is 2.5 fs, very close to the experimentally observed delay of the dication formation. Interestingly, the energy of this orbital is in the window of two-photon ionisation from the NIR pulse, which is in agreement with the experimental observation that two NIR photons are required for the stabilisation.

While the rate-equation approach is easy to understand and it provides a clear physical explanation of the experimental findings, it is an overly simplified description. More refined ab-initio calculations are required to further validate our interpretation and provide a predictive framework to address similar phenomena in other molecular complexes. To this end, we performed many-

body time-dependent simulations to take into account both the electron dynamics triggered by the XUV photo-ionisation and the absorption of a delayed NIR pulse. By solving the equations of motion for the non-equilibrium Green’s function and using an efficient propagation scheme based on the generalized Kadanoff-Baym ansatz, we can obtain an accurate and controlled treatment of shake-up processes^{25,26} (see SI). From the calculations, we extract the orbital-resolved occupations and the spatial variation of the electronic density, all reported in Fig. 4. When only the XUV photoionisation is considered (Fig. 4b), we can confirm the results obtained with the rate equations: while most of the states exhibit sub-femtosecond rise-times, the LUMO+6 occupation (shown in green) rises slowly over several femtoseconds. Fig. 4c shows snapshots of the change in electron density, with respect to time zero. We notice a significant electronic charge inflation more than 3 Å away from the molecular plane that builds up over time. The spatial distribution of this density variation resembles the one of the LUMO+6 orbital (see SI) underlining its dominant role in the overall electron dynamics. Furthermore, we could speculate that this rapid delocalisation far from the plane of the bonds allows for minimising the probability of bond breaking after photo-excitation. Our simulations indicate that LUMO+6 can only be accessed when ionisation is triggered by an XUV pulse polarised perpendicularly to the molecular plane. Therefore, the relative orientation between the molecule and the attosecond pulse can potentially be exploited to achieve more refined control of the stabilisation process.

Finally, we have included the NIR absorption in the simulation and calculated the time-resolved NIR-induced depletion of the LUMO+6 (Fig. 4d), for different pump–probe delays. The depletion shows an onset in the window of 2–4 fs and increases with larger delays. To highlight this delay-dependent increase, Fig. 4(e) illustrates how the average depletion after the end of the NIR pulse changes as a function of the pump–probe delay. The trend reproduces, remarkably, the one measured for the adenine dication yield (green solid line in Fig. 2). We point out that only the LUMO+6 state is characterised by this slow onset (other states in SI) and we can therefore conclude that the slow shake-up dynamics identified for the LUMO+6 state explains why the NIR pulse has to be optimally delayed in order to produce the stable dication. To summarise, our theoretical calculations singled out a special excited state, described by one KS orbital, which mediates

the observed laser assisted stabilisation process in photoionised adenine. The peculiarity of this LUMO+6 state can be attributed to the following characteristics: I) it has a few-femtoseconds shake-up time, compatible with the experimentally observed delay in the dication formation, II) it is a delocalised excited state that extends away from the molecular plane and III) it couples very efficiently to the NIR pulse. Experimental findings indicate that the NIR pulse must be sent in a relative narrow time window ($\tau_2 \approx 24$ fs) after ionisation to stabilise the molecule. Our simulations cannot describe at this stage what defines the length of this time-window, since we are not treating the combined electron and nuclear dynamics. We could however speculate that the observed decay rate is due to relaxation of this special excited state via vibronic couplings.

Control over molecular dissociation is fundamental to achieve new molecular functionalities. We have identified a robust and simple stabilisation mechanism based on a many body effect in a DNA base, where adding energy to the system actually opens a non-dissociative relaxation path. We have characterised the intrinsic time required for a specific shake-up process to occur, which to our knowledge has not been measured in real time for any polyatomic molecule before. A key aspect of the stabilisation mechanism is the efficient depletion of this particular shake-up state induced by a control NIR probe pulse. Our findings demonstrate that extreme time resolution is required for the real-time tracking of many-body effects and for acting on the system before it relaxes via non-adiabatic couplings. By complementing the experiments with covariant detection of electrons and ions and with the support of time-dependent many-body methods, which also account for the nuclear motion, we could identify ad hoc stabilisation pathways for different class of molecules. We envisage the possibility to extend this control scheme to larger molecules (including nucleobase pairs and nucleosides), thus paving the way to a new protection protocol against ionisation-induced damage.

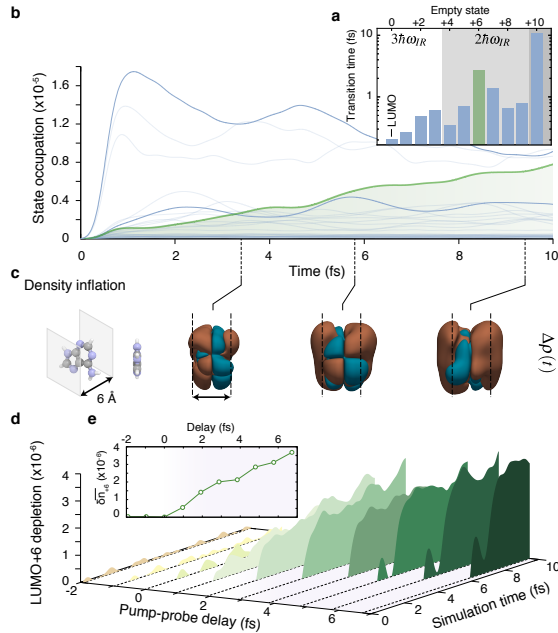


Figure 4: **Identification of states involved in the stabilisation process.** (a) Transition times to a given shake-up state calculated with a Fermi's Golden rule approach. The LUMO+6 state is highlighted in green and shows a characteristic time of 2.5 fs. The states are ordered by energy and grouped (shades of gray) by the number of NIR photons (1, 2 or 3) required to ionise a second electron. The LUMO+6 state falls in the two NIR-photon group. (b) Time-dependent occupations of the adenine bound excited states after photoionisation by the XUV, calculated with the ab-initio non equilibrium Green's function method. The special state (LUMO+6), highlighted in green, is populated via a shake-up process and rises over several femtoseconds to one of the largest values. (c) Snapshots of the variation of the electronic density with respect to the density immediately after the XUV pulse. We observe that the electronic density inflates considerably away from the molecular plane. The noticeable inflation of the electronic density can be attributed to the increasing population of the LUMO+6 state (see SI). (d) Temporal evolution of the LUMO+6 state depletion due to the combined action of XUV and NIR pulses as a function of the delay. The depletion shows a significant onset in the window of 2-4 fs and it keeps increasing with larger delays as shown in (e) where we report the state depletion averaged in a 1 fs window after NIR pulse.

References

1. Shukla, M. K. & Leszczynski, J. (eds.) *Radiation Induced Molecular Phenomena in Nucleic Acids* (Springer Netherlands, 2008).
2. Calegari, F., Sansone, G., Stagira, S., Vozzi, C. & Nisoli, M. Advances in attosecond science. *Journal of Physics B: Atomic, Molecular and Optical Physics* **49**, 062001 (2016).
3. Pilling, S. *et al.* Dissociative photoionization of adenine following valence excitation. *Rapid Communications in Mass Spectrometry* **21**, 3646–3652 (2007).
4. Khanna, K. K. & Jackson, S. P. DNA double-strand breaks: signaling, repair and the cancer connection. *Nature Genetics* **27**, 247–254 (2001).
5. Pan, S., Sun, X. & Lee, J. K. DNA stability in the gas versus solution phases: A systematic study of thirty-one duplexes with varying length, sequence, and charge level. *Journal of the American Society for Mass Spectrometry* **17**, 1383 – 1395 (2006).
6. Cederbaum, L. S. & Zobeley, J. Ultrafast Charge Migration by Electron Correlation. *Chem. Phys. Lett.* **307**, 205–210 (1999).
7. Calegari, F. *et al.* Ultrafast electron dynamics in phenylalanine initiated by attosecond pulses. *Science* **346**, 336–339 (2014).
8. Drescher, M. *et al.* Time-resolved atomic inner-shell spectroscopy. *Nature* **419**, 803–807 (2002).
9. Averbukh, V. *et al.* Interatomic electronic decay processes in singly and multiply ionized clusters. *Journal of Electron Spectroscopy and Related Phenomena* **183**, 36 – 47 (2011). Electron Spectroscopy Kai Siegbahn Memorial Volume.
10. Nisoli, M., Decleva, P., Calegari, F., Palacios, A. & Martín, F. Attosecond electron dynamics in molecules. *Chemical Reviews* **117**, 10760–10825 (2017). PMID: 28488433.

11. Sansone, G., Pfeifer, T., Simeonidis, K. & Kuleff, A. I. Electron correlation in real time. *ChemPhysChem* **13**, 661–680 (2012).
12. Marciniak, A. *et al.* Electron correlation driven non-adiabatic relaxation in molecules excited by an ultrashort extreme ultraviolet pulse. *Nature Communications* **10**, 337 (2019).
13. Corkum, P. B. Plasma perspective on strong field multiphoton ionization. *Phys. Rev. Lett.* **71**, 1994–1997 (1993).
14. Sola, I. J. *et al.* Controlling attosecond electron dynamics by phase-stabilized polarization gating. *Nature Physics* **2**, 319–322 (2006).
15. Marques, M. A., Castro, A., Bertsch, G. F. & Rubio, A. octopus: a first-principles tool for excited electron–ion dynamics. *Computer Physics Communications* **151**, 60–78 (2003).
16. Castro, A. *et al.* octopus: a tool for the application of time-dependent density functional theory. *physica status solidi (b)* **243**, 2465–2488 (2006).
17. Andrade, X. *et al.* Real-space grids and the octopus code as tools for the development of new simulation approaches for electronic systems. *Physical Chemistry Chemical Physics* **17**, 31371–31396 (2015).
18. Runge, E. & Gross, E. K. U. Density-Functional Theory for Time-Dependent Systems. *Phys. Rev. Lett.* **52**, 997–1000 (1984).
19. Bertsch, G. F., Iwata, J. I., Rubio, A. & Yabana, K. Real-space, real-time method for the dielectric function. *Phys. Rev. B* **62**, 7998–8002 (2000).
20. Alonso, J. L. *et al.* Efficient Formalism for Large-Scale *Ab Initio* Molecular Dynamics based on Time-Dependent Density Functional Theory. *Physical Review Letters* **101**, 096403 (2008).
21. Alvarado, F., Bari, S., Hoekstra, R. & Schlathölter, T. Interactions of neutral and singly charged keV atomic particles with gas-phase adenine molecules. *The Journal of Chemical Physics* **127**, 034301 (2007).

22. Brédy, R. *et al.* Fragmentation of adenine under energy control. *The Journal of Chemical Physics* **130**, 114305 (2009).
23. van der Burgt, P. J. M., Finnegan, S. & Eden, S. Electron impact fragmentation of adenine: partial ionization cross sections for positive fragments. *The European Physical Journal D* **69**, 173 (2015).
24. Cucinotta, C. S., Hughes, D. & Ballone, P. Real-time real-space TD-DFT for atoms: Benchmark computations on a nonspherical logarithmic grid. *Phys. Rev. B* **86**, 045114 (2012).
25. Perfetto, E. & Stefanucci, G. CHEERS: a tool for correlated hole-electron evolution from real-time simulations. *Journal of Physics: Condensed Matter* **30**, 465901 (2018).
26. Covito, F., Perfetto, E., Rubio, A. & Stefanucci, G. Real-time dynamics of auger wave packets and decays in ultrafast charge migration processes. *Physical Review A* **97**, 061401 (2018).

Funding F.Ca. acknowledges support from the European Research Council under the ERC-2014-StG STARLIGHT (Grant Agreement No. 637756). F.L. and V.W. acknowledge the Fonds de recherche du Québec - Nature et technologies (FRQNT) and the National Science and Engineering Research Council (NSERC). V.W. acknowledges support from the Vanier Canada Graduate Scholarship (Vanier CGS) program. S. L. acknowledges support from the Alexander von Humboldt foundation. A. R. acknowledge financial support from the European Research Council(ERC-2015-AdG-694097). The Flatiron Institute is a division of the Simons Foundation. G.S. and E.P. acknowledge EC funding through the RISE Co-ExAN (Grant No. GA644076), the European Union project MaX Materials design at the eXascale H2020- EINFRA-2015-1, Grant Agreement No. 676598, Nanoscience Foundries and Fine Analysis-Europe H2020-INFRAIA-2014-2015, Grant Agreement No. 654360 and Tor Vergata University for financial support through the Mission Sustainability Project 2DUTOPI. J. B. G. acknowledge support from the EPSRC (UK) grant number EP/M001644/1.

Author contributions S.L., E.P, G.S., L.P., F.L., M.N., A.R. and F.Ca. supervised the project. E.M., V.W., M.G. and M.C. performed the measurements, with resource contributions from F.F. and J.G. S.L., F.Co., E.P. and G.S. performed the simulations. E.M., S.L., F.Co., H.H., U.D., A.T. and F.Ca. wrote the manuscript.

Competing interests The authors declare no competing interests.

Supplementary information is available online. (Supplementary Text, Figures S1 to S18, Tables S1 to S2 and References 27–49.)

Correspondence and requests for materials should be addressed to F.Ca.

Laser-assisted ionisation of adenine as a protection mechanism against radiation damage: Supplementary Information

Erik P. Månsson, Simone Latini, Fabio Covito, Vincent Wanie, Mara Galli, Enrico Perfetto, Gianluca Stefanucci, Hannes Hübener, Umberto De Giovannini, Mattea C. Castrovilli, Andrea Trabattoni, Fabio Frassetto, Luca Poletto, Jason B. Greenwood, Francois Légaré, Mauro Nisoli, Angel Rubio and Francesca Calegari

This PDF file includes: Supplementary Text, Figures S1 to S18, Tables S1 to S2 and References 27–49.

I. EXPERIMENT

1. Experimental set-up and data acquisition

Carrier-envelope-phase stable laser pulses with 4 fs duration, 2.5 mJ energy and a central wavelength of approximately 750 nm are used to drive the attosecond pump-probe setup^{7,27,28}. The beamline is based on a Mach-Zehnder-type interferometer where one arm (70 % of the initial energy) is used for XUV generation while the other arm provides the NIR probe pulse at adjustable delays. Collinear recombination of the two beams is achieved with a drilled mirror reflecting the IR and transmitting the XUV in the central hole. Sub-300 as XUV pulses are generated in krypton or xenon (depending on the desired cut-off energy) by polarisation gating¹⁴. A typical spectrum generated in krypton is shown in Figure S1. A 100-nm-thick aluminium filter is used to remove the residual NIR (as well as harmonics below 15 eV) from the XUV arm. The attosecond interferometer is actively delay-stabilised with a residual RMS of 20 as.

Adenine powder (Sigma-Aldrich, >99 %) is evaporated at 463 K in a resistively heated stainless steel oven with a flow of helium acting as carrier and buffer cooling gas. According to vibrational spectroscopy on adenine from a similar source, the lowest-energy tautomer (9H amino) dominates²⁹. The jet passes through a 1-mm

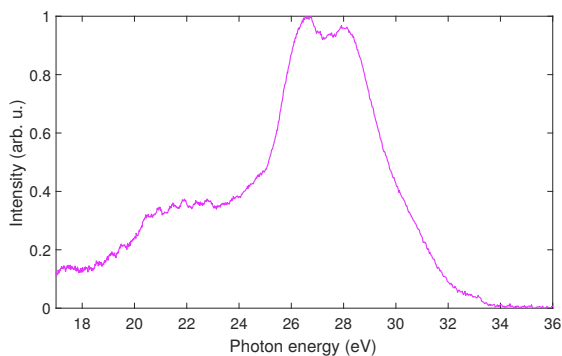


Figure S1. XUV spectrum of isolated attosecond pulse generated in krypton.

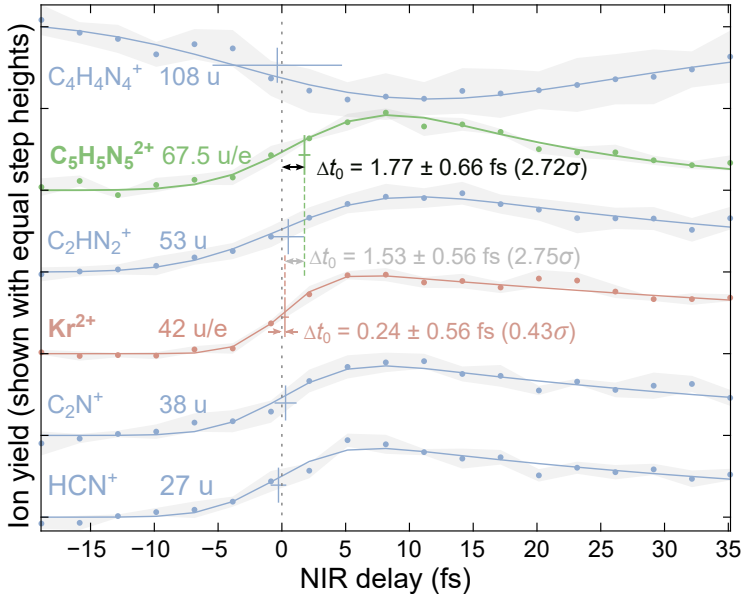


Figure S2. Pump-probe scan with Kr^{2+} (42 u/e) as atomic time reference. Three Δt_0 parameters, extracted using the first fitting procedure described in the previous section, are displayed: the difference between Ade^{2+} and the reference cations (black text), the difference between Ade^{2+} and Kr^{2+} (grey text) and the difference between Kr^{2+} and the reference cations (red text). Ade^{2+} is significantly delayed while the cationic fragments are simultaneous with the Kr^{2+} reference.

diameter skimmer and down to the optical interaction region of a standard velocity map imaging spectrometer³⁰ operated as a time of flight mass spectrometer. The voltages of the microchannel plate (MCP) and phosphor screen are gated to avoid detecting the helium gas at short times of flight.

Pump-probe data were acquired by scanning the delay in alternating directions over multiple traces (7 in the main dataset used, 5 for the atomic time reference scan). Each trace was normalised to the total yield to account for a slow sample depletion. These multiple traces have been used to calculate the errorbars shown for the experimental signal, as a shaded grey area in Fig. 2 and Figure S2.

2. Residual gas removal for Fig. 1

Since fragment H_2CN^+ has the same molecular mass as nitrogen gas (28 u/e) we show in Fig. 1 of the main article a mass spectrum where any residual gas background was removed using the following generic technique. The technique requires two mass spectra, $y_{\text{full}}(m)$ and $y_{\text{reduced}}(m)$, to be recorded with identical conditions (e.g. XUV spectrum and residual gas density) but with different density of the adenine sample, achieved by changing the oven temperature. We use a scaling factor $0 < x < 1$ to represent the remaining adenine density in y_{reduced} with respect to the full density in y_{full} :

$$\begin{cases} y_{\text{full}}(m) &= y_{\text{background}}(m) + y_{\text{sample}}(m) \\ y_{\text{reduced}}(m) &= y_{\text{background}}(m) + x y_{\text{sample}}(m) \end{cases} \quad (1)$$

To determine the scaling factor, a region of the mass spectrum is defined as background-free, e.g. the region covering the parent cation. Solving equation (1) for x in the background-free region, where $y_{\text{background}}(m) =$

$0, m \in M_{\text{parent}}$, gives

$$x = \frac{\sum_{m \in M_{\text{parent}}} y_{\text{reduced}}(m)}{\sum_{m \in M_{\text{parent}}} y_{\text{full}}(m)} \quad (2)$$

$$y_{\text{background}}(m) = \frac{y_{\text{reduced}}(m) - x y_{\text{full}}(m)}{1 - x} \quad (3)$$

$$y_{\text{sample}}(m) = y_{\text{full}}(m) - y_{\text{background}}(m) \quad (4)$$

As the separation is based on the difference between two mass spectra, the output contains some noise and artefacts. A simple correction that was made was to require both the background and sample signals to be non-negative. After evaluating (3), $y_{\text{background}}$ is updated at individual mass/charge-bins m to ensure that $0 \leq y_{\text{background}}(m) \leq y_{\text{full}}(m)$. The latter inequality ensures that also the final y_{sample} remains non-negative when computed as in (4).

The resulting separated adenine and background mass spectra are shown in Figure S3 for masses above 20 u/e. In this range, the adenine mass spectrum consists of 81% fragments and 19% parent cation.

The background gas removal procedure was not applied to pump-probe data, as it was introduced for the unique purpose of estimating the total fragment yield.

3. Adenine dication formation as a function of the XUV photon energy

We show that the stable adenine dication yield is maximised when the NIR probe pulse is sent at a small but nonzero delay after the XUV pump. As a complement to the delay-dependence curves of individual ions in Fig. 2 we show mass spectra at negative and positive NIR delay in Figure S4, together with the XUV-only case.

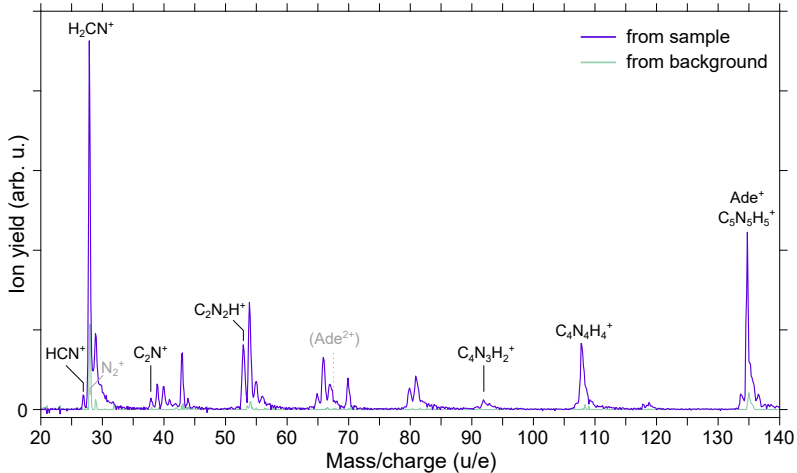


Figure S3. Separation of background and adenine contributions to the mass XUV-spectrum. Of the raw peak at 28 u/e, 16% was deduced to be N_2^+ from the background instead of HCNH^+ from adenine. The dotted line indicates where Ade^{2+} would appear (67.5 u/e), but it is essentially absent when no NIR photon is present (compare Figure S4).

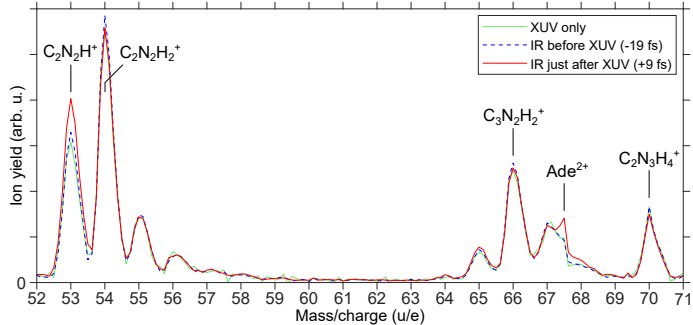


Figure S4. Appearance of the adenine dication. Zoom-in on the mass spectrum where the dication clearly appears at a small positive NIR delay but is negligible by the XUV alone or with the NIR at a negative delay.

Since sending the NIR pulse before the XUV pulse gives the same result as the XUV only case, we conclude that there is no NIR-pump–XUV-probe contribution.

At 67.5 u/e, where the dication appears, there is also a background contribution due to the width of the adjacent fragment at 67 u/e. Since the unambiguous part of the 67 u/e peak shows no delay-dependence, this additional constant background will not have any influence on the results concerning delay-dependence (such as Fig. 2). Estimating the absolute yield of the dication, however, requires the background to be subtracted. From the perturbed curve shape, we estimated a 0.2 % production of adenine dication with XUV only, which we consider almost negligible.

In Figure S5 we examine the effect of limiting the XUV photon energy on the pump–probe dynamics. The three panels show the NIR-induced change in the yields of the two cationic fragments with the largest (absolute) change as well as the adenine dication. Solid lines correspond to the normal case where the XUV photon energy of the attosecond pulses extends from 17 to 35 eV, employing XUV generation in Kr and an aluminium filter. Dotted lines show a scan where the XUV generated in Xe is limited to photon energies below 17 eV by an indium filter (about 5.2 eV below the dication ground state). In this last case, the absorption of one XUV photon and a few NIR photons is not able to produce any stable dication. Consequently, we could conclude that population of the special state (identified as responsible of the stabilisation process) can be only observed if ionisation occurs using the higher-energy part of the XUV spectrum. We also note that with the reduced cut-off, many fragments disappear, even the largest NIR-induced absolute step for the 53 u/e fragment. For 108 u/e there may still be a negative step, but close to the noise level.

4. Number of NIR photons required to observe a stable dication

A sequence of short scans were made over a range of NIR intensities from 7×10^{12} to 1.4×10^{13} W/cm² to estimate the number of NIR-photons driving the XUV+NIR process that produces each ion. We first extracted the step height, h_m , of the pump-probe signal for each ion (at mass/charge) at different NIR intensities. We then fitted the NIR intensity dependent data with the power law $h_m(I) = (c_m I)^{n_m}$, where I represents the laser intensity and n_m represents the number of NIR-photons driving the process in addition to the single XUV photon (see top panels of Figure S6). We acknowledge that there is some uncertainty (possibly 25 %) in the absolute NIR intensities in Figure S6, but a linear rescaling of the intensities would not affect the determination of the nonlinearity order n_m , only the yield coefficient c_m .

The results of the fitting procedure are reported in the bottom panel of Figure S6: the step heights of the small fragments scale approximately linearly while the adenine dication’s step height scales approximately quadratically with the NIR intensity. This result suggests that 2 NIR probe photons are required to doubly ionising adenine and stabilise it.

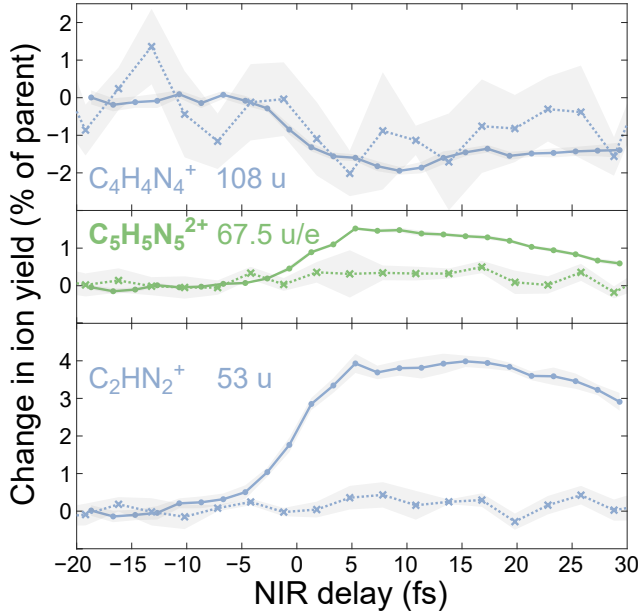


Figure S5. Pump-probe results for different XUV photon energies. Pump-probe scan signals are shown in solid lines for the main scan (35 eV cut-off) and dotted lines for indium-filtered HHG from xenon (17 eV cut-off).

5. Fitting of the pump-probe signals

When an initial state populates the probed state at rate $1/\tau_1$, and the probed state decays with the rate $1/\tau_2$, the general solution to the rate equations allows the population of the probed state to be expressed as:

$$N(t) = \begin{cases} N_1 \frac{1}{1-\tau_1/\tau_2} (e^{-t/\tau_2} - e^{-t/\tau_1}) & , t > 0 \\ 0 & , t < 0 \end{cases} \quad (5)$$

under the condition that $0 \leq \tau_1 < \tau_2$, i.e. the state population will rise to a positive peak and then decay. Here, t is the pump-probe delay axis of the scan, positive when the NIR pulse comes after the XUV attosecond pulse. An arbitrary coefficient N_1 is included for generality.

To model experimental pump-probe scans, the population function should be convoluted with an instrument response function and the temporal overlap of the XUV and NIR pulses needs to be defined with a t_0 -parameter. We allow for a constant background level b and name the step height parameter h . Since convolution is a linear operation, we can convolve the two terms in (5) separately and express the complete curve model as

$$f(t) = b + \frac{h}{1 - \tau_1/\tau_2} (g_{\tau_2}(t - t_0) - g_{\tau_1}(t - t_0)). \quad (6)$$

Here, $g_\tau(t)$ represents the convolution of a single exponentially decaying step function with a Gaussian instrument response function³¹ of full-width at half-maximum $W = 2\sqrt{2 \ln 2} \sigma_{\text{IRF}}$. The convolution is evaluated using

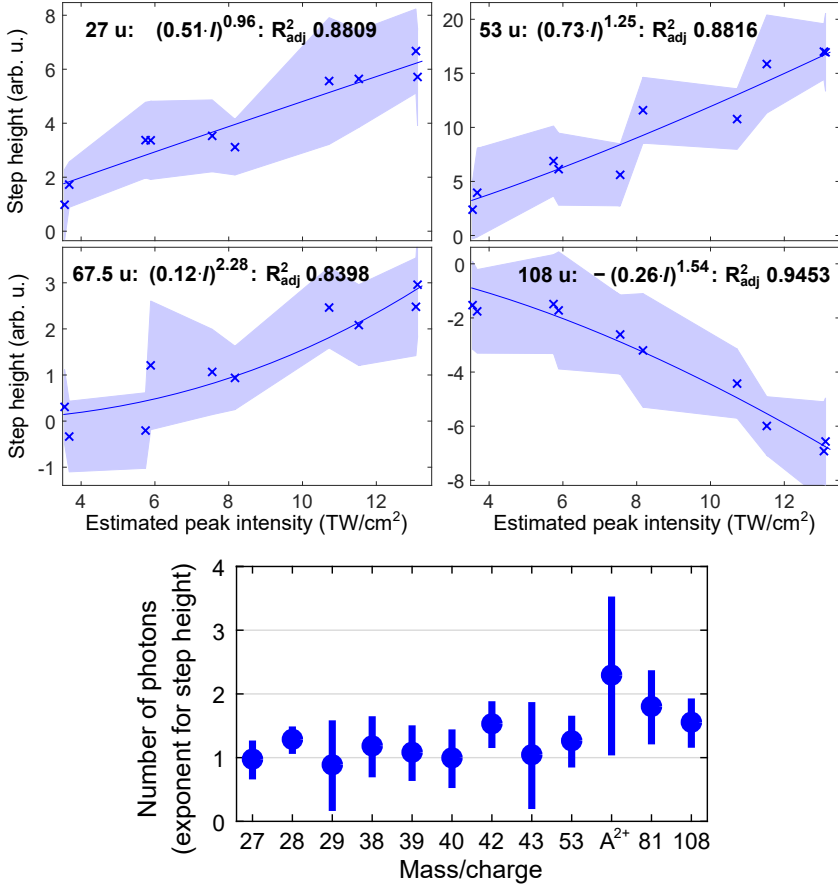


Figure S6. Scaling of step heights with NIR-intensity. The delay-dependent step height scales linearly with NIR-intensity for several small fragments but approximately quadratically for the adenine dication.

the expression³²

$$g_{\tau}(t) = \frac{1}{2} \operatorname{erfc} \left(\frac{\sigma_{\text{IRF}}}{\tau\sqrt{2}} - \frac{t}{\sigma_{\text{IRF}}\sqrt{2}} \right) \times \exp(-t/\tau + \sigma_{\text{IRF}}^2/(2\tau^2)) \quad (7)$$

and normalized ($\int_{-\infty}^{\infty} g_{\tau}(t) dt = \tau$) such that the step height before convolution is 1. For an initial overview, we employed the simplest possible scheme where separate fits were made for each ion, with independent values for t_0 and W , and with simple step functions ($\tau_1 = 0$). From the result in Figure S7(a), it is clear that a later t_0 -parameter is needed for the dication. We compute $\Delta t_0 = t_0(\text{Ad}^{2+}) - t_0(\text{reference cations}) = 1.82 \pm 0.33$ fs. A classical time-difference like Δt_0 is however not physically meaningful. To obtain a result which can be compared with the theoretically extracted shake-up time, we introduced a risetime of the adenine dication signal, by using a variable τ_1 in the function for Ade²⁺. The t_0 -parameter is now common for all ions and defines the zero of the NIR-delay axis, and for robustness we use a common W -parameter and perform a global fit of all the shown

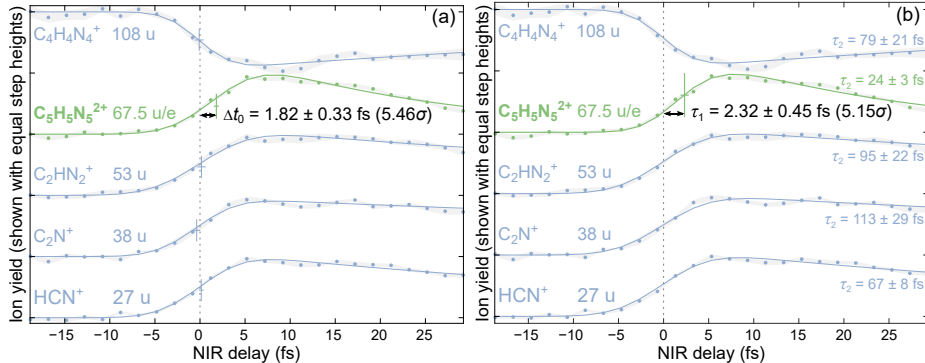


Figure S7. Pump–probe scan fitted using different approaches. (a) Simple step functions (having $\tau_1 = 0$) at individually variable t_0 were fitted without constraints. We find that the adenine dication ($\text{C}_5\text{H}_5\text{N}_5^{2+}$, 67.5 u/e) has a distinct delay with respect to the weighted t_0 -average of the cationic fragments, and show the NIR-delay axis relative to the cation average. (b) To obtain the more theoretically meaningful risetime of the adenine dication signal, τ_1 was included in the function for the dication. The t_0 -parameter is now common for all ions and defines the zero of the NIR-delay axis, and for robustness we use a common W -parameter fitted to 9.9 ± 0.5 fs. The dication and the 108 u/e fragment were assigned as 2-photon processes for the best fit (in agreement with section I 4), meaning that their Gaussian width was $W/\sqrt{2}$ instead of W . Panel (b) corresponds to Fig. 2 in the main article.

ions. The dication and the 108 u/e fragment were assigned as 2-photon processes for the best fit (in agreement with section I 4), meaning that their Gaussian width was $W/\sqrt{2}$ instead of W since a *two*-photon signal scales with the *square* of NIR intensity envelope. The results in Figure S7(b) show a significantly nonzero risetime for the dication $\tau_1 = 2.32 \pm 0.45$ fs, which we can now compare to the theoretically extracted shake-up time (see main text).

6. Verification of zero time delay

In our main analysis we discuss the delay of the adenine dication under the assumption that the steps of many cations occur directly at the temporal overlap of XUV and NIR pulses. Although this is the natural assumption when so many fragments appear synchronised, one could still speculate that some common molecular motion is required before the NIR probe influences any cation fragment yield, shifting all steps to a positive NIR delay. To rule this possibility out, we performed another experiment where a small amount of the atomic gas krypton was simultaneously injected into the vacuum chamber with adenine. The Kr^{2+} yield in Figure S2 exhibits a sharp step (2-photon process meaning width parameter $W/\sqrt{2}$) for which any molecular dynamics can be excluded. For simplicity, we used only the first fitting procedure described in the previous section to extract a t_0 -parameter for Kr^{2+} to be compared with the other cationic fragments. The results of the fitting are shown in Figure S2. We find that the Kr^{2+} step almost coincides with the steps for the adenine fragments and that Ade^{2+} is the only significantly delayed ion.

II. THEORY

1. Equilibrium Properties

Ground state ab-initio characterisation of the Adenine molecule (sketched in Fig. S8) has shown that if the geometry is allowed to relax, it is possible to find a stable molecule both for the singly and doubly ionised state. The effect of the geometry relaxation on the charged states of Adenine is relatively small as it can be seen from Fig. S9 for the singly (a) and doubly (b) ionised case. In such a figure, we report the relative variation

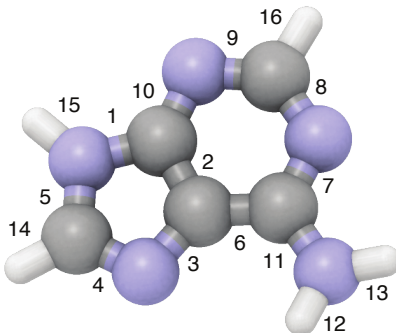


Figure S8. Adenine molecule bond numbering

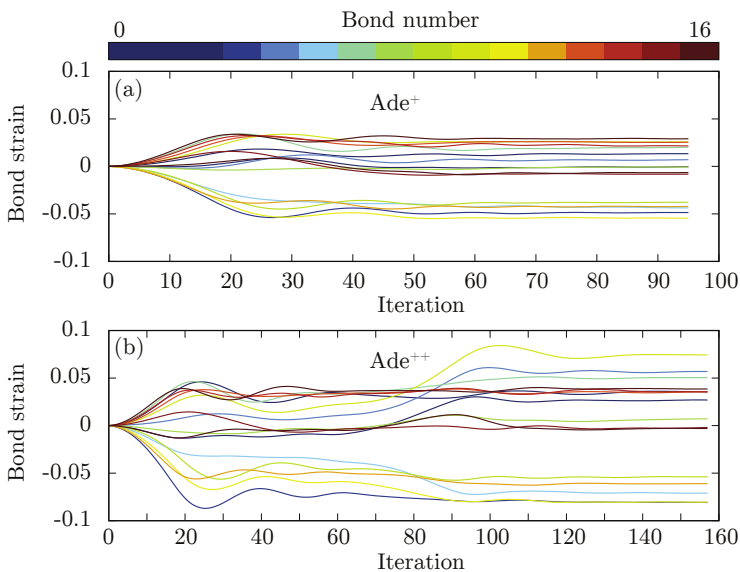


Figure S9. Geometry relaxation. relative variation of the bond length as a function of the optimisation steps for singly (a) and doubly (b) ionised adenine. The reference bond length is the one for the neutral state.

(with respect to the optimised neutral structure) of the bond lengths at each optimisation step. To quantify the importance of geometry relaxation in the stabilisation of ionised adenine, we evaluated the total energy difference of singly (Ade^+) and doubly charged (Ade^{2+}) state with respect to the neutral (Ade) state. The values are reported in Tab. S1 for the unrelaxed and relaxed structures. We can infer that the minimum energy that the XUV+IR pulses have to transfer to the system in order to reach the stable dication state is ~ 15 eV, which is in agreement with the experimental observation that the stabilisation is not observed if the high energy part of the XUV spectrum is filtered out.

The calculations have been performed with the Octopus code³³ within a DFT framework where a PBE functional has been used. A grid spacing of $h = 0.28$ Bohr has been used for the simulations.

To reproduce the first ionisation energy of adenine reported in the experimental literature of 8.48 eV³⁴ we applied the so called averaged density self-interaction correction (ADSIC)³⁵ which corrects the Coulomb potential tails poorly described by the PBE functional. As it can be noted from Tab. S2 the ionisation energy (which according to Koopman’s theorem is equivalent to the energy of the HOMO) calculated with the SIC gets much closer to the experimental one compared to the uncorrected one. For the following results all the calculations are performed with the PBE-SIC functional.

2. Spontaneous Fragmentation

In this section we demonstrate that ionised adenine is not stable if the molecule is not allowed to dissipate energy after ionisation. For such a proof we perform a sudden single and double ionisation and we let the electronic and nuclear system propagate in time by means of TDDFT+Ehrenfest dynamics^{20,36}. In our calculations, the removal of electrons is orbital specific, in Fig. S10(a) we show the bond length dynamics for singly ionised adenine where the electron has been suddenly removed at the beginning of the time propagation from a given orbital. In all the outer valence orbitals investigated the ionisation leads to bond breaking. For completeness in Fig. S10(b) we also report the bond breaking dynamics in the case adenine is doubly ionised by removing 2 electrons from the HOMO. As expected, the bond rupture is faster in this case.

We conclude that the adenine molecule, in order to reach a stable ionised form has to relax the energy by means of internal relaxation processes which transfer the excess energy to the outgoing ionised electrons.

3. Modelling the internal relaxation processes with rate equations

a. Shake-up matrix elements

Owing to electron-electron correlation an ionised system can undergo an electronic rearrangement, in which previously unoccupied bound states become populated through a so called shake-up process, which is depicted in the central panel of Fig. S11.

Driven by Coulomb interaction, the electron in ϕ_m fills the hole in ϕ_c and transfers the energy to the electron in ϕ_n which is then excited to the state ϕ_i . Overall, the shake-up process has to conserve energy, i.e. $\epsilon_i - \epsilon_n = \epsilon_m - \epsilon_c$. Here we are interested in calculating the rate for such a process for the adenine molecule following XUV photoionisation. Using Fermi’s golden rule such a rate is given by:

$$W_{FI} = 2\pi |\langle \Psi_F | \hat{V}_C | \Psi_I \rangle|^2 \delta(\epsilon_F - \epsilon_I). \quad (8)$$

where Ψ_I and Ψ_F are the initial and final many-body wavefunctions, \hat{V}_C the Coulomb interaction operator and the Dirac delta ensures energy conservation. Let us first restrict our analysis to the four specific single particle states $\phi_c, \phi_m, \phi_n, \phi_i$. In such a basis, the Coulomb interaction, that we consider as the perturbation that drives

Table S1. Ground State Energy differences

$E^{1+} - E^0$ (eV)	$E^{2+} - E^0$ (eV)	$E_{\text{rel}}^{1+} - E^0$ (eV)	$E_{\text{rel}}^{2+} - E^0$ (eV)
8.17	22.21	1.88	14.99

Table S2. Homo energies PBE and PBE+ADSIC

$\epsilon_{\text{H}}^{\text{PBE}}$ (eV)	$\epsilon_{\text{H}}^{\text{PBE+ADSIC}}$ (eV)
-5.57	-7.40

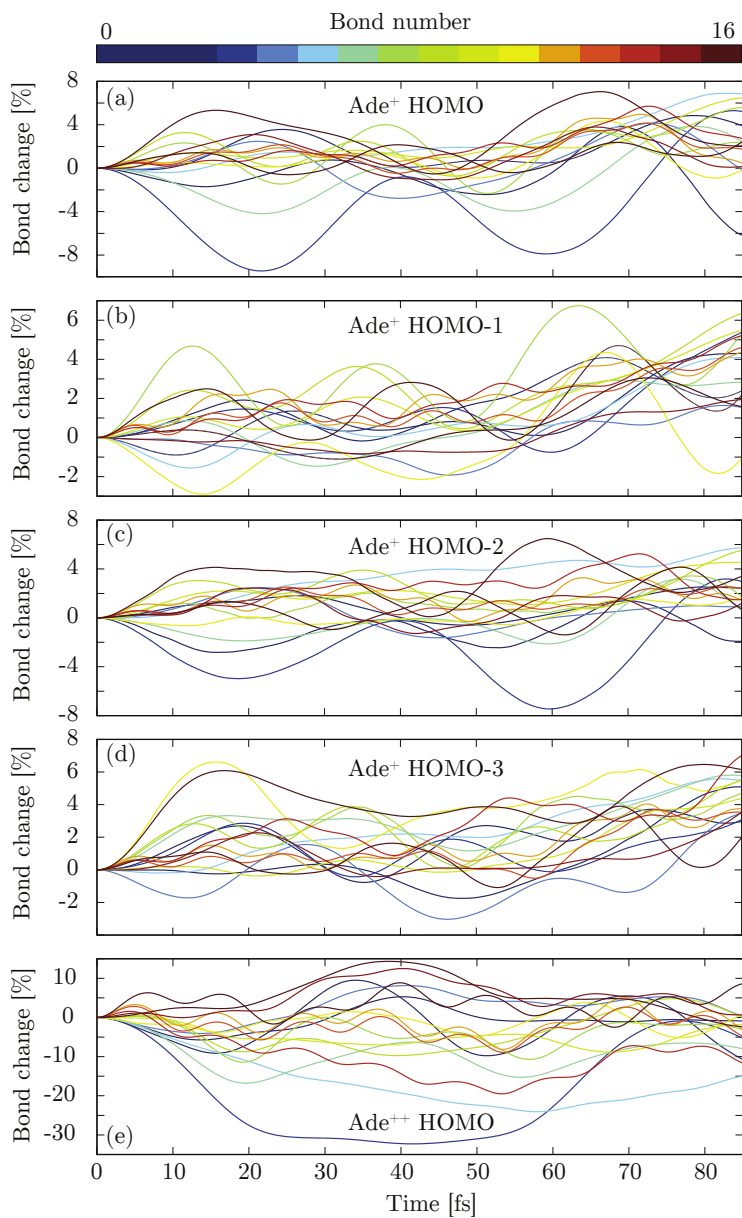


Figure S10. Bond length variations following sudden Ionisation with TDDFT. Adenine cations are time propagated following a sudden removal of an electron from different orbitals of the cation Ade⁺, (a) HOMO, (b) HOMO-1, (c) HOMO-2, (d) HOMO-3 and two electrons from the HOMO (d). In all situations appears that sudden ionisation leads to fragmentation if no dissipative process occurs.

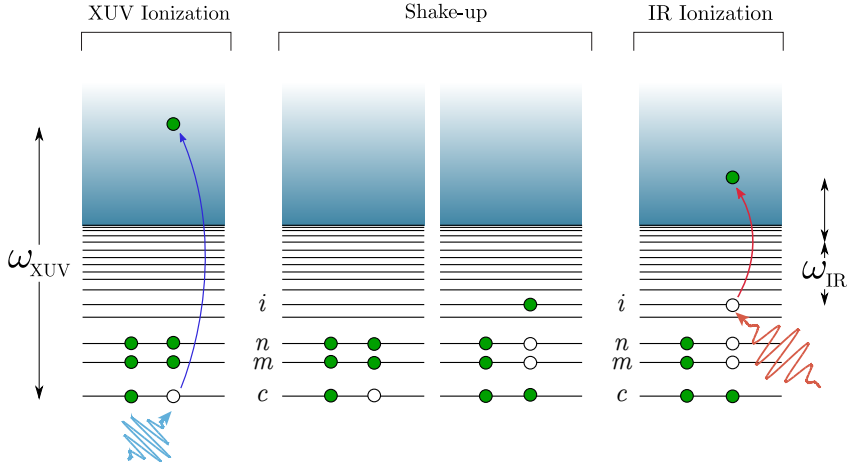


Figure S11. Three step model for stabilisation-by-ionisation. The molecule is ionised by the XUV pulse leaving it with hole in the core state c . During the shake-up process, this core-hole moves up to the valence region, through the excitation of an electron from the occupied level $n(m)$ to the unoccupied level i and the refilling of the core hole by an electron from level $m(n)$. Finally the IR pulse ionises an electron from this excited level, leaving the molecule doubly ionised.

the shake-up, can be written (in second quantization) as:

$$\hat{V}_{mn}^C = \frac{1}{2} \sum_{\sigma\sigma' \in \{\uparrow\downarrow\}} \left\{ v_{cimn} c_{c\sigma}^\dagger c_{i\sigma'}^\dagger c_{m\sigma'} c_{n\sigma} + v_{icmn} c_{i\sigma}^\dagger c_{c\sigma'}^\dagger c_{m\sigma'} c_{n\sigma} + h.c. \right\}, \quad (9)$$

where we have defined the Coulomb integrals as:

$$v_{ijmn} = \int d\mathbf{r} d\mathbf{r}' \phi_i^*(\mathbf{r}) \phi_j^*(\mathbf{r}') \frac{1}{|\mathbf{r} - \mathbf{r}'|} \phi_m(\mathbf{r}') \phi_n(\mathbf{r}). \quad (10)$$

In our picture, the initial state of a shake-up process is the one resulting from the XUV photo-ionisation and, without loss of generality, we choose it to be $|\Psi_I\rangle = c_{n\uparrow} |\Psi_0\rangle$, with $|\Psi_0\rangle$ consisting of doubly occupied i, m and n orbitals. The application of the Coulomb perturbation on such an initial state can be evaluated as follows:

$$\begin{aligned} \hat{V}_{mn}^C |\Psi_I\rangle &= \frac{1}{2} \sum_{\sigma\sigma' \in \{\uparrow\downarrow\}} \left\{ v_{cimn} c_{c\sigma}^\dagger c_{i\sigma'}^\dagger c_{m\sigma'} c_{n\sigma} + v_{icmn} c_{i\sigma}^\dagger c_{c\sigma'}^\dagger c_{m\sigma'} c_{n\sigma} + h.c. \right\} c_{n\uparrow} |\Psi_0\rangle \\ &= \frac{1}{2} \sum_{\sigma \in \{\uparrow\downarrow\}} \left\{ v_{cimn} c_{i\sigma}^\dagger c_{c\uparrow}^\dagger c_{n\uparrow} c_{m\sigma} + v_{icmn} c_{i\sigma}^\dagger c_{c\uparrow}^\dagger c_{m\uparrow} c_{n\sigma} \right\} c_{n\uparrow} |\Psi_0\rangle \end{aligned} \quad (11)$$

where the h.c. does not contribute because it contains terms of the type $c_{m\sigma}^\dagger c_{n\sigma'}^\dagger$. Knowing the result of the Coulomb operator on the initial state and assuming the final state to be $|\Psi_F\rangle = |\Psi_i^{mn}\rangle = c_{i\uparrow}^\dagger c_{m\uparrow} c_{n\uparrow} |\Psi_0\rangle$ (again, without loss of generality) we can apply the Fermi golden rule in Eq. (8) and write:

$$R_{imnc}^{\text{Sh-up}} = \frac{\pi}{2} |v_{icmn} + v_{cimn}|^2 \delta(\epsilon_i - \epsilon_n - (\epsilon_m - \epsilon_c)) \quad (12)$$

In general for a given initial core-hole state c and a final occupied excited state i there might be several m and n state combinations compatible with the shake-up process. For this reason the rate of the shake-up independent of the orbital localization of the two final holes is given by:

$$R_{ic}^{\text{Sh-up}} = \frac{\pi}{2} \sum_{n \geq m} |v_{icmn} + v_{cimn}|^2 \delta(\epsilon_i - \epsilon_n - (\epsilon_m - \epsilon_c)). \quad (13)$$

Note that we restricted the sum to $n \geq m$ to avoid the double counting that would arise from the fact that the holes are identical. For practical purposes the delta function in the formula above is replaced by a Lorentzian, $L_{\epsilon_j}^{\gamma_j}(\omega) = \frac{1}{2\pi} \frac{\gamma_j}{(\omega - \epsilon_j)^2 + (\gamma_j/2)^2}$, as follows:

$$R_{ic}^{\text{Sh-up}} = \frac{\pi}{2} \sum_{n \geq m} |v_{icmn} + v_{cimn}|^2 L_{\epsilon_m + \epsilon_n - \epsilon_i - \epsilon_c}^{\eta}(\omega = 0), \quad (14)$$

where the width η enters as a parameter.

b. Ionisation rate: Evaluating orbital dependent cross-sections

The initial state in the shake-up process is created by the XUV pulse (see leftmost panel of Fig. S11) and the probability of creating the initial hole in a state ϕ_i is determined by the XUV photoionisation probability of such a state which is given by:

$$\begin{aligned} P_i^{\text{Ion}}(\omega) &= 2\pi n_{\text{spin}} \sum_{\mathbf{k}} |\langle \phi_{\mathbf{k}} | e^{i\mathbf{q} \cdot \hat{\mathbf{r}}} | \phi_i \rangle|^2 \delta(\omega - (\epsilon_{\mathbf{k}} - \epsilon_i)) \\ &= \frac{2\pi}{V} \sum_{\mathbf{k}} \left| \int d\mathbf{r} e^{i(\mathbf{k} + \mathbf{q}) \cdot \mathbf{r}} \phi_i(\mathbf{r}) \right|^2 \delta\left(\frac{k^2}{2} - (\omega + \epsilon_i)\right), \end{aligned} \quad (15)$$

where ω is the energy of the perturbation, $|\phi_{\mathbf{k}}\rangle$ the outgoing electron wavefunction, which in the second step we assume to be a plane wave, and $A_I e^{i\mathbf{q} \cdot \hat{\mathbf{r}}}$ the spatial component of the electromagnetic field. In the long wavelength limit ($\mathbf{q} \rightarrow 0$) we can recognize the Fourier transform of the wavefunction $\tilde{\phi}_i(\mathbf{k}) = \int d\mathbf{r} e^{i(\mathbf{k}) \cdot \mathbf{r}} \phi_i(\mathbf{r})$ and write:

$$P_i^{\text{Ion}}(\omega) = \frac{2\pi}{V} \sum_{\mathbf{k}} |\tilde{\phi}_{i\mathbf{k}}|^2 \delta\left(\frac{k^2}{2} - (\omega + \epsilon_i)\right). \quad (16)$$

Using this formula, we evaluated the orbital dependent ionisation probability for the 15 outer valence KS orbitals reported in Fig. S12(a).

By convoluting these photoionisation probabilities with an energy distribution function $f^{\text{XUV}}(\omega)$ for the XUV pulse, we can get the orbital resolved ionisation rate as:

$$R_c^{\text{XUV}} = \int d\omega f^{\text{XUV}}(\omega) P_c^{\text{Ion}}(\omega). \quad (17)$$

In our calculations we make the easiest assumption by choosing $f^{\text{XUV}}(\omega)$ as a stepwise window function between 19.5 and 30.5 eV (as in the experiment) and extract the time it takes for a given valence orbital to be fully ionised as the inverse of the ionisation rates, see Fig. S12(b).

c. The shake-up process and the characteristic time delay

We can finally combine the XUV photoionisation probability with the state resolved shake-up rates and get the characteristic shake-up times. More specifically the probability that an empty bound state gets populated

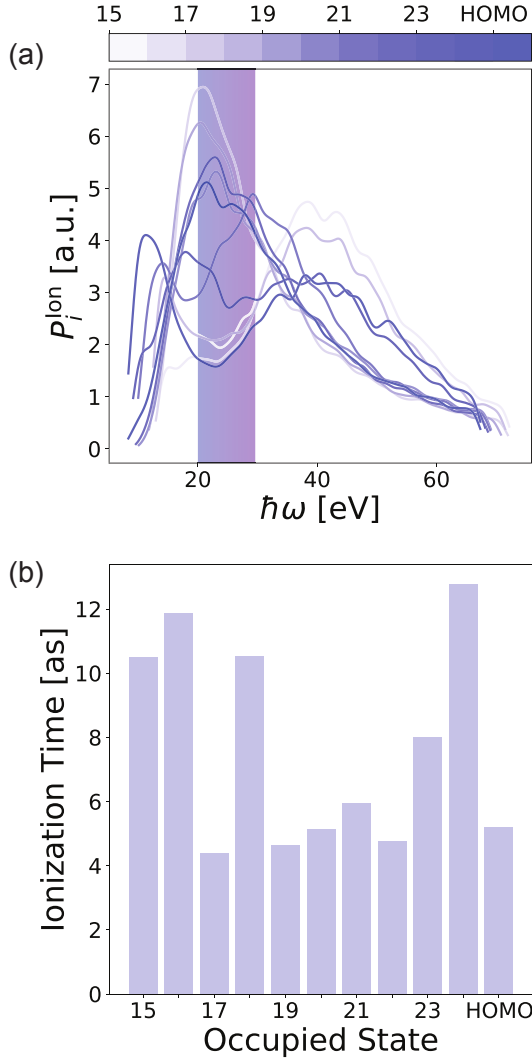


Figure S12. (a) XUV-photoionisation rate for the occupied orbitals calculated with Eq. (16). (b) Orbital dependent ionisation time calculated by integrating the curves in (a) within the XUV energy window.

by shake-up processes following XUV ionisation can be written as:

$$P_i^{\text{Sh-up}}(t) = 1 - e^{-R_i^{\text{tot}} t} \quad (18)$$

where the total rate is given by:

$$R_i^{\text{tot}} = \sum_c \left(1 - e^{-R_c^{\text{XUV}} T^{\text{XUV}}} \right) R_{ic}^{\text{Sh-up}} \quad (19)$$

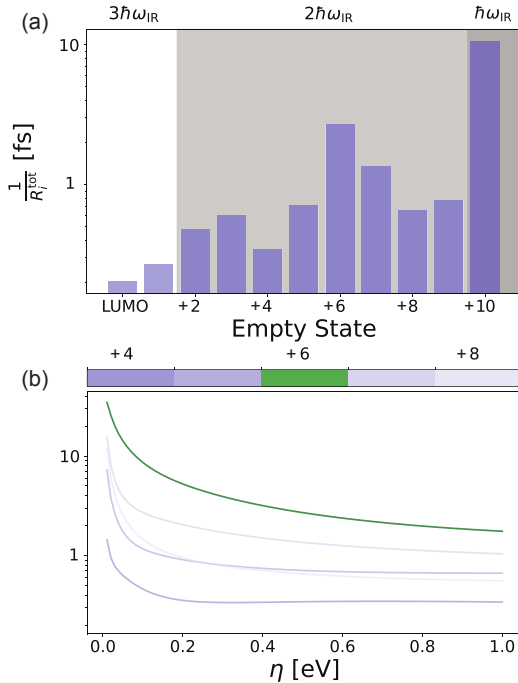


Figure S13. Shake-up rates for the first unoccupied orbitals: (a) Shake-up rates where the Dirac delta has been approximated by a Lorentzian with width $\eta = 0.1$ eV and a photoionisation time ($T_{\text{XUV}} = 100$ as). (b) Same rates as a function of the broadening parameter η .

i.e. the probability of having a hole in state c times the rate of shake-up towards a state i summed over all initial holes. The probability of creating initial holes takes into account the actual duration of the XUV pulse T^{XUV} .

In Fig. S13(a) we show the characteristic electronic shake-up times as reported in the main text. For more thorough validation of this result we computed the same quantities as a function of the artificial parameter η . These results are reported in Fig. S13(b) for the final empty states ionised with two IR photons and it is apparent that the variation of the characteristic times with respect to η is small for any $\eta > 0.1$ eV which is safe to assume considering typical quasiparticle lifetimes in molecules³⁷.

4. Non-equilibrium Green's Function approach

a. Theoretical description

In this section we discuss the details of the ab-initio real-time propagation presented in the main paper. We use the non-equilibrium Green's function (NEGF) formalism and solve numerically the Kadanoff-Baym equations (KBE's)^{38–40} within the Generalized Kadanoff-Baym Ansatz (GKBA)⁴¹. Within the GKBA the KBE's collapse into a single equation for the single-particle density matrix $\rho(t)$

$$\frac{d}{dt}\rho(t) + i[h_{\text{HF}}(t), \rho(t)] = -[I_{\text{corr}}(t) - I_{\text{ion}}(t) + \text{h.c.}]. \quad (20)$$

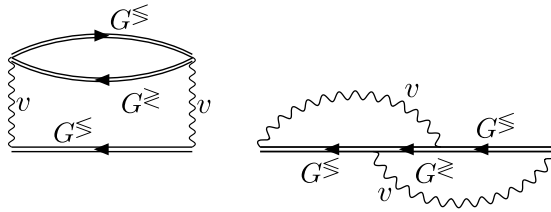


Figure S14. Diagrammatic representation of the second Born self-energy. The double line represents the Green's function G^S while the wiggly line represents the Coulomb interaction v .

The left-hand side contains the commutator between ρ and the time-dependent Hartree-Fock (HF) Hamiltonian

$$h_{\text{HF}}(t) = h_{\text{KS}} - V_{\text{Hxc}} + V_{\text{HF}}(t) + \mathcal{E}(t) \cdot \mathbf{d}, \quad (21)$$

where h_{KS} is the Kohn-Sham (KS) Hamiltonian, V_{Hxc} is the Hatree-exchange-correlation potential (both h_{KS} and V_{Hxc} are evaluated at the equilibrium KS density), $V_{\text{HF}}(t) = V_{\text{HF}}[\rho(t)]$ is the time-dependent HF potential, $\mathcal{E}(t)$ is the external pulse, and $\mathbf{d} = (d_x, d_y, d_z)$ is the molecular dipole vector. Correlation effects are included in the right-hand side of Eq. (20) via the *collision integral*

$$I_{\text{corr}}(t) = \int_0^t dt' [\Sigma_{\text{corr}}^>(t, t') G^<(t', t) - \Sigma_{\text{corr}}^<(t, t') G^>(t', t)], \quad (22)$$

where G^{\lessgtr} is the lesser (greater) non-equilibrium Green's function, and $\Sigma_{\text{corr}}^{\lessgtr}$ is the correlation lesser (greater) non-equilibrium self-energy. Here we approximate Σ_{corr} at the second Born (2B) level, see Fig. S14 for its diagrammatic representation. The GKBA consists in approximating the lesser and greater Green's functions as

$$G^<(t, t') = -G^R(t, t')\rho(t') + \rho(t)G^A(t, t'), \quad (23)$$

$$G^>(t, t') = G^R(t, t')\bar{\rho}(t') - \bar{\rho}(t)G^A(t, t'), \quad (24)$$

where $\bar{\rho}(t) = 1 - \rho(t)$ and

$$G^R(t, t') = [G^A(t', t)]^\dagger = -i\theta(t - t')T[e^{-i\int_{t'}^t d\bar{t} h_{\text{HF}}(\bar{t})}]. \quad (25)$$

The second term appearing on the right-hand side of Eq. (20) is the *ionisation integral*

$$I_{\text{ion}}(t) = \int_0^t dt' \Sigma_{\text{ion}}^>(t, t') G^<(t', t), \quad (26)$$

with $\Sigma_{\text{ion}}^>$ the ionisation self-energy. This term describes the excitation of bound electrons to continuum states occurring during the ionisation process induced by the pulse $\mathcal{E}(t)$.

The numerical solution of Eq. (20) with Σ_{corr} in the 2B approximation scales quadratically with the maximum propagation time. This favourable scaling (in comparison to the cubic scaling of the KBE) allows us to follow the dynamics of molecules with $\sim 10^2$ active electrons for tens of femtoseconds.

b. Computational method

In this section we discuss how Eq. (20) is practically solved to study the ultrafast electron dynamics of adenine after the action of a XUV pulse. We first obtain the KS ground state (GS) of the molecule using the Octopus

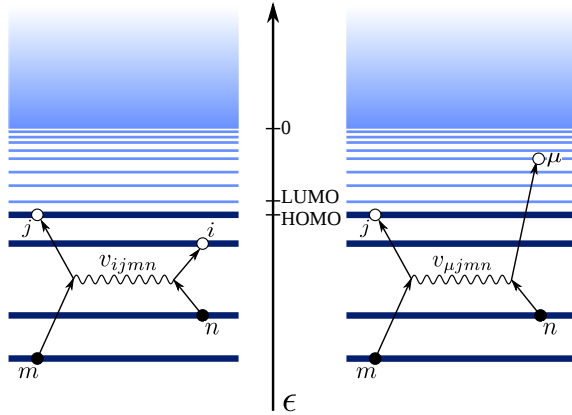


Figure S15. Schematic illustration of scattering processes. Left: scattering involving electrons in initially occupied states (labelled by roman indices). Right: shake-up scatterings leading to the transition of an electron in an initially unoccupied state (labeled by μ). The initially occupied and unoccupied states are represented by a dark blue and a light blue line, respectively. The shaded area represents the continuum – no scattering is considered in this area.

code³³, with HSCV pseudopotentials⁴², the PBE approximation for the exchange-correlation potential⁴³ and the averaged density self-interaction correction (ADSIC)³⁵. The grid is a sphere of radius 20 Bohr with spacing 0.25 Bohr. The lowest 57 KS orbitals are bound and constitute the *active space* to describe the molecular ρ . The remaining KS orbitals (with KS energy $\epsilon_k^{\text{KS}} > 0$) up to energies $\sim 41\text{eV}$ (about 3000 states) are instead used to build Σ_{ion} .

We then solve the equilibrium HF problem (with $\mathcal{E} = 0$) in the active space. Since correlation effects are typically weak in the ground state of biomolecules^{44–46}, we set $\rho(0) = \rho_{\text{HF}}$ as initial condition for Eq. (20). It is therefore convenient to work in the HF basis $\{\varphi_i^{\text{HF}}(\mathbf{r})\}$. In this basis the equilibrium HF Hamiltonian h_{HF} is diagonal and the 2B self-energy reads

$$\Sigma_{\text{corr},ij}^{\leq}(t,t') = \sum_{nmpqsr} v_{irpn}(2v_{mqsj} - v_{mqjs}) \times G_{nm}^{\leq}(t,t')G_{pq}^{\leq}(t,t')G_{sr}^{\leq}(t',t), \quad (27)$$

where the Coulomb integrals v_{irpn} are computed like in (10) with the HF basis functions. The correlation self-energy in Eq. (27) is numerically evaluated using the *dissection algorithm*⁴⁷ implemented in the CHEERS code⁴⁸. Additionally only those Coulomb integrals with at most one index above the HF-HOMO are retained, see Fig. S15. This amounts to including only shake-up processes for electrons visiting HF states initially unoccupied. A similar approximation has been recently used in the context of Auger decays⁴⁹, finding excellent agreement with Configuration Interaction calculations. The approximation reduces the number of Coulomb integrals involved in Σ_{corr} : from N_{tot}^4 , where $N_{\text{tot}} = 57$ is the dimension of the active space, to $N_{\text{occ}}^4 + 4N_{\text{occ}}^3(N_{\text{tot}} - N_{\text{occ}})$, where $N_{\text{occ}} = 27$ is the number of initially occupied states; hence about an order of magnitude less. Furthermore, $\rho(0) = \rho_{\text{HF}}$ is a stationary solution of Eq. (20) in the absence of external fields.

The ionisation self-energy in the HF basis reads

$$\Sigma_{\text{ion},ij}^>(t,t') = -i \sum_{k: \epsilon_k^{\text{KS}} > 0} [\mathcal{E}(t) \cdot \mathbf{d}_{ik}] e^{-i\epsilon_k^{\text{KS}}(t-t')} [\mathcal{E}(t') \cdot \mathbf{d}_{kj}], \quad (28)$$

where

$$\mathbf{d}_{ij} = \int d\mathbf{r} \varphi_i^{\text{HF}}(\mathbf{r}) \mathbf{r} \varphi_j^{\text{HF}}(\mathbf{r}), \quad (29)$$

and $\varepsilon_k^{\text{KS}} = \varepsilon_k^{\text{HF}}$ since we discard the Coulomb repulsion of HF electrons in the continuum. The main physical process left out by this further approximation is the Auger decay which, however, can be safely ignored for XUV pulses. We also emphasise that the ionisation self-energy in Eq. (28) is suitable only for single-photon ionisation processes (like the ones induced by the XUV pulse of the present experiment). The inclusion of multiphoton processes would lead to a different dependence of Σ_{ion} on \mathcal{E} .

The NEGF-GKBA Eq. (20) is solved numerically using the CHEERS code⁴⁸. From the single-particle density matrix we can easily calculate the time-dependent electronic density according to

$$n_{\text{el}}(\mathbf{r}, t) = \sum_{ij} \varphi_i^{\text{HF}}(\mathbf{r}) \rho_{ij}(t) \varphi_j^{\text{HF}}(\mathbf{r}). \quad (30)$$

c. Ionisation

In our simulations we have studied the electron dynamics of adenine under the influence of the experimental XUV laser pulse. The latter has a full-width at half-maximum of ~ 300 as and a central frequency of ~ 27 eV (see the inset of Fig. S16 for the temporal shape of the pulse and for its power spectrum). In Fig. S16 we show the time-dependent variation of the occupations $\delta n_i(t) = n_i(t) - n_i(0)$ of the bound KS orbitals $\{\varphi_i^{\text{KS}}\}$ during the ionisation process. The occupations $n_i(t)$ are obtained according to

$$n_i(t) = \sum_{mn} U_{im} \rho_{mn}(t) U_{ni}^\dagger, \quad (31)$$

where $U_{im} = \int d\mathbf{r} \varphi_i^{\text{KS}}(\mathbf{r}) \varphi_m^{\text{HF}}(\mathbf{r})$ is the change of basis transformation matrix.

The inspection of Fig. S16 shows that all initially occupied (unoccupied) KS states depopulate (populate) with superimposed oscillations following the cycles of the laser pulse. We point out that the initially unoccupied KS states get populated mainly through ultrafast shake-up processes. Longer timescale dynamics are discussed in the main paper.

d. Charge migration

As stated in the main text, the simulations reveal an inflation of the electron density of the molecule over time, caused by the population of the particular KS state LUMO+6 on a timescale compatible with the delay observed in the yield of stable adenine dication. The inflation indicates that the electrons move away from the molecule over time. Defining a slab around the molecular plane of thickness $d = 6 \text{ \AA}$ and integrating the electron density outside of this area, we have a measure of the molecular inflation. In Fig. S17 we show how this integrated electron density reflects the timescale of the inflation, as expected. The observed behaviour is consistent for different slab thicknesses. This effect is due to the population of the delocalised bound states, as reported in the main text, and in fact has the two characteristic time scales observed in the population of the initially unoccupied KS states, the slower one being the one associated with the delayed shake-up transition.

5. NIR-induced ionisation

To support the analysis on the role of the LUMO+6 state in the stabilisation dynamics of adenine we observe the behaviour of the system when the additional NIR pulse is introduced. In our simulation we have used a pulse with carrier frequency 1.7eV and \sin^2 envelope of total duration 200a.u. $\simeq 4.8$ fs. Of particular interest is the time-dependent occupation of the shake-up states as the NIR pulse acts on the system. In fig. S18 the total NIR-induced state depletion for the different shake-up states as a function of XUV-NIR delay is shown. These

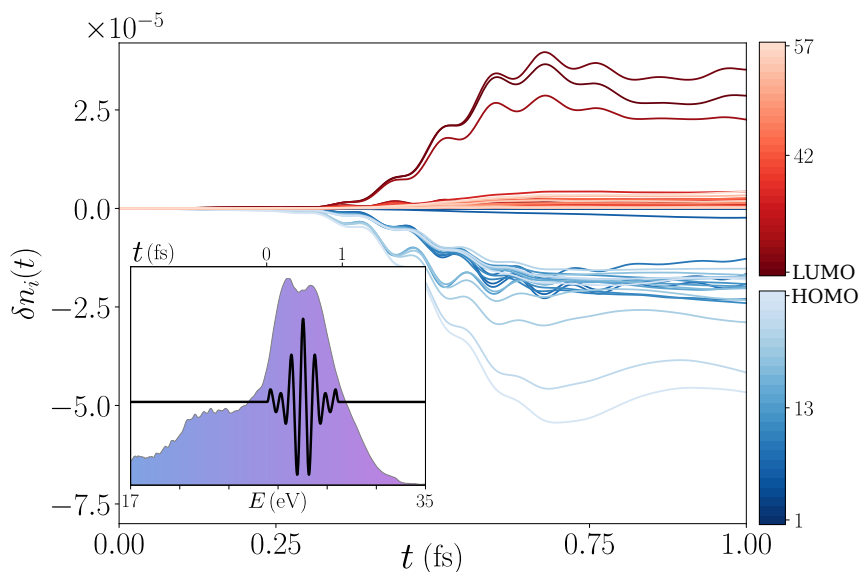


Figure S16. Time-dependent variation of the population. Change of the population of the occupied (blue) and unoccupied (red) bound KS states of adenine excited by the XUV pulse perpendicular to the plane of the molecule. The inset shows the spectrum and the temporal profile of the pump pulse.

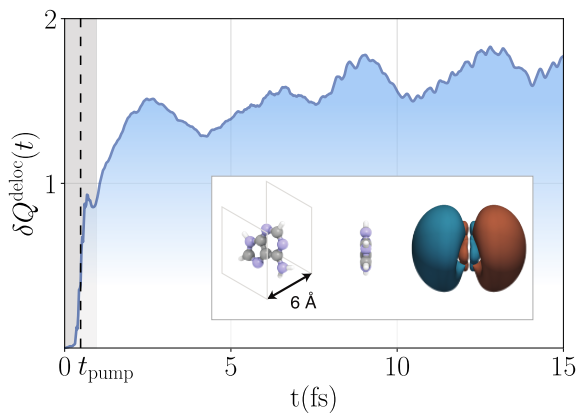


Figure S17. Inflation. Integrated time-dependent electron density more than 3 \AA away from the molecular plane. The grey shaded area represents the time-window of the pump pulse, having its peak at $t_{\text{pump}} = 0.48 \text{ fs}$. The y-axis has been rescaled by a factor of 10^5 . The inset shows the molecule and the planes defining the integration region (left) and the wavefunction of the special Kohn-Sham state LUMO+6 (right).

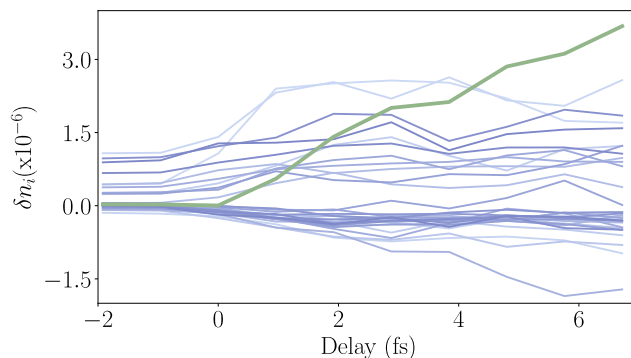


Figure S18. Shake-up state depletion. Average shake-up states depletion as a function of XUV-NIR delay. The average has been performed in a window of 1fs after the end of the pulses. In accordance to the main text, the LUMO+6 is drawn in green while the rest in shades of light blue.

are defined as the averaged value of the NIR-induced variation of the state occupation in a window of 1fs after the end of the NIR pulse. As stated in the main paper the NIR-induced depletion of the LUMO+6 state has an onset of 2 – 4fs and reproduces the behaviours of the adenine dication yield. Moreover, the LUMO+6 state is the only one, of all the shake-up states, showing these characteristics.

REFERENCES

- ¹Shukla, M. K. & Leszczynski, J. (eds.) *Radiation Induced Molecular Phenomena in Nucleic Acids* (Springer Netherlands, 2008).
- ²Calegari, F., Sansone, G., Stagira, S., Vozzi, C. & Nisoli, M. Advances in attosecond science. *Journal of Physics B: Atomic, Molecular and Optical Physics* **49**, 062001 (2016).
- ³Pilling, S. *et al.* Dissociative photoionization of adenine following valence excitation. *Rapid Communications in Mass Spectrometry* **21**, 3646–3652 (2007).
- ⁴Khanna, K. K. & Jackson, S. P. DNA double-strand breaks: signaling, repair and the cancer connection. *Nature Genetics* **27**, 247–254 (2001).
- ⁵Pan, S., Sun, X. & Lee, J. K. DNA stability in the gas versus solution phases: A systematic study of thirty-one duplexes with varying length, sequence, and charge level. *Journal of the American Society for Mass Spectrometry* **17**, 1383 – 1395 (2006).
- ⁶Cederbaum, L. S. & Zobeley, J. Ultrafast Charge Migration by Electron Correlation. *Chem. Phys. Lett.* **307**, 205–210 (1999).
- ⁷Calegari, F. *et al.* Ultrafast electron dynamics in phenylalanine initiated by attosecond pulses. *Science* **346**, 336–339 (2014).
- ⁸Drescher, M. *et al.* Time-resolved atomic inner-shell spectroscopy. *Nature* **419**, 803–807 (2002).
- ⁹Averbukh, V. *et al.* Interatomic electronic decay processes in singly and multiply ionized clusters. *Journal of Electron Spectroscopy and Related Phenomena* **183**, 36 – 47 (2011). Electron Spectroscopy Kai Siegbahn Memorial Volume.
- ¹⁰Nisoli, M., Decleva, P., Calegari, F., Palacios, A. & Martín, F. Attosecond electron dynamics in molecules. *Chemical Reviews* **117**, 10760–10825 (2017). PMID: 28488433.
- ¹¹Sansone, G., Pfeifer, T., Simeonidis, K. & Kuleff, A. I. Electron correlation in real time. *ChemPhysChem* **13**, 661–680 (2012).
- ¹²Marciniak, A. *et al.* Electron correlation driven non-adiabatic relaxation in molecules excited by an ultrashort extreme ultraviolet pulse. *Nature Communications* **10**, 337 (2019).
- ¹³Corkum, P. B. Plasma perspective on strong field multiphoton ionization. *Phys. Rev. Lett.* **71**, 1994–1997 (1993).
- ¹⁴Sola, I. J. *et al.* Controlling attosecond electron dynamics by phase-stabilized polarization gating. *Nature Physics* **2**, 319–322 (2006).
- ¹⁵Marques, M. A., Castro, A., Bertsch, G. F. & Rubio, A. octopus: a first-principles tool for excited electron–ion dynamics. *Computer Physics Communications* **151**, 60–78 (2003).
- ¹⁶Castro, A. *et al.* octopus: a tool for the application of time-dependent density functional theory. *physica status solidi (b)* **243**, 2465–2488 (2006).

- ¹⁷Andrade, X. *et al.* Real-space grids and the octopus code as tools for the development of new simulation approaches for electronic systems. *Physical Chemistry Chemical Physics* **17**, 31371–31396 (2015).
- ¹⁸Runge, E. & Gross, E. K. U. Density-Functional Theory for Time-Dependent Systems. *Phys. Rev. Lett.* **52**, 997–1000 (1984).
- ¹⁹Bertsch, G. F., Iwata, J. I., Rubio, A. & Yabana, K. Real-space, real-time method for the dielectric function. *Phys. Rev. B* **62**, 7998–8002 (2000).
- ²⁰Alonso, J. L. *et al.* Efficient Formalism for Large-Scale *Ab Initio* Molecular Dynamics based on Time-Dependent Density Functional Theory. *Physical Review Letters* **101**, 096403 (2008).
- ²¹Alvarado, F., Bari, S., Hoekstra, R. & Schlathöler, T. Interactions of neutral and singly charged keV atomic particles with gas-phase adenine molecules. *The Journal of Chemical Physics* **127**, 034301 (2007).
- ²²Brédy, R. *et al.* Fragmentation of adenine under energy control. *The Journal of Chemical Physics* **130**, 114305 (2009).
- ²³van der Burgt, P. J. M., Finnegan, S. & Eden, S. Electron impact fragmentation of adenine: partial ionization cross sections for positive fragments. *The European Physical Journal D* **69**, 173 (2015).
- ²⁴Cucinotta, C. S., Hughes, D. & Ballone, P. Real-time real-space TD-DFT for atoms: Benchmark computations on a nonspherical logarithmic grid. *Phys. Rev. B* **86**, 045114 (2012).
- ²⁵Perfetto, E. & Stefanucci, G. CHEERS: a tool for correlated hole-electron evolution from real-time simulations. *Journal of Physics: Condensed Matter* **30**, 465901 (2018).
- ²⁶Covito, F., Perfetto, E., Rubio, A. & Stefanucci, G. Real-time dynamics of auger wave packets and decays in ultrafast charge migration processes. *Physical Review A* **97**, 061401 (2018).
- ²⁷Månsson, E. P. *et al.* Ultrafast dynamics in the DNA building blocks thymidine and thymine initiated by ionizing radiation. *Phys. Chem. Chem. Phys.* **19**, 19815–19821 (2017).
- ²⁸Seiffert, L. *et al.* Attosecond chronoscopy of electron scattering in dielectric nanoparticles. *Nature Physics* **13**, 766–770 (2017).
- ²⁹Plützer, C., Nir, E., de Vries, M. S. & Kleinermanns, K. IR–UV double-resonance spectroscopy of the nucleobase adenine. *Physical Chemistry Chemical Physics* **3**, 5466–5469 (2001).
- ³⁰Eppink, A. T. J. B. & Parker, D. H. Velocity map imaging of ions and electrons using electrostatic lenses: Application in photoelectron and photofragment ion imaging of molecular oxygen. *Review of Scientific Instruments* **68**, 3477–3484 (1997).
- ³¹Galbraith, M. C. E. *et al.* Few-femtosecond passage of conical intersections in the benzene cation. *Nature Communications* **8** (2017).
- ³²Lacoursière, J., Meyer, M., Nahon, L., Morin, P. & Larzillière, M. Time-resolved pump-probe photoelectron spectroscopy of helium using a mode-locked laser synchronized with synchrotron radiation pulses. *Nuclear Instruments and Methods in Physics Research Section A: Accelerators, Spectrometers, Detectors and Associated Equipment* **351**, 545–553 (1994).
- ³³Andrade, X. *et al.* Real-space grids and the octopus code as tools for the development of new simulation approaches for electronic systems. *Phys. Chem. Chem. Phys.* **17**, 31371–31396 (2015).
- ³⁴Lin, J. *et al.* Ultraviolet photoelectron studies of the ground-state electronic structure and gas-phase tautomerism of purine and adenine. *Journal of the American Chemical Society* **102**, 4627–4631 (2002).
- ³⁵Legrand, C., Suraud, E. & Reinhard, P.-G. Comparison of self-interaction-corrections for metal clusters. *Journal of Physics B: Atomic, Molecular and Optical Physics* **35**, 1115 (2002).
- ³⁶Andrade, X. *et al.* Modified Ehrenfest Formalism for Efficient Large-Scale *ab initio* Molecular Dynamics. *Journal of Chemical Theory and Computation* **5**, 728–742 (2009).
- ³⁷Caruso, F., Rinke, P., Ren, X., Rubio, A. & Scheffler, M. Self-consistent g w: All-electron implementation with localized basis functions. *Physical Review B* **88**, 075105 (2013).
- ³⁸Kadanoff, L. P. & Baym, G. A. *Quantum statistical mechanics: Green's function methods in equilibrium and nonequilibrium problems* (Benjamin, 1962).
- ³⁹Stefanucci, G. & van Leeuwen, R. *Nonequilibrium Many-Body Theory of Quantum Systems: A Modern Introduction* (Cambridge University Press, Cambridge, 2013).
- ⁴⁰Balzer, K. & Bonitz, M. *Nonequilibrium Green's Functions Approach to Inhomogeneous Systems* (Springer, 2012).
- ⁴¹Lipavský, P., Špička, V. & Velický, B. Generalized kadanoff-baym ansatz for deriving quantum transport equations. *Phys. Rev. B* **34**, 6933–6942 (1986).
- ⁴²Vanderbilt, D. Optimally smooth norm-conserving pseudopotentials. *Phys. Rev. B* **32**, 8412–8415 (1985).
- ⁴³Perdew, J. P., Burke, K. & Ernzerhof, M. Generalized gradient approximation made simple. *Phys. Rev. Lett.* **77**, 3865–3868 (1996).
- ⁴⁴Kuleff, A. I., Breidbach, J. & Cederbaum, L. S. Multielectron wave-packet propagation: General theory and application. *The Journal of Chemical Physics* **123**, 044111 (2005).
- ⁴⁵Kuleff, A. I. & Cederbaum, L. S. Charge migration in different conformers of glycine: The role of nuclear geometry. *Chemical Physics* **338**, 320 – 328 (2007). Molecular Wave Packet Dynamics.
- ⁴⁶Ruberti, M., Decleva, P. & Averbukh, V. Multi-channel dynamics in high harmonic generation of aligned CO₂: *ab initio* analysis with time-dependent b-spline algebraic diagrammatic construction. *Phys. Chem. Chem. Phys.* **20**, 8311–8325 (2018).
- ⁴⁷Perfetto, E. & Stefanucci, G. The dissection algorithm for the second-born self-energy. *Physica Status Solidi b* (2019).
- ⁴⁸Perfetto, E. & Stefanucci, G. Cheers: a tool for correlated hole-electron evolution from real-time simulations. *Journal of Physics: Condensed Matter* **30**, 465901 (2018).
- ⁴⁹Covito, F., Perfetto, E., Rubio, A. & Stefanucci, G. Real-time dynamics of auger wave packets and decays in ultrafast charge migration processes. *Phys. Rev. A* **97**, 061401 (2018).

Chapter 3

Introduction to TDDFT

This chapter is dedicated to an introduction to the TDDFT formalism for the study of thermo-electric transport in nanojunctions. TDDFT [20, 48–52] is an exact reformulation of the many-body problem where the central quantity is the electronic density. The progress in this subject achieved within this work will be presented in publications V and VI, displayed at the end of the chapter.

3.1 Basics of (TD)DFT

Ground-state Density-Functional Theory is based on the idea of describing a system in terms of its electronic density, in contrary to the Schrödinger equation, where the wavefunction plays this role. Hohenberg and Kohn, in their seminal paper [9], proved the existence of a 1:1 mapping between the ground-state electronic density and the external potential influencing the system. As a consequence, the ground-state energy of a system can be found through the minimization of the energy, expressed as a functional of the electronic density. To understand how, we start by expressing the Hamiltonian operator as

$$\hat{H} = \hat{T} + \hat{H}_{\text{int}} + \hat{V} , \quad (3.1)$$

where \hat{H}_{int} —defined in the previous chapter—is the electron-electron interaction, \hat{T} is the kinetic energy operator and \hat{V} is the external potential energy. To link to the Hamiltonian presented in the previous chapter, \hat{T} and \hat{V} make up the single-

particle Hamiltonian. The operator \hat{V} is associated with a local potential $V(\vec{r})$ that takes into account the nuclear potential, the effect of external static electric fields, etc. Being local, we have $\hat{V} = \int d\vec{r} V(\vec{r})\hat{n}(\vec{r})$, with $\hat{n}(\vec{r})$ the density operator. The minimization principle of the energy with respect to the density can be understood through the so-called constrained search algorithm [53, 54]. Essentially, we first minimize the energy for a certain density $n(\vec{r})$ inside the space of all possible wavefunctions giving the density $n(\vec{r})$:

$$\begin{aligned} \tilde{E}[n] &= \min_{\psi \rightarrow n(\vec{r})} \langle \psi | \hat{H} | \psi \rangle \\ &= F[n] + \int d\vec{r} V(\vec{r})n(\vec{r}) , \end{aligned} \quad (3.2)$$

where the term associated with the potential $V(\vec{r})$ takes on this form due to its local nature and the functional $F[n]$ is defined as

$$F[n] \equiv \min_{\psi \rightarrow n(\vec{r})} \langle \psi | \hat{T} + \hat{H}_{\text{int}} | \psi \rangle . \quad (3.3)$$

The distinctive feature of the functional $F[n]$ is that it is independent of the particular $V(\vec{r})$ specifying the system, i.e. it is the same for all systems; it is, in fact, called the “universal” functional. To find the ground-state energy of the system we are now left to minimize the energy $\tilde{E}[n]$ with respect to all possible densities:

$$E[V] = \min_{n(\vec{r})} \left\{ \tilde{E}[n] \right\} = \min_{n(\vec{r})} \left\{ F[n] + \int d\vec{r} V(\vec{r})n(\vec{r}) \right\} . \quad (3.4)$$

Note the dependence of the ground-state energy on the external potential, since this specifies the system. The minimum condition (3.4) is equivalent to the requirement of the functional $\tilde{E}[n]$ to have vanishing functional derivative with respect to the density at the true ground-state density. Assuming such functional

derivative exists¹, we have

$$\frac{\delta \tilde{E}[n]}{\delta n(\vec{r})} = 0 \implies \frac{\delta F[n]}{\delta n(\vec{r})} = -V(\vec{r}) . \quad (3.5)$$

The mentioned minimum conditions are satisfied for the ground-state density, but do not guarantee that to a ground-state density corresponds one and one only external potential. Hohenberg and Kohn proved exactly this condition, ensuring that two distinct potentials, i.e. differing for more than a trivial constant, necessarily yield distinct ground-state densities². The implications of this statement are profound: from the ground-state density one can uniquely determine the associated external potential, hence the Hamiltonian and, through the Schrödinger equation, access *all* the properties of the system.

The principles presented up to now, while giving an elegant approach to the ground-state problem, do not help with a practical solution of the problem, since the form of the universal functional $F[n]$ remains unknown. Finding approximations to the universal functional, while in principle possible, is not a straightforward path to follow. The strategy proposed by Kohn and Sham in 1965 [10] provides a much more practical way of solving the problem. The approach is based on the idea that the ground-state density of an interacting system can be represented by the ground-state density of a fictitious non-interacting system moving in an external potential V_{KS} . For this fictitious system, called the Kohn-Sham (KS) system, similarly to the interacting system, the minimization conditions read

$$E_{\text{KS}}[V_{\text{KS}}] = \min_{n(\vec{r})} \{E_s[n]\} = \min_{n(\vec{r})} \left\{ T_s[n] + \int d\vec{r} V_{\text{KS}}(\vec{r})n(\vec{r}) \right\} , \quad (3.6a)$$

¹Although we make the assumption of existing functional derivatives of the quantities introduced, this is a non-trivial subject. The functional $F[n]$ might not be well-defined for all densities, and more so its functional derivative, but restricting ourselves to “safe” densities representing normal physical processes, it is harmless to make our assumption.

²The opposite is, in general, not true. For the case of degenerate ground-states, in fact, an external potential can be associated with different ground-state densities of the same energy.

$$\frac{\delta T_s[n]}{\delta n(\vec{r})} = -V_{\text{KS}}(\vec{r}) , \quad (3.6b)$$

where $T_s[n]$ is the kinetic energy functional of the non-interacting system. At the ground-state density, which is the same for both the interacting and non-interacting systems, the functional derivative of the energy functional $E[n]$ (or $E_s[n]$) with respect to the density vanishes. Therefore, we have

$$\begin{aligned} 0 &= \frac{\delta \tilde{E}[n]}{\delta n(\vec{r})} = \frac{\delta E_s[n]}{\delta n(\vec{r})} , \\ \frac{\delta F[n]}{\delta n(\vec{r})} + V(\vec{r}) &= \frac{\delta T_s[n]}{\delta n(\vec{r})} + V_{\text{KS}}(\vec{r}) . \end{aligned} \quad (3.7)$$

We can use this last equality to define the KS potential as

$$\begin{aligned} V_{\text{KS}}[n](\vec{r}) &= \frac{\delta(F[n] - T_s[n])}{\delta n(\vec{r})} + V(\vec{r}) \\ &\equiv \frac{\delta E_{\text{Hxc}}[n]}{\delta n(\vec{r})} + V(\vec{r}) , \end{aligned} \quad (3.8)$$

where we defined the Hartree-exchange-correlation energy $E_{\text{Hxc}}[n]$ as the difference between the universal functional and the kinetic energy functional of the non-interacting system. This difference contains the effects of interaction and the difference in the kinetic energy of the two systems. From this energy we can further extract the electrostatic component of the electron-electron interaction (Hartree contribution), which can be explicitly written, obtaining

$$E_{\text{Hxc}}[n] = E_{\text{H}}[n] + E_{\text{xc}}[n] . \quad (3.9)$$

The exchange-correlation energy $E_{\text{xc}}[n]$ encodes the difference in the kinetic energy of the two systems and the effect of interaction beyond the electrostatic effect. It is therefore small compared to the Hartree and non-interacting kinetic energies. This gives the hope that its approximation may not introduce too severe errors.

Going back to the definition of the Kohn-Sham potential (3.8), we have

$$V_{\text{KS}}[n](\vec{r}) = V_{\text{H}}[n](\vec{r}) + V_{\text{xc}}[n](\vec{r}) + V(\vec{r}) , \quad (3.10)$$

where the potentials $V_{\text{H}}[n]$ and $V_{\text{xc}}[n]$ are the functional derivatives of the corresponding energy functionals. Being a system of non-interacting particles, the time-independent Schrödinger equation for the KS system, the so-called Kohn-Sham equation, is easily found

$$\left[-\frac{\hbar^2}{2m} \nabla^2 + V(\vec{r}) + V_{\text{H}}(\vec{r}) + V_{\text{xc}}(\vec{r}) \right] \phi_i(r, \vec{\sigma}) = \epsilon_i \phi_i(\vec{r}, \sigma) , \quad (3.11)$$

where the $\phi_i(\vec{r}, \sigma)$ are the Kohn-Sham orbitals, i labels the states, σ labels spin and, for simplicity, we disregarded spin. The density is then calculated from the KS orbitals, i.e. $n(\vec{r}) = \sum_{i\sigma} |\phi_i(\vec{r}, \sigma)|^2$.

To summarize, finding the ground-state density of the non-interacting KS system in presence of the KS potential (3.10) is equivalent to finding the ground-state of the interacting system moving in a potential $V(\vec{r})$. What we gain in this is considerable: given that we have an approximation for the exchange-correlation potential, the many-body problem is reduced to finding the ground-state of a non-interacting system.

Before introducing TDDFT, it is important to notice that the matters of interest are quite different between a time-dependent framework and the ground-state case. While in DFT we consider equilibrium properties such as, equilibrium geometries of crystals, phonon spectra, and so on, in TDDFT the focus is on the time evolution of the system, excitation energies, the response of the density density to an external perturbation, etc.

Time-Dependent DFT, as the name suggests, is the extension of ground-state DFT to the time domain, whose foundation lies in the Runge-Gross theorem [20]. Similarly to the Hohnberg-Kohn theorem, it is based on the idea of mapping from densities to potentials, which in this case are all time-dependent quantities, with a few differences from the ground-state case. The Runge-Gross theorem states that two time-dependent densities which evolve from the same initial state under the

influence of two external time-dependent potentials differing by more than a time-dependent constant, *must* be different. This means that the map is $V[\psi_0, n](\vec{r}, t)$, since the initial state dependence of the time-evolved system cannot be discarded. Moreover, it is important to notice that the potential depends on the density at all previous times, highlighting the role of memory in time-dependent scenarios. For the special case of choosing the ground state as the starting point of the time-evolution, the dependence on the initial state can be dropped, since the ground-state density $n(t_0)$ is in a 1:1 correspondence with the ground state ψ_0 . In the same way we find a practical solution to ground-state counterpart, in TDDFT, we can construct a local potential $V_{\text{KS}}(\vec{r}, t)$ that generates the density $n(\vec{r}, t)$ of the interacting system, when we let a non-interacting system evolve under its influence. This potential can be written as

$$V_{\text{KS}}[n](\vec{r}, t) = V(\vec{r}, t) + V_{\text{H}}[n](\vec{r}, t) + V_{\text{xc}}[n](\vec{r}, t) , \quad (3.12)$$

where, similar to the ground-state case, $V(\vec{r}, t)$ is the external potential, $V_{\text{H}}(\vec{r}, t)$ is the Hartree contribution, $V_{\text{xc}}(\vec{r}, t)$ is the exchange-correlation potential and, of course, the latter two are functionals of the density. The time-dependent Kohn-Sham equation, then, reads

$$i\hbar \frac{\partial}{\partial t} \phi_i(\vec{r}, \sigma, t) = \left[-\frac{\hbar^2}{2m} \nabla^2 + V_{\text{KS}}(\vec{r}, t) \right] \phi_i(\vec{r}, \sigma, t) . \quad (3.13)$$

Again, the time-dependent density can be calculated from the time-evolved KS states through $n(\vec{r}, t) = \sum_{i\sigma} |\phi_i(\vec{r}, \sigma, t)|^2$.

3.2 Adiabatic functionals

It is not in the scope of this document to delve into the details of the search for approximations to the exchange-correlation potential of (TD)DFT: this is an active field of research on its own [55–57]. On the other hand, it is necessary to discuss the implications of the commonly used exchange-correlation potentials. Before elaborating on this, it is important to appreciate how the exchange-correlation po-

tential in (TD)DFT plays a role similar to the self-energy in NEGF. In fact, both these frameworks are, in principle, an exact reformulation of the many-body problem and how faithfully they describe physical phenomena depends on the level of approximation used for the self-energy or the xc functional.

The vast majority of approximations to the exchange-correlation potential used nowadays belongs to the adiabatic category. These approximations are based on the assumption that the exchange-correlation potential $V_{xc}(\vec{r}, t)$ only depends on the instantaneous density $n(\vec{r}, t)$, i.e. memory effects are discarded. In other words, the functional becomes “local in time”. This allows us to use ideas developed in ground-state DFT in a time-dependent framework through the simple substitution $n(\vec{r}) \rightarrow n(\vec{r}, t)$ in the expression of the xc potential. This is not the case in the NEGF framework, since the collision integral, embodying the effect of correlations beyond HF, is performed over all times. In this case, though, the catch is in the much more computationally demanding equations of the NEGF approach.

3.3 Transport within TDDFT

A transport setup is generally composed of a microscopic device connected to one or multiple (macroscopic) contacts used to drive or measure the junction, see Fig. 3.1. Examples of such devices are transistors, nowadays on the scale of tens of nanometers, or other kinds of junctions, up to the micrometer scale. Given the (possible) considerable size of these devices, studying their behavior with an efficient method like TDDFT is particularly appealing. The advantages do not only come from the low computational cost associated with TDDFT calculations: one can further exploit the properties of the KS system mapping the true setup. Once we are dealing with the non-interacting KS system, it is advantageous to employ the embedding scheme presented in the previous chapter to model the interaction of the device itself with the macroscopic leads, which are, in general, too sizeable to be described microscopically. Moreover, the (TD)DFT framework can be combined with probably the most successful and widespread theory to describe electric transport: the Landauer-Büttiker formalism [58–63]. This formalism, ap-

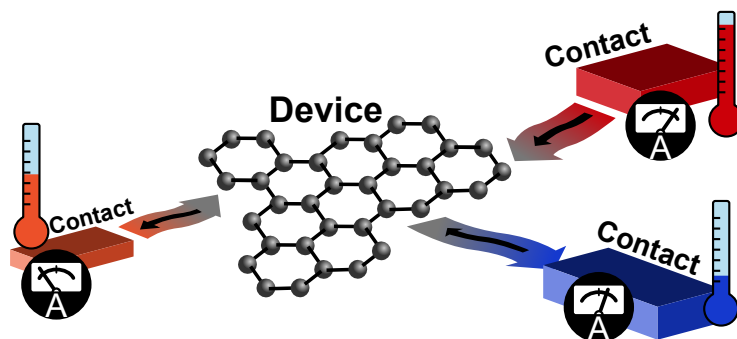


Figure 3.1: Schematic representation of a general transport setup. Although conventional transport setups comprise of the device and two contacts used for measuring and inducing dynamics, the presented approach is general and can deal with any number of contacts. The arrows between the contacts and the device represent the charge currents (black) and heat flow (colored). The contacts are at different temperatures, as indicated by the thermometers. The current flowing to the dot from the leads is measured through the use of the depicted ammeters.

plicable precisely to non-interacting systems, describes transport like a scattering problem. This means that the charge flow is expressed in terms of the transmission function of the device and the occupation functions of the leads that, being macroscopic, are considered in equilibrium. Moreover, it is also possible to consider the effect of temperature with the use of a thermomechanical potential, introduced by Luttinger [64], which couples to the local energy density of the system, hence rescaling the energy locally. In a nutshell, considering this idea in the context of transport translates into a rescaling of the occupation functions of the leads according to their temperature. Moreover, in principle, the thermomechanical potential can be used to consider temperature gradients across the device. In recent years, Luttinger's idea has been developed further to propose a novel DFT approach for the description of thermo-electric transport [65–68], where a generalization of the exchange-correlation potential for studying charge and energy flow is put forward. The described approach represents an efficient way of treating the transport problem. This efficiency can be boosted by employing the WBLA for the description of

the interaction of the impurity with the leads. Although widely used and studied, the implications of adopting this approximation in the context of thermo-electric transport have not been addressed yet. In publication [V](#) we investigate whether the WBLA induces any artifacts when studying both charge and heat transport through a nanoscale device. Lastly, the possibility of going beyond the standard adiabatic functionals presented in the previous section has been explored in publication [VI](#), where a construction for a non-adiabatic exchange-correlation functional for lattice models is proposed. The findings of the publications and their implications are discussed in the following, together with a more detailed introduction to each work.

Publication V

Transient Charge and Energy Flow in the Wide-Band Limit

Fabio Covito, Florian G. Eich, Riku Tuovinen, Michael A. Sentef and Angel Rubio, *Journal of Chemical Theory and Computation*, **14**, pp 2495–2504 (2018).

Electrical circuits have nowadays reached a size where quantum effects can no longer be disregarded. A microscopical description of their behavior is in order to understand how we can further control and manipulate such devices. The characterization of quantum devices is highly non-trivial due to difficulties in the description of interaction in combination with the size of such devices. For this reason a wealth of approximations have been introduced and studied over the years to best describe the physical behavior of quantum devices. Approximations can be, at times, not perfectly controlled and the repercussions of using them might introduce spurious effects in our analysis. In the study of transport, the WBLA is a commonly used approximation. The WBLA disregards the structure of the density of states of the leads, assuming their bandwidth to be infinite. To model the effect of temperature in transport setups, we can make use of Luttinger's thermomechanical potential. This potential encodes the effect of temperature on the leads by rescaling their energy density. It is, therefore, legitimate to ask what are the implications of using the WBLA in conjunction to Luttinger's thermomechanical potential, since this would imply the rescaling of an infinite band. In this publication we address exactly this question in the study of the time-dependent thermoelectric transport through nanoscale devices. We find a pathological behavior of both the charge and the heat transient currents under certain circumstances. In particular, we observe an unphysical jump in the heat current when we apply a voltage bias to the device and in the charge current when we apply a temperature bias. Even more severe is the behavior of the transient heat current when

the device is exposed to a potential quench and a temperature gradient; this, in fact, diverges as $(t - t_0)^{-1}$, where t_0 is the time at which we induce dynamics by switching on the potential and temperature biases. We identify the problem to be related to the absence of an energy cutoff for the WBLA embedding self-energy, not properly damping highly energetic transitions. We show that this pathological behavior can be alleviated by considering that changes induced by temperature variations affect the boundary between the leads and the impurity other than the leads exclusively. The divergence of the heat current, though, persists, becoming logarithmic. Although the instantaneous switch-on of voltage biases and temperature gradients is not realizable in practice, the simulation time-step required for resolving the dynamics observed in modern transport experiments is comparable to the time interval at which we observe the pathological behavior.

In the following, I add a remark, which is not explicitly addressed in the published manuscript, but complements the discussion of the work.

Importance of the overall lifetime. For non-interacting impurities and time-independent driving of the leads, the retarded/advanced Green's function of the impurity in energy space reads

$$\mathbf{G}^{R/A}(\omega) = \frac{1}{\omega - \mathbf{H} - \Sigma_{\text{emb}}^{R/A} \pm i\eta}, \quad (3.14)$$

where $\eta \ll 1$ and $1/\eta$ represents the timescale of the complete equilibration of the system. The time the system need to reach a steady state is much longer than any transient timescale of the system, but much shorter than this time $1/\eta$. In the analytical calculation of, e.g. heat or electric currents, integrals containing the spectral function appear. A commonly used equality for the spectral function is

$$\begin{aligned} \mathbf{A}(\omega) &= i [\mathbf{G}^R(\omega) - \mathbf{G}^A(\omega)] \\ &= i \left[\mathbf{G}^R(\omega) (\mathbf{G}^A(\omega))^{-1} \mathbf{G}^A(\omega) - \mathbf{G}^R(\omega) (\mathbf{G}^R(\omega))^{-1} \mathbf{G}^A(\omega) \right] \\ &= i \mathbf{G}^R(\omega) \left[(\mathbf{G}^A(\omega))^{-1} - (\mathbf{G}^R(\omega))^{-1} \right] \mathbf{G}^A(\omega) \\ &= i \mathbf{G}^R(\omega) [\Sigma_{\text{emb}}^R(\omega) - \Sigma_{\text{emb}}^A(\omega)] \mathbf{G}^A(\omega), \end{aligned} \quad (3.15)$$

where we used the definition (3.14) and the fact that $\eta \ll 1$. When evaluating integrals over the spectral function, though, its contribution linearly dependent on η *cannot* be discarded if undamped states are present. This is already clear at a physical level: undamped states have to eventually decay in the infinite time limit; this is exactly the role of η . Put in formulas, for a general integral over the spectral function, we have

$$\begin{aligned} \mathbf{I}(t) &= \int_{-\infty}^{\infty} \frac{d\omega}{2\pi i} \mathbf{A}(\omega) \\ &= i \int_{-\infty}^{\infty} \frac{d\omega}{2\pi i} \mathbf{G}^R(\omega) [\Sigma_{\text{emb}}^R(\omega) - \Sigma_{\text{emb}}^A(\omega)] \mathbf{G}^A(\omega) \\ &\quad - 2\eta \int_{-\infty}^{\infty} \frac{d\omega}{2\pi i} \mathbf{G}^R(\omega) \mathbf{G}^A(\omega) . \end{aligned} \quad (3.16)$$

If the GFs only have poles with a finite lifetime, the last term of the previous equation is

$$-2\eta \int_{-\infty}^{\infty} \frac{d\omega}{2\pi i} \mathbf{G}^R(\omega) \mathbf{G}^A(\omega) = 2\eta \sum_m \text{Res} [\mathbf{G}^R(\omega_m)] \mathbf{G}^A(\omega_m) , \quad (3.17)$$

where we close the contour in the lower half of the complex plane and ω_m are the poles of the retarded GF. We readily see that the integral vanishes in the limit of $\eta \rightarrow 0$. This is not the case when bare poles are present. For the sake of simplicity, let us take an example of a single bare pole at zero energy. The contribution to the integral of the spectral function linearly dependent on η reads

$$\begin{aligned} -2\eta \int_{-\infty}^{\infty} \frac{d\omega}{2\pi i} \frac{1}{\omega + i\eta} \frac{1}{\omega - i\eta} &= -2\eta \int_{-\infty}^{\infty} \frac{d\omega}{2\pi i} \frac{1}{\omega^2 + \eta^2} \\ &= -\frac{1}{\pi} \eta \left[\frac{1}{\eta} \arctan\left(\frac{\omega}{\eta}\right) \right]_{-\infty}^{+\infty} = -1 . \end{aligned} \quad (3.18)$$

As we can see, this term does is independent of η and has to be taken into account if one uses the equality (3.15) in the calculation of integrals of the kind (3.16). This observation holds for any general integral of the product between the spectral

function and any function of the energy, e.g. the calculation of the initial density matrix.



Transient Charge and Energy Flow in the Wide-Band Limit

F. Covito,[†] F. G. Eich,^{*,†} R. Tuovinen,[†] M. A. Sentef,[†] and A. Rubio^{†,‡,§,||}

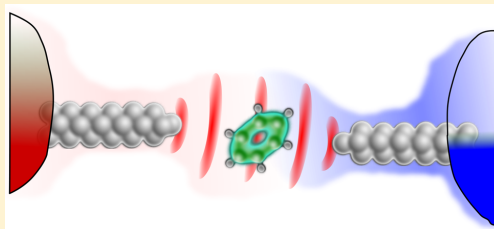
[†]Max Planck Institute for the Structure and Dynamics of Matter, Luruper Chaussee 149, 22761 Hamburg, Germany

[‡]Center for Free-Electron Laser Science, Luruper Chaussee 149, 22761 Hamburg, Germany

[§]Center for Computational Quantum Physics (CCQ), The Flatiron Institute, 162 Fifth Avenue, New York, New York 10010, United States

^{||}Nano-Bio Spectroscopy Group, Departamento de Física de Materiales, Universidad del País Vasco, 20018 San Sebastián, Spain

ABSTRACT: The wide-band limit is a commonly used approximation to analyze transport through nanoscale devices. In this work we investigate its applicability to the study of charge and heat transport through molecular break junctions exposed to voltage biases and temperature gradients. We find by comparative simulations that while the wide-band-limit approximation faithfully describes the long-time charge and heat transport, it fails to characterize the short-time behavior of the junction. In particular, we show that the charge current flowing through the device shows a discontinuity when a temperature gradient is applied, while the energy flow is discontinuous when a voltage bias is switched on and even diverges when the junction is exposed to both a temperature gradient and a voltage bias. We provide an explanation for this pathological behavior and propose two possible solutions to this problem.



1. INTRODUCTION

Over the last decades great effort has been spent to miniaturize electric circuits. The goal is to realize the fundamental building blocks of electronic circuits, such as transistors, on the scale of single molecules. There has been great success in shrinking electronic devices down experimentally. In order to understand the properties of molecular break junctions, a quantum mechanical description of the device is required. Perhaps the most successful and widespread theory to describe how charge flows through a nanoscale junction is the so-called Landauer–Büttiker approach,^{1–3} which describes the charge transport as a scattering problem. Essentially, the flow of charge through a molecular junction is determined by the transmission function of the device—describing how impinging electrons are scattered—and the occupation function of the electrons in the (metallic) leads connected to the junction.

In recent years there has been renewed interest in addressing not only the charge flow but also the energy (or heat) flow through nanoscale devices. Understanding how charge and energy flow depend on voltage and temperature biases across the device provides crucial insight for the development of thermoelectric circuits, which could be used to convert waste heat into useful electric energy.^{4,5} Furthermore, recent experiments demonstrate that local temperatures in nanoscale conductors can be measured with a spatial resolution of tens of nanometers.^{6,7} A common path to address the effect of temperature gradients across the nanoscale device is to allow for different temperatures in the occupation functions characterizing the leads in the Landauer–Büttiker formula. Conceptually this can only be justified if the leads are

considered to be disconnected from the device initially (partitioned approach). This artificial partitioning of the system, however, is problematic, for it assumes that it is possible to perfectly decouple the leads from the molecular junction—a rather optimistic assumption if one considers atomic-scale devices. For times much larger than the typical time scale of molecular break junctions, which are on the order of femtoseconds,^{8–11} the assumption of a decoupled initial state does not play a crucial role. However, for transient dynamics the initial state matters. As pump–probe experiments are now able to investigate phenomena happening at this time scale^{12–15} it is important to properly describe the initial state.

An alternative to the partitioned approach is to couple the device and leads at all times and trigger the charge flow by switching a potential bias.¹⁶ This *partition-free* approach leads to the same steady state as the partitioned approach, but the transient dynamics of the device will, in general, be different.¹⁷ The advantage of the partition-free approach is that the transient charge and energy/heat flows are not spoiled by the dynamics induced by connecting leads and device, because the electronic states in the device are allowed to hybridize with the leads before any temperature or voltage bias is applied. Importantly, it is also possible to take into account temperature differences in the leads within the partition-free approach: We consider a *thermomechanical potential*, which couples to the *local* energy density of the system—much like the usual electric potential couples to the charge density.¹⁸ This thermomechanical

Received: January 26, 2018

Published: April 16, 2018

ical potential acts as mechanical “proxy”¹⁹ for local temperature variations. An intuitive way to understand this is to consider the occupation function, which is determined from the ratio of the energy and the temperature. Accordingly, a change in occupations due to a change in temperature can alternatively be viewed as a change in energy keeping the temperature fixed. The thermomechanical potential rescales the energy locally, thereby mimicking a locally varying temperature. Applying this idea in the context of transport means that different temperatures in the leads are described by rescaling the bandwidth of the leads.²⁰

A widespread simplification used to describe transport through nano junctions is the so-called wide-band limit (WBL). The WBL assumes that the detailed structure of the density of states in the leads is not important for the description of transport, which substantially simplifies computations. The WBL for charge transport is justified when the bandwidth is large compared to the applied bias.^{21–27} An important requirement for the WBL is that it should not induce any spurious, unphysical dynamics. Its only purpose is to allow for an efficient description of dynamics in large scale open quantum systems.

In this work we investigate whether the WBL can be employed in conjunction with the thermomechanical potential. An immediate question that comes to mind is: What is the meaning of rescaling an infinite band? In the following we will show that the steady state is well described in the WBL, provided the WBL is taken properly. The transient currents, however, exhibit peculiarities at short times. Specifically, we see that the charge current jumps at the initial time when the device is exposed to a temperature gradient and, similarly, the heat current behaves discontinuously when a voltage bias, but no temperature bias, is switched on. Even more dramatically, the heat current diverges as $(t - t_0)^{-1}$, with t_0 being the time at which a temperature and charge bias are applied to the system. By comparing the WBL transient charge and heat currents to results obtained at finite bandwidth, we highlight that this pathological behavior of the WBL can be attributed to the fact that—at short times—the natural cutoff, provided by the finite bandwidth, plays a crucial role for the dynamics.

2. MODEL AND METHOD

We consider a simple tight-binding model Hamiltonian to describe a molecular break junction. A single molecular level is connected to two metallic leads (cf. sketch in Figure 1). The Hamiltonian reads

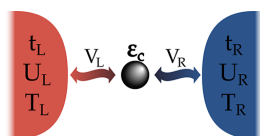


Figure 1. Molecular break junction: Schematic representation of the system considered in this work. A single impurity site, representing a molecular level with energy ϵ_c , is coupled via hopping amplitudes V_α to metallic leads with a bandwidth $4t_\alpha$ ($\alpha = R, L$). Charge and energy flow is triggered by applying a potential bias U_α to the leads and/or changing the temperature T_α in the leads.

$$\hat{H} = \epsilon_c \hat{\phi}_c^\dagger \hat{\phi}_c + \sum_{ak} \epsilon_{ak} \hat{\phi}_{ak}^\dagger \hat{q}_{ak} + \sum_{ak} (\hat{\phi}_{ak}^\dagger V_{(ak)c} \hat{\phi}_c + \hat{\phi}_c^\dagger V_{c(a)k} \hat{\phi}_{ak}) \quad (1)$$

where ϵ_c is the energy of the molecular level, $\hat{\phi}_{ak}^\dagger$ and $\hat{\phi}_{ak}$ are the field operators of the leads, with $\alpha = L(\text{eft}), R(\text{ight})$ and k labels the basis functions in the leads, and $\hat{\phi}_c^\dagger, \hat{\phi}_c$ representing the field operators associated with the molecular level. The matrix elements $V_{(ak)c} = [V_{c(a)k}]^*$ take the coupling between the molecular level and the leads into account. In the following we will drop the subscript “c” of $V_{(ak)c}$ since we are only considering a single site. The leads are modeled as non-interacting one-dimensional tight-binding chains, i.e., the dispersion of the electrons in the leads is given by

$$\epsilon_{ak} = -2t_\alpha \cos(k) + c_\alpha \quad (2)$$

where t_α is the nearest neighbor hopping in lead α , yielding a bandwidth of $4t_\alpha$. The energy c_α corresponds to the center of the band of the lead α ; that is, it determines the alignment of the band with respect to the chemical potential, which we take to be at zero energy. Finally the hopping to the central site is $V_{ak} = V_\alpha \sin(k)$. This picture may be extended to more complicated lead structures and couplings.²⁸ The embedding self-energy due to lead α is then given by

$$\begin{aligned} \Sigma_\alpha^{R/A}(z) &= \sum_k V_{ak} g_{ak}^{R/A}(z) V_{ak}^* \\ &= \frac{|V_\alpha|^2}{t_\alpha} S\left(\frac{z - c_\alpha}{2t_\alpha}\right) \end{aligned} \quad (3)$$

with $g_{ak}^{R/A}(z)$ being the retarded/advanced Green’s function of the isolated lead α . The function $S(z)$ is given by

$$S(z) = z - \sqrt{z-1} \sqrt{z+1} \quad (4)$$

where the character of the function $S(z)$, i.e., whether it is the advanced or retarded self-energy, is determined by the sign of the imaginary part of z . The function $S(z)$ has a branch cut on the real axis from $z = -1 \rightarrow z = 1$. The Green’s function for the molecular level is then simply given by

$$G^{R/A}(z) = \left[z - \epsilon_c - \sum_\alpha \Sigma_\alpha^{R/A}(z) \right]^{-1} \quad (5)$$

The inverse of the imaginary part of the self-energy yields a finite lifetime for the quasi-particles in the molecular junction, and the real part of the self-energy shifts the energy of the quasi-particles.

The WBL is defined as the limit $t_\alpha \rightarrow \infty$ (infinite bandwidth) while keeping the ratio $|V_\alpha|^2/t_\alpha$ which corresponds to the decay rate into lead α , constant. Expanding the expression of the self-energy for large t_α we obtain

$$[\Sigma_\alpha^{R/A}(z)]_{\text{WBL}} = \mp i \frac{|V_\alpha|^2}{t_\alpha} = \mp i \frac{\Gamma_\alpha}{2} \quad (6)$$

where the \mp sign refers to the retarded/advanced self-energy, respectively. As we can see from this expression, the only effect of the leads is to provide a decay-mechanism for the quasi-particles.

Expressing the field operators $\hat{\phi}$ in the Heisenberg picture and using their equations of motion, the charge and heat currents are given by^{20,29–31}

$$I_\alpha = -\partial_t \sum_k \langle \hat{\phi}_{ak}^\dagger(t) \hat{\phi}_{ak}(t) \rangle \quad (7a)$$

$$Q_\alpha = -\partial_t \left[\sum_k \epsilon_{ak} \langle \hat{\phi}_{ak}^\dagger(t) \hat{\phi}_{ak}(t) \rangle + \frac{1}{2} \sum_k (V_{ak} \langle \hat{\phi}_{ak}^\dagger(t) \hat{\phi}_c(t) \rangle + \text{h. c.}) \right] \quad (7b)$$

Note that we define the heat current Q_α as the temporal change in the energy within the leads *plus* half the coupling energy.³² Since we are working in the partition-free approach our initial state is described by a grand canonical ensemble determined by the global chemical potential μ and the (inverse) temperature β . Without loss of generality we can assume that the chemical potential defines the zero in energy, which implies that in definition 7b the energy flow due to the convective motion of the electrons is properly accounted for; that is, the shift $Q_\alpha \rightarrow Q_\alpha - \mu I_\alpha$ does not change the heat current. All energy levels in our model are measured with respect to the chemical potential.

3. TRANSPORT SETUP

In this work, we investigate the validity of the WBL in the case of dynamical heat and charge transport in the junction described in the previous section. Once a nonequilibrium situation is created by applying a potential bias and/or temperature gradient, transient dynamics will take place and electrons will move, resulting in charge and heat currents flowing across the junction. We focus on the specific cases of quenches; that is, the electric and thermomechanical potentials suddenly change at a certain time t_0 . Transient dynamics—induced by changing the potentials—occur on the order of a characteristic time scale τ given by the inverse of the decay rate due to the leads, i.e.,

$$\tau^{-1} = \sum_\alpha \frac{V_\alpha^2}{t_\alpha} \quad (8)$$

For times $t \gg \tau$ the junction will reach a steady state. We choose the hopping $V_L = V_R = V$ as our unit of energy: the molecular energy level is taken to be at $\epsilon_c = 0.2V$, the nearest neighbor hopping of the leads $t_L = t_R = 5V$, the chemical potential defines the zero of the energy, the centers of the band of the leads are aligned with it ($\epsilon_\alpha = \mu = 0$), and the (inverse) temperature $\beta = (k_B T_0)^{-1} = 100V^{-1}$.

For $t < t_0$ the system is taken to be in thermal equilibrium at temperature T_0 . In order to induce a charge current, the left lead is shifted up in energy by $U = 2V$ for $t \geq t_0$; that is, the energy dispersion of the left lead is given by

$$\epsilon_{Lk} = \begin{cases} -2t_L \cos(k), & \text{for } t < t_0, \\ -2t_L \cos(k) + U & \text{for } t \geq t_0. \end{cases} \quad (9)$$

In order to describe a temperature gradient across the junction—in addition to the potential bias—we apply a thermomechanical potential $\psi = \frac{T_\alpha - T_0}{T_0} = 1$ in the left lead, which rescales the bandwidth for $t \geq t_0$. This thermomechanical potential effectively doubles the temperature in the left lead:

$$\epsilon_{Lk} = \begin{cases} -2t_L \cos(k), & \text{for } t < t_0 \\ (1 + \psi)(-2t_L \cos(k) + U) & \text{for } t \geq t_0 \end{cases} \quad (10)$$

Figure 2 sketches of the molecular junction in the initial equilibrium and in the steady-state limit, showing that in the

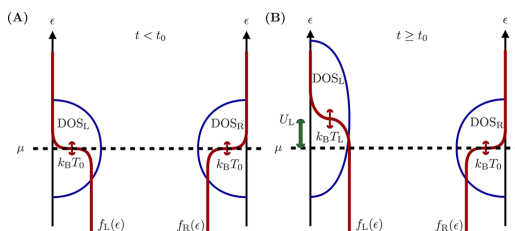


Figure 2. Comparison of initial and steady state: (A) Initial state of the junction. The leads–molecule system is equilibrated at a unique temperature T_0 and chemical potential μ (represented by the dashed horizontal line). (B) Graphical representation of the steady state. At t_0 a thermomechanical potential and the potential bias is applied. This results in a steady state in which the occupation function of the left lead corresponds to a Fermi function with $T_L = 2T_0$ and $\mu_L = \mu + U_L$.

steady-state the energy dispersion of the left lead is broadened by a factor of 2. In Figure 3 we depict the time-dependent

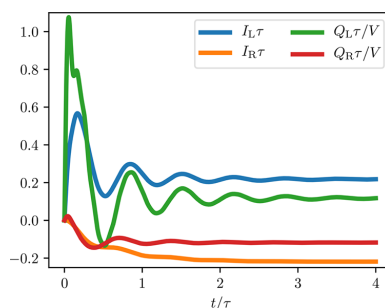


Figure 3. Charge and heat currents: Transient charge (I_α) and heat currents (Q_α) flowing between the left lead ($\alpha = L$) and the right lead ($\alpha = R$) and the molecular junction, respectively. The results are obtained taking into account the full frequency dependence of the embedding self-energy. The currents are triggered by a sudden change in the temperature and potential in the left lead at $t_0 = 0$.

charge and heat currents through the molecular junction. In this calculation, both a charge bias and a temperature gradient are applied across the junction and we observe fast transient oscillation of the currents on the time scale τ followed by a saturation to a steady current.

4. RESULTS

In order to test the WBL we compute the time-dependent charge and heat currents flowing from the leads into the impurity in the WBL and compare the results to calculations taking the full frequency dependence of the lead self-energy [cf. eq 4 and Figure 3] into account. Specifically, we rescale the bandwidth of the leads, making it effectively wider, while keeping the ratio $|V_\alpha|^2/t_\alpha$ constant. Hence, we use

$$V_{\alpha}^{\lambda} = \sqrt{\lambda} V_{\alpha}, \quad t_{\alpha}^{\lambda} = \lambda t_{\alpha} \quad (11)$$

with a rescaling factor λ , which allows us to approach the WBL as $\lambda \rightarrow \infty$. We focus on two different scenarios: (1) A situation where only a potential bias is applied to the left lead [cf. eq 9], (2) A situation where both a potential bias and a temperature difference are applied across the junction [cf. eq 10]. The numerical algorithm to compute the transient currents—taking the full frequency dependence of the embedding self-energy into account—has already been discussed in ref 33. In the following we refer to these results as the “full” calculation. Very recently progress has been made in evaluating the time-dependent currents in tight-binding models within the WBL analytically.^{34,35} It turns out that this is also possible if a thermomechanical potential—describing temperature gradients—is present. Accordingly, all WBL results are obtained analytically. The explicit derivation of the analytical expression will be presented elsewhere.

Steady State Currents. For times much longer than the characteristic lifetime τ the system reaches a steady state. In general we find that the steady state currents obtained in the WBL coincide with the results of the full calculation when the scaling factor λ is increased. However, there is a subtle point in the evaluation of the heat current in the steady state: it turns out to be crucial to take the WBL at the end of the calculation and *not* inside the integral defining the steady state current. The difference between taking the WBL inside the integral and taking the WBL after performing the integral is only present if two leads at different temperatures are connected to the same state in the device. This is trivially the case for a molecular junction modeled by a single site. We present a careful derivation in Appendix B showing that the order of limits matters.

Transient Charge Current. The transient charge induced by a potential bias alone is nicely reproduced in the WBL [cf. Appendix A for the corresponding plots]. This is consistent with earlier studies of the transient charge dynamics in nanoscale junctions.^{21,25} If a temperature gradient—in addition to the potential bias—is applied, the charge current exhibits a jump at the initial time but otherwise represents the full calculation for times $t \gtrsim \tau$. In Figure 4 we depict the charge current for $t \ll \tau$ (a plot of I_{α} for $t \gtrsim \tau$ is provided in Appendix A). It can be shown analytically that the jump, ΔI_{α} at the initial time is proportional to

$$\Delta I_{\alpha} \propto \bar{V}_{\alpha} \left(\frac{V_{\alpha}}{t_{\alpha}} - \frac{\bar{V}_{\alpha}}{\bar{t}_{\alpha}} \right) \quad (12)$$

where the hopping amplitude inside the leads for $t < t_0$ is denoted by t_{α} and that for $t \geq t_0$ is denoted by \bar{t}_{α} . Similarly, we could write the coupling between lead α and the molecular region as V_{α} before t_0 and \bar{V}_{α} afterward. In our setup the couplings are held constant at all times, i.e., $\bar{V}_{\alpha} = V_{\alpha}$ and the temperature gradient is mimicked by changing the hopping inside the leads as discussed in section 3. Specifically, from eq 10 we have $\bar{t}_{\alpha} = (1 + \psi)t_{\alpha}$, which means that the charge current has a finite jump when a temperature gradient is applied across the molecular junction. Equation 12, however, suggests that the jump can be avoided if the temperature bias is mimicked by scaling the couplings V_{α} in the same way as the hopping inside the leads. This would imply that $\bar{V}_{\alpha}/\bar{t}_{\alpha} = V_{\alpha}/t_{\alpha}$ which is sufficient to make ΔI_{α} vanish even in the presence of a temperature gradient. We stress that this cannot be achieved in

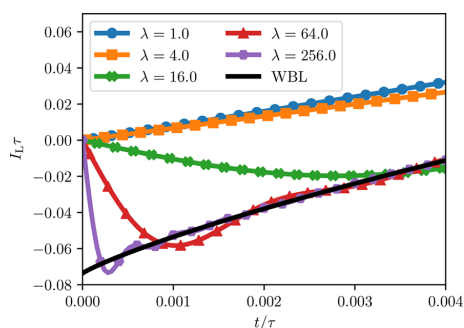


Figure 4. Short-time dynamics of charge current: Time-dependent charge current flowing from the left lead to the impurity under the influence of a potential bias and a temperature gradient. The full calculation approaches the WBL result as the scaling factor increases. However, there is an apparent discontinuity developing at $t = 0$ for $\lambda \rightarrow \infty$. While in the full calculation the charge current always vanishes for $t \rightarrow 0$, in the WBL a finite value is obtained.

the partitioned approach, because V_{α} is zero by definition for $t < t_0$ if the system is initially decoupled.

Transient Heat Current. Turning to the transient heat current we find that if only a potential bias is applied, the heat current of the full calculation is reproduced in the WBL for times $t \gtrsim \tau$ but exhibits a jump at t_0 . The short time behavior $t \ll \tau$ is depicted in Figure 5 (cf. Appendix A for $t \gtrsim \tau$). Similar

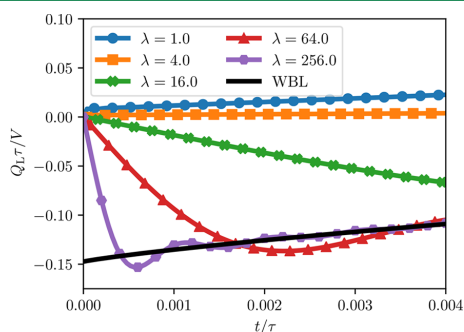


Figure 5. Transient heat current driven by a potential bias: Similar to the case of a charge current driven by a temperature gradient [cf. Figure 4] in the limit of infinite bandwidth, $\lambda \rightarrow \infty$, the heat current develops a step at t_0 . This means that the heat currents in the WBL tend to a finite value.

to the case of the charge current induced by a temperature gradient, we can see that the WBL approximates a discontinuity at t_0 in the limit $\lambda \rightarrow \infty$ in the full calculation. Again, the heat current in the full calculation always vanishes as $t \rightarrow t_0$, but the WBL leads to a finite step in the heat current already in the presence of only a potential bias. In contrast to the charge current it is not possible to extract a simple expression as eq 12, but instead the jump depends on the details of the molecular junction, i.e., on the quasi-particle energy levels.

If a temperature gradient is applied across the junction the heat current flowing from the left lead into the molecule depends strongly on the bandwidth for short times, even in the full calculation. In Figure 6 we can see that the heat current

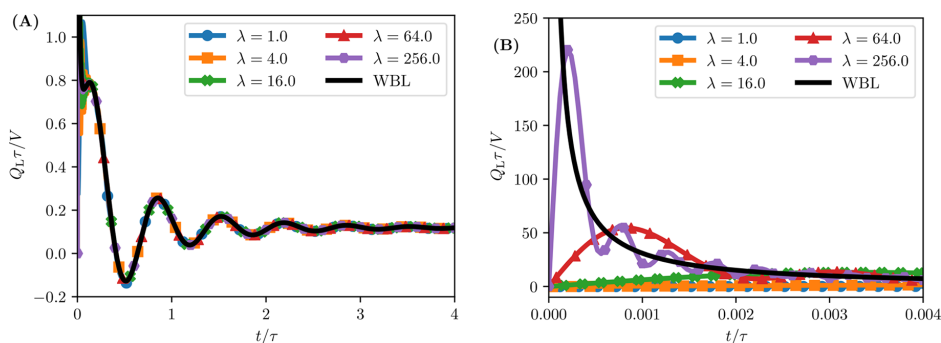


Figure 6. Heat current induced by temperature gradient: (A) Transient heat current for time comparable to the quasi-particle lifetime driven by a potential bias and a temperature gradient. For $t \gtrsim \tau$ the WBL reproduces the full calculations. (B) Transient heat current for $t \ll \tau$. The heat current in the full calculation exhibits a sharp spike which increases in height and gets closer to t_0 as the bandwidth, which is proportional to λ , increases. The WBL results diverge as $(t - t_0)^{-1}$.

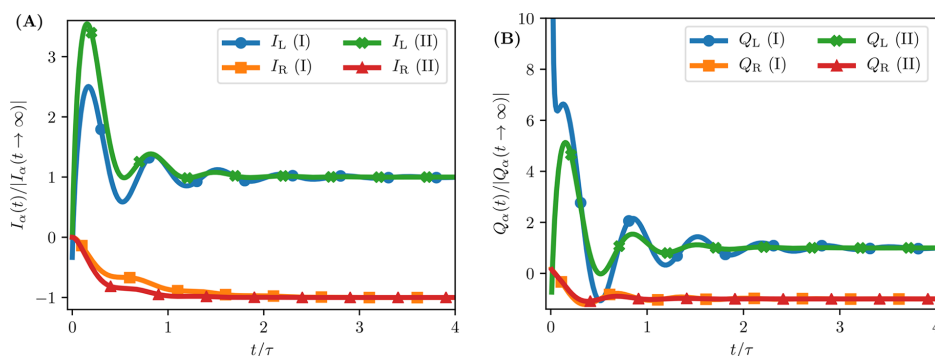


Figure 7. Fixing the short-time behavior of the currents: (A) Transient charge current for times comparable to the quasi-particle lifetime driven by a potential bias and a temperature gradient. (B) Transient heat current. In both panels we compare the WBL results obtained by applying the thermomechanical potential only inside the leads (I) to the WBL currents obtained by applying the thermomechanical potential also to the coupling between the leads and the device (II). The currents are normalized by their respective steady-state limit.

oscillates strongly for $t \lesssim \tau$ with a frequency proportional to the bandwidth (which, in turn, is proportional to λ). These oscillations correspond to transitions between the band edges of the leads and have already been observed in ref 33. In the WBL these oscillations are absent since there are no band edges, but instead the heat current diverges as

$$Q_\alpha \sim \bar{V}_\alpha \left(\frac{V_\alpha}{t_\alpha} - \frac{\bar{V}_\alpha}{\bar{t}_\alpha} \right) \frac{1}{t - t_0} \quad (13)$$

In the partition-free approach this divergence can be tamed by rescaling the couplings V_α in the same way as t_α , i.e., by applying the thermomechanical potential not only inside the leads but also on the boundary of the junction. It turns out, however, that the subleading order for the heat current exhibits a logarithmic divergence as $t \rightarrow t_0$. This is shown in Figure 7, where we compare the transient charge and heat currents in the WBL scaling only the hopping inside the leads (I) and scaling also the coupling to the impurity (II). We can see that the charge current starts from zero for both leads if also the coupling V_L is rescaled with the temperature, but it exhibits a finite jump in the lead where the temperature is changed if the temperature only rescales the hopping inside the lead. For the

heat current we see that currents in all leads exhibit a logarithmic divergence as $t \rightarrow t_0$ if both t_α and V_α are rescaled due to the change in temperature. If only t_α is rescaled, we see the aforementioned $(t - t_0)^{-1}$ divergence.

5. DISCUSSION AND CONCLUSION

In this work we have carefully examined the WBL for the transient and steady-state charge and heat currents through a molecular break junction. While we find that the long-time dynamics are faithfully captured in the WBL, at short times the WBL deviates considerably from a calculation taking the full frequency dependence of the embedding self-energy into account. This can be understood intuitively by considering that short times imply a wide spread in energy, and therefore, the dynamics will be sensitive to whether the self-energies have a high frequency cutoff (or decay) or whether they are constant for all frequencies. Specifically we have shown that the charge current induced by a temperature gradient and the heat current induced by a potential bias exhibit an unphysical jump at the initial time, when the system is suddenly quenched. Even more dramatically, the heat current diverges shortly after the quench if in addition to the potential bias also a temperature gradient is applied to the system. We have shown that these unphysical

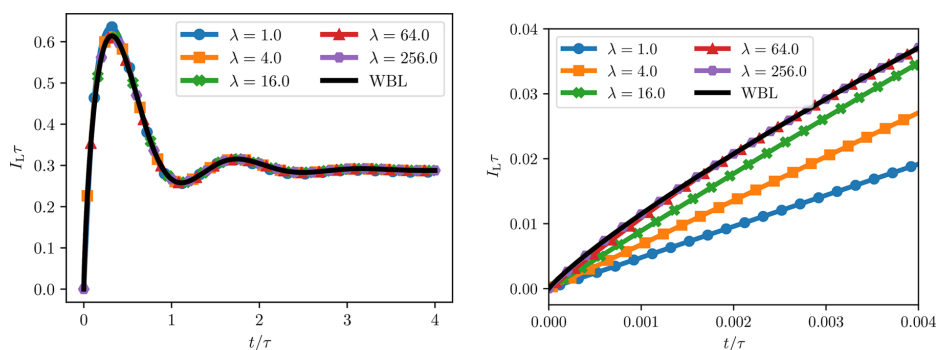


Figure 8. Time-dependent charge current flowing from the left lead to the impurity when only a potential bias is applied. The left panel shows the current for times comparable to τ , while the right panel depicts the transient current at $t \ll \tau$.

behaviors of the charge and heat current due to a temperature quench can be mitigated by considering that the temperature change affects not only the metallic leads but also the boundary between the leads and the molecular junction. Since, in practice, this boundary is not sharply defined, we consider this a legitimate fix for the WBL. We stress that this fix can only be applied in the partition-free approach to the transport problem, i.e., when the coupling between the metallic lead and the molecular junction is already taken into account in the initial state of the system (before the quench). While this fix renders the charge current physical, in the sense that the initial current vanishes, the divergence in the heat current remains but is only logarithmic.

In order to address this, we see two possible solutions:

- (1) In an actual experiment temperature gradients and potential biases will never be switched on infinitely fast, so a description as a sudden quench is questionable—to say the least—considering short time transient dynamics. It seems plausible that a sufficiently smooth continuous switching will lead to a physical result (zero initial charge and heat currents). However, from a mathematical point of view any kind of switch-on process should be representable in terms of a sequence of quenches.³⁶ In fact, the $(t - t_0)^{-1}$ divergence implies that making the intervals of the quenches shorter and shorter will not lead to a continuous heat current. Furthermore, we emphasize that even if experimentally realizable switching times are longer than the time scale at which we see the pathological behavior of the heat current, the typical time scale for transient dynamics is given by the (inverse) of maximal spread of energy levels in the nanoscale junction. The length of the required time steps to resolve such dynamics in a numerical propagation scheme is indeed comparable to the time interval of the problematic behavior observed in our simulations.
- (2) The second possible “solution” concerns the very definition of the energy or heat current between the leads and the device.^{29–31} In this work, the *heat current* Q_α has been defined as the change in time of the *internal energy* of the leads plus half of the coupling energy. Alternatively, the *energy current* J_α from a certain lead α could be defined excluding the energy associated with the coupling to the device. The divergence at small times is due to the internal energy of the leads, which occurs in

both the energy (J_α) and the heat current (Q_α). However, there is yet another possible definition of the energy flowing between the leads and the device; that is, we can define an energy current, E_α via the change of the energy stored in the device excluding the coupling. This leads to an expression $\partial_t \langle H \rangle = \sum_\alpha E_\alpha$ where $\langle H \rangle$ is the expectation value of the energy inside the junction excluding the coupling energy due to the attached leads. For a simple one-site model we have trivially $E_\alpha = \epsilon_\alpha J_\alpha$; that is, the new energy current is proportional to the charge current. However, for a multistate device region, this is not necessarily the case. From the perspective of the leads we could alternatively say that the energy of the leads, whose rate of change defines the energy current associated with each lead [cf. eq 7b], is defined as the internal energy of the leads plus the entire energy associated with the coupling between the lead and the device.

We point out that from a numerical point of view it would be highly desirable to employ the WBL to compute transient charge and heat currents, because it affords an analytical solution in terms of the quasi-particle states and energies in the molecular device. Harnessing this analytical solution would allow for an efficient simulation of mesoscopic devices. An approach somewhat intermediate between taking the full frequency dependence of the self-energy into account and the WBL could be to approximate the self-energies by Lorentzians, which provide a self-energy with the proper decay at high frequencies while allowing also for a (semi)analytic solution of the transport problem.^{22,24}

In this work we only consider the noninteracting case. Through the Keldysh formalism^{37–39} a generalization of the Landauer–Büttiker formula for interacting electrons is also possible.⁴⁰ There is a very interesting alternative approach for tackling the interacting transport problem using time-dependent density-functional theory (TD-DFT),^{41,42} where the interacting problem is mapped onto a fictitious noninteracting problem. This implies that the Landauer–Büttiker formula applies. The effect of the electron–electron interaction is taken into account via an effective potential, which renormalizes the effective bias driving the charge flow.^{43–45} Furthermore, the coupling to a thermomechanical potential can be used to generalize TD-DFT to allow for a direct description of *charge and energy flow*.^{46,47} We are confident that the combination of

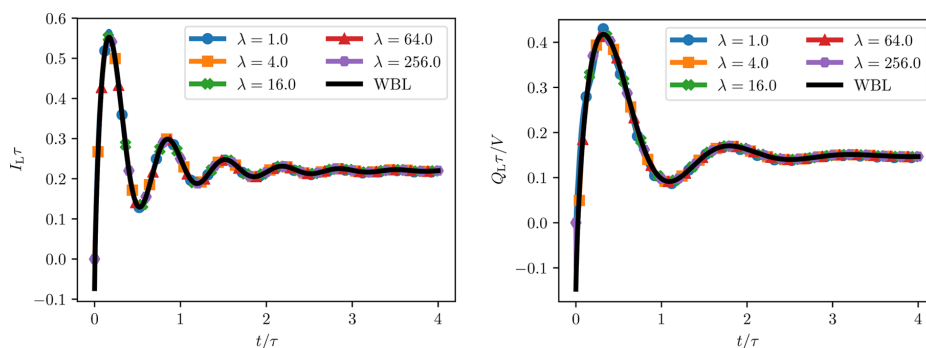


Figure 9. (left panel) Time-dependent charge current flowing from the left lead to the impurity when a potential bias and temperature gradient are applied across the junction. (right panel) Heat current induced by applying a potential bias only.

these approaches holds promise for studying the transient charge and energy flow in large molecular junctions for interacting systems.

■ APPENDIX A: ADDITIONAL PLOTS FOR THE TRANSIENT CURRENTS

In this appendix we provide additional plots comparing the full results to the WBL. Figure 8 shows the transient charge currents for times comparable to the quasi-particle lifetime τ (left panel) and for very short times (right panel). It clearly shows that the WBL represents the $\lambda \rightarrow \infty$ limit of the full calculation.

Figure 9 shows the charge and heat current for times comparable to the quasi-particle lifetime. The charge current is shown for the second scenario, i.e., when a potential bias and a temperature gradient is applied. The heat current is shown for the first scenario, i.e., when only a potential bias is applied at t_0 . We see that in both cases the WBL currents correspond to the $\lambda \rightarrow \infty$ currents obtained in the full calculation for times $t \geq t_0$. However, in the WBL both currents approach a finite value for $t \rightarrow 0$ as discussed in section 4.

■ APPENDIX B: DERIVATION OF THE STEADY-STATE ENERGY CURRENT

Here we present the analytical evaluation for the steady-state energy current discussed in section 4. In our derivation we consider a generic Hamiltonian of the form

$$\hat{H} = \hat{\Phi}^\dagger \cdot \underline{H} \cdot \hat{\Phi} + \sum_{ak} \epsilon_{ak} \hat{\phi}_{ak}^\dagger \hat{\phi}_{ak} + \sum_{ak} (\hat{\phi}_{ak}^\dagger \underline{V}_{ak}^\dagger \cdot \hat{\Phi} + \hat{\Phi}^\dagger \cdot \underline{V}_{ak} \hat{\phi}_{ak}) \quad (14)$$

which is the generalization of the Hamiltonian introduced in section 2, eq 1 to multiple states in the molecular junction. We denote vectors in the single-particle state space of the impurity by bold symbols, e.g., $\hat{\Phi}$ or \underline{V}_{ab} and matrices by underlined bold symbols, e.g., \underline{H} . In the WBL the retarded (R) and advanced (A) Green's function are given by

$$\underline{G}^R(z) = \sum_n \frac{\underline{R}_n \underline{A}_n^\dagger}{z - \omega_n} \quad (15a)$$

$$\underline{G}^A(z) = \sum_m \frac{\underline{A}_m \underline{R}_m^\dagger}{z - \omega_m^\star} \quad (15b)$$

The vectors \underline{R}_n are the *right* eigenvectors of the retarded eigenproblem and the vectors \underline{A}_m are the *right* eigenvectors to the corresponding advanced eigenproblem, i.e.,

$$\left(\underline{H} - i \frac{1}{2} \underline{\Gamma} \right) \cdot \underline{R}_n = \omega_n \underline{R}_n \quad (16a)$$

$$\left(\underline{H} + i \frac{1}{2} \underline{\Gamma} \right) \cdot \underline{A}_n = \omega_n^\star \underline{A}_n \quad (16b)$$

They are normalized by requiring $\underline{A}_m^\dagger \underline{R}_n = \delta_{nm}$. The Landauer–Büttiker formula for the energy current explicitly reads

$$J_\alpha = i \sum_{\alpha'} \sum_{nm} \underline{R}_m^\dagger \underline{\Gamma}_\alpha \cdot \underline{R}_n \underline{A}_n^\dagger \cdot \underline{\Gamma}_{\alpha'} \cdot \underline{A}_m \times \int_{-\infty}^{\infty} \frac{d\epsilon}{2\pi i} \epsilon [f(\epsilon_\alpha) - f(\epsilon_{\alpha'})] \frac{1}{\epsilon - \omega_n} \frac{1}{\epsilon - \omega_m^\star} \quad (17)$$

where we introduced the short hand $\epsilon_\alpha = \frac{\beta_\alpha}{\beta}(\epsilon - U_\alpha)$, with β_α being the (inverse) temperature, and U_α the potential in lead α (note that $\beta_\alpha/\beta = [1 + \psi_\alpha]^{-1}$). Using the representation of the Fermi function in terms of a Matsubara summation, i.e.,

$$f(z) = \frac{1}{2} - \frac{1}{\beta} \sum_f \frac{1}{z - iz_f} \quad (18)$$

with the Matsubara poles $z_f = (2f + 1)\pi/\beta$, we arrive at

$$J_\alpha = -i \sum_{\alpha'} \sum_{nm} \underline{R}_m^\dagger \cdot \underline{\Gamma}_\alpha \cdot \underline{R}_n \underline{A}_n^\dagger \cdot \underline{\Gamma}_{\alpha'} \cdot \underline{A}_m \times [C_{nm}^\alpha - C_{nm}^{\alpha'}] \quad (19)$$

with

$$C_{nm}^\alpha = \frac{1}{\beta} \sum_f \int_{-\infty}^{\infty} \frac{d\epsilon}{2\pi i} \frac{\epsilon}{\epsilon_\alpha - iz_f} \frac{1}{\epsilon - \omega_n} \frac{1}{\epsilon - \omega_m^\star} \quad (20)$$

Using

$$\frac{\epsilon}{(\epsilon - \omega_n)(\epsilon - \omega_m^\star)} = \frac{\omega_n}{\omega_n - \omega_m^\star} \frac{1}{\epsilon - \omega_n} + \frac{\omega_m^\star}{\omega_m^\star - \omega_n} \frac{1}{\epsilon - \omega_m^\star} \quad (21)$$

we can further decompose

$$C_{mm}^{\alpha} = \frac{1}{\omega_n - \omega_m^{\star}} [F_n^{\alpha} + (F_m^{\alpha})^{\star}] \quad (22a)$$

$$F_n^{\alpha} = \omega_n \frac{1}{\beta} \sum_f \int_{-\infty}^{\infty} \frac{d\epsilon}{2\pi i} \frac{1}{\epsilon_{\alpha} - iz_f} \frac{1}{\epsilon - \omega_n} \quad (22b)$$

The integral can be evaluated by closing the integration contour in the upper half of the complex plane, leading to

$$F_n^{\alpha} = \omega_n \frac{1}{\beta} \sum_{f>0} \frac{1}{iz_f - \omega_{n\alpha}} \quad (23)$$

The sum (eq 23) does not converge, but it can be combined with the corresponding sum from C_{mm}^{α} , i.e.,

$$\begin{aligned} F_n^{\alpha} - F_n^{\alpha'} &= \omega_n \frac{1}{\beta} \sum_{f>0} \left(\frac{1}{iz_f - \omega_{n\alpha}} - \frac{1}{iz_f - \omega_{n\alpha'}} \right) \\ &= \omega_n \frac{1}{\beta} \sum_{f>0} \frac{\omega_{n\alpha} - \omega_{n\alpha'}}{(iz_f - \omega_{n\alpha})(iz_f - \omega_{n\alpha'})} \end{aligned} \quad (24)$$

Expression 24 can be summed explicitly using

$$\frac{1}{\beta} \sum_{f>0} \frac{1}{iz_f - x} \frac{1}{iz_f - y} = \frac{D(-x) - D(-y)}{x - y} \quad (25)$$

where we defined

$$D(z) \equiv -\frac{1}{2\pi i} \psi_0 \left(\frac{1}{2} - i \frac{z\beta}{2\pi} \right) \quad (26)$$

in terms of the Digamma function $\psi_0(z)$. This leads to the final result

$$\begin{aligned} C_{mm}^{\alpha} - C_{mm}^{\alpha'} &= \frac{\omega_m^{\star}}{\omega_m^{\star} - \omega_n} [D(\omega_{m\alpha}^{\star}) - D(\omega_{m\alpha'}^{\star})] \\ &\quad + \frac{\omega_n}{\omega_n - \omega_m^{\star}} [D(-\omega_{n\alpha}) - D(-\omega_{n\alpha'})] \end{aligned} \quad (27)$$

where we used that $[D(z)]^{\star} = -D(-z^{\star})$, which follows from $[\psi_0(z)]^{\star} = \psi_0(z^{\star})$, we can see that the expression for the energy current is a real number.

In the derivation presented above we have replaced the frequency dependent self-energies by the frequency independent WBL approximation inside the integrand. In the following we will repeat the calculation keeping a “minimal” frequency dependence, i.e.,

$$\Sigma_{\alpha}^{\text{R/A}}(\epsilon) \approx \frac{1}{2} \Gamma_{\alpha} \frac{\lambda}{\epsilon \pm i\lambda} \quad (28)$$

which reduces to the WBL as $\lambda \rightarrow \infty$. Only at the end of the calculation, the limit $\lambda \rightarrow \infty$ is taken. Equation 28 implies that in the integral for F_n^{α} we have an additional factor of

$$\frac{\lambda^4}{(\epsilon - i\lambda)^2(\epsilon + i\lambda)^2} = \partial_x \partial_y \frac{\lambda^2}{(\epsilon - i\lambda x)(\epsilon + i\lambda y)} \Big|_{x=y=1} \quad (29)$$

Accordingly, we have

$$\begin{aligned} F_n^{\alpha} &= \omega_n \lambda^2 \partial_x \partial_y \left(\frac{1}{\beta} \sum_f \frac{1}{i\lambda x_{\alpha} - iz_f} \frac{1}{i\lambda(x+y)(i\lambda x - \omega_n)} \right. \\ &\quad \left. + \frac{1}{\beta} \sum_{f>0} \frac{\left(\frac{\beta}{\beta}\right)^2}{(iz_f - i\lambda x_{\alpha})(iz_f + i\lambda y_{\alpha})(iz_f - \omega_{n\alpha})} \right)_{x=y=1} \end{aligned} \quad (30)$$

Now we use

$$\sum_f \frac{1}{z - iz_f} = D(z) - D(-z) \quad (31a)$$

$$\begin{aligned} \sum_{f>0} \frac{1}{iz_f - a} \frac{1}{iz_f - c} \frac{1}{iz_f - b} \\ = \frac{D(-a)}{(a-b)(a-c)} + \frac{D(-b)}{(b-a)(b-c)} \\ + \frac{D(-c)}{(c-b)(c-b)} \end{aligned} \quad (31b)$$

to arrive at

$$\begin{aligned} F_n^{\alpha} &= \omega_n \lambda^2 \partial_x \partial_y \left(\frac{D(i\lambda x_{\alpha})}{i\lambda(x+y)(i\lambda x - \omega_n)} + \frac{D(i\lambda y_{\alpha})}{i\lambda(x+y)(i\lambda y + \omega_n)} \right. \\ &\quad \left. + \frac{D(-\omega_{n\alpha})}{(\omega_n - i\lambda x)(\omega_n + i\lambda y)} \right)_{x=y=1} \end{aligned} \quad (32)$$

From the asymptotic expansion of the Digamma function, $\psi_0(z) \sim \log(z)$, it follows that

$$D(i\lambda z_{\alpha}) \sim -\frac{\log \left[\lambda \frac{z\beta}{2\pi} \right]}{2\pi i} \quad (33)$$

which, in turn, leads to the asymptotic expansion

$$\begin{aligned} F_n^{\alpha} \sim \omega_n \partial_x \partial_y \left(\frac{D(-\omega_{n\alpha})}{xy} + \frac{\log \left[\frac{\lambda x\beta}{2\pi} \right]}{2\pi i(x+y)x} + \frac{\log \left[\frac{\lambda y\beta}{2\pi} \right]}{2\pi i(x+y)y} \right)_{x=y=1} \end{aligned} \quad (34)$$

Combining the terms due to the different leads yields

$$F_n^{\alpha} - F_n^{\alpha'} \sim \omega_n \left(D(-\omega_{n\alpha}) - D(-\omega_{n\alpha'}) - i \frac{1}{2\pi} \log \left[\beta_{\alpha} / \beta_{\alpha'} \right] \right) \quad (35)$$

Equation 35 does not depend on λ anymore, and we can safely take the limit $\lambda \rightarrow \infty$, because the neglected terms in the asymptotic expansion are of order λ^{-1} . Plugging eq 35 into eqs 22a and 19 finally gives

$$\begin{aligned}
 J_{\alpha} = & -i \sum_{\alpha'} \sum_{nm} \mathbf{R}_m^{\dagger} \cdot \boldsymbol{\Gamma}_{\alpha'} \cdot \mathbf{R}_n \cdot \mathbf{A}_n^{\dagger} \cdot \boldsymbol{\Gamma}_{\alpha'} \cdot \mathbf{A}_m \\
 & \times \left(\frac{\omega_n}{\omega_n - \omega_m^*} [D(-\omega_{n\alpha'}) - D(-\omega_{m\alpha'})] + \frac{\omega_m^*}{\omega_m^* - \omega_n} \right. \\
 & \left. [D(\omega_{m\alpha'}) - D(\omega_{n\alpha'})] \right) + \frac{1}{2\pi} \sum_{\alpha'} \text{Tr}[\boldsymbol{\Gamma}_{\alpha'} \cdot \boldsymbol{\Gamma}_{\alpha'}] \log \left(\frac{T_{\alpha}}{T_{\alpha'}} \right) \quad (36)
 \end{aligned}$$

The first term corresponds to the result when taking the WBL inside the integral. The second term is the correction if, instead, the WBL is taken after the integration. This correction term vanishes if there is no temperature gradient between the leads. Furthermore, it vanishes if the coupling matrices do not overlap in the single-particle state space of the molecular Hamiltonian. In the results presented in this work this correction is crucial in order to reproduce the steady-state heat currents in the WBL.

AUTHOR INFORMATION

Corresponding Author

*E-mail: florian.eich@mps.d.mpg.de.

ORCID

F. G. Eich: [0000-0002-0434-6100](https://orcid.org/0000-0002-0434-6100)

Notes

The authors declare no competing financial interest.

ACKNOWLEDGMENTS

F.G.E. has received funding from the European Union's Framework Programme for Research and Innovation Horizon 2020 (2014-2020) under the Marie Skłodowska-Curie Grant Agreement No. 701796. R.T. and M.A.S. acknowledge funding by the DFG through the Emmy Noether programme (SE 2558/2-1). A.R. acknowledges financial support from the European Research Council (ERC-2015-AdG-694097) and Grupos Consolidados (ITS78-13).

REFERENCES

- Landauer, R. Spatial Variation of Currents and Fields Due to Localized Scatterers in Metallic Conduction. *IBM J. Res. Dev.* **1957**, *1*, 223–231.
- Büttiker, M.; Imry, Y.; Landauer, R.; Pinhas, S. Generalized many-channel conductance formula with application to small rings. *Phys. Rev. B: Condens. Matter Mater. Phys.* **1985**, *31*, 6207–6215.
- Landauer, R. Conductance determined by transmission: probes and quantised constriction resistance. *J. Phys.: Condens. Matter* **1989**, *1*, 8099.
- Goldsmid, H. J. *Introduction to Thermoelectricity*; Springer Series in Materials Science; Springer, 2009.
- Dubi, Y.; Di Ventra, M. Thermoelectric Effects in Nanoscale Junctions. *Nano Lett.* **2009**, *9*, 97–101.
- Mecklenburg, M.; Hubbard, W. A.; White, E. R.; Dhall, R.; Cronin, S. B.; Aloni, S.; Regan, B. C. Nanoscale temperature mapping in operating microelectronic devices. *Science* **2015**, *347*, 629–632.
- Halbatal, D.; Cuppens, J.; Shalom, M. B.; Embon, L.; Shadmi, N.; Anahory, Y.; Naren, H. R.; Sarkar, J.; Uri, A.; Ronen, Y.; Myasoedov, Y.; Levitov, L. S.; Joselevich, E.; Geim, A. K.; Zeldov, E. Nanoscale thermal imaging of dissipation in quantum systems. *Nature* **2016**, *539*, 407–410. Letter.
- Kinoshita, I.; Mitsu, A.; Munakata, T. Electronic excited state of NO adsorbed on Cu(111): A two-photon photoemission study. *J. Chem. Phys.* **1995**, *102*, 2970–2976.
- Gauyacq, J.; Borisov, A.; Raşev, G. Lifetime of excited electronic states at surfaces: CO(2*) resonance on Cu(111) and Cu(100) surfaces. *Surf. Sci.* **2001**, *490*, 99–115.

- Kirchmann, P. S.; Loukakos, P. A.; Bovensiepen, U.; Wolf, M. Ultrafast electron dynamics studied with time-resolved two-photon photoemission: intra- and interband scattering in C 6 F 6 /Cu(111). *New J. Phys.* **2005**, *7*, 113.
- Chulkov, E. V.; Borisov, A. G.; Gauyacq, J. P.; Sánchez-Portal, D.; Silkin, V. M.; Zhukov, V. P.; Echenique, P. M. Electronic Excitations in Metals and at Metal Surfaces. *Chem. Rev.* **2006**, *106*, 4160–4206.
- Myllyperkiö, P.; Herranen, O.; Rintala, J.; Jiang, H.; Mudimela, P. R.; Zhu, Z.; Nasibulin, A. G.; Johansson, A.; Kauppinen, E. I.; Ahlskog, M.; Pettersson, M. Femtosecond Four-Wave-Mixing Spectroscopy of Suspended Individual Semiconducting Single-Walled Carbon Nanotubes. *ACS Nano* **2010**, *4*, 6780–6786.
- Cocker, T. L.; Jelic, V.; Gupta, M.; Molecules, S. J.; Burgess, J. A. J.; Reyes, G. D. L.; Titova, L. V.; Tsui, Y. Y.; Freeman, M. R.; Hegmann, F. A. An ultrafast terahertz scanning tunnelling microscope. *Nat. Photonics* **2013**, *7*, 620.
- Ni, G. X.; Wang, L.; Goldflam, M. D.; Wagner, M.; Fei, Z.; McLeod, A. S.; Liu, M. K.; Keilmann, F.; Özyilmaz, B.; Castro Neto, A. H.; Hone, J.; Fogler, M. M.; Basov, D. N. Ultrafast optical switching of infrared plasmon polaritons in high-mobility graphene. *Nat. Photonics* **2016**, *10*, 244.
- Karnetzky, C.; Zimmermann, P.; Trummer, C.; Duque-Sierra, C.; Wörle, M.; Kienberger, R.; Holleitner, A. Towards femtosecond on-chip electronics. *ArXiv e-prints* 2017.
- Cini, M. Time-dependent approach to electron transport through junctions: General theory and simple applications. *Phys. Rev. B: Condens. Matter Mater. Phys.* **1980**, *22*, 5887–5899.
- Stefanucci, G.; Almladh, C.-O. Time-dependent partition-free approach in resonant tunneling systems. *Phys. Rev. B: Condens. Matter Mater. Phys.* **2004**, *69*, 195318.
- Luttinger, J. M. Theory of Thermal Transport Coefficients. *Phys. Rev.* **1964**, *135*, A1505–A1514.
- Shastry, B. S. Electrothermal transport coefficients at finite frequencies. *Rep. Prog. Phys.* **2009**, *72*, 016501.
- Eich, F. G.; Principi, A.; Di Ventra, M.; Vignale, G. Luttinger-field approach to thermoelectric transport in nanoscale conductors. *Phys. Rev. B: Condens. Matter Mater. Phys.* **2014**, *90*, 115116.
- Zhu, Y.; Maciejko, J.; Ji, T.; Guo, H.; Wang, J. Time-dependent quantum transport: Direct analysis in the time domain. *Phys. Rev. B: Condens. Matter Mater. Phys.* **2005**, *71*, 075317.
- Maciejko, J.; Wang, J.; Guo, H. Time-dependent quantum transport far from equilibrium: An exact nonlinear response theory. *Phys. Rev. B: Condens. Matter Mater. Phys.* **2006**, *74*, 085324.
- Zheng, X.; Wang, F.; Yam, C. Y.; Mo, Y.; Chen, G. Time-dependent density-functional theory for open systems. *Phys. Rev. B: Condens. Matter Mater. Phys.* **2007**, *75*, 195127.
- Zhang, Y.; Chen, S.; Chen, G. First-principles time-dependent quantum transport theory. *Phys. Rev. B: Condens. Matter Mater. Phys.* **2013**, *87*, 085110.
- Verzijl, C. J. O.; Seldenthuis, J. S.; Thijssen, J. M. Applicability of the wide-band limit in DFT-based molecular transport calculations. *J. Chem. Phys.* **2013**, *138*, 094102.
- Shi, P.; Hu, M.; Ying, Y.; Jin, J. Noise spectrum of quantum transport through double quantum dots: Renormalization and non-Markovian effects. *AIP Adv.* **2016**, *6*, 095002.
- Báldea, I. Invariance of molecular charge transport upon changes of extended molecule size and several related issues. *Beilstein J. Nanotechnol.* **2016**, *7*, 418–431.
- Myöhänen, P.; Stan, A.; Stefanucci, G.; van Leeuwen, R. Kadanoff-Baym approach to quantum transport through interacting nanoscale systems: From the transient to the steady-state regime. *Phys. Rev. B: Condens. Matter Mater. Phys.* **2009**, *80*, 115107.
- Arrachea, L.; Moskalets, M.; Martin-Moreno, L. Heat production and energy balance in nanoscale engines driven by time-dependent fields. *Phys. Rev. B: Condens. Matter Mater. Phys.* **2007**, *75*, 245420.

- (30) Esposito, M.; Ochoa, M. A.; Galperin, M. Nature of heat in strongly coupled open quantum systems. *Phys. Rev. B: Condens. Matter Mater. Phys.* **2015**, *92*, 235440.
- (31) Ludovico, M.; Arrachea, L.; Moskalets, M.; Sánchez, D. Periodic Energy Transport and Production in Quantum Electronics. *Entropy* **2016**, *18*, 419.
- (32) Ludovico, M. F.; Lim, J. S.; Moskalets, M.; Arrachea, L.; Sánchez, D. Dynamical energy transfer in ac-driven quantum systems. *Phys. Rev. B: Condens. Matter Mater. Phys.* **2014**, *89*, 161306.
- (33) Eich, F. G.; Di Ventra, M.; Vignale, G. Temperature-driven transient charge and heat currents in nanoscale conductors. *Phys. Rev. B: Condens. Matter Mater. Phys.* **2016**, *93*, 134309.
- (34) Tuovinen, R.; Perfetto, E.; Stefanucci, G.; van Leeuwen, R. Time-dependent Landauer-Büttiker formula: Application to transient dynamics in graphene nanoribbons. *Phys. Rev. B: Condens. Matter Mater. Phys.* **2014**, *89*, 085131.
- (35) Ridley, M.; MacKinnon, A.; Kantorovich, L. Current through a multilead nanojunction in response to an arbitrary time-dependent bias. *Phys. Rev. B: Condens. Matter Mater. Phys.* **2015**, *91*, 125433.
- (36) Ruggenthaler, M.; Penz, M.; van Leeuwen, R. Existence, uniqueness, and construction of the density-potential mapping in time-dependent density-functional theory. *J. Phys.: Condens. Matter* **2015**, *27*, 203202.
- (37) Keldysh, L. V. Diagram technique for nonequilibrium processes. *Zh. Eksp. Teor. Fiz.* **1964**, *47*, 1515–1527.
- (38) Keldysh, L. V. Diagram technique for nonequilibrium processes. *Sov. Phys. JETP* **1965**, *20*, 1018–1026.
- (39) Stefanucci, G.; van Leeuwen, R. *Nonequilibrium Many-Body Theory of Quantum Systems: A Modern Introduction*; Cambridge University Press: Cambridge, 2013.
- (40) Meir, Y.; Wingreen, N. S. Landauer formula for the current through an interacting electron region. *Phys. Rev. Lett.* **1992**, *68*, 2512–2515.
- (41) Runge, E.; Gross, E. K. U. Density-Functional Theory for Time-Dependent Systems. *Phys. Rev. Lett.* **1984**, *52*, 997.
- (42) Ullrich, C. A. *Time-Dependent Density-Functional Theory: Concepts and Applications*; Oxford Graduate Texts; Oxford University Press: Oxford, 2012.
- (43) Kurth, S.; Stefanucci, G.; Almladh, C.-O.; Rubio, A.; Gross, E. K. U. Time-dependent quantum transport: A practical scheme using density functional theory. *Phys. Rev. B: Condens. Matter Mater. Phys.* **2005**, *72*, 035308.
- (44) Stefanucci, G.; Kurth, S.; Gross, E.; Rubio, A. In *Molecular and Nano Electronics: Analysis, Design and Simulation*; Seminario, J., Ed.; Theoretical and Computational Chemistry Supplement C; Elsevier, 2007; Vol. 17; pp 247–284.
- (45) Kurth, S.; Stefanucci, G. Dynamical Correction to Linear Kohn-Sham Conductances from Static Density Functional Theory. *Phys. Rev. Lett.* **2013**, *111*, 030601.
- (46) Eich, F. G.; Di Ventra, M.; Vignale, G. Density-Functional Theory of Thermoelectric Phenomena. *Phys. Rev. Lett.* **2014**, *112*, 196401.
- (47) Eich, F. G.; Ventra, M. D.; Vignale, G. Functional theories of thermoelectric phenomena. *J. Phys.: Condens. Matter* **2017**, *29*, 063001.

Publication VI

Non-adiabatic electron dynamics in tunneling junctions: lattice Exchange-Correlation potential

Fabio Covito, Angel Rubio and Florian G. Eich, *Journal of Chemical Theory and Computation*, accepted, (2019).

As mentioned in the previous chapters, the study of electrical circuits at the microscopical level is a matter of high technological relevance. A widespread theoretical framework for the description of transport through nanoscale devices is TDDFT. Within TDDFT, the exchange correlation functional plays a fundamental role. Over the years, numerous approximations to this functional have been developed to best capture the effects of the Coulomb interaction in quantum systems. Practically all functionals used nowadays are adiabatic, meaning memory effects are disregarded altogether. Although the success of adiabatic functionals is undoubtable, many non-equilibrium phenomena can only be faithfully described by taking into account memory. The development of functionals going beyond the adiabatic approximation is, therefore, an appealing subject. In fact, this would not only provide a powerful tool for the study of strongly correlated quantum phenomena, but would give us insight into the exact functional, final ambition of TDDFT. This publication contributes to the understanding of non-adiabatic effects by putting forward a non-adiabatic exchange-correlation functional for lattice models describing a generic transport setup. The construction is based on the potential proposed in Ref. [69], which is found by reverse-engineering the analytic solution of a single impurity coupled to a reservoir. We generalize this exchange-correlation potential by exploiting gauge symmetry: in an impurity-reservoir system, applying a potential to the impurity is equivalent to applying the opposite potential to the reservoir. Making use of this argument we first extend the potential of Ref. [69]

to a reservoir-dot-reservoir system and, finally to a generic lattice model. The proposed functional reduces to the Adiabatic Local Density Approximation in the static limit, i.e. no current flowing through the device, and to the exact result for a single dot transport setup [70]. For one-dimensional tight-binding chains our exchange-correlation potential correctly describes Coulomb blockade physics. Additionally, at the particle-hole symmetric point, another feature appears as a softening of the Coulomb blockade at roughly constant βU , where β is the inverse temperature and U the on-site repulsion.

An interesting direction to pursue would be the generalization of the proposed functional to deal with situations beyond lattice models. This is, indeed, highly-desirable as it would give us insight into the role of non-adiabaticity in the description of correlated phenomena, other than provide us with a valuable tool to study quantum systems. Finally, the proposed exchange-correlation potential could be generalized to include the effects of temperature to study thermo-electric transport employing thermal TDDFT [65–68].

In the following, I add a few remarks, which are not explicitly addressed in the published manuscript, but complement the discussion of the work.

Convergence of the exchange-correlation potential. It is well known, from exact results, that the step-like form of the exchange-correlation (xc) potential is a necessary feature for the description of correlation. Unfortunately, this characteristic gives rise to sharp local features, which are emphasized at low temperature. For this reason, the self-consistent determination of the xc potential is especially problematic as temperature decreases. Simple mixing schemes, in fact, completely fail to converge the proposed xc potential as we approach the transition temperature to the Coulomb Blockade regime. A possible route is to consider more sophisticated mixing schemes that account for the sharp localized features. As an example, we experimented with the method used in Ref. [71], in which the potential at each site is found while keeping currents and potentials fixed everywhere else in the system and repeating the procedure for all sites, going back and forth in the chain, until convergence. This method is indeed more efficient than simple linear mixing. Due to the sharp localized features, it appears reasonable to

assume that methods considering averages of errors or more delocalized quantities fail to efficiently converge the xc potential. Surprisingly, we found that the Pulay method, the one used in this publication, outperforms the above-mentioned method used in Ref. [71], even though it only considers the average deviations at each self-consistent cycle to construct the updated guess.

Low temperature regime. As highlighted in the previous paragraph, the convergence of the xc potential becomes challenging as temperatures decreases. Before looking for more complex and efficient convergence methods, though, it is important to make an observation regarding the xc potential proposed in this work. The starting point of the construction is, in fact, a potential obtained by a reverse-engineering procedure of a rate equations solution [69], which may not be the best route to follow to describe low-temperature physics. For this reason, a more careful study is needed to understand the temperature range of applicability of this potential derived and, in turn, of the one derived in this publication.

Choice of the pre-factors. The choice of the pre-factors $\alpha_k = 1/N$ for the construction of the non-adiabatic exchange-correlation potential presented in the paper is based on the dependence of the functional itself on the current. This, in fact, is written in terms of the dimensionless “normalized” currents c . For each current associated with a link of the lattice, the normalization factor is expressed in terms of the characteristic time of the link, given by the inverse of its hopping amplitude. Nonetheless, a more in-depth study of the implications of different choices of α_k might provide insight into ways of improving the proposed construction.

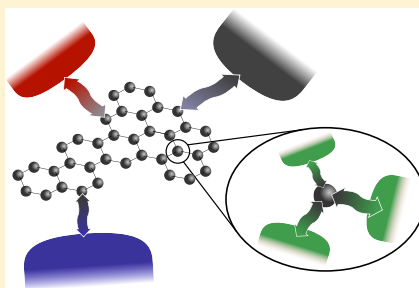


Nonadiabatic Electron Dynamics in Tunneling Junctions: Lattice Exchange-Correlation Potential

Fabio Covito,^{*†} Angel Rubio,^{*†} and Florian G. Eich^{*†}

Max Planck Institute for the Structure and Dynamics of Matter and Center for Free Electron Laser Science, 22761 Hamburg, Germany

ABSTRACT: The search for exchange-correlation functionals going beyond the adiabatic approximation has always been a challenging task for time-dependent density-functional theory. Starting from known results and using symmetry properties, we put forward a nonadiabatic exchange-correlation functional for lattice models describing a generic transport setup. We show that this functional reduces to known results for a single quantum dot connected to one or two reservoirs and furthermore yields the adiabatic local-density approximation in the static limit. Finally, we analyze the features of the exchange-correlation potential and the physics it describes in a linear chain connected to two reservoirs where the transport is induced by a bias voltage applied to the reservoirs. We find that the Coulomb blockade is correctly described for a half-filled chain, while additional effects arise as the doping of the chain changes.



1. INTRODUCTION

The miniaturization of electrical circuits is of great importance for future technologies. Fundamental building blocks for circuits can implement their functionality within single molecules, e.g., by trapping them in mechanically controllable break junctions, and transport can be studied experimentally.^{1–9} At these length scales, the understanding of such devices requires a quantum mechanical description. A wealth of approaches can be used to study said devices, and through the years, a lot of effort has been put into this matter. One of the most successful theories for describing charge transport through nanoscale devices is the Landauer–Büttiker (LB) approach,^{10–12} where transport is expressed as a scattering problem. In the LB framework, the electrons traverse the device ballistically; i.e., electron–electron scattering is ignored. However, the LB approach can be generalized for interacting electrons within nonequilibrium Green’s (NEGF) function theory.^{13,14} A numerically more efficient alternative to NEGF for the description of interacting quantum systems is density-functional theory (DFT).^{15,16} Since transport is by definition a nonequilibrium phenomenon, time-dependent DFT (TD-DFT)^{17–19} has to be employed for studying molecular transport.²⁰ This leads to the remarkable result that, in principle, the steady-state flow of interacting electrons through a transport device can be computed from the LB formula, provided it is evaluated using non-interacting Kohn–Sham (KS) electrons of TD-DFT moving in an effective local potential. In practice, however, this approach is limited by the quality of the available approximations to the effective potential. A common approach is to use approximations derived in the context of equilibrium or ground state DFT in order to evaluate the effective potential in the device region. This procedure is referred to as adiabatic approximation within TD-

DFT, which ignores dynamical effects (memory).^{21–23} Embedding approaches, like dynamical mean-field theory²⁴ or density matrix embedding theory,²⁵ have received a lot of attention recently due to their ability to describe strongly correlated electrons. In the context of density-functional theories, impurity models, such as the Anderson impurity model,²⁶ have been studied extensively over the past years in the Kondo and Coulomb blockade regime.^{27–39} These studies provided important insight in how to describe strongly correlated physics within DFT approaches by reverse engineering the (nearly) exact effective potentials for simple model systems. A big remaining challenge is to generalize these effective potentials for generic transport setups.

In this work, we put forward an effective potential based on its analytical derivation for the case of a single impurity coupled to one lead.³⁸ A recent study comparing results using this effective potential to results from numerically exact, time-dependent density-matrix renormalization group demonstrated the quality of this effective potential for an impurity site coupled to a single lead.⁴⁰ We generalize the effective potential to any tight-binding transport setup. The generalization to any system is carried out by exploiting a simple gauge symmetry argument: in a system composed of an impurity connected to a lead, the application of a potential to the impurity is equivalent to the application of the opposite potential to the lead. We first show how this argument can be used to generalize the effective potential of the one site–one lead setup³⁸ to a simple transport setup composed of one site coupled to two leads. The resulting effective potential yields the known exact results, which reproduce Coulomb blockade

Received: September 6, 2019

Published: November 18, 2019

physics in the single impurity Anderson model.³⁹ Then, we further generalize the effective potential to a generic setup employing a local-density (or embedding)-like approximation, which reduces to the known adiabatic local-density approximation (LDA) for lattice models²⁷ in the static limit.

2. MODEL

In this work, we consider a tight-binding model for a generic transport device, sketched in Figure 1. The Hamiltonian for the system studied reads

$$\begin{aligned} \hat{H} = & - \sum_{i\sigma} t \left[\hat{\phi}_{i\sigma}^\dagger \hat{\phi}_{(i+1)\sigma} + \hat{\phi}_{(i+1)\sigma}^\dagger \hat{\phi}_{i\sigma} \right] + \sum_{\alpha k\sigma} \epsilon_{\alpha k} \hat{\phi}_{\alpha k\sigma}^\dagger \hat{\phi}_{\alpha k\sigma} \\ & + \sum_{\alpha, i \in C_{\alpha\sigma}} \left[\hat{\phi}_{\alpha k\sigma}^\dagger V_{(ak)} \hat{\phi}_{i\sigma} + \hat{\phi}_{i\sigma}^\dagger V_{i(ak)} \hat{\phi}_{\alpha k\sigma} \right] \\ & + U \sum_i \hat{\phi}_{i\uparrow}^\dagger \hat{\phi}_{i\uparrow} \hat{\phi}_{i\downarrow}^\dagger \hat{\phi}_{i\downarrow} + g \hat{N} \end{aligned} \quad (1)$$

Here, $\hat{\phi}_{i\sigma}^\dagger$ and $\hat{\phi}_{i\sigma}$ are the field operators of site i and spin σ of the device, t is the energy associated with the hopping between sites, g is the gate voltage applied to the device, U is the on-site coulomb interaction, and \hat{N} is the particle number operator of the device. The chemical potential μ is set to zero. The field operators $\hat{\phi}_{\alpha k\sigma}^\dagger$ and $\hat{\phi}_{\alpha k\sigma}$ add and remove electrons in lead α , and the dispersion relation of the electrons inside the leads is given by $\epsilon_{\alpha k}$. Finally, $V_{(ak)}$ is the hopping amplitude and C_α is the set of sites of the device that are connected to lead α . In this work, the leads are modeled as non-interacting one-dimensional tight-binding chains, giving the dispersion $\epsilon_{ak} = -2t \cos k$. This means that the electrons have the same hopping amplitude in the leads and in the device region. In the following, we consider the spin unpolarized case; i.e., observables do not depend on spin, e.g., $n_{i\uparrow} = n_{i\downarrow} \equiv n_i/2$. We use a TD-DFT approach to numerically describe the dynamics of the system. This means that the evolution of the charge density for the system governed by Hamiltonian (1) is computed from an effectively non-interacting system. This is governed by a Hamiltonian similar to eq 1, where the interaction term is replaced by an effective local potential, the so-called KS potential. Once an approximation for the effective potential is given, the charge flow can be computed from the non-interacting system. In the steady state (SS), this charge flow is completely determined by the spin-

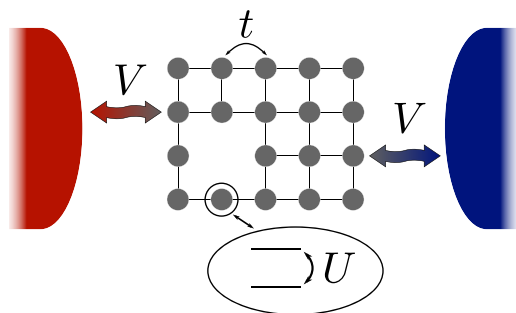


Figure 1. Sketch of a typical lattice model used to describe transport devices. The electrons can hop to the nearest neighbors with amplitude t and to the connected leads with amplitude V and have an on-site interaction U .

summed density matrix of the device region, D^{SS} , the currents between sites i and j of the device, I_{ij}^{SS} , and the currents from the device to lead α , I_α^{SS} . For the non-interacting system, they are given by

$$D^{\text{SS}} = 2 \sum_{\alpha} \int \frac{d\epsilon}{2\pi} D_{\alpha}(\epsilon) f(\epsilon + b_{\alpha}) \quad (2a)$$

$$I_{ij}^{\text{SS}} = -\text{Im}([H, D^{\text{SS}}]_{ij}) \quad (2b)$$

$$I_{\alpha}^{\text{SS}} = 2 \sum_{\alpha'} \int \frac{d\epsilon}{2\pi} T_{\alpha\alpha'}(\epsilon) [f(\epsilon + b_{\alpha}) - f(\epsilon + b_{\alpha'})] \quad (2c)$$

Here, $f(\epsilon + b_{\alpha})$ is the Fermi function of lead α with associated voltage bias b_{α} , and the matrices D_{α} and $T_{\alpha\alpha'}$ are defined as

$$D_{\alpha}(\epsilon) \equiv G^{\text{R}}(\epsilon) \Gamma_{\alpha} G^{\text{A}}(\epsilon) \quad (3a)$$

$$T_{\alpha\alpha'}(\epsilon) \equiv \text{Tr}[\Gamma_{\alpha} G^{\text{R}}(\epsilon) \Gamma_{\alpha'} G^{\text{A}}(\epsilon)] \quad (3b)$$

$$\Gamma_{\alpha} \equiv 2 \frac{|V_{\alpha}|^2}{t} \quad (3c)$$

D_{α} is the density of states of the device projected on lead α , and the off-diagonal matrix elements of $T_{\alpha\alpha'}(\epsilon)$ are the transmission coefficients between leads. Both are defined in terms of the advanced/retarded Green's function of the device region, $G^{\text{A/R}}$, and the decay rate associated with lead α , Γ_{α} . The trace is performed over the device region. In principle, Γ_{α} is energy dependent, however, here we take the wide-band limit approximation. This disregards the energy dependence of the leads' density of states, taking it constant and equal to its value at the Fermi energy.^{41–47} This is justified when the applied bias is small compared to the leads' bandwidth. One major advantage of taking the wide-band limit is that it allows for an analytical evaluation of the LB formula at finite temperatures.^{48–50}

3. GENERALIZED NONADIABATIC EXCHANGE-CORRELATION FUNCTIONAL

The effective potential contains two contributions: the scattering induced by the nuclei or the boundaries of the device and the effect of electron–electron collisions. The former is commonly referred to as “external potential” and characterizes the device, while the latter is the so-called (Hartree-)exchange-correlation (Hxc) potential. The Hxc potential derived in ref 38 for a quantum dot coupled to a single reservoir is given by

$$\begin{aligned} \epsilon_{\text{Hxc}}(n, c) &= \frac{1}{\beta} \log \left[\frac{\sqrt{g^2 + (2-C)C} - g}{C} \right] \\ &= -\frac{1}{\beta} \log \left[\frac{\sqrt{g^2 + (2-C)C} + g}{2-C} \right] \end{aligned} \quad (4)$$

with $g = (1-C) \exp(U\beta/2) - C \sinh(U\beta/2)$, $C = n - c$, $c = -\dot{n}/\Gamma = I/\Gamma$, where Γ is the decay rate associated with the only reservoir, U is the interaction strength, and β is the inverse temperature. We point out that there is a typo in the corresponding formula (equation 8b in ref 38) that has been corrected here. Note the dependence of the functional on the normalized current c : this will be important in the generalization to generic lattice geometries. The potential (4) can be rewritten as a functional of the density n and current to the dot I by using

the continuity equation $I \equiv -\dot{n}$. The two forms of the functional given in eq 4 are equivalent but numerically stable in different regimes: the first one is stable for $n - I/(2\Gamma) > 1$, while the second one is stable for $n - I/(2\Gamma) < 1$. These expressions differ from the one given in ref 38 by a constant of $U/2$. This constant shift ensures half-filling at vanishing chemical potential ($\mu = 0$) for any interaction strength. Starting from this functional, we first present a generalization to a reservoir-dot-reservoir system, then to a dot connected to any number of leads, and finally to any transport setup in the tight-binding model.

The functional (4) provides a form for the dot potential in the dot-reservoir system. By gauge symmetry, the dynamics are not altered if one applies the opposite potential to the reservoir instead. In general, any pair of dot (v_{Hxc}) and reservoir (V_{xc}) potentials

$$v_{\text{Hxc}} = \alpha \epsilon_{\text{Hxc}}(n, c) \quad (5a)$$

$$V_{\text{xc}} = (\alpha - 1) \epsilon_{\text{Hxc}}(n, c) \quad (5b)$$

with $0 \leq \alpha \leq 1$ gives rise to equivalent dynamics by gauge symmetry.

The crucial aspect of the previous argument is that we can subdivide the system into two parts. When we consider a transport scenario, where an additional reservoir is attached to the device, there are two possible ways of subdividing the system by grouping the dot either with the left or the right lead. For both configurations, we can apply the procedure leading to eq 5a, and summing the resulting potentials leads to

$$v_{\text{Hxc}} = \alpha_1 \epsilon_{\text{Hxc}}(n, c) + \alpha_2 \epsilon_{\text{Hxc}}(n, -c) \quad (6a)$$

$$V_{\text{xc}}^1 = (\alpha_1 - 1) \epsilon_{\text{Hxc}}(n, c) + \alpha_2 \epsilon_{\text{Hxc}}(n, -c) \quad (6b)$$

$$V_{\text{xc}}^2 = \alpha_1 \epsilon_{\text{Hxc}}(n, c) + (\alpha_2 - 1) \epsilon_{\text{Hxc}}(n, -c) \quad (6c)$$

where we use the fact that in the steady state the currents flowing from the dot to the two leads are opposite to each other by Kirchhoff's law and that both leads are characterized by the same decay rate. By imposing the additional condition $\alpha_1 + \alpha_2 = 1$, one can ensure that in the limit of vanishing current the potentials in the reservoirs are identically zero. This means that the density of the dot does not induce a potential anywhere else but locally when no currents flow (LDA).

The generalization to any number of leads connected to a dot follows immediately from the previous considerations, and the potentials read

$$v_{\text{Hxc}} = \sum_k \alpha_k \epsilon_{\text{Hxc}}(n, c^k) \quad (7a)$$

$$V_{\text{xc}}^k = (\alpha_k - 1) \epsilon_{\text{Hxc}}(n, c^k) + \sum_{l \neq k} \alpha_l \epsilon_{\text{Hxc}}(n, c^l) \quad (7b)$$

where $c^k = I^k/\Gamma_k$ is the normalized current flowing to reservoir k . Again, the condition $\sum_k \alpha_k = 1$ leads to a local approximation in the adiabatic limit (no currents), and V_{xc}^k is identically zero for all k 's. This condition is still not enough to fix an arbitrary number of α 's. We make the choice $\alpha_k = \alpha$ motivated by the fact that only the dimensionless currents, c^k , enter the functional. As a direct consequence, the first order nonadiabatic correction for the potential v_{Hxc} , i.e., the correction due to having finite but small currents flowing, vanishes by virtue of Kirchhoff's law (charge conservation in the steady state) provided all decay rates are identical. With the aforementioned considerations, the potentials can be rewritten as

$$v_{\text{Hxc}} = \frac{1}{N_L} \sum_k \epsilon_{\text{Hxc}}(n, c^k) \quad (8a)$$

$$V_{\text{xc}}^k = v_{\text{Hxc}} - \epsilon_{\text{Hxc}}(n, c^k) \quad (8b)$$

where N_L is the number of reservoirs connected to the dot. From the expressions (8a and 8b), it is evident how the electron density of the dot induces a potential locally and on the reservoirs, i.e., the elements connected to it. This is important for the generalization to any tight-binding model, where the dot is connected not only to leads but also to other sites.

For each site, we have the local potential v_{Hxc} and the nonlocal contributions V_{xc} coming from other sites. When only nonlocal contributions due to directly connected sites are considered, the exchange-correlation potential of a general site i can be written as

$$v^i = v_{\text{Hxc}}^i + \sum_{\langle k|i \rangle} V_{\text{xc}}^{ik} \quad (9)$$

where the first term is the local contribution and the remainder is the sum of the nonlocal ones. The local component v_{Hxc}^i is eq 8a calculated with the density n_i and the normalized currents c_i^k going out of site i . The nonlocal part, $V_{\text{xc}}^{ik} \equiv v_{\text{Hxc}}^k - \epsilon_{\text{Hxc}}(n_i, c_i^k)$, is the nonlocal contribution (8b) evaluated at the density of the nearest neighbors and the associated currents going to site i . Finally, $\langle k|i \rangle$ indicates the restriction of the sums to the nearest neighbors only. In equilibrium, when no currents are flowing in the system, the nonlocal contribution vanishes and the effective potential reduces to the LDA for lattice systems. For the reservoirs, the local component, v_{Hxc}^i , cannot be defined as no density can be associated with them in the wide-band limit and, like in the expression for the reservoir-dot-reservoir, only the nonlocal contributions appear. It is important here to notice the dependence of the functional on c_i^k : this is the normalized (dimensionless) current flowing from site i to site k . The normalization factor, Γ^k , can only be evaluated for sites connected to leads. For currents between sites in the device region, eq 3c can be evaluated for $V_a \rightarrow t$, yielding $2t$ for the normalization factor. Equation 9 represents the main result of this paper. It is applicable to any lattice system of any dimensionality and connectivity with local interactions. In the following section, an analysis of the effect of this nonadiabatic functional is presented.

4. RESULTS

In this section, we investigate the influence of the derived exchange-correlation functional on the transport properties of nanojunctions. In particular, we analyze the steady state of tight-binding chains connected to two leads, one at each end of the chain. The development of a steady state is a consequence of the application of a potential difference to the leads. The xc-potential (9) is then found self-consistently as it depends on the steady state densities and currents and vice versa. To compare results coming from different functionals or different interaction strengths, we tune the gate voltage to have a fixed number of electrons in the chain. The reason for choosing this approach stems from the strong dependence of the number particles on the temperature of the leads (for a fixed gate), which is reflected, e.g., in the resistance, and this can be different for different functionals/interaction strengths.

The tight-binding parameters chosen for the simulations expressed in units of the hopping amplitude, which is set to $t = 1$ eV, are temperature $0 < k_B T = \beta^{-1} \leq t$ and bias voltage

$b_{L,R} = \pm t/8$. The other parameters that determine the junction are not constant for all calculations and will be specified when needed. All resistances shown in the following are normalized by the resistance (R_0) of a non-interacting infinite chain at zero temperature at the particle-hole symmetric point with hybridization $\Gamma = 0.5$.

4.1. Half-Filling. When the gate voltage is set to 0, the junction is at the particle-hole symmetric point, meaning there are N electrons in it, with N being the length of the chain. In Figure 2, the resistance of a junction of length $N = 80$ at different interaction strengths is shown as a function of the temperature of the system. As expected, the non-interacting system is metallic; i.e., its resistance is a monotonically increasing function of the temperature and becomes linear at high temperatures. In this regime, the effect of the interaction is negligible as the energy

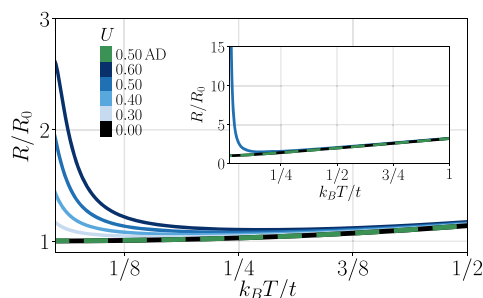


Figure 2. Normalized resistance of a junction of length $N = 80$ with different interaction strengths (solid line) and with the adiabatic functional with interaction strength $U = 0.5$ (dashed line) as a function of temperature. The temperature is defined in units of $k_B T/t$. The inset shows the resistance of the one site impurity model, where the functional coincides with the one in ref 39.

scale associated with temperature is much larger than interaction strength. The role of the interactions becomes more important at lower temperatures, where it hinders transport, resulting in an increase of the resistance due to the Coulomb blockade. Furthermore, Figure 2 shows that at half-filling a larger interaction strength results in higher resistance. This effect is due to the potential induced in the leads, which suppresses the bias voltage, effectively shrinking the transport window, resulting in a smaller current flowing through the junction. The adiabatic functional, in turn, gives rise to only a minimal (negligible) increase in the resistance and does not describe the Coulomb blockade physics, as it misses this nonlocal potential induced in the leads. As stated before, the correct Coulomb blockade physics of the single impurity model is caught by the functional;³⁹ see the inset of Figure 2.

When considering lower temperatures, a peculiar feature appears in the resistance of the junction shown as a softening of the Coulomb blockade effect. In the upper panel of Figure 3, we report the resistance of junctions of length $N = 80$ with different interaction and hybridization strengths: $U \in \{0.3, 0.4, 0.5\}$ and $\Gamma \in \{0.32, 0.5, 1.125\}$. The value of Γ determines the high-temperature behavior of the resistance, since the interaction becomes irrelevant when $T \gg U$, as observed above. We observe, as expected, a higher resistance for lower values of Γ , since this is related to the hopping amplitude to the leads, facilitating tunneling through the junction at higher values. For fixed Γ , the interaction strength dictates the temperature at

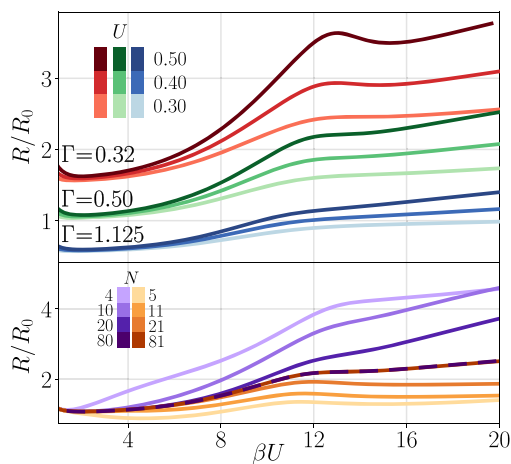


Figure 3. Upper panel: junction resistance as a function of βU for different interaction and hybridization strengths. Lower panel: convergence of the junction resistance as a function of the system length for $U = 0.5$ and $\Gamma = 0.5$.

which the system transitions to the Coulomb blockade regime and also the position of the softening feature. In particular, the feature appears at higher temperatures when there is a higher interaction. Moreover, for fixed U , the softening appears amplified as the hybridization strength deviates from the hopping t , linking this peculiar feature to the dynamics of the edge regions. In fact, even though finite size and odd–even effects affect the resistance of the junction, its qualitative behavior persists up to convergence with the system size; see the lower panel of Figure 3. In all the previous calculations, the shown results do not go down to $T = 0$; they stop in fact at $\beta U = 20$, as for example in Figure 3. This is due to practical difficulties in the convergence of the self-consistent exchange–correlation potential. Its determination is, in fact, a fixed point iteration with a function (ϵ_{Hxc}) highly nonlinear in the density and current. Moreover, the exchange–correlation potential is an oscillating function in a chain junction, stemming from the underlying Friedel’s oscillation of the non-interacting case. These complications are worsened at lower temperatures, where the Fermi–Dirac distribution becomes step-like, sharpening all the nontrivial features of the functional. An undamped self-consistent iteration, in fact, fails to converge as temperature goes down and cannot reach the regime where the Coulomb blockade is established. Advanced mixing schemes are needed to converge the functional at low temperatures: in this work, we use a Pulay mixing scheme.⁵¹ At each iteration, this method exploits the history of guesses for the quantity needed to establish a better guess for minimizing the error in the next iteration. In the presented results, the potential has been mixed with a history length of 9. This is found to give faster and more stable convergence for this problem.

4.2. Doped Regime. By applying a gate voltage to the chain junction, we can tune the number of particles occupying the system and move it away from the particle-hole symmetric point. This affects the transport properties of the system itself. Different functionals and/or different interaction strengths yield a different number of particles in the junction for a fixed gate potential. For this reason, we choose to compare results by

tuning the gate voltage to have a fixed number of electrons in the chain for all temperatures. In the top panel of Figure 4, we compare the resistances of a chain of length $N = 80$ with a fixed total number of particles $N_{\text{el}} = 60$ resulting from the adiabatic and nonadiabatic functionals at different interaction strengths. In accordance with ref 23, the nonadiabatic approximation yields a higher resistance. An additional distinction is given by

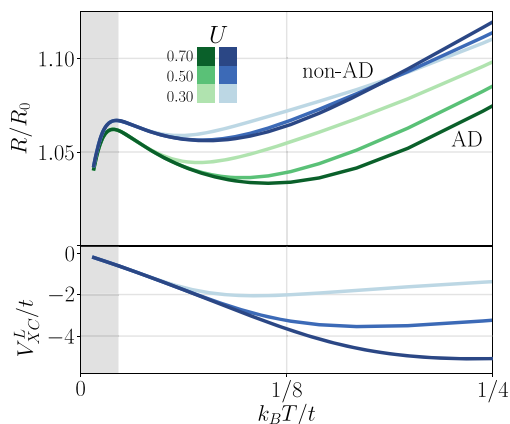


Figure 4. Upper panel: normalized resistance of a junction of length $N = 80$ at a fixed number of particles $N_{\text{el}} = 60$ as a function of $k_B T/t$ for different interaction strengths for the nonadiabatic functional (shades of blue) and the adiabatic functional (shades of green). Lower panel: potential induced in the left lead in units of t . The y-axis has been scaled by a factor of 10^3 . The gray shaded area displays the temperatures at which finite size effects occur.

the qualitative behavior of the resistances. While the adiabatic functional becomes less resistive as the interaction strength increases (behavior in agreement with mean-field results, not shown), the nonadiabatic approximation exhibits a crossover. In fact, the resistances for different interaction strengths cross at a temperature $k_B T/t \approx 0.18$. The decrease in the resistance for increasing interaction strength in the adiabatic functional is explained simply by the change induced in the transmission functions T_{tot} due to the exchange-correlation potential. For the nonadiabatic case, this effect competes with the suppression of the transport window caused by the nonlocal potential induced in the leads. At high temperatures, the transmission functions are unaltered by the interaction; hence, the effect of the bias renormalization, although small in amplitude, dominates. At a fixed temperature, $|V_{\text{xc}}^L|$ is larger for larger interaction strengths; this explains why larger U 's produce larger resistances. As temperature decreases, the two effects have comparable impacts and compete with one another. $|V_{\text{xc}}^L|$ starts decreasing roughly at a constant $k_B T/U$, meaning different temperatures for different interaction strengths; see the lower panel of Figure 4. This results in a stronger drop in the resistance for, e.g., $U = 0.70$ while the transport window suppression for weaker interaction is still growing, resulting in the crossing of the resistances. This effect is amplified as we move away from the particle-hole symmetric point, since by doing so the magnitude of the bias renormalization drops. At a fixed number of particles $N_{\text{el}} = 76$, in fact, the resistances do not cross and the results are similar to the ones at particle-hole symmetry.

5. CONCLUSIONS AND OUTLOOK

In this work, we have derived a novel nonadiabatic, nonlocal exchange-correlation potential for studying transport in devices modeled by lattice Hamiltonians within TD-DFT. Our exchange-correlation potential is based on the solution for a single quantum dot coupled to a reservoir, which exhibits a step-like feature important for the description of Coulomb blockade.³⁸

The derivation is built by exploiting gauge symmetry: the dynamics of a reservoir-dot device stay unchanged if a potential is applied to the dot or to the reservoir with opposite sign. For a generic lattice model, we apply this idea to every link through which a current flows, independent of whether it connects two sites or a site to a lead. The proposed functional reduces to the LDA²⁷ in the static limit; i.e., nonadiabaticity and nonlocality of the potential are linked closely together in our construction. In the nonequilibrium situation, our approximation reduces to the exact result for a single dot transport setup.³⁹

We have analyzed the effect of this exchange-correlation potential in chain systems connected by the ends to two reservoirs. We found that the “step” in the approximation for the effective potential makes it challenging to find a self-consistent solution for low temperatures/strong interactions, since the step sharpens as βU increases. First results for two-dimensional tight-binding models indicate that this is amplified for lattices with higher coordination. To this end, it would be interesting to develop alternative strategies for converging self-consistent approaches based on new insights.⁵² For one-dimensional tight-binding chains, we have shown how Coulomb blockade physics is well described by this functional as an effect of the suppression of the transport window due to an induced potential in the leads opposite to the voltage bias applied. At the particle-hole symmetric point, an additional feature appears at roughly constant βU , showing a softening of the Coulomb blockade effect. The amplitude of this softening depends on the decay rate of the leads Γ . Away from particle-hole symmetry, the nonadiabatic functional differs qualitatively from the LDA as the on-site attraction (repulsion) competes with the renormalization of the transport window produced by the nonlocality of the functional. We believe that TD-DFT for tight-binding models offers a numerically efficient scheme for studying transport in quantum systems approaching mesoscopic scales. The aim of this work was to propose an approximation for the effective potential taking electron–electron scattering effects into account, which are believed to play an important role in so-called superballistic transport and has recently received a lot of attention.^{53–55} An interesting route to explore is to study thermoelectric transport using a novel DFT approach proposed recently,^{50,56–59} by generalizing the exchange-correlation potential for describing the combined charge and energy flow through the transport device.

AUTHOR INFORMATION

Corresponding Authors

*E-mail: fabio.covito@mpsd.mpg.de.

*E-mail: angel.rubio@mpsd.mpg.de.

*E-mail: florian.eich@mpsd.mpg.de.

ORCID

Fabio Covito: 0000-0001-7103-5006

Angel Rubio: 0000-0003-2060-3151

Florian G. Eich: 0000-0002-0434-6100

Funding

We acknowledge financial support from the European Research Council (ERC-2015-AdG-694097) and Grupos Consolidados (IT1249-19).

Notes

The authors declare no competing financial interest.

REFERENCES

- (1) Aviram, A.; Ratner, M. A. Molecular rectifiers. *Chem. Phys. Lett.* **1974**, *29*, 277–283.
- (2) Reed, M. A.; Zhou, C.; Muller, C. J.; Burgin, T. P.; Tour, J. M. Conductance of a Molecular Junction. *Science* **1997**, *278*, 252–254.
- (3) Cuniberti, G.; Fagas, G.; Richter, K. Introducing Molecular Electronics: A Brief Overview. *Introducing Molecular Electronics; Lecture Notes in Physics* **2006**, *680*, 1.
- (4) Reddy, P.; Jang, S.-Y.; Segalman, R. A.; Majumdar, A. Thermoelectricity in Molecular Junctions. *Science* **2007**, *315*, 1568–1571.
- (5) Kim, K.; Chung, J.; Hwang, G.; Kwon, O.; Lee, J. S. Quantitative Measurement with Scanning Thermal Microscope by Preventing the Distortion Due to the Heat Transfer through the Air. *ACS Nano* **2011**, *5*, 8700–8709.
- (6) Kim, K.; Jeong, W.; Lee, W.; Reddy, P. Ultra-High Vacuum Scanning Thermal Microscopy for Nanometer Resolution Quantitative Thermometry. *ACS Nano* **2012**, *6*, 4248–4257.
- (7) Kim, Y.; Jeong, W.; Kim, K.; Lee, W.; Reddy, P. Electrostatic control of thermoelectricity in molecular junctions. *Nat. Nanotechnol.* **2014**, *9*, 881–885.
- (8) Mecklenburg, M.; Hubbard, W. A.; White, E. R.; Dhall, R.; Cronin, S. B.; Aloni, S.; Regan, B. C. Nanoscale temperature mapping in operating microelectronic devices. *Science* **2015**, *347*, 629–632.
- (9) Halbertal, D.; Cuppens, J.; Shalom, M. B.; Embon, L.; Shadmi, N.; Anahory, Y.; Naren, H. R.; Sarkar, J.; Uri, A.; Ronen, Y.; Myasoedov, Y.; Levitov, L. S.; Joselevich, E.; Geim, A. K.; Zeldov, E. Nanoscale thermal imaging of dissipation in quantum systems. *Nature* **2016**, *539*, 407–410.
- (10) Landauer, R. Spatial Variation of Currents and Fields Due to Localized Scatterers in Metallic Conduction. *IBM J. Res. Dev.* **1957**, *1*, 223–231.
- (11) Büttiker, M.; Imry, Y.; Landauer, R.; Pinhas, S. Generalized many-channel conductance formula with application to small rings. *Phys. Rev. B: Condens. Matter Mater. Phys.* **1985**, *31*, 6207–6215.
- (12) Landauer, R. Conductance determined by transmission: probes and quantised constriction resistance. *J. Phys.: Condens. Matter* **1989**, *1*, 8099.
- (13) Meir, Y.; Wingreen, N. S. Landauer formula for the current through an interacting electron region. *Phys. Rev. Lett.* **1992**, *68*, 2512–2515.
- (14) Stefanucci, G.; van Leeuwen, R. *Nonequilibrium Many-Body Theory of Quantum Systems: A Modern Introduction*; Cambridge University Press: Cambridge, 2013.
- (15) Hohenberg, P.; Kohn, W. Inhomogeneous Electron Gas. *Phys. Rev.* **1964**, *136*, B864–B871.
- (16) Kohn, W.; Sham, L. J. Self-Consistent Equations Including Exchange and Correlation Effects. *Phys. Rev.* **1965**, *140*, A1133–A1138.
- (17) Runge, E.; Gross, E. K. U. Density-Functional Theory for Time-Dependent Systems. *Phys. Rev. Lett.* **1984**, *52*, 997.
- (18) Marques, M. A. L.; Maitra, N. T.; Nogueira, F. M. S.; Gross, E. K. U.; Rubio, A., Eds. *Fundamentals of Time-Dependent Density Functional Theory*; Lecture Notes in Physics; Springer: Berlin, Heidelberg, 2012; Vol. 837.
- (19) Ullrich, C. A. *Time-Dependent Density-Functional Theory: Concepts and Applications*; Oxford Graduate Texts; Oxford University Press: Oxford, 2012.
- (20) Stefanucci, G.; Kurth, S.; Gross, E.; Rubio, A. In *Molecular and Nano Electronics: Analysis, Design and Simulation*; Seminario, J., Ed.; Theoretical and Computational Chemistry Supplement C; Elsevier, 2007; Vol. 17, pp 247–284.
- (21) Sai, N.; Zwolak, M.; Vignale, G.; Di Ventra, M. Dynamical Corrections to the DFT-LDA Electron Conductance in Nanoscale Systems. *Phys. Rev. Lett.* **2005**, *94*, 186810.
- (22) Koentopp, M.; Burke, K.; Evers, F. Zero-bias molecular electronics: Exchange-correlation corrections to Landauer's formula. *Phys. Rev. B: Condens. Matter Mater. Phys.* **2006**, *73*, 121403.
- (23) Vignale, G.; Di Ventra, M. Incompleteness of the Landauer formula for electronic transport. *Phys. Rev. B: Condens. Matter Mater. Phys.* **2009**, *79*, 014201.
- (24) Georges, A.; Kotliar, G.; Krauth, W.; Rozenberg, M. J. Dynamical mean-field theory of strongly correlated fermion systems and the limit of infinite dimensions. *Rev. Mod. Phys.* **1996**, *68*, 13–125.
- (25) Knizia, G.; Chan, G. K.-L. Density Matrix Embedding: A Simple Alternative to Dynamical Mean-Field Theory. *Phys. Rev. Lett.* **2012**, *109*, 186404.
- (26) Anderson, P. W. Localized Magnetic States in Metals. *Phys. Rev.* **1961**, *124*, 41–53.
- (27) Lima, N. A.; Silva, M. F.; Oliveira, L. N.; Capelle, K. Density Functionals Not Based on the Electron Gas: Local-Density Approximation for a Luttinger Liquid. *Phys. Rev. Lett.* **2003**, *90*, 146402.
- (28) Verdozzi, C. Time-Dependent Density-Functional Theory and Strongly Correlated Systems: Insight from Numerical Studies. *Phys. Rev. Lett.* **2008**, *101*, 166401.
- (29) Stefanucci, G.; Kurth, S. Towards a Description of the Kondo Effect Using Time-Dependent Density-Functional Theory. *Phys. Rev. Lett.* **2011**, *107*, 216401.
- (30) Tröster, P.; Schmitteckert, P.; Evers, F. Transport calculations based on density functional theory, Friedel's sum rule, and the Kondo effect. *Phys. Rev. B: Condens. Matter Mater. Phys.* **2012**, *85*, 115409.
- (31) Bergfield, J. P.; Liu, Z.-F.; Burke, K.; Stafford, C. A. Bethe Ansatz Approach to the Kondo Effect within Density-Functional Theory. *Phys. Rev. Lett.* **2012**, *108*, 066801.
- (32) Schmitteckert, P.; Dzierzawa, M.; Schwab, P. Exact time-dependent density functional theory for impurity models. *Phys. Chem. Chem. Phys.* **2013**, *15*, 5477–5481.
- (33) Kurth, S.; Stefanucci, G. Dynamical Correction to Linear Kohn-Sham Conductances from Static Density Functional Theory. *Phys. Rev. Lett.* **2013**, *111*, 030601.
- (34) Stefanucci, G.; Kurth, S. Kondo effect in the Kohn–Sham conductance of multiple-level quantum dots. *Phys. Status Solidi B* **2013**, *250*, 2378–2385.
- (35) Stefanucci, G.; Kurth, S. Steady-State Density Functional Theory for Finite Bias Conductances. *Nano Lett.* **2015**, *15*, 8020–8025.
- (36) Kurth, S.; Stefanucci, G. Nonequilibrium Anderson model made simple with density functional theory. *Phys. Rev. B: Condens. Matter Mater. Phys.* **2016**, *94*, 241103.
- (37) Karlsson, D.; Verdozzi, C. Effective bias and potentials in steady-state quantum transport: A NEGF reverse-engineering study. *J. Phys.: Conf. Ser.* **2016**, *696*, 012018.
- (38) Dittmann, N.; Spletstoesser, J.; Helbig, N. Nonadiabatic Dynamics in Single-Electron Tunneling Devices with Time-Dependent Density-Functional Theory. *Phys. Rev. Lett.* **2018**, *120*, 157701.
- (39) Kurth, S.; Stefanucci, G. Time-dependent i-DFT exchange-correlation potentials with memory: applications to the out-of-equilibrium Anderson model. *Eur. Phys. J. B* **2018**, *91*, 118.
- (40) Dittmann, N.; Helbig, N.; Kennes, D. M. Dynamics of the Anderson impurity model: Benchmarking a nonadiabatic exchange-correlation potential in time-dependent density-functional theory. *Phys. Rev. B: Condens. Matter Mater. Phys.* **2019**, *99*, 075417.
- (41) Zhu, Y.; Maciejko, J.; Ji, T.; Guo, H.; Wang, J. Time-dependent quantum transport: Direct analysis in the time domain. *Phys. Rev. B: Condens. Matter Mater. Phys.* **2005**, *71*, 075317.
- (42) Maciejko, J.; Wang, J.; Guo, H. Time-dependent quantum transport far from equilibrium: An exact nonlinear response theory. *Phys. Rev. B: Condens. Matter Mater. Phys.* **2006**, *74*, 085324.
- (43) Zheng, X.; Wang, F.; Yam, C. Y.; Mo, Y.; Chen, G. Time-dependent density-functional theory for open systems. *Phys. Rev. B: Condens. Matter Mater. Phys.* **2007**, *75*, 195127.

(44) Zhang, Y.; Chen, S.; Chen, G. First-principles time-dependent quantum transport theory. *Phys. Rev. B: Condens. Matter Mater. Phys.* **2013**, *87*, 085110.

(45) Verzijl, C. J. O.; Seldenthuis, J. S.; Thijssen, J. M. Applicability of the wide-band limit in DFT-based molecular transport calculations. *J. Chem. Phys.* **2013**, *138*, 094102.

(46) Shi, P.; Hu, M.; Ying, Y.; Jin, J. Noise spectrum of quantum transport through double quantum dots: Renormalization and non-Markovian effects. *ALP Adv.* **2016**, *6*, 095002.

(47) Bâldea, I. Invariance of molecular charge transport upon changes of extended molecule size and several related issues. *Beilstein J. Nanotechnol.* **2016**, *7*, 418–431.

(48) Tuovinen, R.; Perfetto, E.; Stefanucci, G.; van Leeuwen, R. Time-dependent Landauer-Büttiker formula: Application to transient dynamics in graphene nanoribbons. *Phys. Rev. B: Condens. Matter Mater. Phys.* **2014**, *89*, 085131.

(49) Ridley, M.; MacKinnon, A.; Kantorovich, L. Current through a multilead nanojunction in response to an arbitrary time-dependent bias. *Phys. Rev. B: Condens. Matter Mater. Phys.* **2015**, *91*, 125433.

(50) Covito, F.; Eich, F. G.; Tuovinen, R.; Sentef, M. A.; Rubio, A. Transient Charge and Energy Flow in the Wide-Band Limit. *J. Chem. Theory Comput.* **2018**, *14*, 2495–2504.

(51) Pulay, P. Convergence acceleration of iterative sequences. the case of scf iteration. *Chem. Phys. Lett.* **1980**, *73*, 393–398.

(52) Penz, M.; Laestadius, A.; Tellgren, E. I.; Ruggenthaler, M. Guaranteed Convergence of a Regularized Kohn-Sham Iteration in Finite Dimensions. *Phys. Rev. Lett.* **2019**, *123*, 037401.

(53) Guo, H.; Ilseven, E.; Falkovich, G.; Levitov, L. S. Higher-than-ballistic conduction of viscous electron flows. *Proc. Natl. Acad. Sci. U. S. A.* **2017**, *114*, 3068.

(54) Krishna Kumar, R.; Bandurin, D. A.; Pellegrino, F. M. D.; Cao, Y.; Principi, A.; Guo, H.; Auton, G. H.; Ben Shalom, M.; Ponomarenko, L. A.; Falkovich, G.; Watanabe, K.; Taniguchi, T.; Grigorieva, I. V.; Levitov, L. S.; Polini, M.; Geim, A. K. Superballistic flow of viscous electron fluid through graphene constrictions. *Nat. Phys.* **2017**, *13*, 1182.

(55) Braem, B. A.; Pellegrino, F. M. D.; Principi, A.; Rösli, M.; Gold, C.; Hennel, S.; Koski, J. V.; Berl, M.; Dietsche, W.; Wegscheider, W.; Polini, M.; Ihn, T.; Ensslin, K. Scanning gate microscopy in a viscous electron fluid. *Phys. Rev. B: Condens. Matter Mater. Phys.* **2018**, *98*, 241304.

(56) Eich, F. G.; Di Ventra, M.; Vignale, G. Density-Functional Theory of Thermoelectric Phenomena. *Phys. Rev. Lett.* **2014**, *112*, 196401.

(57) Eich, F. G.; Principi, A.; Di Ventra, M.; Vignale, G. Luttinger-field approach to thermoelectric transport in nanoscale conductors. *Phys. Rev. B: Condens. Matter Mater. Phys.* **2014**, *90*, 115116.

(58) Eich, F. G.; Di Ventra, M.; Vignale, G. Temperature-driven transient charge and heat currents in nanoscale conductors. *Phys. Rev. B: Condens. Matter Mater. Phys.* **2016**, *93*, 134309.

(59) Eich, F. G.; Di Ventra, M. D.; Vignale, G. Functional theories of thermoelectric phenomena. *J. Phys.: Condens. Matter* **2017**, *29*, 063001.

Chapter 4

Conclusion

In this thesis I presented the progress I achieved in the study of electron dynamics in many-body interacting systems. A novel first-principles method based on non-equilibrium Green's functions is put forward. While conventional NEGF-based approaches succeed in describing correlated physics, they become computationally prohibitive for virtually all non-trivial systems. The proposed method pushes the limits of what can be achieved in terms of system size and propagation time by introducing approximations which have minimal impact on accuracy while yielding a major speed-up in terms of computation time. The main simplification involves identifying and selecting only the electronic transitions dominating the dynamics for the studied phenomena without affecting the accuracy to which they are described. Having a reduced set of transitions directly translates into a lower computational complexity in the calculation of the self-energy—the main bottleneck of NEGF simulations. The underlying idea is general and independent of the system studied or the level of approximation chosen for the self-energy.

The selection of the transitions, or equivalently the Coulomb integrals v_{ijkl} , contributing to the self-energy, is based on physical grounds. In fact, the 2B self-energy depends quadratically on Coulomb integrals, justifying the exclusion of elements $\ll 1$. This argument is further exploited when considering transitions that scatter occupied states into the less localized unoccupied or unbound ones. The associated Coulomb integrals responsible for these processes, in fact, plummet with the number of unoccupied/unbound states involved in the scattering, arising from their small overlap with bound states. Considering transitions involving at

most one unoccupied/unbound state greatly reduces the computational burden of calculating the self-energy. Additionally, we showed how, within the GKBA, we can take advantage of this approximation to reduce the size of the propagated density matrix. In the case of the Auger decay, in fact, one can treat the unbound states representing the outgoing Auger electron on a different footing, finally leading to only including their occupation in the equation of motion, instead of all the off-diagonal elements associated with them. I proved that this method, named coupled NEGF approach, can be successfully employed to describe real-time Auger decay in ultrafast charge migration (UCM) processes in atomic systems, comparing it with conventional NEGF+GKBA and Configuration Interaction calculations. Additionally, I predicted a highly asymmetric spatial profile of the Auger wavepacket exhibiting temporal ripples, whose period depends on the energy of the Auger electron. Making use of the same method, I subsequently analyzed UCM in the Adenine molecule to study its behavior under the influence of extreme ultraviolet (XUV) radiation. Under normal conditions, interaction with XUV light causes the ionization of Adenine, eventually leading to fragmentation. My study shed light on recent experimental evidence of a possible stabilization path involving particular correlation-driven shake-up transitions. The states populated by these transitions can be accessed and ionized by a secondary near-infrared (NIR) pulse, providing a viable relaxation pathway leaving the molecule intact.

Returning to the calculation of the self-energy, we analyzed an efficient scheme for its calculation at the 2B level based on rewriting its expression through the use of tensor contractions. By using commonly available low-level linear algebra libraries, we were able to demonstrate a speed-up in the computation of the self-energy compared to the naïve evaluation of its expression. This translates into a more advantageous scaling of the computation time of the self-energy with respect to the size of the basis used for the simulations, decreasing from N^5 to $\sim N^{4.3}$.

Although the proposed method greatly pushes the domain of applicability of NEGF-based approaches, large systems up to the micron scale are still out of reach. In this context a more efficient method is TDDFT. Virtually all modern applications of TDDFT make use of adiabatic functionals, which, opposed to the self-energies of NEGF, completely disregard memory effects. These are vital for the description

of strongly correlated physical phenomena. Understanding how non-adiabaticity plays a role in TDDFT, is therefore an important line of research. In this work, I explored this subject within the study of thermo-electric transport in nanoscale devices. To this extent I first analyzed the implications of the commonly used WBL approximation on the charge and heat flow through non-interacting nano-junctions, finding a pathological behavior of these currents under certain circumstances. In particular, the heat current exhibits a discontinuity when a potential quench is applied to the device. More strikingly, When a temperature gradient is present, the charge current is found to be discontinuous while the heat current shows a divergence at short times. Subsequently, I more closely investigated the role of memory by proposing a non-adiabatic exchange-correlation functional for general lattice models within transport setups. The construction is based on known results for a simple dot-reservoir system and generalized through the use of symmetry arguments. The potential is shown to correctly describe Coulomb blockade physics while being applicable to a large class of model systems.

From my perspective, the future of the theoretical study of non-equilibrium electron dynamics is bright and full of possibilities. In the context of the coupled NEGF approach, a direct step forward would be its application for the study of more complex correlation-driven phenomena, e.g. UCM and Auger decay in chemically and biologically relevant molecules, Resonant-inelastic X-ray Scattering (RIXS), and so on. As an example, the latter would involve the inclusion of photonic and phononic degrees of freedom. This makes the problem much more complicated and the method itself has to be assessed in these conditions ¹.

Additionally, while the proposed NEGF method is general and can be applied in these contexts, problems arise in the construction of the basis to perform the NEGF calculations. In fact, the description of both core and continuum states and the calculation of the relative Coulomb integrals is a complicated task. The complication comes from the heavily localized character of core states, which require dense grids to be resolved and from the heavily delocalized features of continuum states, demanding large spaces for the simulations. The accuracy needed for the

¹The interest sparked by this complex, yet attractive problem has led to the beginning of a new PhD project, in which I will also be involved.

construction of basis is therefore not directly achievable even with state-of-the-art simulation codes. This stems from the nature of the Coulomb integrals, depending on the overlap of the states, which, as explained require great resolution. The coupled NEGF approach can also be extended to deal with periodic systems. In this case, the implications of the employed approximations are to be tested and understood in the context of extended systems, where the assumption made in finite systems may not apply. Moreover, the inclusion of nuclear motion and/or quantized electromagnetic fields in the proposed framework is highly non-trivial and the approximations introduced have to be generalized in order to hold in this case.

Finally, it is important to highlight the connection between NEGF and TD-DFT. In fact, within the GKBA, the central quantity of the NEGF equations becomes the density matrix, whose diagonal in a real space basis is the electron density of TDDFT². The density matrix, then, appears in the collision integrals encoding the effect of correlations on the dynamics. Therefore, a joint effort to unravel the characteristics of non-adiabaticity and correlation might be an ambitious, yet exciting path to pursue. A possible way of attacking the problem could be to combine the coupled NEGF approach with the linearized Sham-Schlüter equation to gain insight into correlations and, possibly, generating non-adiabatic approximations for the exchange-correlation functionals of TDDFT. This would, indeed, be a formidable accomplishment as the combined approach would profit from the efficiency of TDDFT while harnessing the accurate description of correlations of NEGF.

²This is not true, in principle, since the Green's functions are defined as statistical averages. Although, we are evolving our density matrix starting from a pure state in NEGF, as it is done in TDDFT, justifying the equality.

Contribution of the author

This thesis contains the work performed by the author during his Ph.D. at the Max Planck Institute for the Structure and Dynamics of Matter of Hamburg, in the Theory department and at the university of Hamburg. The idea at the basis of the main project of the thesis, regarding the contents of Chapter 2 and the respective publications, was conceived by and evolved through the discussions between Angel Rubio, Gianluca Stefanucci, Enrico Perfetto and the author. The complementary project, regarding the contents of Chapter 3 and the respective publications, was inspired and initiated by the discussions between Florian Eich, Angel Rubio and the author. In the following the contributions of the authors to the publications presented in this thesis are specified, even though the precise extent of each individual to the crucial discussions leading to a publication cannot, in general, be specified.

Publication I: The method has been developed by G. Stefanucci and E. Perfetto with contributions from the author. The simulations and testing were performed by the author. All authors contributed to the analysis of the data and to the formulation of the manuscript.

Publication II: The simulations and testing were performed by the author. The data analysis was performed by the author. All authors contributed to the discussion of the results and the writing the manuscript.

Publication III: The simulations were performed by R. Tuovinen with the help of the author. All authors contributed to writing the manuscript.

Publication IV: Concerning the theoretical part of the study, the rate equations model has been developed by S. Latini and A. Rubio and the NEGF simulations were performed and tested by the author. The experiments were done by the group of Prof. Calegari. All authors contributed to the analysis of the results and the writing of the manuscript. There is an extension of the theoretical results presented here to all DNA bases that will be sent for publication soon and where the author has played a fundamental role in obtaining the results and analyzing

them.

Publication V: The derivation of the analytic results was carried out by F. G. Eich together with the author and R. Tuovinen. The simulations in the WBLA were performed by the author, while the calculations using the full embedding self-energy were performed by F. G. Eich with the help of the author. All authors contributed to the analysis of the results and the formulation of the manuscript.

Publication VI: The derivation of the exchange-correlation potential was carried out by F. G. Eich together with the author. The simulations were performed by the author. All authors contributed to the analysis of the results and to the formulation of the manuscript.

Bibliography

- [1] E. Schrödinger, *Physical Review* **1926**, 28, 1049–1070.
- [2] A. L. Schawlow, C. H. Townes, *Phys. Rev.* **1958**, 112, 1940–1949.
- [3] T. H. Maiman, *Nature* **1960**, 187, 493–494.
- [4] F. Krausz, M. Ivanov, *Rev. Mod. Phys.* **2009**, 81, 163–234.
- [5] M. Born, R. Oppenheimer, *Annalen der Physik* **1927**, 389, 457–484.
- [6] C. Cohen-Tannoudji, J. Dupont-Roc, G. Grynberg, *Frontmatter*, John Wiley & Sons, Ltd, **2008**.
- [7] F. Faisal, *Theory of Multiphoton Processes, of Physics of Atoms and Molecules*, Springer US, **2013**.
- [8] C. D. Sherrill, H. F. Schaefer, Vol. 34 of *Advances in Quantum Chemistry*, P.-O. Löwdin, J. R. Sabin, M. C. Zerner, E. Brändas (Eds.), Academic Press, **1999**, pp. 143 – 269.
- [9] P. Hohenberg, W. Kohn, *Phys. Rev.* **1964**, 136, B864–B871.
- [10] W. Kohn, L. J. Sham, *Phys. Rev.* **1965**, 140, A1133–A1138.
- [11] J. Paldus, J. Čížek, I. Shavitt, *Phys. Rev. A* **1972**, 5, 50–67.
- [12] M. Caffarel, P. Claverie, *The Journal of Chemical Physics* **1988**, 88, 1088–1099.
- [13] A. Georges, G. Kotliar, W. Krauth, M. J. Rozenberg, *Rev. Mod. Phys.* **1996**, 68, 13–125.

- [14] G. Stefanucci, R. van Leeuwen, *Nonequilibrium Many-Body Theory of Quantum Systems: A Modern Introduction*, Cambridge University Press, **2013**.
- [15] L. Kadanoff, G. Baym, *Quantum statistical mechanics: Green's function methods in equilibrium and nonequilibrium problems*, of *Frontiers in physics*, W.A. Benjamin, **1962**.
- [16] P. C. Martin, J. Schwinger, *Phys. Rev.* **1959**, *115*, 1342–1373.
- [17] G. Baym, L. P. Kadanoff, *Phys. Rev.* **1961**, *124*, 287–299.
- [18] L. V. Keldysh, *Zh. Eksp. Teor. Fiz.* **1964**, *47*, 1515–1527, [*Sov. Phys. JETP*20,1018(1965)].
- [19] P. Danielewicz, *Annals of Physics* **1984**, *152*, 239 – 304.
- [20] E. Runge, E. K. U. Gross, *Phys. Rev. Lett.* **1984**, *52*, 997–1000.
- [21] K. Balzer, M. Bonitz, *Nonequilibrium Green's Functions Approach to Inhomogeneous Systems, Vol. 867*, Springer Berlin Heidelberg, **2013**.
- [22] G. C. Wick, *Phys. Rev.* **1950**, *80*, 268–272.
- [23] P. Myöhänen, A. Stan, G. Stefanucci, R. van Leeuwen, *EPL (Europhysics Letters)* **2008**, *84*, 67001.
- [24] A.-M. Uimonen, E. Khosravi, A. Stan, G. Stefanucci, S. Kurth, R. van Leeuwen, E. K. U. Gross, *Phys. Rev. B* **2011**, *84*, 115103.
- [25] M. Bonitz, D. Kremp, D. C. Scott, R. Binder, W. D. Kraeft, H. S. Köhler, *Journal of Physics: Condensed Matter* **1996**, *8*, 6057–6071.
- [26] M. Bonitz, D. Semkat, H. Haug, *The European Physical Journal B - Condensed Matter and Complex Systems* **1999**, *9*, 309–314.
- [27] K. Balzer, S. Hermanns, M. Bonitz, *Journal of Physics: Conference Series* **2013**, *427*, 012006.
- [28] E. Perfetto, A.-M. Uimonen, R. van Leeuwen, G. Stefanucci, *Journal of Physics: Conference Series* **2016**, *696*, 012004.

- [29] N. E. Dahlen, R. van Leeuwen, *Phys. Rev. Lett.* **2007**, *98*, 153004.
- [30] E. Perfetto, D. Sangalli, A. Marini, G. Stefanucci, *Phys. Rev. B* **2016**, *94*, 245303.
- [31] P. Lipavský, V. Špička, B. Velický, *Phys. Rev. B* **1986**, *34*, 6933–6942.
- [32] H. Haug, *physica status solidi (b)* **1992**, *173*, 139–148.
- [33] H. S. Köhler, *Phys. Rev. E* **1996**, *53*, 3145–3153.
- [34] R. Binder, H. S. Köhler, M. Bonitz, N. Kwong, *Phys. Rev. B* **1997**, *55*, 5110–5116.
- [35] Q. T. Vu, H. Haug, *Phys. Rev. B* **2000**, *62*, 7179–7185.
- [36] H. Haug, A.-P. Jauho, *Quantum Kinetics in Transport and Optics of Semiconductors*, Springer Berlin Heidelberg, Berlin, Heidelberg, **2008**.
- [37] G. Pal, Y. Pavlyukh, W. Hübner, H. C. Schneider, *The European Physical Journal B* **2011**, *79*, 327–334.
- [38] A. Marini, *Journal of Physics: Conference Series* **2013**, *427*, 012003.
- [39] M. Cini, *Solid State Communications* **1977**, *24*, 681 – 684.
- [40] G. A. Sawatzky, *Phys. Rev. Lett.* **1977**, *39*, 504–507.
- [41] C. Verdozzi, M. Cini, A. Marini, *Journal of Electron Spectroscopy and Related Phenomena* **2001**, *117-118*, 41 – 55, Strongly correlated systems.
- [42] V. Strassen, *Numerische Mathematik* **1969**, *13*, 354–356.
- [43] E. Perfetto, G. Stefanucci, *physica status solidi (b)* **2019**, *256*, 1800573.
- [44] L. Cederbaum, J. Zobeley, *Chemical Physics Letters* **1999**, *307*, 205 – 210.
- [45] M. Drescher, M. Hentschel, R. Kienberger, M. Uiberacker, V. Yakovlev, A. Scrinzi, U. Westerwalbesloh, Thand Kleineberg, U. Heinzmann, F. Krausz, *Nature* **2002**, *419*, 803–807.

- [46] V. Averbukh, P. Demekhin, P. Kolorenč, S. Scheit, S. Stoychev, A. Kuleff, Y.-C. Chiang, K. Gokhberg, S. Kopelke, N. Sisourat, L. Cederbaum, *Journal of Electron Spectroscopy and Related Phenomena* **2011**, *183*, 36 – 47, Electron Spectroscopy Kai Siegbahn Memorial Volume.
- [47] F. Calegari, D. Ayuso, A. Trabattoni, L. Belshaw, S. De Camillis, S. Anumula, F. Frassetto, L. Poletto, A. Palacios, P. Decleva, J. B. Greenwood, F. Martín, M. Nisoli, *Science* **2014**, *346*, 336–339.
- [48] R. van Leeuwen, *International Journal of Modern Physics B* **2001**, *15*, 1969–2023.
- [49] C. Ullrich, *Time-Dependent Density-Functional Theory: Concepts and Applications*, of *Oxford Graduate Texts*, OUP Oxford, **2011**.
- [50] M. Marques, N. Maitra, F. Nogueira, E. Gross, A. Rubio, *Fundamentals of Time-Dependent Density Functional Theory*, of *Lecture Notes in Physics*, Springer Berlin Heidelberg, **2012**.
- [51] M. Ruggenthaler, J. Flick, C. Pellegrini, H. Appel, I. V. Tokatly, A. Rubio, *Phys. Rev. A* **2014**, *90*, 012508.
- [52] M. Ruggenthaler, N. Tancogne-Dejean, J. Flick, H. Appel, A. Rubio, *Nature Reviews Chemistry* **2018**, *2*, 0118 EP –, Review Article.
- [53] M. Levy, *Phys. Rev. A* **1982**, *26*, 1200–1208.
- [54] E. H. Lieb, *International Journal of Quantum Chemistry* **1983**, *24*, 243–277.
- [55] D. Rappoport, N. R. M. Crawford, F. Furche, K. Burke, *Which functional should I choose?*, E. I. Solomon, R. B. King, R. A. Scott (Eds.), Wiley, Chichester. Hoboken: Wiley, John & Sons, Inc., **2009**.
- [56] P. Elliott, J. I. Fuks, A. Rubio, N. T. Maitra, *Phys. Rev. Lett.* **2012**, *109*, 266404.
- [57] Y. Suzuki, L. Lacombe, K. Watanabe, N. T. Maitra, *Phys. Rev. Lett.* **2017**, *119*, 263401.

- [58] R. Landauer, *IBM J. Research and Development* **1957**, *1*, 223–231.
- [59] M. Büttiker, Y. Imry, R. Landauer, S. Pinhas, *Phys. Rev. B* **1985**, *31*, 6207–6215.
- [60] N. D. Lang, P. Avouris, *Phys. Rev. Lett.* **1998**, *81*, 3515–3518.
- [61] J. Taylor, H. Guo, J. Wang, *Phys. Rev. B* **2001**, *63*, 121104.
- [62] G. Stefanucci, C.-O. Almbladh, *Europhysics Letters (EPL)* **2004**, *67*, 14–20.
- [63] R. Tuovinen, E. Perfetto, G. Stefanucci, R. van Leeuwen, *Phys. Rev. B* **2014**, *89*, 085131.
- [64] J. M. Luttinger, *Phys. Rev.* **1964**, *135*, A1505–A1514.
- [65] F. G. Eich, M. Di Ventura, G. Vignale, *Phys. Rev. Lett.* **2014**, *112*, 196401.
- [66] F. G. Eich, A. Principi, M. Di Ventura, G. Vignale, *Phys. Rev. B* **2014**, *90*, 115116.
- [67] F. G. Eich, M. Di Ventura, G. Vignale, *Phys. Rev. B* **2016**, *93*, 134309.
- [68] F. G. Eich, M. D. Ventura, G. Vignale, *Journal of Physics: Condensed Matter* **2017**, *29*, 063001.
- [69] N. Dittmann, J. Splettstoesser, N. Helbig, *Phys. Rev. Lett.* **2018**, *120*, 157701.
- [70] S. Kurth, G. Stefanucci, *The European Physical Journal B* **2018**, *91*, 118.
- [71] G. Xianlong, A.-H. Chen, I. V. Tokatly, S. Kurth, *Phys. Rev. B* **2012**, *86*, 235139.